A Density Functional Study of Point Defects in Nanoelectronic Materials

by Meaad Salim Al-Hadidi

A thesis submitted to Newcastle University for the degree of Doctor of Philosophy.
September 2015.

Dedicated to

My family and my beloved parents

Declaration

This thesis has not previously been submitted by the candidate for a degree in this or any other university.

Meaad Al-Hadidi

September 2015.

Certificate

This is to certify that the entitled thesis "A Density Functional Study of Point Defects in Nanoelectronic Materials" has been prepared under my supervision at the school of Electrical and Electronic Engineering /Newcastle University for the degree of PhD in the field of ((Nanoelectronics) Nanoscale and Technology).

Signature
Supervisor: Dr Jonathan Goss
Date:

Signature
Student: Meaad Salim Al-Hadidi
Date:

Acknowledgements

After God, I would like to express my gratitude to my supervisors Dr. Jonathan Goss and Prof. Patrick Briddon for their support and advice throughout this project. It has been a great pleasure to work with them. Thank you.

During this PhD, I have had the privilege to work with exceptional colleagues and friends in the Emerging Technologies and Materials (ETM) research group and Aimpro group. In particular, I would like to thank Dr. Raied Al-Hamadany, Dr. Mariam Ahmed, Dr. Fernando Urena, Dr. Andrew Lawson, Sami Ramadan, Dr. Amit Tiwari, Dr. Mohammed Atumi, Dr.Fadil Shrif, Oras Al-ani, Dr. Abdusalam Gsiea and Chloe Peaker for sharing their knowledge and experience and for long friendly discussions.

I would like to give my special thanks to my family for their unconditional love and for always believing in me. I am especially grateful to my husband Fairs Al-Hamdany, who has been my best friend. I am lucky to have him as husband.

Most especially I thank my mother, sisters and brothers without whose love and support, and even tears, I could never have been who I am now.

Finally, I would also like to thank Iraqi Ministry of Higher Education and Scientific Research (MOHESR), University of Mosul for the financial support. A special word of thanks goes to all the personnel at Iraqi Ministry of Higher Education and Scientific Research, Iraqi cultural attache/London and University of Mosul for their administrative efforts.

Abstract

Materials used in technology, from the development of nano-electronics to the efficient conversion of solar energy to electrical power are under constant optimisation. The factors that govern the size of field effect transistors, such as leakage current through the gate or the on-state power consumption, and those that impact upon the efficiency of optoelectronic devices such as non-radiative recombination and device aging arising from defect migration are specific to the elements and compounds deployed in these devices. Defects, whether intentionally incorporated such as electrical doping, or unintentional contamination such as oxygen in silicon, may have a qualitative impact upon the materials properties (*e.g.* conductivity), or limits in processing that need to be accommodated in both the manufacture of devices, and in their operation.

Device miniaturisation for CPUs and photovoltaic efficiency improvements are two areas developing in parallel for which a detailed understanding of the composition and evolution of defects, dopants and impurities are particularly important.

In the project presented in this thesis, first principles density functional calculations within a supercell approach have been performed, with particular focus on selected impurities in a range of technologically relevant materials, where the impurities are likely to be incorporated due to their presence in the growth environment. The host materials are divided into those relevant for nano-electronic devices and high capacitance structures, being the perovskite titanates ($SrTiO_3$, $BaTiO_3$ and $PbTiO_3$), and material that has a role in the energy sector in photovoltaic cells, being cadmium

telluride (CdTe).

In the case of the titanate films, it is important to recognise that thin films are often grown using organic precursors, and therefore carbon contamination is of key importance. Although it is generally assumed that carbon is incorporated in such materials in the form of carbonates, the results of the calculations performed for this study challenge this, showing that a distribution of multiple sites occurs, depending upon growth conditions and the Fermi level. Observable calculated for these structures, including their electrical properties and vibrational modes are presented to aid the identification of the carbon sites in future experimental studies. Critically, carbon substitution at the Sr, Ba or Pb site leads to electrical effects not present for Ti substitution. The similarities and differences between the three titanates are reviewed.

For CdTe, it has long been understood that oxygen is a common impurity grown in thin-films, occurring in high concentrations across a range of growth methods. Vibrational modes observed in experiment at 1096.78 and 1108.35 cm^{-1} have been variously assigned to oxygen-containing point defects, but most recently to SO_2 molecules dissolved in the lattice. However, the precise structure and location of these centres, as well as the electrical properties of the defect, are yet to be determined. As with the analysis of carbon in the titanates, density-functional simulations of SO_2 in various locations in CdTe show that several possible structures are low in energy, with the equilibrium form depending upon growth conditions and the Fermi-level. It is shown that a plausible candidate for the vibrational centre is an interstitial species, based upon the frequencies and isotopic splittings.

Contents

List of Figures

List of Tables

Publications and Conferences

List of Publications

1. Raied AL-Hamadany, J. P. Goss, P. R. Briddon, Shahin A. Mojarad, **Meaad AL-Hadidi**, A. G. O'Neill and M. J. Rayson, Oxygen vacancy migration in compressively strained $SrTiO_3$, *J. Appl. Phys.* **113**, 024108, (2013).

2. **Meaad AL-Hadidi**, J. P. Goss, P. R. Briddon, Raied AL-Hamadany and Mariam Ahmed, Carbon at the Ti site in strontium titanate from first principles, *Journal of Physics: Conference Series* **472**, 012006, (2013).

3. **Meaad AL-Hadidi**, J. P. Goss, P. R. Briddon, Raied AL-Hamadany, Mariam Ahmed and M. J. Rayson, Carbon impurities in $SrTiO_3$ from first principles, *Modelling Simul. Mater. Sci. Eng.* **23**, 015002, (2015).

List of Conferences

1. **Annual Research Conference 2012 (ARC-2012)**, 25 - 26 January 2012, School of Electrical & Electronic Engineering, Newcastle University, Newcastle upon Tyne, UK. **(Oral presentation)**

2. **19^{th} Workshop on Oxide Electronics (WOE19)**, 30 September - 3 October 2012, Palace't Loo, Apeldoorn, Netherlands. **(Poster presentation)**

3. **Ferroelctric UK 2013**, 17 - 18 January 2013, University of Sheffield, Sheffield, UK. **(Poster presentation)**

4. **Annual Research Conference 2013 (ARC-2013)**, 21 - 22 January 2013, School of Electrical & Electronic Engineering, Newcastle University, Newcastle upon Tyne, UK. **(Oral presentation)**

5. **Dielectric 2013**, 10 - 12 April 2013, Univesity of Reading, Reading, UK. **(Poster presentation)**

6. **AIMPRO.2013**, 3 - 7 June 2013, University of Surrey, Guildford, UK. **(Poster presentation)**

7. **EURODIM 2014**, 13 - 19 July 2014, Univesity of Kent, Canterbury, UK. **(Poster presentation)**

Chapter 1

Introduction

Global technology and modern industries are often looking for new materials to improve the performance of electrical devices, trying to make them faster, lower in power consumption, more efficient and smaller. For several decades, the dominant material in electronic applications has been silicon. This is partly due to the fact that its native oxide allows for the production of a dielectric from the same material as that which comprises the electrically active regions, as in the field of transistor applications, for example, and this material is low in impurities, optically transparent, low cost and suitable for a wide range of operating temperatures. However, silicon suffers from a number of problems which mean that it is highly desirable to move towards different materials in specific applications. In the context of optical materials, bulk silicon, due to its indirect band-gap, is of no practical use as an optical emitter, and as a consequence most light-emitting solid-state devices are manufactured from compound semiconductors such as CdTe and gallium arsenide (GaAs). The semiconductor CdTe is an important compound used in photovoltaic (PV) devices, particularly solar cells. CdTe is the only thin film photovoltaic technology which surpasses crystalline silicon PV in terms of lower cost and flexibility.

Even in the applications where silicon has traditionally been an effective material, problems are emerging, driven predominantly by the desire to continually miniaturize device components into thicknesses of a few nanometres. As length scales become

smaller, the advantages of silicon native oxide as a material are lost as the required thickness of the gate dielectrics mean that devices are prone to breaking down. This has led to substantial efforts to produce alternative dielectric materials that can be integrated with conventional electronic materials such as silicon. Of these, possibly the most promising are the metal-oxides, such as TiO_2, HfO_2, and perovskite titanates such as $SrTiO_3$, $BaTiO_3$ and $PbTiO_3$. However, the optical and electrical properties of these materials are much less understood than for silicon, with specific problems arising in the reproducibility of doping, and knowledge is lacking concerning the microscopic structure of the defects responsible for the conduction that is obtained.

Contributing to the development of these materials, computational methods have proved to be effective in the determination of the properties of materials. They have a long history of applications in the study of materials used in different kinds of technology. Numerous properties of materials can now be determined from first-principles, providing new insights into critical problems in physics, chemistry and materials science. Amongst the first-principles approaches, density functional theory has become one of the most widely used methods. This method may be used to predict the properties of new materials as well as to model the properties of existing systems.

In this project, the use of state-of-the-art simulation software based on quantum-mechanical density functional theory will allow for the investigation of electronic materials in the contexts of semiconductors and dielectrics, with a particular focus on the likely impurities to be incorporated due to their presence in the growth environment. The host materials have been divided into those relevant for nano-electronic devices and high capacity capacitors, which are the perovskite titanates ($SrTiO_3$, $BaTiO_3$ and $PbTiO_3$), and a material that has a role in the energy sector in photovoltaic cells, cadmium telluride (CdTe).

1.1 Thesis structure

The thesis is divided into three parts; concerning theory and AMPRO modelling, applications, and conclusions and future work. Each part is divided into chapters and a summary of the contents of each chapter is provided below, along with general references that might be helpful to the reader.

1.1.1 Part I - Theory and method

Part I outlines the methodology employed in order that the semiconductor problem of interest can be understood.

Chapter 2 - Computational background and the AIMPRO package

In this chapter, a brief overview is provided of quantum mechanics density functional theory and some approximations required to identify the ground state of a system of electrons and ions in interaction are demonstrated. However, the main aim is to discuss the AIMPRO formalism, including the methods and approximations adopted for the calculations of experimental observables.

Chapter 3 -The AIMPRO calculation of observables

Based upon the fundamental approximations highlighted in chapter 2, there are additional approximations in their application, such as local vibrational modes, electrical levels and thermodynamic stability. This chapter focuses on a number of the more commonly used experimental techniques and explains the relationships which link density functional theory with the relevant experimental techniques.

These background chapters are followed by four chapters containing the results of the *ab initio* calculations.

1.1.2 Part II - Applications

This part includes the results of *ab initio* calculations which have been obtained using the `AIMPRO` modelling package. These results are discussed in the context of the relevant experimental results.

Chapter 4 - Carbon impurities in strontium titanate

Given the potential importance of carbon contamination, and the relative paucity of theoretical data, first principles calculations have been performed on the geometry, electrical levels, electronic structure, vibrational modes, reorientation barriers and formation energies of carbon defects for different sites in $SrTiO_3$.

Chapter 5 - Carbon impurities in lead titanate

This chapter considers the role of carbon impurities in tetragonal $PbTiO_3$. The structural, electrical, electronic, vibrational and energetic properties of carbon defects for different sites in tetragonal $PbTiO_3$ have been studied. The results for each of the most plausible configurations are presented, and a simple thermodynamical model is applied to determine which are most likely to appear in practice.

Chapter 6 - Carbon impurities in barium titanate

Again, the role of carbon impurities in perovskite titanate with different material and structure, rhombohedral $BaTiO_3$, has been investigated. The first principles calculations in the frame of density functional theory have been used to determine the accurate formation energy of pure $BaTiO_3$, and then this is extended to explore the stable structures of carbon impurities in rhombohedral $BaTiO_3$. All possible carbon sites have been considered in a range of possible charge states. In addition, the physical properties, including geometries, electronic structures, electrical levels and vibrational modes for the stable structures have been investigated and compared with the relevant experimental results.

Chapter 7 - Comparison of the properties of perovskite titanates

This chapter focuses on the main difference and similarity points of carbon defects in three perovskite materials such as structural configuration, electrical levels, vibrational modes, activation energy and formation energies.

Chapter 8 - SO_2 impurity in cadmium telluride

The final applications chapter focuses on one of the most important materials used in photovoltaic cells. The main aim of the present chapter is to resolve questions regarding the likely site of the SO_2 or related centre within the lattice, and to reflect upon the possible mechanisms for motional averaging. Furthermore, evidence is provided for the SO_2 impurity in CdTe.

1.1.3 Part III - Conclusions

Chapter 9 - Summary

The final chapter presents the summary of the research work conducted and the major conclusions drawn from the results reported in individual chapters. However, this thesis is by no means the end of the story. There are still numerous interesting problems surrounding these advanced materials, both in in terms of theory and applications. Possible future investigations are described which arise from the results of the present research.

1.2 Abbreviations

The following abbreviations have been used within this thesis.

Abbreviation	Definition
AIMPRO	*Ab Initio* Modelling PROgram.
DFT	Density Functional Theory.
HF	Hartree-Fock theory.
BZ	Brillouin Zone.
LDA	Local Density Approximation.
HGH	Hartwigsen-Göedecker-Hutter.
MP	Monkhorst-Pack.
NEB	Nudged Elastic Band.
HOMO	Highest Occupied Molecular Orbital.
LUMO	Lowest Unoccupied Molecular Orbital.
T	Temperature.
IR	Infrared
PV	Photovoltaic.
SC	Self consistent.
G	Gibbs free energy.
P	Pressure.
V	Volume.
S	Entropy.
MEP	Minimum energy path.
ABO_3	perovskite oxides.
f.u.	formula unit.

1.3 Notation

The following notations have been used throughout this thesis.

Notation	Definition
E_{kin}	Kinetic Energy.
V_{ext}	External Potential.
E_{xc}	Exchange Correlation Energy.
U_H	Hartree Energy.
V_{eff}	Effective Potential.
E_g	Kohn-Sham Energy Gap.
E_a	Activation energy for forward migration.
E_b	Activation energy for reverse migration.
p_s	Psudopotential.
E^f	Formation Energy.
r_c	Cut-off Radius.
μ_i	Chemical potential of atom species.
μ_e	Electron chemical potential.
E_v	Valence band top.
α_M	Madelung constant.

Part I

Theory and method

Chapter 2

Computational background and the AIMPRO package

In order to fully describe the quantum-mechanical behaviour of a stationary system which has a number of interacting electrons, it is necessary to calculate its many-electron wavefunction. In principle this can be obtained from the time-independent Schrödinger equation. However, since the motion of each electron is coupled to that of the other electrons in the system, it is not generally possible to solve this problem analytically, and approximations are needed. This chapter gives an introduction to the main concepts in density functional formalism. A brief explanation of the important approximations which are implemented in AIMPRO code is then presented. The AIMPRO code enables the application of density functional theory (DFT) to solve problems in, for example, metals, semiconductors and insulators.

2.1 The many-body problem

Quantum mechanics has been used to provide an accurate description of a system. The use of the Schrödinger equation is the fundamental task in describing the behaviour of systems varying from atoms and molecules to complex solid systems. The problem is finding the solution for a many-body system by solving the eigenvalue problem using

quantum mechanics, where the Schrödinger equation in general is:

$$\hat{H}\Psi_i = E_i\Psi_i \tag{2.1}$$

Here $\hat{H}$ is the Hamiltonian operator, which is a differential operator describing both the kinetic energy and potential energy of the nuclei and electrons. E_i represents the total energy of system and Ψ_i is a wave function which determines the positions and momenta of all the particles in the system:

$$\Psi = \Psi(r_1, r_2, ...; R_1, R_2, ...) \tag{2.2}$$

Here $(r_1, r_2, ...r_N)$ are electron coordinates and $(R_1, R_2, ...R_M)$ are the nuclear coordinates. The electronic Hamiltonian for a molecule is the sum of all the kinetic and potential energies for the electrons and nuclei in the system;

$$\hat{H} = \hat{T}_{\mathrm{e}} + \hat{T}_{\mathrm{N}} + \hat{V}_{\mathrm{Ne}} + \hat{V}_{\mathrm{ee}} + \hat{V}_{\mathrm{NN}} \tag{2.3}$$

Here $\hat{T}_{\mathrm{e}}$ represents the kinetic energy of the electrons, $\hat{T}_{\mathrm{N}}$ represents the kinetic energy of the nuclei, and the three types of interaction $\hat{V}_{\mathrm{Ne}}$, $\hat{V}_{\mathrm{ee}}$ and $\hat{V}_{\mathrm{NN}}$ represent nuclear-electron, electron-electron and nuclear-nuclear interactions respectively. Then:

$$\begin{aligned}\hat{H} \;=\; & -\sum_{i=1}^{N}\frac{\hbar^2}{2m}\nabla_i^2 - \sum_{A=1}^{M}\frac{\hbar^2}{2M_A}\nabla_A^2 - \sum_{i=1}^{N}\sum_{A=1}^{M}\frac{Z_A e^2}{4\pi\varepsilon_0 r_{iA}} \\ & + \sum_{i=1}^{N}\sum_{j>i}^{N}\frac{e^2}{4\pi\varepsilon_0 r_{ij}} + \sum_{A=1}^{M}\sum_{B>A}^{M}\frac{Z_A Z_B e^2}{4\pi\varepsilon_0 R_{AB}}\end{aligned} \tag{2.4}$$

Here

$$r_{ij} = |r_i - r_j|, r_{iA} = |r_i - R_A|, R_{AB} = |R_A - R_B| \tag{2.5}$$

where M_A is the mass of nucleus A, m is the mass of the electron and Z is the nuclei charge. The parameters e, $\hbar$, m and $4\pi\varepsilon_0$ are unity in the atomic units (au) system. Consequently, 1 au in energy is equivalent to 27.212 eV and 1 au of length is equivalent to a Bohr radius (0.5291 Å). Therefore, in atomic units the Hamiltonian can be rewritten as:

$$H = \overbrace{-\sum_{i=1}^{N}\frac{1}{2}\nabla_i^2}^{(1)} \underbrace{-\sum_{A=1}^{M}\frac{1}{2M_A}\nabla_A^2}_{(2)} \overbrace{-\sum_{i=1}^{N}\sum_{A=1}^{M}\frac{Z_A}{r_{iA}}}^{(3)} \underbrace{+\sum_{i=1}^{N}\sum_{j>i}^{N}\frac{1}{r_{ij}}}_{(4)} \overbrace{+\sum_{A=1}^{N}\sum_{B>A}^{M}\frac{Z_A Z_B}{R_{AB}}}^{(5)} \tag{2.6}$$

The first term represents the kinetic energy of the electrons, the second represents the kinetic energy of the nuclei, and the third represents the nuclear Coulombic attraction between the i^{th} electron and the A^{th} nucleus. The fourth term refers to the electron Coulombic repulsion between the i^{th} and j^{th} electrons, and the final term contains the nuclear Coulombic repulsion between the A^{th} nucleus and the B^{th} nucleus.

Solving the Schrödinger equation directly is very difficult because all of the motions of electrons and nuclei are coupled. Therefore important approximations are used.

2.2 The Born-Oppenheimer approximation

The Born-Oppenheimer approximation separates nuclear and electron motion. As nuclei are much heavier and slower than electrons, this approximation therefore removes the nuclear kinetic term from the Hamiltonian to form an electronic Hamiltonian that describes the motion of the electrons about fixed nuclei.

$$\Psi_{\text{total}} = \Psi_{\text{electronic}}\Psi_{\text{nuclear}} \tag{2.7}$$

The electronic Hamiltonian, $\hat{H}$, is usually written as:

$$\hat{H} = -\sum_{i=1}^{N}\frac{1}{2}\nabla_i^2 - \sum_{i=1}^{N}\sum_{A=1}^{M}\frac{Z_A}{r_{iA}} - \sum_{i=1}^{N}\sum_{j>i}^{N}\frac{1}{r_{ij}} = \hat{T}_e + \hat{V}_{Ne} + \hat{V}_{ee} \tag{2.8}$$

This approximation allows the electron problem to be solved separately, which achieves a considerable reduction in the time needed for calculation.

2.3 Density functional theory

DFT [2–4] is a mathematical method that derives the properties of the system based on a determination of the electron density $n(r)$ of that system, rather than in terms

of wave functions. The major challenge of any many-body theory is to reduce the number of parameters needed to describe the system. DFT is an extremely successful quantum mechanical modelling method used in physics and chemistry to describe the electronic interaction of a many-body system in the ground state, such as atoms, molecules, and solids [5]. In this theory, the electrons in solid materials obey the Pauli principle and repulse each other according to the Coulombic potential. The basic variable of the system depends only on three variables: the spatial coordinates x, y and z. The most important advantage of DFT methods is a significant decrease in computing time.

2.3.1 The Hohenberg-Kohn theorems

In 1964, Hohenberg and Kohn [6] proved an exact formal variational principle for the ground-state energy, which is valid for any system consisting of electrons moving under the influence of an external potential $V_{\text{ext}}(r)$. The ground state properties, in general can be derived from the ground state charge density $n(r)$ and the ground state energy functional $E[n(r)]$, can be written according to the first Hohenberg-Kohn theorem as:

$$E[n(r)] = F[n(r)] + \int n(r)V_{\text{ext}}(r)d^3r \tag{2.9}$$

Here $F[n(r)]$ is a universal functional, suitable for any number of particles and any external potential. This functional depends only on the electron density, $n(r)$. A second theorem [5] states that the ground state density minimises the total electronic energy of the system. The correct electron density $n(r)$ is the one that produces the minimum energy.

Although the Hohenberg-Kohn theorems are very powerful, they do not by themselves introduce any way to compute the ground-state density of a system in practice since the functional $E[n(r)]$ is not known.

2.3.2 The Kohn-Sham Equations

In the Kohn-Sham (K-S) formulation of density functional theory, the total energy of a system is expressed as a functional of the charge density, as in:

$$E[n(r)] = T_s[n(r)] + \int n(r)V_{\text{ext}}(r)dr + U_H[n(r)] + E_{xc}[n(r)] \tag{2.10}$$

Here T_s is the K-S kinetic energy of a fictitious non-interacting system of electrons which has the same density $n(r)$ as the real system, $V_{\text{ext}}(r)$ is an external potential acting on the interacting system, E_{xc} is the exchange correlation energy, and U_H is the electron-electron Hartree (or Coulomb) interaction, which is:

$$U_{\text{H}} = \frac{1}{2}\int \frac{n(r)n(r')}{|r-r'|}d^3r d^3r' \tag{2.11}$$

Kohn and Sham derived this by reintroducing one-electron wave functions $\psi_i(r)$ for the fictitious system. Therefore, the electron density can be written as:

$$n(r) = \sum_i |\psi_i(r)|^2 \tag{2.12}$$

Then,

$$T_s[n(r)] = \sum_i -\frac{\hbar^2}{2m_e}\int \psi_i^*(r)\nabla^2\psi_i(r)d^3r \tag{2.13}$$

K-S showed that the potential in the fictitious system is given by:

$$V_{KS}(r) = V_{\text{ext}}(r) + \int \frac{n(\acute{r})}{|r-\acute{r}|}d\acute{r} + \frac{\delta E_{xc}}{\delta n} \tag{2.14}$$

The functions $\psi_i(r)$ are found by solving the K-S equations:

$$-\frac{1}{2}\bigtriangledown^2\psi_i + V_{KS}(r)\psi_i = E_i\psi_i \tag{2.15}$$

Equations 2.12, 2.14 and 2.15 are solved to determine $n(r)$ and this is then used in equation 2.10 to determine the total energy.

The K-S approach thus achieves an exact correspondence of the density and ground state energy of a system consisting of non-interacting Fermions and the real many-body system described by the Schrödinger equation [5, 6].

2.4 The exchange-correlation functional

Practical applications of DFT are based upon approximations for the assumed exchange-correlation energy E_{xc}. As the electrons move they try to avoid the repulsive interaction from each other by creating a hole into which other electrons will not penetrate. This is called the exchange-correlation hole and it gives rise to the term in the total energy. E_{xc} contains the difference between the exact and non-interacting kinetic energies and also the non-classical contribution to the electron-electron interactions, of which the exchange energy is a part. The electron exchange is due to the fermionic nature of electrons (leading to the Pauli exclusion principle) and correlations arises from Coulomb repulsion [7, 8].

Several approximations of the exchange correlation energy E_{xc} have been proposed. One of these approximations is the local density approximation (LDA) [9]. In this approximation, E_{xc} is evaluated from the exchange and correlation energy of a homogeneous electron gas with density $n(r)$. This is an approximation of the form;

$$E_{xc}^{\mathrm{LDA}} = \int n(r)\epsilon_{xc}(n(r))dr \tag{2.16}$$

Here ϵ_{xc} is the exchange-correlation energy density of a uniform electron gas of density $n(r)$. The LDA approximation was expected to perform well for systems with a slowly varying density. But, rather surprisingly, it appears to be very accurate in many other (realistic) cases too. On the other hand, the LDA is inaccurate in strongly correlated systems such as transition metal oxides and in the van de Waals bonding systems. Although the DFT method in the LDA gives a reasonable description of non homogeneous systems, it leads to underestimated values of lattice constants and band gaps. Table 2.1 lists the calculated lattice constants and band gaps for three cubic perovskite crystals, $SrTiO_3$, $BaTiO_3$ and $PbTiO_3$. In this table, the calculated data has been compared with the values obtained previously using the LDA and experimental results. It is clear from Table 2.1 that the LDA calculations underestimate the lattice constant and band gap for all three perovskites. The best agreement with experimental lattice constants was obtained for $SrTiO_3$ at within 0.5%. On average,

the disagreement between the computed lattice constants and experimental values for all three perovskites is no greater than 1.5%. The calculated band gap is dramatically underestimated by around 50%, reflecting the well-documented underestimate arising from the underpinning methodology (see Table 2.1). These calculations confirm the tendency, which is well known in the literature, for the LDA calculations to underestimate the lattice constants and band gap. However, the estimated values for the three perovskites are consistent with previous comparable calculations.

Table 2.1: Equilibrium lattice parameters a_0 and energy band gap E_g for cubic $SrTiO_3$, $BaTiO_3$, and $PbTiO_3$ crystal calculations by using LDA, compared with theoretical and experimental results taken from published studies [10–13].

Parameter	method	$SrTiO_3$	$BaTiO_3$	$PbTiO_3$
a_0/au	This work	3.87	3.94	3.91
	Previous theory	3.86	3.96	3.93
	Experimental	3.89	4.00	3.97
E_g/eV	This work	1.89	1.85	1.55
	Previous theory	1.89	1.81	1.40
	Experimental	3.25	3.20	3.40

2.5 Supercell technique

In order to simulate a defect in crystals substantial computing resources can be required. Therefore, some sort of balance between the computing cost and model size has to be found by choosing an approximate structure. Two types of models have been commonly used for computer simulation: clusters and supercells. A cluster is a small group of atoms or molecules. It is like a big molecule cut out from the crystal. At the boundary of the cluster, the dangling bonds may be saturated with hydrogen

to remove the surface states. However, if the cluster size is not big enough or the position of the defect is not at the centre, defect–surface interaction may be significant. The supercell approach is an important method which has been used to avoid surface interaction by repeating the supercell infinity in all directions to form continuous crystal, and thus each supercell is considered as a unit cell with an associated Brillouin zone (BZ) (Sec. 2.6). The result is a periodic boundary condition and the simulation will be for an infinitely large crystal. Any effect due to the surface is removed. For example, in CdTe, defects are modelled using the supercell approximation, using simple cubic cells with a side length of either $2a_0$ or $3a_0$, containing 64 and 216 host atoms respectively.

With the supercell method, all of the states can be describe as an orthogonal basis set and plane wave using a Fourier transition for the systems cannot be used with a cluster. However, this approach is clearly more suitable for the modelling of a pure crystal. If the supercell contains a defect, then the interactions between defects in neighbouring unit cells becomes important. Therefore, a large unit cell is required.

Calculations presented in the application chapters have all employed the supercell approach.

2.6 Brillouin zone sampling

In order to calculate the physical properties of the systems modelled with a supercell framework, integration over the BZ is required. The first BZ is a uniquely defined primitive cell in reciprocal space. `AIMPRO` code in the DFT formula uses a Monkhorst-Pack (MP) sampling mesh [14,15]. With the MP scheme, the integrals are made from finite numbers of points in the first BZ, which is called a k-points mesh.

In calculations, the density of the k-point sampling grid depends upon the nature of the material. For example, semiconductors and insulators are usually treated using a relatively small number of k-points. However, metal calculations need significantly larger sets of k-points. On the other hand, for similar structures, the calculation of

energy differences should be converged. In this project, MP sampling of $1 \times 1 \times 1$, $2 \times 2 \times 2$ and $3 \times 3 \times 3$ has been performed for the oxygen vacancy defect in bulk $SrTiO_3$ (160 atom supercell), The results are listed in Table 2.2.

Table 2.2: Total energy for oxygen vacancy defect in bulk $SrTiO_3$ model of sampling $1 \times 1 \times 1$, $2 \times 2 \times 2$ and $3 \times 3 \times 3$.

MP sampling:	$1 \times 1 \times 1$	$2 \times 2 \times 2$	$3 \times 3 \times 3$
Final energy (Ha):	-4380.47253	-4380.477769	-4380.477788

From this table, it is clear that the energy difference between $2 \times 2 \times 2$ and $3 \times 3 \times 3$ is about 5.2×10^{-4} eV, which is less than 1 meV. These sampling densities converge by about 3.2 μeV per atom. This value is negligible, and therefore MP sampling of $2 \times 2 \times 2$ has been used for subsequent calculations in this work.

2.7 Basis set functions

Among the types of function used to represent charge density and Kohn-Sham orbitals are plane wave basis sets and the Cartesian Gaussian function. The usual approach adopted within supercell formalisms is to choose plane-wave fitting functions for both the Kohn-Sham orbitals and the electronic charge-density. This choice is natural because of the inherent periodicity of the system. Kohn-Sham orbitals for a point k in the Brillouin zone are expanded in terms of plane waves:

$$\psi_{\lambda k}(r) = \sum_{G} c_{\lambda k}(G) \exp[i(k+G).r] \tag{2.17}$$

Here G is the reciprocal lattice vector, λ refers to occupied bands (including spin) and $\psi_{\lambda k}$ are the Kohn-Sham orbitals. The orthogonality condition for plane waves with different values of G ensures that no instabilities arise through near-linear dependencies in the basis sets. The plane-wave expansion also has the advantage that

there is only one parameter (the maximum $|G|$ value) to be varied, enabling transparency. The number of plane waves that are used in the fitting is determined by the cut-off energy E_{cut} (all plane waves with $G^2/2 < E_{\text{cut}}$ are included). It is worth mentioning that the energy cut-off must be large enough to cover a sufficient number of plane-waves for the accurate expression of the electron charge density in order to achieve qualitative convergence in the calculations. For example, the energy cut-off as a function of total energy for $SrTiO_3$ has been examined. The values of E_{cut} are critical in terms of the impact upon the total energy accuracy. As shown in Fig. 2.1, the total energy of $SrTiO_3$ has been converged at 150 Ha which is the default value used in the working parameters of this thesis.

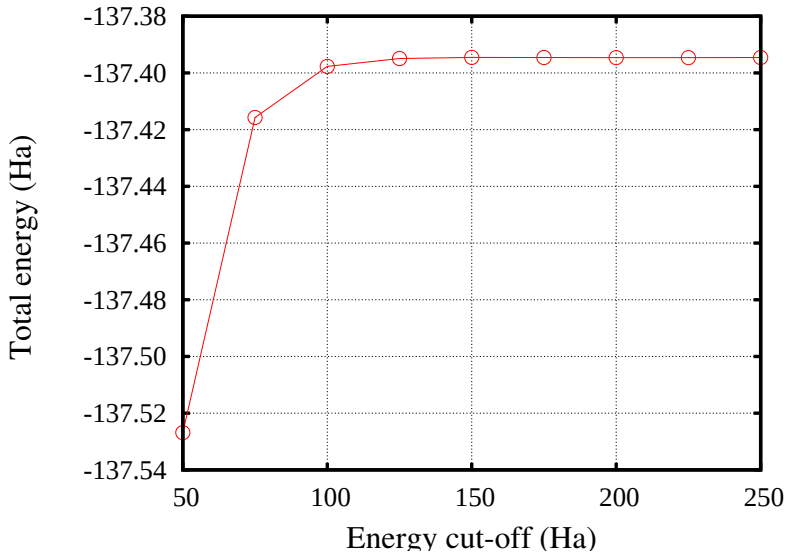

Figure 2.1: Plot illustrating the convergence in the total energy for bulk $SrTiO_3$ as a function of the plane wave energy cut-off. These calculations are performed using a primitive cell of the $SrTiO_3$ lattice, which contains only five atoms.

However, an extremely large number of functions need to be used to represent localised states such as those seen in defects. An alternative is to use localised orbitals:

$$\psi_\lambda(r) = \sum_i c_i^\lambda \phi_i(r) \tag{2.18}$$

Here ϕ may be Gaussian orbitals and c_i are the coefficients varied to minimise the energy. In AIMPRO, Gaussian s-orbitals take the form:

$$\psi(r) = \sum_i c_i \exp[-\alpha_i (r - R_i)^2] \tag{2.19}$$

Here the exponent α_i controls the width of the Gaussian, and R is the centre of the location of the atoms. The Cartesian Gaussian types for p-orbitals are

$$\psi_{p_x}(r) = (x - R_{ix}) \sum_i c_i \exp[-\alpha_i (r - R_i)^2] \tag{2.20}$$

$$\psi_{p_y}(r) = (y - R_{iy}) \sum_i c_i \exp[-\alpha_i (r - R_i)^2] \tag{2.21}$$

$$\psi_{p_z}(r) = (z - R_{iz}) \sum_i c_i \exp[-\alpha_i (r - R_i)^2] \tag{2.22}$$

and for d-orbitals

$$\psi_{x^2}(r) = (x - R_{ix})^2 \sum_i c_i \exp[-\alpha_i (r - R_i)^2] \tag{2.23}$$

$$\psi_{y^2}(r) = (y - R_{iy})^2 \sum_i c_i \exp[-\alpha_i (r - R_i)^2] \tag{2.24}$$

$$\psi_{z^2}(r) = (z - R_{iz})^2 \sum_i c_i \exp[-\alpha_i (r - R_i)^2] \tag{2.25}$$

$$\psi_{xy}(r) = (x - R_{ix})(y - R_{iy}) \sum_i c_i \exp[-\alpha_i (r - R_i)^2] \tag{2.26}$$

$$\psi_{xz}(r) = (x - R_{iy})(z - R_{iz}) \sum_i c_i \exp[-\alpha_i (r - R_i)^2] \tag{2.27}$$

$$\psi_{yz}(r) = (y - R_{iy})(z - R_{iz}) \sum_i c_i \exp[-\alpha_i (r - R_i)^2] \tag{2.28}$$

These are the six terms as the basis for the d-orbital, but mathematically they are only five linearly independent combinations. The additional term is of the form $x^2+y^2+z^2$, which is spherically symmetrical and therefore s-like. So, the set of the d-state is extended as $l = 2$ to generate an additional function with $l = 0$.

The basis set has a significant effect on the results; therefore, the selection of a suitable basis set should be precise. A good example of this is bulk $PbTiO_3$. The

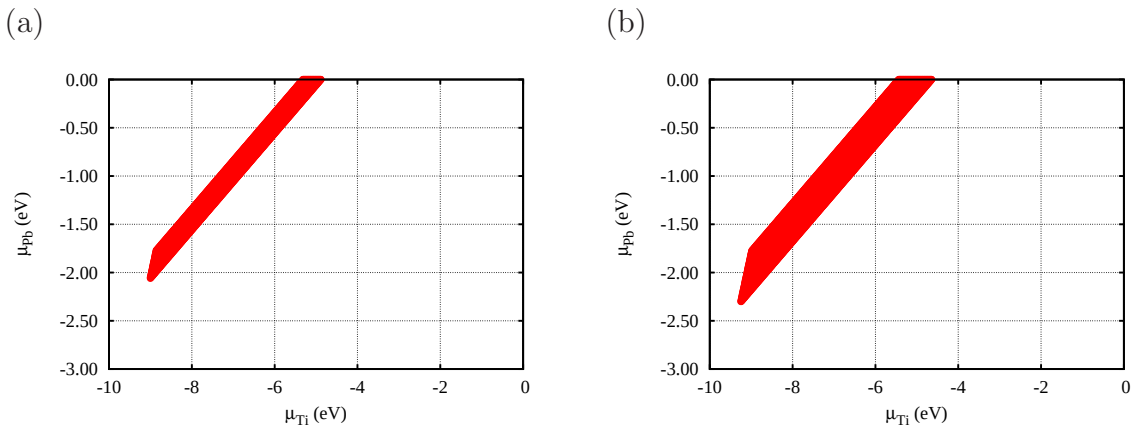

Figure 2.2: Plots showing the equilibrium phases for $PbTiO_3$ related materials as a function of μ_{Pb} and μ_{Ti}, as defined in section 3.4. The Ti basis sets are (a) $PbTiO_3$-*dddd*; and (b) $PbTiO_3$-*ddddd*.

basis sets used to represent Pb, Ti and O in $PbTiO_3$ are optimised so that they yield a minimum in total energy for bulk $PbTiO_3$. Several test calculations were carried out to choose the most promising basis set for every one of these elements. The basis set, $PbTiO_3$–*dddd* has been chosen for Pb and O which consists of 40 functions per atom. The four letters indicate the use of four different exponents, where each letter (*d*) represents exponents of *s*, *p* and *d* functions (10 functions) up to and including the orbital angular momentum $l = 2$. The first exponent is the smallest and the final one is the largest. However, for the Ti atom a $PbTiO_3$–*ddddd* basis set, which consists of 50 functions per atom, has been determined to give the best minimum energy of the $PbTiO_3$ system. This is clearly shown in Fig. 2.2. As shown in this figure, with a non-convergent basis set of Ti ($PbTiO_3$–*dddd*) the phase diagram of $PbTiO_3$ is very narrow Fig. 2.2(a) compares this with the effective basis set ($PbTiO_3$–*ddddd*) in Fig. 2.2(b) and this is very important in specifying the growth conditions. Similar procedures are used in the determination of the exponents for all of the species that are used in the calculations.

2.8 Self-consistent method

The main requirement in solving Kohn-Sham equations is to calculate an accurate minimum energy of the system. The wave function of a system is too complex to be found directly. Therefore, an iterative procedure needs to be used. This procedure is called a self-consistent (SC) calculation. SC means that the calculation runs in loops and convergence is achieved when the results given by solving the SC equations are consistent with the assumptions made at the beginning of the cycle.

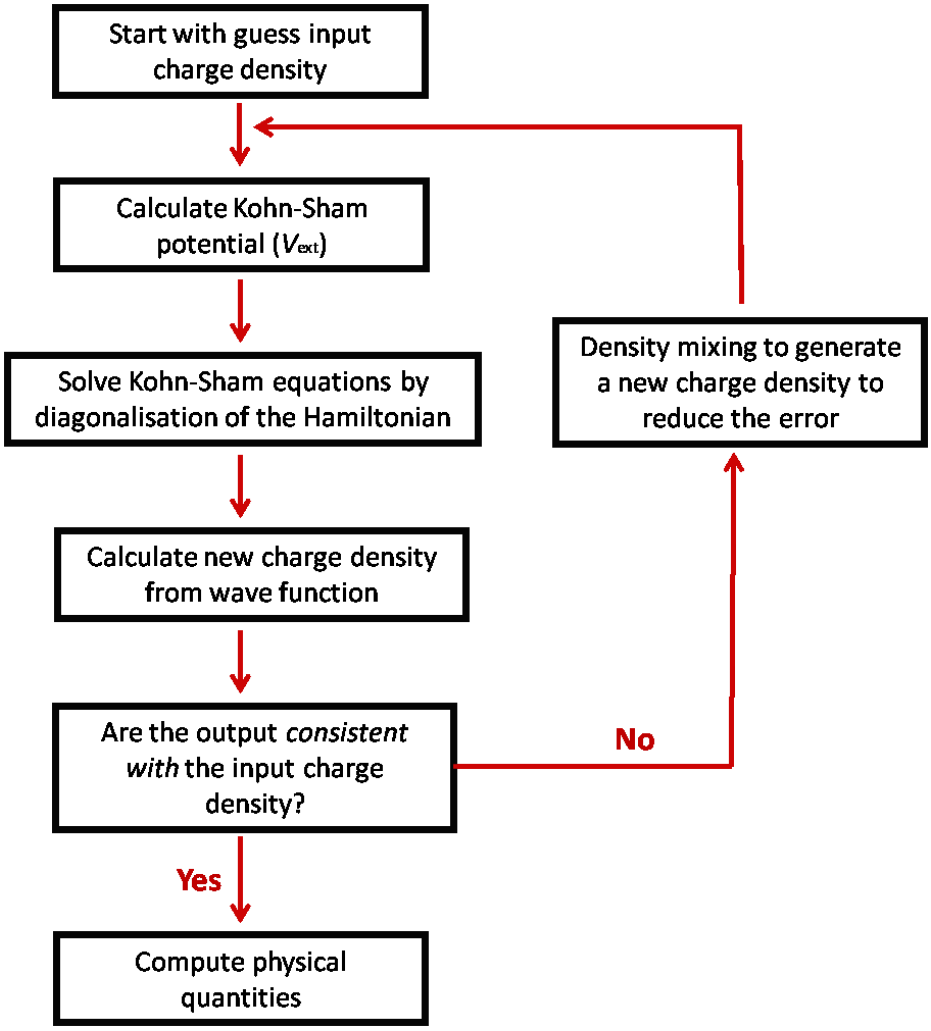

Figure 2.3: Schematic representation of the self-consistent algorithm for a density functional-based calculation.

Before entering the SC cycle, a trial electronic density is build as a first guess. This is taken from either the superposition of neutral atomic charge densities of the system or from the output of a previous calculation. Using this trial density, the total density functional Hamiltonian can be built. Then, the Hamiltonian is diagonalised in order to calculate the energies. Now, a new charge density can be computed. If this new updated charge density agrees with the input charge density, the end point of the loop has been reached. The physical quantities can then be calculated, including the total energy, the band structure, vibrational modes, and so on. On the other hand, if the new charge density is not consistent with the input charge density, SC calculations can precede mixing between the input and output charge density, and then the result can be used as an input to the next cycle. Fig. 2.3 illustrates the major steps of a density functional self-consistent loop.

2.9 Pseudo potentials

In solid systems, chemical bonds are significantly dependent on the valence electrons rather than the tightly bound core electrons. Core electrons are extremely localised to the nucleus and do not participate significantly in chemical bonding. Since the atomic wave-functions are eigen states of the atomic Hamiltonian, they must all be mutually orthogonal. Since the core states are localised in the vicinity of the nucleus, the valence states must oscillate rapidly in this core region in order to maintain this orthogonality with the core electrons. This rapid oscillation results in a large kinetic energy for the valence electrons in the core region, which roughly cancels out the large potential energy due to the strong Coulomb potential. Thus the valence electrons are much more weakly bound than the core electrons. It is therefore suitable to attempt to replace the strong Coulomb potential and core electrons by an effective potential, known as the pseudo potential, and to replace the valence electron wave-functions which oscillate rapidly in the core region with pseudo-wave-functions which vary smoothly in the core region (see Fig. 2.4).

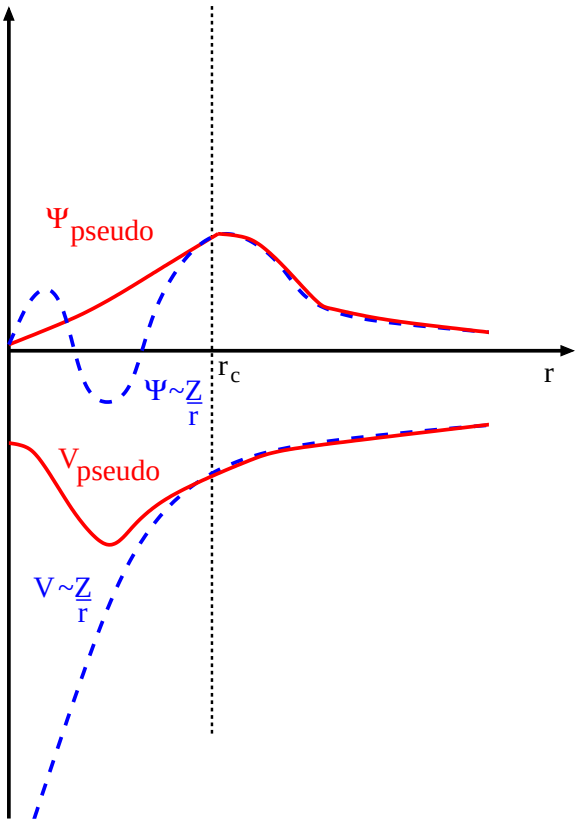

Figure 2.4: Comparison of a wave function in the Coulombic potential of the nucleus (blue) with one in the pseudo potential (red). The real and pseudo-wave function and potentials match above a certain cut-off radius r_c.

The calculation of pseudopotentials has significant benefits over an all-electron calculation. One is that fewer basis functions are required and the numbers of electron states needed for calculations are smaller. The second advantage is that the total energy is not dominated by the core electrons.

In some cases, the core electrons will need to be reinstated if the calculated property is associated with the core electrons, such as with hyperfine interactions. The pseudo potential is fundamentally an approximation; therefore, for different materials a careful choice may be made to minimise this impact.

The pseudo potentials used in AIMPRO come from the work of Harwigsen, Goedecker and Hutter [16] which produced pseudo potentials for all elements.

2.10 Summary

DFT is an important method which can be used to solve Schrödinger equation for a quantum mechanical system consisting of a set of nuclei and electrons. It is implemented in AIMPRO with various approximations, such as pseudo potentials and functionals. With DFT the accuracy of calculations could be very high as shown in terms of the lattice constants of perovskite oxides and similar levels of accuracy are obtained for CdTe and silicon and for a whole range of materials without any empirical input. These are simple examples of an experimental observable that can be derived from DFT, but there are many others; some of which are described in the next chapter.

Chapter 3

The AIMPRO calculation of observables

Several experimental techniques are employed in the study of defects in crystalline solids. However, modelling techniques can be used to analyse many of the complex problems faced in experimental work. Density functional theory is a successful method used to calculate a significant number of experimental observables. This chapter present an outline of the method by which density functional theory can be used to estimate experiment observables.

3.1 Structure optimisation

In the modelling program, the main computational task is finding the stable equilibrium structures of a system. In order to achieve this, the forces on each atom in the system must be calculated. These can be obtained when the self-consistent charge density is determined, as mentioned in section 2.8. The force on any atom in the system is given by the following equation;

$$f_{la} = -\frac{\partial E}{\partial R_{la}} \tag{3.1}$$

where R_{la} is the position of atom a, and l is the direction of the force in three directions (x, y or z). Once the atomic forces have been calculated, the conjugate gradient algorithm is adopted, which displaces the atoms in the direction in which the energy is minimised. The structure that has the least energy is then viewed as the best

estimate of the ground state structure. The structure is considered to be optimised once the energy difference between the sequence of iterations is below 10^{-5}Ha.

This method might give rise to an optimised structure which is not at the global minimum energy. To reduce this uncertainty, several initial atomic forms of the same defective system are modelled and optimised. The structure which has the lowest energy then presumed to be the best estimate of the ground state structure. For example, to calculate the optimised structure of carbon as an interstitial in tetragonal $PbTiO_3$, depending on the symmetry of the crystal, numerous structures have been suggested as a starting point. One of these positions is where the carbon is located at the midway point along the line between neighbouring Pb atoms on the edge of the tetragonal unit cell. Another possibility has the carbon located along the line between Pb and Ti sites in the body diagonal. The third one is which carbon located midway along the line between two Ti neighbours so on. All of these structures have been investigated, either in the polar or equatorial direction. Different minimum energies have been obtained, and based on the calculations two configurations have been found to be the lowest in energy. These may be characterised as CO and CO_3 in terms of the co-ordination with oxygen (see section 5.3.1). A similar process has been conducted for carbon in the different sites in the perovskite oxides and also for SO_2 in the CdTe. These structures are described extensively in application chapters.

3.2 Vibrational modes

In a real crystal, atoms are not fixed at rigid sites on a lattice, but vibrate around their equilibrium positions. Vibrational frequency calculations are very important in identifying types of materials and distinguishing their defects. Infrared and Raman spectroscopy are the powerful experimental tools used to characterise the defects in the materials, where a mode is said to be Raman active if it yields a change in polarizability while it is infrared active if it yields a change in the dipole.

One of the most important requirements for theoretical simulations is to be able

to reproduce quantities that are experimentally observable. The vibration mode calculations throughout this thesis are implemented using AIMPRO via the calculation of second derivatives of the total energy with respect to the atoms displacement. Initially the system must be fully relaxed with a final self-consistent charge density. An atom A is then subjected to a displacement by a small amount ε along the l direction. Atom B then will feel a force along a direction m given by $f^{+}_{mB}(l,A)$. Then atom A is moved by $-\varepsilon$ giving rise to a new force $f^{-}_{mB}(l,A)$ on atom A. Using this procedure, the second derivative, can be determined from

$$\Phi_{lA,mB} = \frac{f^{+}_{mB}(l,A) - f^{-}_{mB}(l,A)}{2\varepsilon} \tag{3.2}$$

At each step of the calculation of the energy double derivatives, the self-consistent energy and forces must be found. The dynamical matrix is then found as

$$D = \frac{\Phi_{lA,mB}}{\sqrt{M_A M_B}} \tag{3.3}$$

where M_A and M_B are the masses of atoms A and B. The eigen vectors of this dynamic matrix are the normal coordinates, whereas the eigen values yield the squares of the vibrational frequencies within a harmonic approximation as $\varepsilon \to 0$. However, the displacement ε is finite. Therefore, some anharmonic terms are included. For this reason, the calculated frequencies are termed quasi-harmonic [17], which is a source of quantitative error in the calculations.

3.3 Band structure

Using first-principles, band-gap calculations have become possible for a wide range of semiconductors and insulators. Each electron in these materials interacts with other electrons. The electron energy states are determined by solving the Kohn-Sham equations. The solution yields a set of continuous functions $\varepsilon_n(k)$, where k is the wave vector and n is an integer number termed the band index. The energy states $\varepsilon_n(k)$ form the band structure of the solid. The energy band that contains electrons is called

the valence band (VB), whereas the empty band is called the conduction band (CB). The band gap is the difference in energy between the valence and conduction bands.

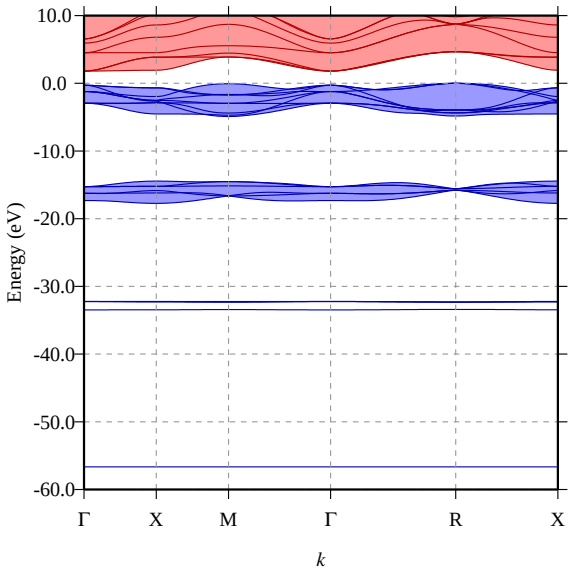

Figure 3.1: Calculated band structure of primitive unit cell $SrTiO_3$ in the first BZ, plotted along high-symmetry branches. Labelling on the x-axis follows the conventions for special points at the zone-boundary for simple cubic BZ. Occupied and empty bands are shown in solid blue and red lines, respectively. The zero on the energy scale is defined to be the highest occupied state.

A large number the electronic structures and band plots have been determined using `AIMPRO` code. The band shape is produced, as shown in Fig. 3.1 which depicts the calculated $SrTiO_3$ band structure along high-symmetry directions in the BZ. This figure shows that there are number of energetically separated low-lying bands. For example, the bands which arise from the O $2s$ state are located around -17 eV. These bands overlap with a group of three narrow bands derived from the Sr $4p$ states positioned around -15 eV. At the valence band region, there is a manifold of nine bands, normally derived from the O $2p$ states. These locations agree well with previous

LDA results [18]. However, systematic error has been observed in the band gap width compared with experimental results, which is related to the LDA. For example, the band gaps of $SrTiO_3$, $BaTiO_3$ and $PbTiO_3$ have been calculated to be underestimated by around 50% compared with the experimental values (see Table 2.1), and that of CdTe is around a third of the experimental value (see chapter 8).

3.4 Formation energy

Defects are the source of many of the most interesting properties of solid materials. Therefore, it is important to calculate the stability and solubility of defects in such materials. With DFT, the formation energy approach has been used to calculate the concentration and stability of defects with respect to the chemical potentials of the atoms. The formation energy is the key quantity that must be calculated to investigate the stability of dopants or intrinsic defects. According to thermodynamics, the chemical potential of a species is the derivative of the Gibbs free energy, G, with respect to the number of particles of the species, n_i, that is

$$\mu_i = \frac{\delta G}{\delta n_i} \tag{3.4}$$

where x may be an atomic species or electrons. The Gibbs free energy equation is;

$$G = E + PV - TS \tag{3.5}$$

where E is the internal energy, P is pressure, V is volume, T is temperature and S is entropy. For rigid crystals, the second term, PV, is assumed to be very small and is neglected, and TS is typically small at low temperature (around room temperature) when compared with the separation between filled and empty electronic states, so this could also be neglected. Hence, the Gibbs free energy can be written as

$$\frac{\delta G}{\delta n_i} = \frac{\delta E}{\delta n_i} \tag{3.6}$$

and then

$$E = \sum_i n_i \mu_i \tag{3.7}$$

In thermodynamic equilibrium conditions, μ_i is constant over the whole system. So, for system X, the formation energy of a defect in the neutral charge state with respect to the chemical potentials of its component species can be expressed as

$$E^f(X,0) = E^{\text{tot}}(X,0) - \sum_i n_i \mu_i \tag{3.8}$$

where $E^{tot}(X,0)$ is the total energy of the system X in the neutral charge state which consist of n_i species of type i. For a system which has defects with different charge states, the chemical potential of the electrons must be considered in the calculations. Therefore, the formation energy can be expressed as

$$E^f(X,q) = E^{\text{tot}}(X,q) - \sum_i n_i \mu_i + q(E_v(X,q) + \mu_e) + \chi(X,q) \tag{3.9}$$

where $E^{\text{tot}}(X,q)$ is the total energy supercell (X) for a supercell in charge state q, n_i and μ_i are the number and chemical potential respectively of the atom species, μ_e is the electron chemical potential, defined as zero at the valence band top E_v, and $\chi(X,q)$ is a correction term to compensate for artifacts of the boundary conditions, including the Madelung term for the charged centres;

$$\chi(X,q) = \alpha_M \frac{q^2}{L\epsilon} \tag{3.10}$$

where α_M is the Madelung constant, L is a lattice parameter and ϵ the permittivity of the material [19]. Equation 3.9 represent the defect formation energy as a linear function of electron chemical potential. The formation energy can be used to calculate the stability of the defect in different sizes of cells. Moreover, the formation energies for all possible charge states of the system can be calculated, and which is the lowest energy for any values of the electron chemical potential across the band gap can be determined.

In crystals, for example, equation 3.9 contains terms representing the chemical potentials under specific formation conditions of the species present, and of the electron reservoir. It is common simply to calculate the range of each μ_i defined by the stability of the solid relative to the elemental phases of each constituent. Several examples of formation energy calculations are discussed in depth in subsequent application chapters.

3.5 Electrical levels

Impurities or intrinsic defects in the crystal often change the electrical properties of the material. They introduce electrical energy levels in the forbidden energy gap. These levels arise from the defects breaking the symmetry of the perfect crystal. They will capture and emit electrons and holes at different rates depending upon the potential that defect produces in the crystal and the background doping and temperature. Donor levels (occupied states) which are located close to the CB are called shallow donors whereas the acceptor levels (empty states) located close to the VB are called shallow acceptors. Deep donor and acceptor levels are located far from the CB and VB respectively (Fig. 3.2). The band gap width and defect states in the gap are responsible for the conductive properties and optical transitions of the materials, particularly at the shallower levels, and hence affect the performance of devices such as solar cells, diodes and transistors.

Formation energy (section 3.4) can be used to calculate the electrical levels which represent transitions between charge states under equilibrium. These levels can be calculated as the electron chemical potential where the formation energies for two charge states are equal.

For example, the donor level $(0/+)$ is the chemical potential of an electron at which the formation energies of neutral and positive charge states are equal (Eq. 3.11), whereas the acceptor level $(-/0)$ is the chemical potential of an electron at which the formation energies of negative and neutral charge states are equal (Eq. 3.12), as shown in Fig 3.3. The plot allows the estimation of the electrical energy levels for the defect.

$$\mu_e(0/+) \quad \text{when} \quad E^f(X,0) = E^f(X,+) \tag{3.11}$$

$$\mu_e(-/0) \quad \text{when} \quad E^f(X,-) = E^f(X,0) \tag{3.12}$$

The effect of periodic boundary conditions and underestimated band gap on the electrical levels is complicated and controversial as to the quantities to estimate.

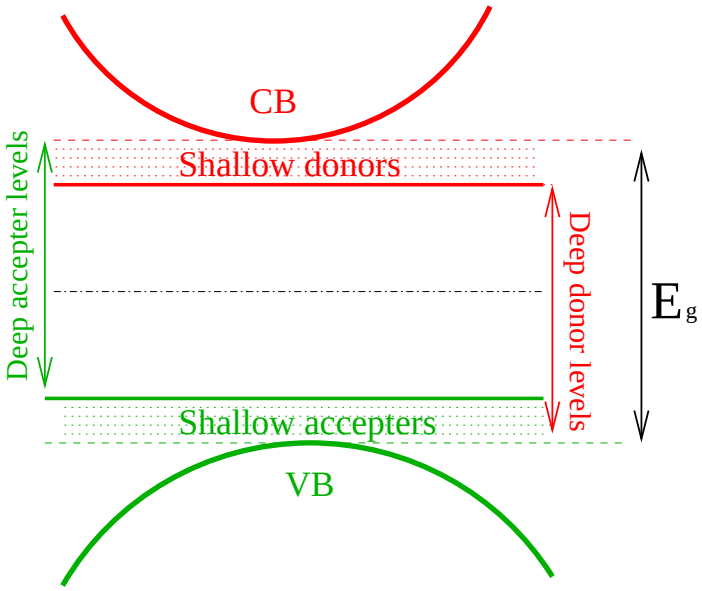

Figure 3.2: Schematic diagram of deep and shallow levels impurities in materials. Red and green curves represent the conduction and valence bands respectively. Red and green lines refer to donor and acceptor levels respectively. The difference between the valence and conduction bands represents the energy gap E_g.

3.6 Diffusion

In general, complex chemical reactions involve several steps of electron transfer, mass transfer, heat transfer, and so on [20]. Chemical reactions are considered as a transitional structure connecting two equilibrium states S_i and S_f (Fig. 3.4). As shown in Fig. 3.4, the particle at initial state S_i can be thermally excited and overcome the activation energy barrier E_a to reach the final state S_f, and this is considered as the forward transition. Similarly, if a particle resides at state S_f, it also has the opportunity to reach state S_i. In this case, however, the reverse activation energy barrier E_b is obviously larger than E_a. The difference between E_a and E_b is the energy difference between states S_i and S_f. In this case, the backward transition is not favoured compared with the forward transition.

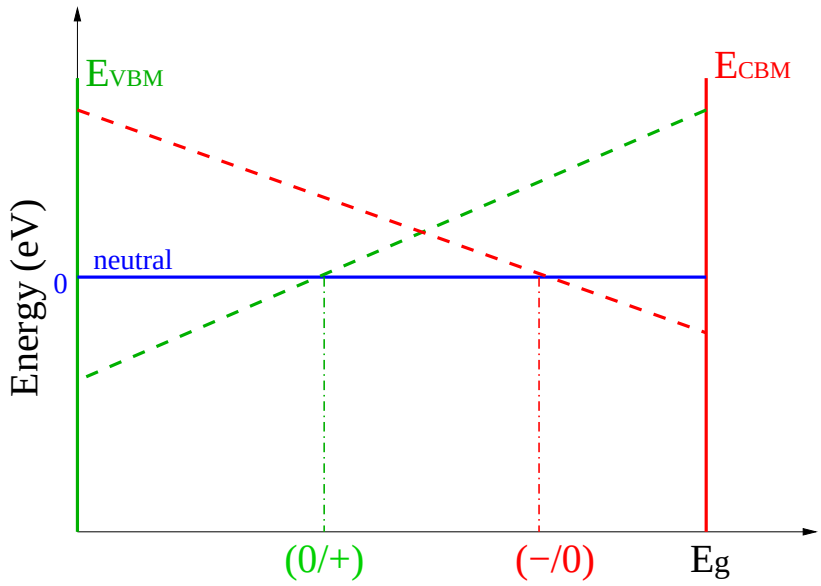

Figure 3.3: Illustration of the use of the formation energy, to obtain acceptor and donor levels for the system X, as a linear function of the electron chemical potential. Red and green dashed lines represent acceptor and donor levels respectively.The solid green and red lines represent the bulk valence and conduction bands respectively.

In fact, usually only a small number of atoms directly participate in the processes of forming or breaking bonds. Many other atoms in the system do not undergo changes in electronic structure. For example, in the reorientation of CO_3 in $BaTiO_3$, for carbon substituting for Ti only four atoms which directly participate in the chemical reaction have been used to calculate the activation energy for CO_3 reorientation (see Fig. 3.5).

Several methods have been used to calculate the activation energy for the diffusion or reorientation of defects inside a material with `AIMPRO` code. The NEB method [21, 22], which is used in this work, is an efficient method used to find saddle points and the minimum energy path (MEP) between a given initial and final structure of a transition.

Briefly, the NEB technique works by generating a chain of images between two equilibrium structures by interpolating the coordinates of the atoms from one mini-

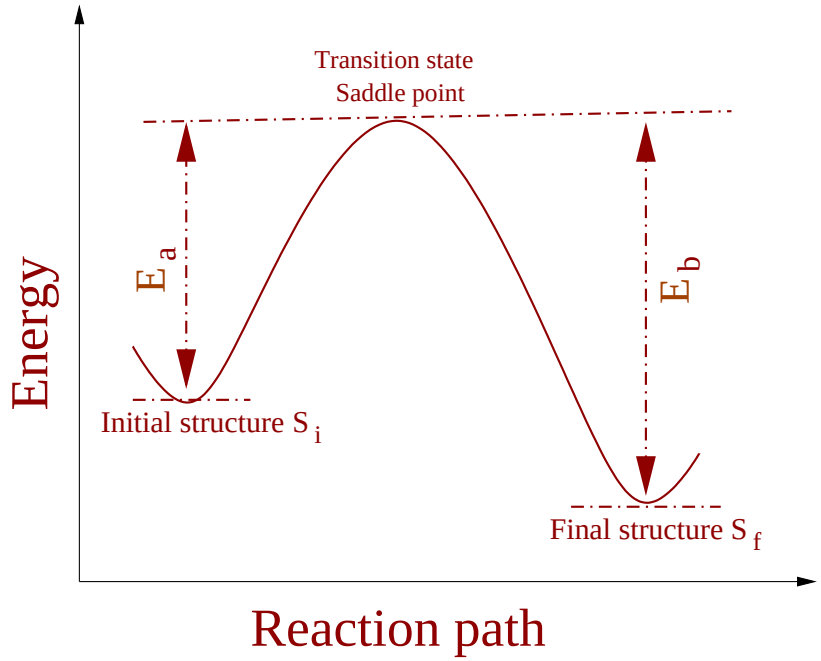

Figure 3.4: Simple scheme representing the location of saddle the point between two relaxed structures. S_i and S_f represent the initial and final states, whereas E_a and E_b respectively represent the forward and reverse activation energy barriers.

mum to another in order to determine the minimum energy path between the initial and final structures. A fictional spring force is assumed between adjacent images in so as to control the spacing between them. By using a modification of the NEB method, termed the climbing image NEB, the highest energy image is driven up to the saddle point. Only the highest image is optimised with the climbing constraint. This image is not affected by the spring forces at all, and the true force at this image along the tangent is inverted. The barrier is optimised until the image forces are less than 10^{-4} au. If it is evident that additional saddle points are present, additional images can be introduced starting from the best estimate from the interpolation (see section 8.3.2).

The saddle point and its energy are important quantities used to study the transition processes. Once the saddle point energy is found numerically, the chemical

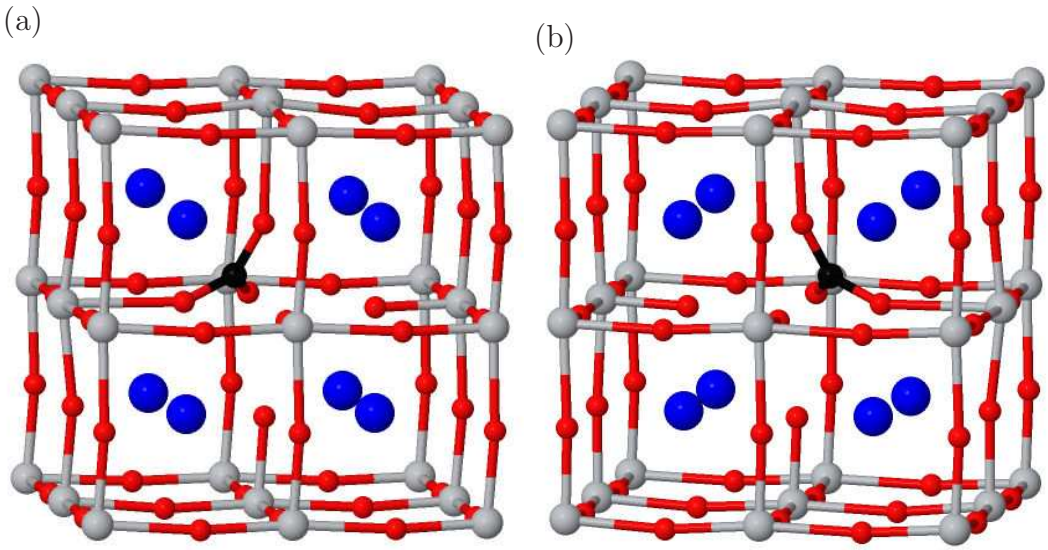

Figure 3.5: Schematic of (a) initial, and (b) final structures of C_{Ti} in $BaTiO_3$ in a simple reorientation process. Blue, grey, red and black atoms represent Ba, Ti, O and C respectively. Vertical and horizontal axes are approximately [001] and [010] respectively, with the tilted view adopted to aid clarity.

transition rate can be derived for reorientation or migration. In addition to estimating the saddle points, NEB calculations can also determine the barrier shape which is important in assessing the route of non-classical events such as tunnelling.

The outline in this section describes the basic principles of energy barrier calculations, and the applications of this method are shown in specific examples in chapter 8.

3.7 Summary

Many important experimental observations of properties can be determined from DFT calculations. A range of these experimental properties have been reviewed in this chapter, such as vibrational modes and electrical levels, which are successfully used in this study. The application of these computational methods with various systems is described and discussed in subsequent applications chapters.

Part II

Applications

Chapter 4

Carbon impurities in strontium titanate

As mentioned in chapter 1, perovskite oxides have attracted both experimental and theoretical attention due to their high permittivity, with $SrTiO_3$ used in waveguides, high capacity computer memory cells and as dielectric elements in electronic devices. Different growth methods yield various qualities of material, and thin-films grown using organic precursors lead to a high probability of carbon contamination. Using density functional calculations, various structural configurations of carbon in $SrTiO_3$ have been investigated, and the associated electronic properties and vibrational modes of carbon-doped cubic $SrTiO_3$ have been analysed. From such calculations it is found that carbon substitution of the host species in $SrTiO_3$ could be either electrically active, such as in the substitution of Sr or O; or electrically passive, which is the case with the iso-electronic substitution of Ti. The highly characteristic vibrational modes predicted for the different configurations provide a route to experimental identification. Additionally, the corresponding formation energies suggest that the carbon substitution of Ti is generally more favourable, but, under O-lean conditions, oxygen substitution becomes significant, and for p-type material the substitution of Sr is also possible.

4.1 Introduction

Recently, perovskite materials have received considerable theoretical and experimental attention. Perovskite-based oxides exhibit many useful properties such as ferroelectricity, piezoelectricity, superconductivity, and oxide–ion conduction, which make them suitable for many applications such as optoelectronics [23], ferroelectric applications [24–26], waveguides [23], high capacity computer memory cells [23,27], dielectric components in electronic devices [23], and optical switches [28].

In its basic and most highly symmetrical form perovskite can be described as a cubic unit cell with the formula ABO_3, where A represents a cation located at the body centre position, in 12 coordination with surrounding oxygen ions. The B cations are located at the cube corner positions, in 6 coordination with surrounding oxygen, while the oxygen atoms themselves inhabit the spaces between the B sites, as shown in Fig. 4.1(a) with an alternative view illustrated in Fig. 4.1(b). The basic structure has been drawn with the A cation located at the cube corners, the B cation at the body centre and O^{-2} ions at the face centres. The structure can also be regarded as a set of BO_6 octahedra arranged in a simple cubic pattern and linked together by shared oxygen ions, with the A cations occupying the spaces in between. Fig. 4.1(c) represents the 3–dimensional perovskite structure with shaded BO_6 octahedra. The cubic unit cell for bulk ABO_3 is completely described by the space-group $Pm\bar{3}m$, and the following basis of atoms at the following positions: A: [0,0,0], B: [0.5,0.5,0.5] and O: [0.5,0.5,0], [0.5,0,0.5] and [0,0.5,0.5].

The use of the perovskite structure derives from its ability to support a wide diversity of cations on its two sites. The cation combinations in the structure which are allowable are governed by charge neutrality and structure constraints. Charge neutrality for the structure

$$A_x^{m+} B_y^{n+} O_3^{2-} \tag{4.1}$$

is given by

$$mx + ny - 6 = 0 \tag{4.2}$$

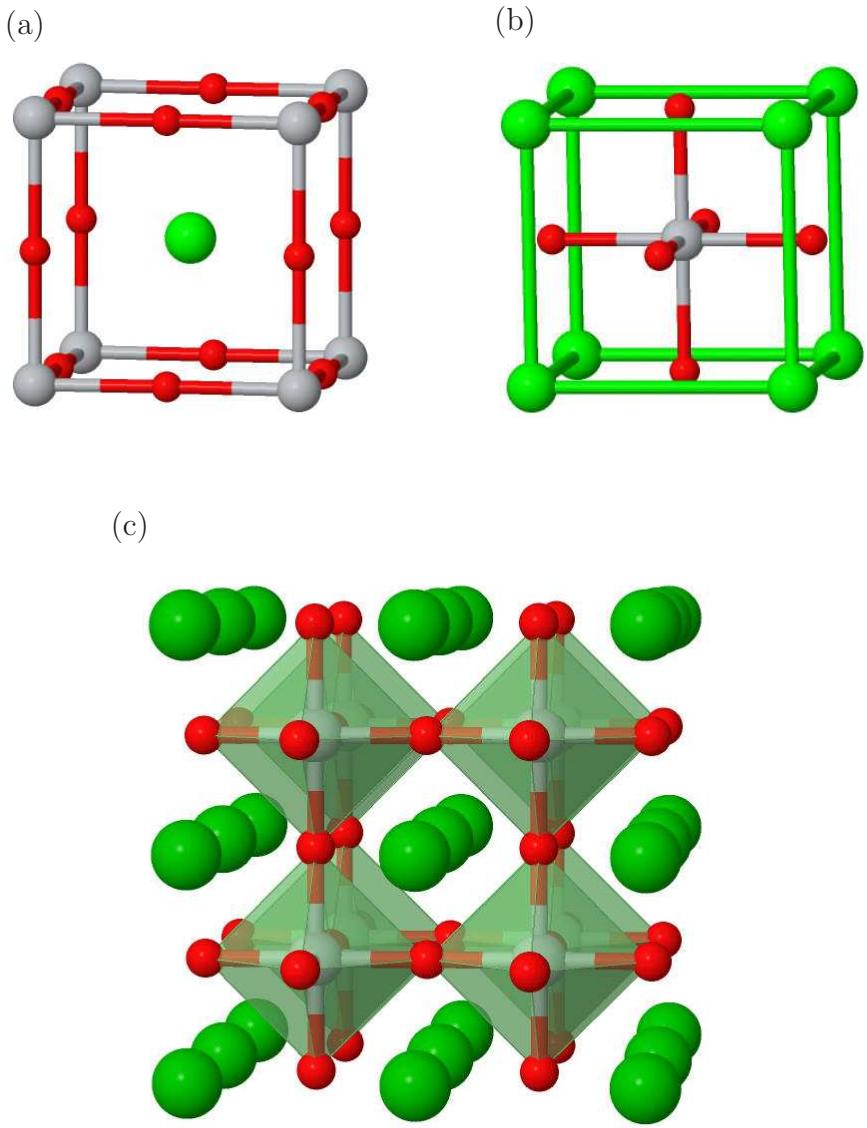

Figure 4.1: Representation of ideal cubic ABO_3 perovskite: (a) A-centred; (b) B-centred; (c) three-dimensional network of BO_6 octahedra. The green spheres represent the A cations, gray spheres represent the B cations, and red spheres represent oxygen anions forming an octahedra. Vertical and horizontal axes are approximately [001] and [010] respectively, with the tilted view adopted to aid clarity.

A simple example of this principle is the material strontium titanate, $SrTiO_3$. Strontium resides on the A site as Sr^{+2}, while titanium resides on the B site as Ti^{+4},

giving overall charge neutrality.

It is common for perovskites to undergo phase transitions as temperature is reduced. For example, $SrTiO_3$ is stable above 105K in a paraelectric cubic structure (Fig. 4.1). $SrTiO_3$ forms randomly oriented dipoles without the application of an external field. However, when an electric field is applied, the dipoles align so as to reduce the strength of the electric field within the material. Removal of the external field results in the dipoles returning to their disordered state (with the polarization in the material returning to zero).

Below 105K, the structure changes to tetragonal symmetry (a = b $\neq$ c, $\alpha = \beta = \gamma$=90°). An orthorhombic phase transition (a $\neq$ b $\neq$ c, $\alpha = \beta = \gamma$=90°) takes place in the range 55–35K. Finally, a further phase transition from orthorhombic to rhombohedral symmetry occurs under 10K. In these phases, the polar axis is aligned from the tetragonal to rhombohedral phase along the $\langle 001 \rangle$, $\langle 110 \rangle$ and $\langle 111 \rangle$ directions [29]. In reality, most perovskite crystals only take on the idealised structures above the Curie temperature T_c. Below this temperature the materials form permanent electric dipoles in the absence of an applied electric field via the displacement of cations relative to anions, giving rise to such properties as ferroelectricity.

In addition to temperature, the perovskite structure is dependent on several other determining factors, which are the Jahn–Teller effect [30–32], composition, and ion size effects. The Jahn–Teller effect appears when there are partially filled *d*-orbitals on the B site (inside the octahedra). Degeneracy in the *d*-orbitals causes distortions in the octahedracite. As the Ti atom is a d^0 ion, the Jahn-Teller effect does not apply to this perovskite, except when foreign atom impurities are introduced. Changing the relative composition of the atoms in a perovskite, for instance creating vacancies such as by the removal of oxygen atoms in $SrTiO_3$, creates another distortion effect [27, 31, 33].

The effects of ion size are clearly important in determining structure. The Goldschmidt tolerance factor (t) [34] has been presented to describe the distortion of the perovskite structure from the ideal configuration by taking into account the ionic radii

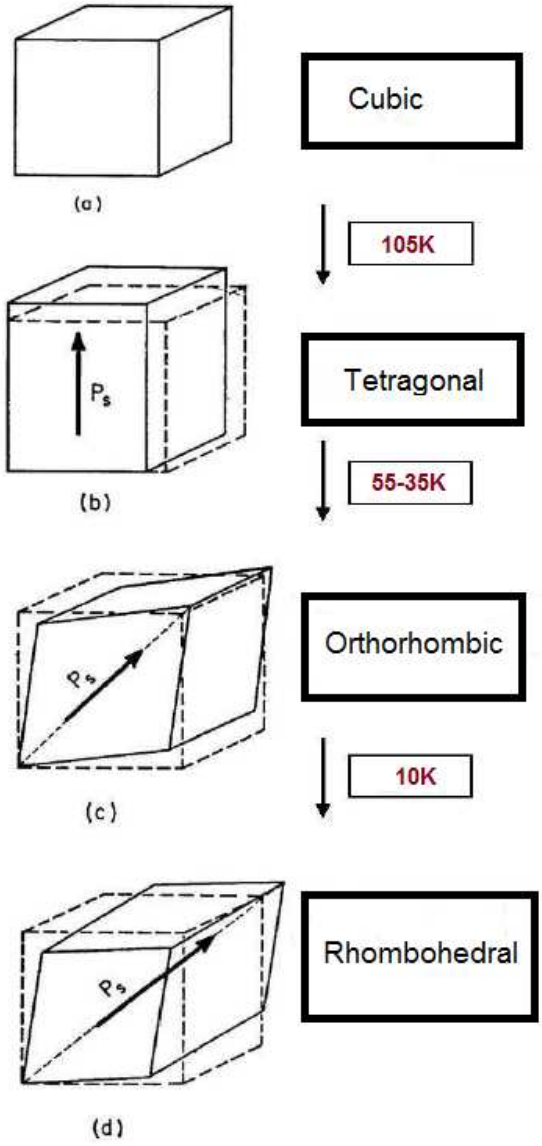

Figure 4.2: Unit cells of the four phases of $SrTiO_3$: (a) cubic; (b) tetragonal; (c) orthorhombic; (d) rhombohedral. The dotted lines in (b), (c), and (d) delineate the original cubic cell. Arrows within the unit cells indicate the direction of the spontaneous polarization in each phase.

of the species A, B and O, where t is defined as

$$t = \frac{(R_A + R_O)}{\sqrt{2}(R_B + R_O)} \tag{4.3}$$

where R_A, R_B and R_O are the ionic radii of the A, B and O ions respectively. The ideally packed perovskite structure presents a tolerance factor t=1. In $SrTiO_3$, the species ionic radii are R_A = 1.44 Å, R_B=0.605 Å and R_O=1.4 Å [35], which gives a value of t=1.00. However, when the B site cation is smaller than the ideal case at t>1, it will shift toward one of the oxygens atoms and the unit cell will contract perpendicular to the direction of the shift, resulting in a tetragonal distortion. This creates electrical polarity in the crystals, making ferroelectricity possible. In contrast, when the A site cation is smaller than the ideal at t<1, the oxygen octahedron will tilt or rotate towards one of the A sites creating a rhombohedral distortion. In practice, most perovskites have tolerance factors between 0.95<t<1.06. However, the Goldschmidt model is only an approximate guide and does not take account of temperature effects. Since perovskites are not entirely ionic compounds, and the effective ionic radii are not constant in all crystals, the value of t is only a rough estimate.

Among the perovskites are ferroelectric crystals such as $BaTiO_3$ and $PbTiO_3$, antiferroelectrics such as $PbZrO_3$ and $NaNbO_3$, and materials such as $SrTiO_3$ that exhibit other, nonpolar instabilities. The presence of different crystal phases can be used to fine-tune and adjust the properties of interest.

$SrTiO_3$ is a good example of a model ABO_3 that has found widespread application in various technologies. Crystalline bulk $SrTiO_3$ has a relative permittivity in the hundreds at room temperature, making it potentially suitable for nano-size devices [36]. However, leakage current is a major issue in thin films, with native point defects, crystallinity and impurities remaining significant problems.

It is well known that pure $SrTiO_3$ is an insulator, with a band gap about 3.2 eV at room temperature in the absence of defects. However, its conductivity could be induced either through the reduction of oxygen in $SrTiO_3$ or through impurity doping, which has important applications in optoelectronic devices [37]. For example, when pure $SrTiO_3$ is heated in a reducing atmosphere, lattice oxygen atoms can diffuse

and recombine into molecular O_2, so that introducing such intrinsic defects or dopant atoms into the structure can cause the appearance of additional energy levels within the band gap, making $SrTiO_3$ a conductor or semiconductor.

In addition to its electrical properties, strain-induced ferroelectricity makes $SrTiO_3$ suitable for microwave devices [38, 39]. Moreover, piezoelectric phenomena have been observed on $SrTiO_3$ thin films, which make it suitable for microelectromechanical systems (MEMS) such as actuators [40]. Reduced $SrTiO_3$ also has the high Seebeck coefficient necessary for thermoelectric applications [41], and reduced $SrTiO_3$ was the first ternary oxide discovered to be superconducting within the temperature range 0.1-0.28K [42]. A large number of experimental studies have analysed the wide variations in physical properties of bulk $SrTiO_3$ and the role of native defects and dopants. For example, the imaginary part of the dielectric function is significantly affected by compositional variations and interfacial strain in $SrTiO_3$ [43]. Amongst the point defects commonly grown into $SrTiO_3$, oxygen vacancies V_O have a significant optical, electrical, and microstructural effect [44], and transition-metal dopants have a considerable impact upon the optical gap [45–48].

Simultaneously, numerous first-principles computational studies have resolved the physical and chemical characteristics of $SrTiO_3$. For instance, the structural and electronic properties of single and double oxygen vacancy defects in bulk $SrTiO_3$ have been predicted to decrease the lattice constant and bulk modulus, and to move the Fermi level towards the conduction band [49]. Additionally, the properties of doping $SrTiO_3$ have been investigated for species such as N and La, with N/La-codoping with La substituting for Sr predicted to be favourable for photocatalytic activity under visible light [50].

Different deposition methods have been used to grow $SrTiO_3$ thin films, including chemical vapour deposition [51], molecular beam epitaxy [52], and pulsed laser deposition [53]. Recently, atomic layer deposition, which is sometimes referred to as atomic layer epitaxy, has attracted more attention due to its accurate thickness control and superior conformal growth [54, 55]. However, the organic Sr precursors

lead to contamination [56, 57], and of particular note is the fact that carbon impurities have been reported in SrO and $SrTiO_3$ films [58]. In the case of SrO films, the current understanding of carbon contamination [59] concerns the formation of $SrCO_3$ within the SrO, and the appearance of the carbon contamination may be interpreted in terms of the incompleteness of the growth reactions [56]. Many first-principles simulation studies focusing on the electronic properties of impurities in $SrTiO_3$ have been published, but relatively few relate to carbon. In one density functional simulation [60], carbon was assumed to lie on an oxygen site, where it was found to generate a mid-gap $2p$-atomic orbital-like, partially occupied state. Another study compared different sites, and it was suggested that the Ti site is more favourable [61], where it was proposed to introduce an empty band a little below the host conduction band minimum. A third study investigated the effects of carbon and sulphur cation doping on the electronic structures and optical properties of $SrTiO_3$. The C cation introduced O $2p$+C $2s$ hybrid orbitals at the top of the valence bands, the band gap of $SrTiO_3$ is narrowed, and a red shift of the absorption edge is predicted [62]. This relates to the experimental observation of improved photocatalytic activity in C-S co-doped $SrTiO_3$ where the absorption edge was shifted from 400 to 700 nm, and the photocatalytic activity levels were about twice those of pure $SrTiO_3$.

Given the potential importance of carbon contamination, and the relative paucity of theoretical data, first-principles calculations have been performed on the geometry, electrical levels, electronic structures, vibrational modes and formation energies of carbon defects for different sites in $SrTiO_3$. The results for each of the most plausible configurations are presented in this chapter, and a simple thermodynamical model applied to determine which are most likely to appear in practice.

4.2 Computational Method

First-principles density-functional theory within the local-density approximation [63], as implemented in AIMPRO computer code [64,65], have been employed, as described

in chapter 2. Atoms are modeled using norm-conserving, separable pseudo potentials, as discussed in section 2.9 [16], where the valence sets for Sr, Ti, O, and C are $4s^2 4p^6 5s^2$, $3s^2 3p^6 3d^2 4s^2$, $2s^2 2p^4$ and $2s^2 2p^2$, respectively, and the Kohn-Sham eigenfunctions are expanded using atom centred Gaussian basis sets [66]. The bases consist of independent sets of s-, p- and d-type Cartesian Gaussian functions of four widths, yielding 40 functions per atom for Ti, O, and C; while five width of s- and p-Gaussians, yielding 20 functions per atom, are centred at each Sr site. Matrix elements of the Hamiltonian are determined using a plane-wave expansion of the density and Kohn-Sham potential [67] with a cut-off of 150 Ha, resulting in absolute convergence of the total energy with respect to the expansion of the charge density to better than 0.03 meV/atom.

Structures are optimised using conjugate-gradients (see section 3.1), with the optimised structures having forces of $< 10^{-3}$ atomic units, and the final structural optimization step is required in order to give a reduction in the total energy of less than 10^{-5} Ha.

$SrTiO_3$ has a cubic perovskite structure at room temperature, with the Ti^{+4} sixfold coordinated to O^{-2} ions, and each Sr^{+2} is surrounded by four TiO_6 octahedron (Fig. 4.1). However, at very low temperatures, $SrTiO_3$ undergoes a small antiferroelectric distortion [29] with alternate TiO_6 groups rotating about a [001] axis in opposite senses by 1.89°, as shown in Fig. 4.3. For bulk cubic $SrTiO_3$, the computational approach yields an equilibrium lattice parameter of 3.87 Å, which is within 1% of experimental data [68]. The calculated band-gap is 1.89 eV, reflecting the well-documented underestimate arising from the underpinning methodology. The estimated value is consistent with previous comparable calculations [69, 70].

To model the defects, the standard supercell approximation has been used. In particular, a non-primitive supercell with lattice vectors $2\sqrt{3}[a\bar{a}\bar{a}]$, $2\sqrt{3}[\bar{a}a\bar{a}]$ and $2\sqrt{3}[\bar{a}\bar{a}a]$ is used, where a is the lattice constant in the cubic unit cell. This supercell is comprised of 32 formula units, meaning that the supercell is $Sr_{32}Ti_{32}O_{96}$ (see section 2.5). In all cases the Brillouin zone is sampled using uniform $2 \times 2 \times 2$

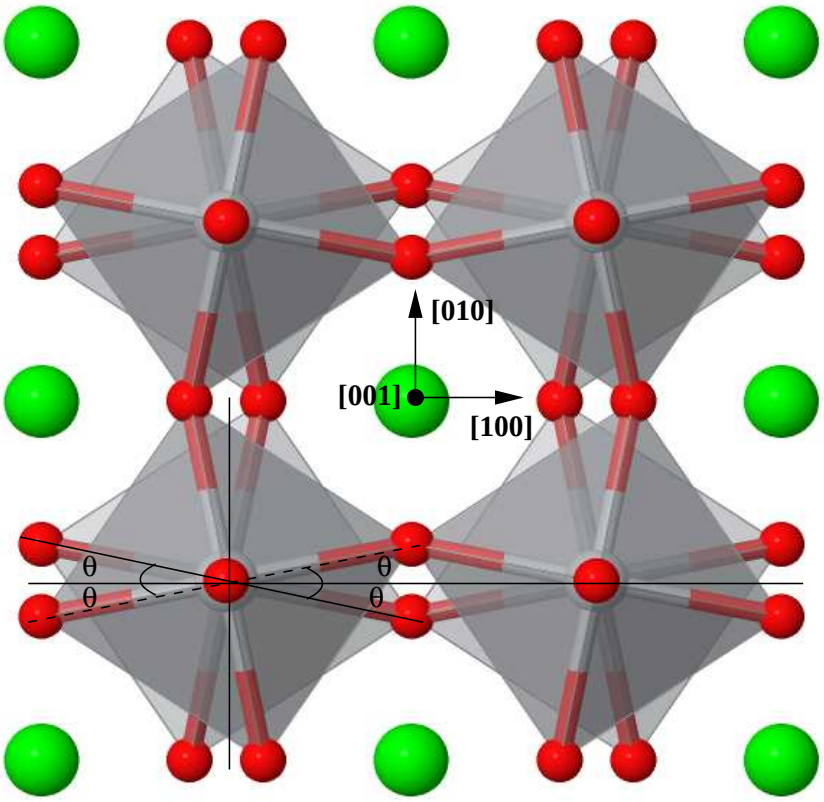

Figure 4.3: Schematic structure showing a small antiferroelectric distortion via the opposite rotation of adjacent shaded TiO_6 units around the [001] direction with θ. Green spheres represent the Sr cations, gray spheres represent the Ti cations, and red spheres represent oxygen anions forming an octahedron.

Monkhorst-Pack mesh [14].

Vibrational modes have been calculated by obtaining the second derivatives of the energy with respect to atomic positions, which are then assembled into the dynamic matrix, as mentioned in section 3.2. The second derivatives are obtained from a finite difference approximation involving the forces calculated on atom i when displacing atom j in each of the three Cartesian directions.

With respect to the activation energies, the climbing nudged elastic band method has been used [21, 22], and the convergence of the saddle point energy with respect to

the number of images and the image-forces has been established to within a few meV (see section3.6).

The formation energy $E^{\mathrm{f}}(X, q)$ of a defect in the q charge state with respect to the chemical potentials of the atoms, along with the Fermi level, have been calculated using Eq. 3.9 (Chapter. 3), where μ_i denotes the chemical potential of the species (i =Sr, Ti, O and C in this calculations). First, the limitations of the atomic chemical potentials have been assessed by considering the energies of bulk $SrTiO_3$ and related materials. The chemical potentials of components μ_{Sr}, μ_{Ti} and μ_{O} are related through

$$\mu_{\mathrm{Sr}} + \mu_{\mathrm{Ti}} + 3\mu_{\mathrm{O}} = \mu_{\mathrm{STO(bulk)}} \tag{4.4}$$

Here μ_{STO} is the total energy per formula unit (f.u.) of pure $SrTiO_3$, and μ_{Sr} is the energy per atom of pure Sr metal. Similarly, μ_{Ti} is defined as the energy per atom in hexagonal-close packed Ti. μ_{O} is the energy of the oxygen atom calculated from the energy of an O_2 molecule, using a cubic supercell $16\,\text{Å} \times 16\,\text{Å} \times 16\,\text{Å}$ to avoid image-image interaction and the Γ point for k-point sampling, and the spin polarized ($S = 1$) calculation was performed for that case. The $SrTiO_3$ enthalpy of formation is, $\Delta H_{\mathrm{SrTiO_3}} = \mu_{\mathrm{SrTiO_{3(bulk)}}} - \mu_{\mathrm{Sr}} - \mu_{\mathrm{Ti}} - 3\mu_{\mathrm{O}}$, which is found to be $-18\,\text{eV}$, and this is in reasonable agreement with the experimental value of $-17.13\,\text{eV}$ [71]. A parameter space describing the values of the chemical potentials for which $SrTiO_3$ is stable can be established in terms of μ_{Ti} and μ_{Sr} using Eq. 4.4, with boundaries formed where related materials become thermodynamically more stable than $SrTiO_3$. For example, for sufficiently high values of the Ti and Sr chemical potentials, it would become more favourable to form bulk metals rather than the composite. Other boundaries are formed by SrO, SrO_2, TiO, Ti_2O_3, TiO_2, and oxygen gas

$$\Delta H_{\mathrm{SrO}} = \mu_{\mathrm{SrO(bulk)}} - \mu_{\mathrm{Sr}} - \mu_{\mathrm{O}} \tag{4.5}$$

$$\Delta H_{\mathrm{SrO_2}} = \mu_{\mathrm{SrO_2(bulk)}} - \mu_{\mathrm{Sr}} - 2\mu_{\mathrm{O}} \tag{4.6}$$

$$\Delta H_{\mathrm{TiO}} = \mu_{\mathrm{TiO(bulk)}} - \mu_{\mathrm{Ti}} - \mu_{\mathrm{O}} \tag{4.7}$$

$$\Delta H_{\mathrm{TiO_2}} = \mu_{\mathrm{TiO_2(bulk)}} - \mu_{\mathrm{Ti}} - 2\mu_{\mathrm{O}} \tag{4.8}$$

$$\Delta H_{\mathrm{Ti_2O_3}} = \mu_{\mathrm{Ti_2O_3(bulk)}} - 2\mu_{\mathrm{Ti}} - 3\mu_{\mathrm{O}} \tag{4.9}$$

To provide a benchmark for these calculations, the calculated properties for Sr, Ti and their composites in addition to the calculated heats of formation are presented in Table 4.1. This shows that the heats of formation are in good agreement with experimental values and previous calculations. The lattice constants are calculated to within about 4%, reflecting the tendency of LDA calculations to underestimate lattice constants, particularly, in the case of Sr metal. In order to determine the properties of the phases in Table 4.1, the same computational settings as for $SrTiO_3$ have been employed, but the number of k-points and the basis set for each material are varied so as to ensure a convergence of the total energy.

The shaded area in Fig. 4.4(a) shows the resulting phase diagram for the stable $SrTiO_3$ growth as a function of μ_{Sr} and μ_{Ti}, which agrees reasonably with a previous similar treatment [76, 77].

Following the procedure adopted for the Cr doping of $SrTiO_3$ [76], the selection of the impurity chemical potential based upon the appropriate carbon containing phase is required. μ_{C} has been calculated based upon graphite (C), TiC, SrC_2, CO_2 gas, and $SrCO_3$. Similar to the above limits were imposed for the μ_{C} calculations. For instance, the formation enthalpy of $SrCO_3$ was $\mu_{\mathrm{Sr}} + \mu_{\mathrm{C}} + 3\mu_{\mathrm{O}} \leq \Delta H_{\mathrm{SrCO_3}}$, where the upper bound of $\mu_{\mathrm{C}} = \mu_{\mathrm{SrCO_3}} - \mu_{\mathrm{Sr}} - 3\mu_{\mathrm{O}}$. Using the same procedure, the constraints for other relevant compounds have been calculated. Other systems containing carbon, such as CO and CO_3 gas, were examined but were not found to be in equilibrium phase under the computational conditions specified. The equilibrium form of carbon as a function of μ_{Sr} and μ_{Ti} (μ_{O} is defined by Eq. 4.4) can be determined by calculating which of the various candidates (graphite, TiC, etc.) is lowest in energy. Fig. 4.4(b) shows the results of this analysis. For example, for with $\mu_{\mathrm{Ti}} = -10\,\mathrm{eV}$ and $\mu_{\mathrm{Sr}} = -4\,\mathrm{eV}$, the equilibrium form of carbon is $SrCO_3$, whereas when $\mu_{\mathrm{Ti}} = -4\,\mathrm{eV}$ and $\mu_{\mathrm{Sr}} = -10\,\mathrm{eV}$ the equilibrium form of carbon is graphite. When the calculated formation energies of carbon containing defects are presented later in this chapter, the carbon chemical potential is specified in this way, and the various regions of chemical

Table 4.1: Calculated and experimental bulk properties and formation enthalpies for Sr, Ti and their composites. Lattice constant (a_0, Å), axial ratio (c/a) and enthalpy of formation (ΔH^f, eV/f.u. are shown, which experimental and theoretical data taken from published studies [71–75]

	Current calculations	Experiment	Previous calculations
$SrTiO_3$, simple cubic ($Pm\bar{3}m$)			
ΔH^f	-18.00	-17.13	-16.20
Sr, cubic close-packed ($Fm\bar{3}m$)			
a_0	5.81	6.04	5.78
SrO, sodium chloride ($Fm\bar{3}m$)			
a_0	5.13	5.16	5.15
ΔH^f	-6.39	-6.14	-6.32
Ti, hexagonal-close packed (hcp)			
a_0	2.86	2.95	2.85
c/a	1.58	1.58	1.58
TiO, sodium chloride($Fm\bar{3}m$)			
ΔH^f	-5.74	-5.62	-5.66
TiO_2, rutile ($P4_2/mnm$)			
a_0	4.55	4.57	4.56
c/a	0.64	0.66	0.64
ΔH^f	-10.44	-9.79	-10.93
Ti_2O_3, rhombohedral ($R\bar{3}c$)			
a_0	5.43	5.43	-
ΔH^f	-16.89	-15.75	-16.9

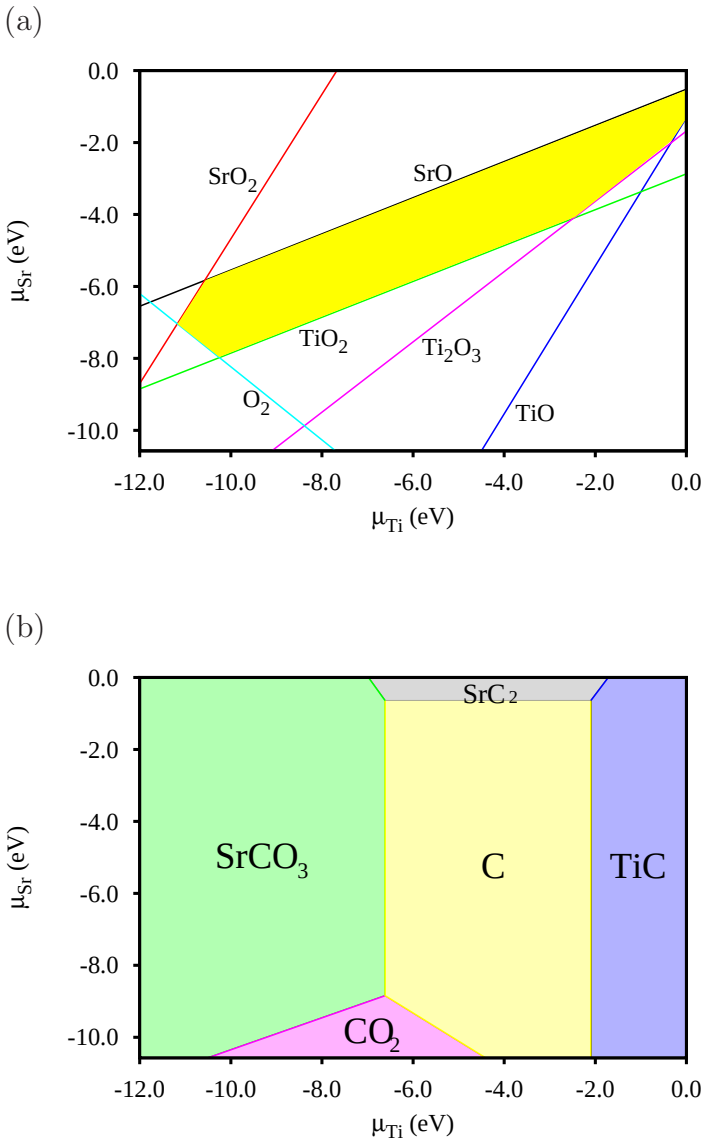

Figure 4.4: Plots showing the equilibrium phases for $SrTiO_3$ related materials as a function of μ_{Sr} and μ_{Ti}: (a) shows the $SrTiO_3$ stable region of the parameter space, indicated by the shaded area; whereas (b) shows the stable phases containing carbon over the same ranges of chemical potentials.

stability for carbon shown, such as in Fig.4.18 on page 70.

Using Eq. 3.9 and by considering the $SrTiO_3$ stability conditions, the likely location of carbon in $SrTiO_3$ has been examined, as discussed below in section 4.3.5.

4.3 Results and discussion

There are four principal ways to include carbon atom into the $SrTiO_3$ lattice: carbon substitution at the Sr, Ti or O sites, and insertion in an interstitial position. Each of these configurations has been analysed, and their observable properties assessed. First, to provide a benchmark for these calculations, the calculated properties of the free CO and CO_3 species are presented in Table 4.2, showing that the bond lengths are in excellent agreement with experiments, and the vibrational modes are calculated within about 5%. For comparison, the properties of a carbon monoxide anion, CO^{-2} have also been calculated. The ground state is $S = 1$, in line with the spin-triplet ground state of the isoelectronic oxygen molecule. The population of the π^* orbital increases the bond length to 1.44 Å, and the reduction in bond-order yields a corresponding reduction in vibrational frequency, which is calculated to be just 1047 cm^{-1} although here there are no experimental values for comparison.

Table 4.2: Bond lengths (d, Å) and angles ∠OCO (θ, degrees) and vibrational modes (ν, cm^{-1}), for CO and CO_3^{-2}. Corresponding experimental values are taken from previous studies [78–80].

	CO	CO_3^{-2}
	Calculated	
d	1.14	1.28
θ	—	120
ν	2051	1380, 1026, 864, 655
	Experiment	
d	1.12	1.29
θ	—	120
ν	2139	1415, 1063, 879, 680

The analysis of these molecular calculations and the bulk $SrTiO_3$ quantities pre-

sented in section 4.2 provide both confidence that the computational method is appropriate and sufficient for the subject matter, and this provides the context for the data given below for carbon-containing point defects.

4.3.1 Interstitial C

The first case is that of a carbon atom added to an otherwise pristine $SrTiO_3$ crystal. By varying the starting location of the interstitial carbon (C_i), several different minima in energy may be obtained. In general, carbon can form covalent bonds with one, two, or three host oxygen atoms. However, two configurations, which may be characterized as CO and CO_3 in terms of co-ordination with oxygen (Fig. 4.5), are of particular importance, being the lowest in energy for different charge states.

The CO structure has C_{2v} symmetry with the principal axis along the single C–O bond (Fig. 4.5(b)). The C–O bond-length of 1.24 Å is consistent with a CO^{-2} ion substituting for a host oxygen ion. This structure is stabilised by a partial *p*-*d* covalent bonding between the carbon atom and the two nearest Ti ions. This is confirmed by the molecular orbital analysis, as shown in Fig. 4.6(a). The C–Ti distances have been calculated to be 2.06 Å, which is 6% longer than the original Ti–O in pure $SrTiO_3$.

The CO_3 structure (Fig. 4.5(c)) has a more dramatic impact upon the host, with the formation of three C–O bonds yielding a centre close to C_{3v} symmetry. Since the normal charge state of the carbonate ion is -2, the formation of this geometry may be viewed as unlikely: the CO_3^{-2} ion is effectively replacing three host O^{-2} ions, leading to a surplus of four electrons. The C–O distances have been found to be 1.28 Å and the bond angles are 119°, which are close to the bond length and angles respectively of CO_3^{-2} ions. However, the structure in the +2 charge state is non-planar compared with the +4 charge state. The reason for this is that the addition of electrons leads to the bond angles becoming smaller since the bonding interaction between Ti and carbon increases the strength of the bonds. Indeed, it is shown below that, although the carbonate form is metastable in the neutral charge state, it is expected to act as a donor and thus favour positive charge states.

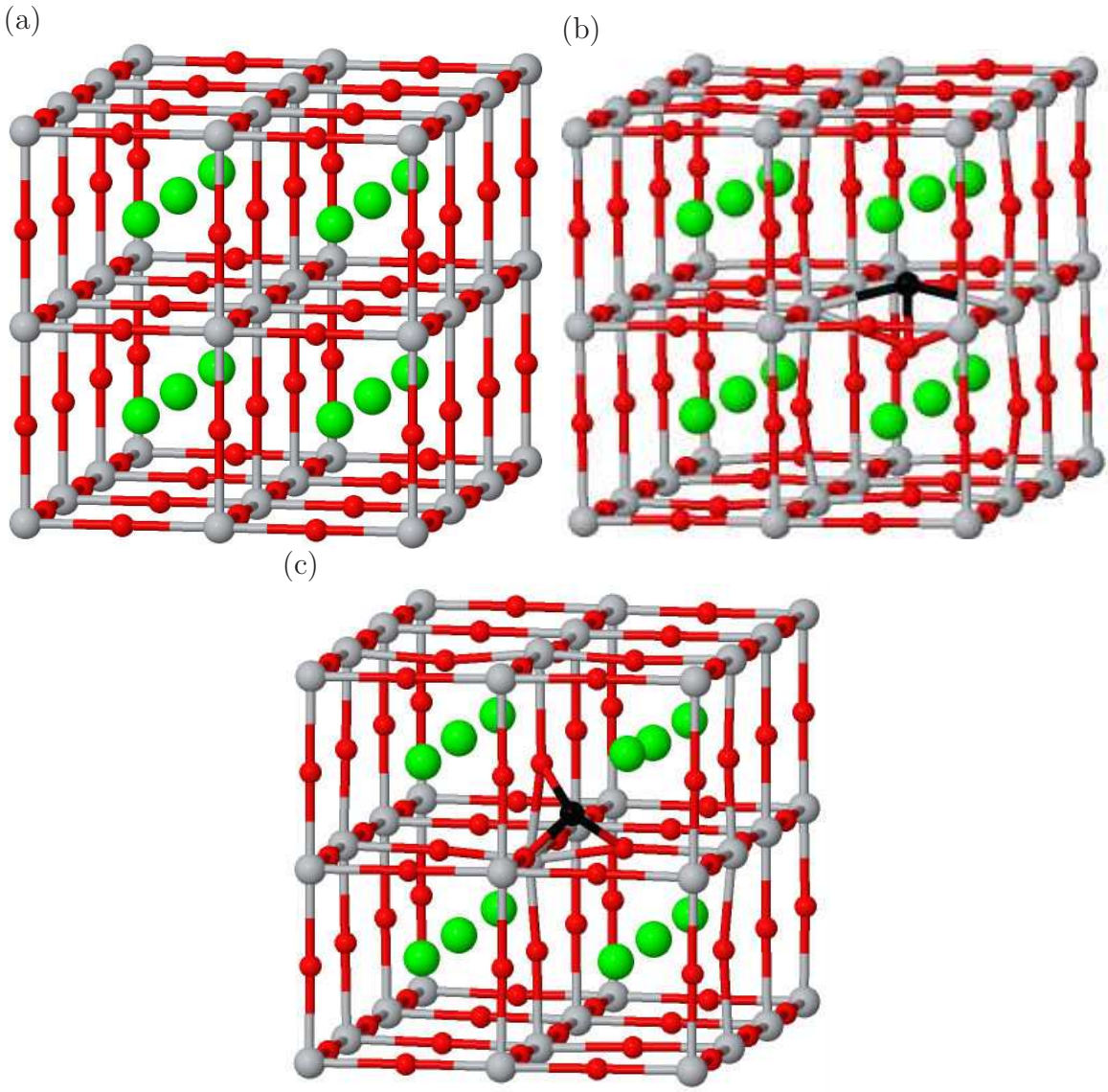

Figure 4.5: Schematics of the (b) CO and (c) CO_3 forms of C_i in $SrTiO_3$. An equivalent section of defect free $SrTiO_3$ is shown in (a) for comparison. Green, grey, red, and black spheres represent Sr, Ti, O, and C atoms respectively. Vertical and horizontal axes are approximately [001] and [010] respectively, with the tilted view adopted to aid clarity.

The band structures in the vicinity of the band-gap for the neutral charge state of the CO form and the overall +2 charge state of the carbonate form are shown in

Fig. 4.7. For the CO form there are both occupied and empty bands within the gap, which may be broadly characterised as the two π^* CO molecular orbitals, split by the crystal field. The wave function of the states are plotted in Fig. 4.6. The lowest energy occupied state wave function is depicted in Fig. 4.6(a), whereas Fig. 4.6(b) represents the wave function of the higher empty state in the gap.

The carbonate group is not so simply accommodated. If all components adopted their normal formal oxidation states, this would result in an overall +4 charge since the CO_3^{-2} ion accounts for only one of the three oxygen atoms affected. The band structure for the +2 charge state configuration (Fig. 4.7(b)) consists of a single occupied band in the upper half of the band-gap. The state is a combination of a molecular orbital on the carbonate group and the neighbouring Ti cation. It is made up of parallel p orbital on all four sites, but in anti-bonding combinations between C and the three oxygens, with the Ti d-orbital forming a σ bond with the p-orbital on the carbon as is quite clear in Fig. 4.8.

Based upon the band structures and expected oxidation states of CO and CO_3, it is natural to expect electrical levels to be present for interstitial carbon. The charge-dependent formation energies are shown in Fig. 4.7(c), indicating that the neutral charge state of the CO configuration and the +2 and +3 charge states of the CO_3 configuration are stable. According to the calculations, however, the +4 charge state is not favourable, although for $\mu_e = 0\,\text{eV}$ the +4 charge state is only very slightly higher in energy than +3.

In addition to the electrical levels, local modes corresponding to C–O stretches would be expected. For the neutral, CO-bonded configuration, the stretch mode is estimated at $1554\,\text{cm}^{-1}$, which is much lower than the vibrational mode of CO gas. In the +4 charge, local vibrational modes are calculated for the approximate C_{3v} CO_3 centre. There is an E-mode (an anti-symmetric combination of C–O stretches) at around $1429\,\text{cm}^{-1}$, and a non-degenerate breathing-mode at $1094\,\text{cm}^{-1}$. These are close to those of gas phase CO_3^{-2} (table 4.2). Similarly, the +3 charge state is predicted to have E and A_1 modes at 1154 and $942\,\text{cm}^{-1}$ respectively, whereas for +2

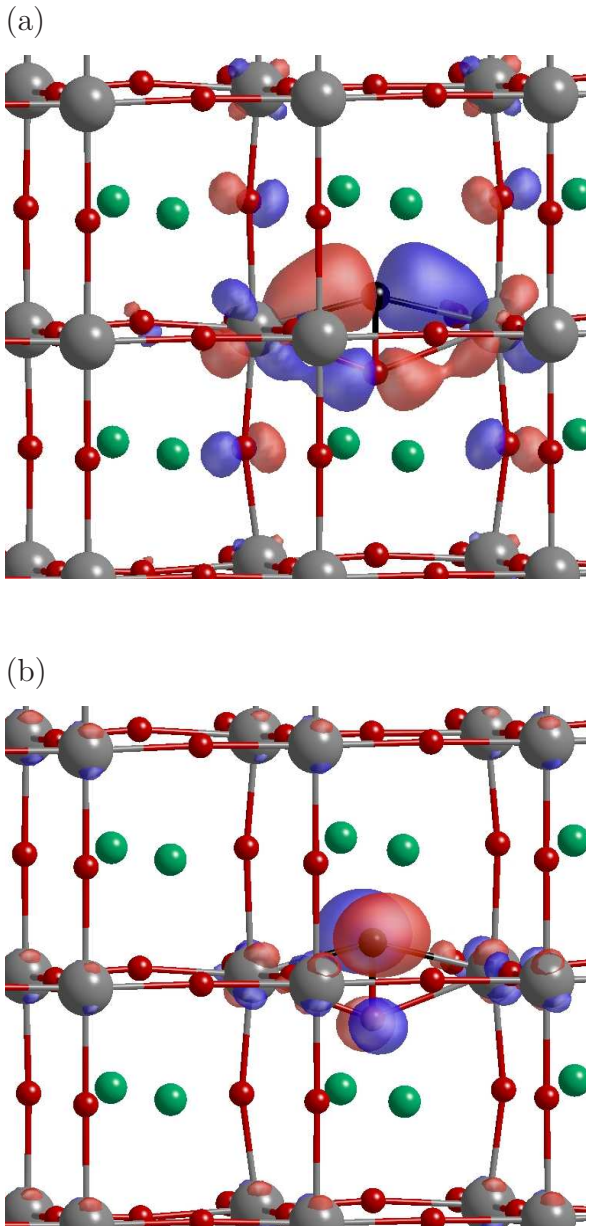

Figure 4.6: Plot of the wavefunction distribution of CO C_i configurations in $SrTiO_3$: (a) a partial *p*-*d* covalent bonding between the carbon atom and the two nearest Ti ions in CO form; and (b) π^* CO molecular orbitals associated with the empty state in the gap. Red and blue volumes showing wave function iso-surfaces of equal magnitude (0.1) and opposite sign. Colours and orientation are as indicated in Fig. 4.5.

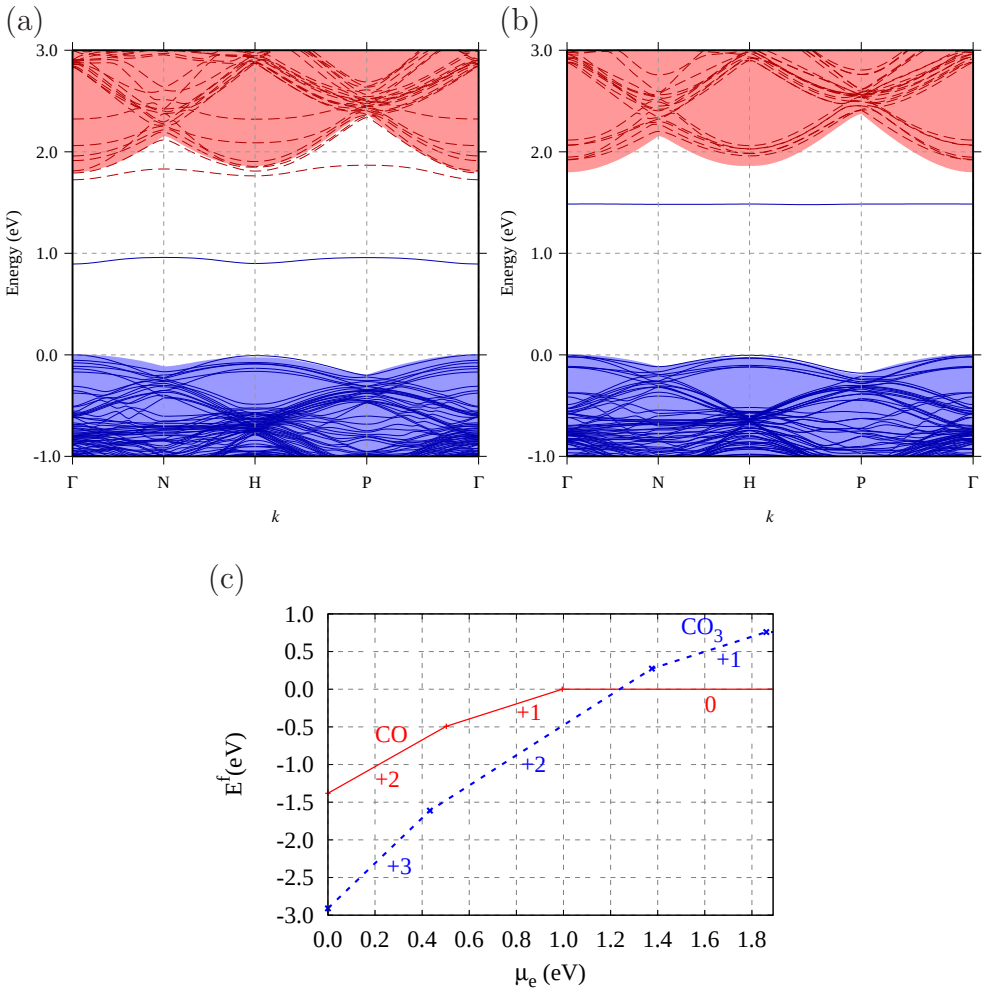

Figure 4.7: Band structures in the vicinity of the band-gap for C_i in: (a) the CO; and (b) the $(CO_3)^{+2}$ configuration, plotted along high-symmetry branches in the first Brillouin zone; and (c) shows $E^f(\mu_e)$ for various charge states of each structure. Occupied and empty bands in (a) and (b) are shown in solid (blue) and dashed (red) lines, respectively. The underlying shaded areas show the regions of the bands for the corresponding bulk supercell. The energy scale is defined such that the valence band maxima are at zero. In (c) the (red) solid line and (blue) dashed line represent the CO and CO_3 configurations, respectively. The gradient indicates the charge state, and the energy scale is defined by $E^f((CO)^0) = 0\,\text{eV}$.

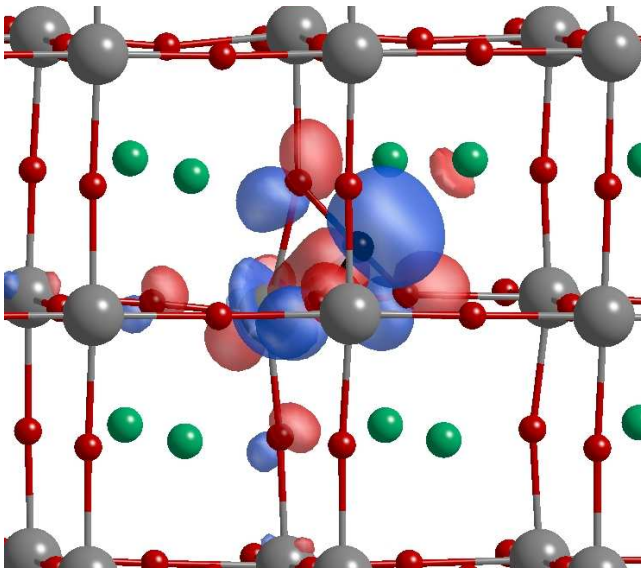

Figure 4.8: Wave function of the orbital state for the CO_3 C_i configuration in $SrTiO_3$. Red and blue volumes showing isosurfaces of the wave function of equal magnitude (0.1) and opposite sign. Colours and orientation are as indicated in Fig. 4.5.

these are at 1018 and 854 cm^{-1}. The increase in frequency with increasing positive charge results from the differences in bonding, with the σ-bond between the Ti and C atoms resulting in a non-planar CO_3 group in the +2 charge state being lost by +4 where the CO_3 group is close to planar.

4.3.2 C substituting for O

A possible naive expectation of the location of carbon in an oxide, based upon relative proximity in the periodic table, would be substitution at the oxygen site. The optimized atomic structure of such a centre (C_O), is shown in Fig. 4.9(a). The bond-lengths of a simple substitution are very similar to those of the host, with the Ti–C bond-length at 1.98 Å only slightly longer than the Ti–O bond at 1.94 Å, which is in agreement with previous calculations [62].

However, this structure is relatively unstable, and chemical reactions between car-

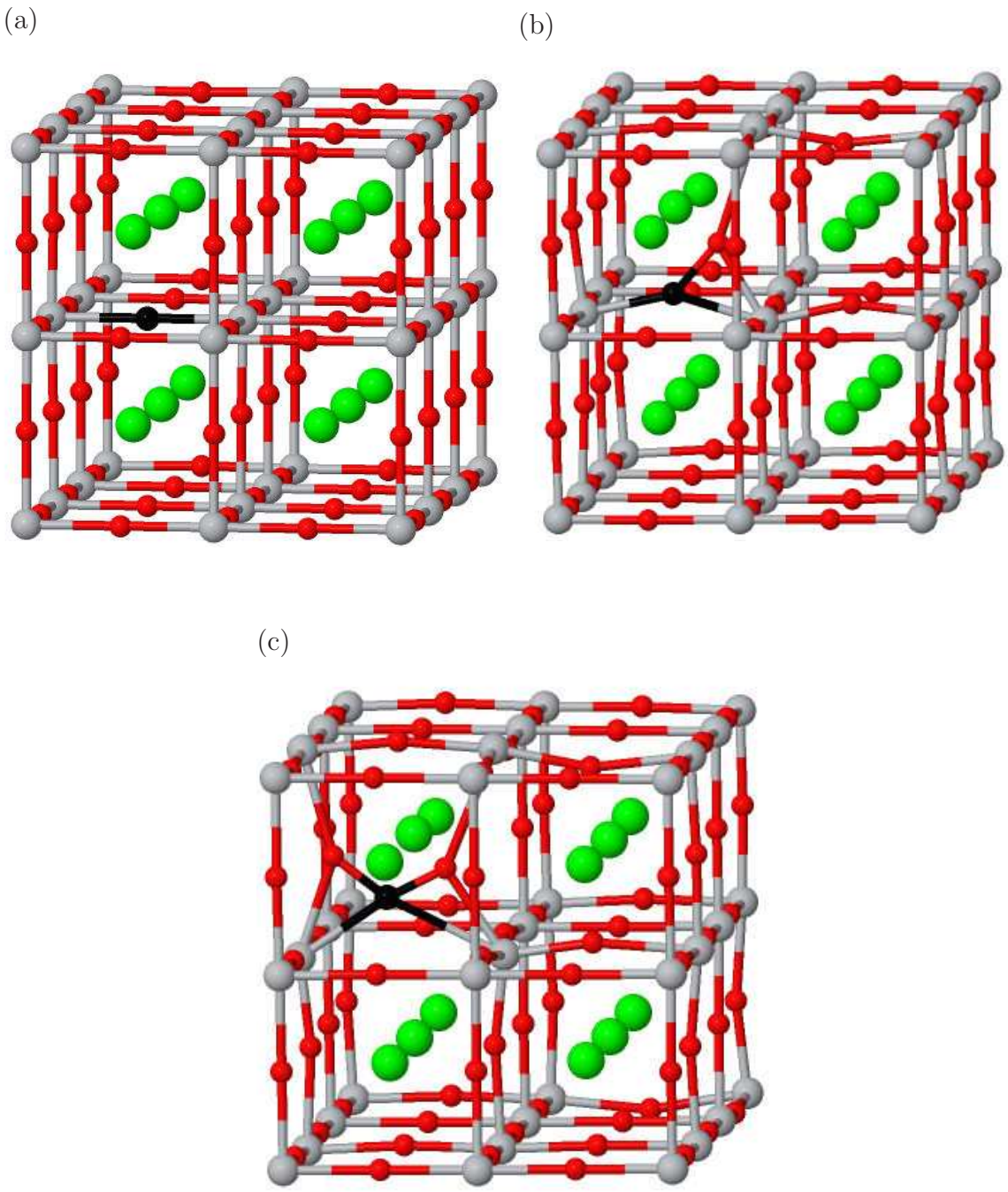

Figure 4.9: Schematics of (a) C_O, (b) $(CO)_{(2O)}$ and (c) $(CO_2)_{(3O)}$ in $SrTiO_3$. Colours and orientation are as indicated in Fig. 4.5.

bon and nearby host oxygen ions are energetically favourable for the neutral charge state. Fig. 4.9(b) shows the resulting structure for the neutral charge state, which can

be characterized as a CO species shared between two oxygen sites, $(CO)_{(2O)}$. In the neutral charge state, the C–O bond-length at 1.44 Å is significantly longer than a CO molecule, but close to that of a free CO^{-2} ion. This long bond is due to a combination of the charge state of the group and bonding interactions with the neighbouring Ti atoms. The C–O bond length is shorter for +1 and +2 charge states, being 1.36 and 1.28 Å respectively, which is consistent with the depopulation of an anti-bonding orbital.

The band structures for the two configurations are instructive in terms of the origin of their relative stabilities. The on-site form (Fig. 4.10(a)) has two C-related levels in the band-gap, which are largely comprised of an occupied p-state along the Ti-C-Ti axis and a partially filled, degenerate pair made up of the perpendicular p components. To clarify the combination of orbitals between the carbon dopant and adjacent host atoms, wave functions for the isosurface near the carbon dopant have been calculated, and the results are illustrated in Fig. 4.11. The on-site centre would therefore be expected to act as a donor.

Fig. 4.10(b) shows the electronic structure of the $(CO)_{(2O)}$ structure in the neutral charge state. The states in the upper part of the band-gap are related to the combination of π^* CO and σ_{pd} with the neighbouring Ti atoms, illustrated in Fig. 4.12.

Again, the electrical levels have been estimated, with the formation energies plotted in Fig. 4.10(c). As might be expected, the on-site centre can accept an electron, but the addition of a second electron which would render it isoelectronic with oxygen is not energetically favoured. The picture for the chemically reacted system is slightly more complex. The existence of the occupied states in the band-gap are found to result in single and double donor levels, with the depopulation of the π^* state corresponding to a decrease in the C–O bond-length. However, removal of three or four electrons is also possible, but with a spontaneous reconstruction to form a centre where C is bonded to *two* oxygen neighbors, $(CO_2)_{(3O)}$ (see Fig. 4.9(c)).

As with C_i, C_O is likely to give rise to characteristic vibrational modes. For the on-site form a stretching vibrational modes lies at 875 cm^{-1} in the −1 charge state, which

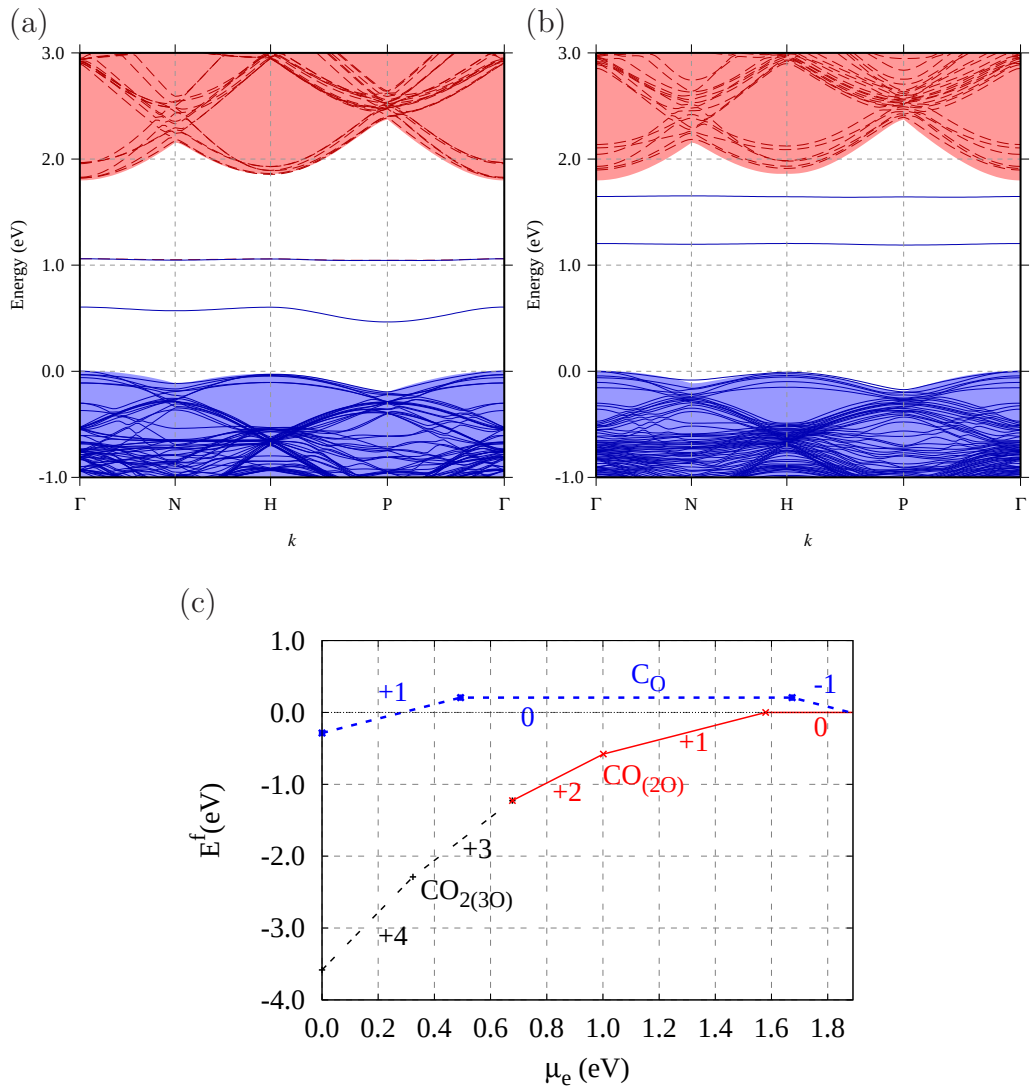

Figure 4.10: Band structures in the vicinity of the band-gap for C_O in: (a) the on-site and (b) the $(CO)_{(2O)}$ configurations, plotted along high-symmetry branches in the first Brillouin zone; and (c) showing $E^f(\mu_e)$ for various charge states of each structure. Lines, shading and scales in (a) and (b) are as defined in Fig. 4.7. In (c) the (red) solid line, (blue) dashed line, and (black) dotted line represent the $(CO)_{(2O)}$, C_O, and $(CO_2)_{(3O)}$ configurations respectively. The gradient indicates the charge state, and the energy scale is defined by $E^f(((CO)_{(2O)})^0) = 0\,\text{eV}$.

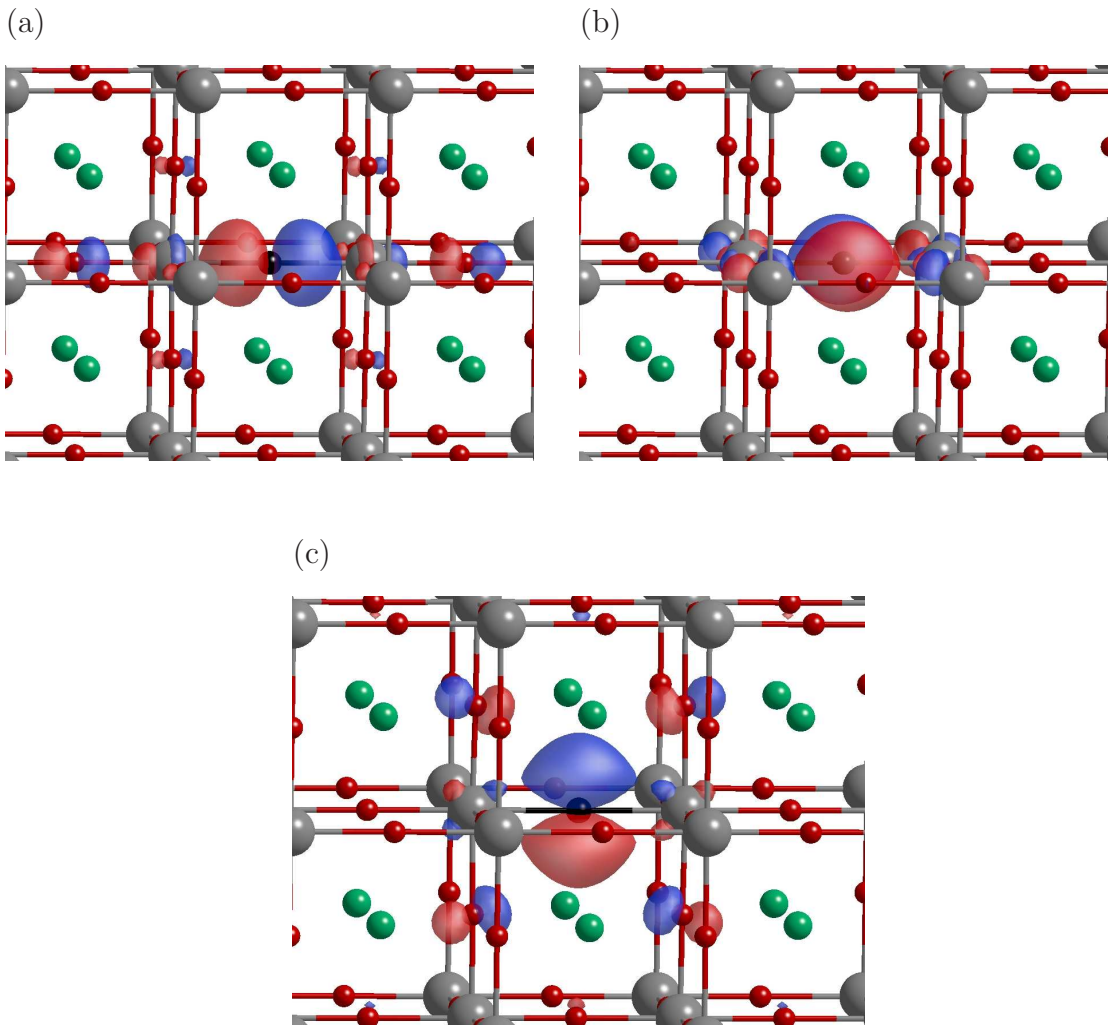

Figure 4.11: Schematics showing wave functions of C_O: (a) lowest occupied p-state along the Ti-C-Ti axis; (b) and (c) a partially filled, degenerate pair made up of the perpendicular p components. Red and blue volumes show wave function iso-surfaces of equal magnitude (0.1) and opposite sign. Colours and orientation are as indicated in Fig. 4.5.

is in reasonable agreement with calculations of Ti–C modes in TiC nanostructures [81]. The vibrational modes of the $(CO)_{(2O)}$ provide further insight into the nature of the defect. In the neutral charge state a mode at 943 cm^{-1} is calculated, which is close to the calculated vibrational mode of CO^{-2}. In the +1 charge state the vibrational

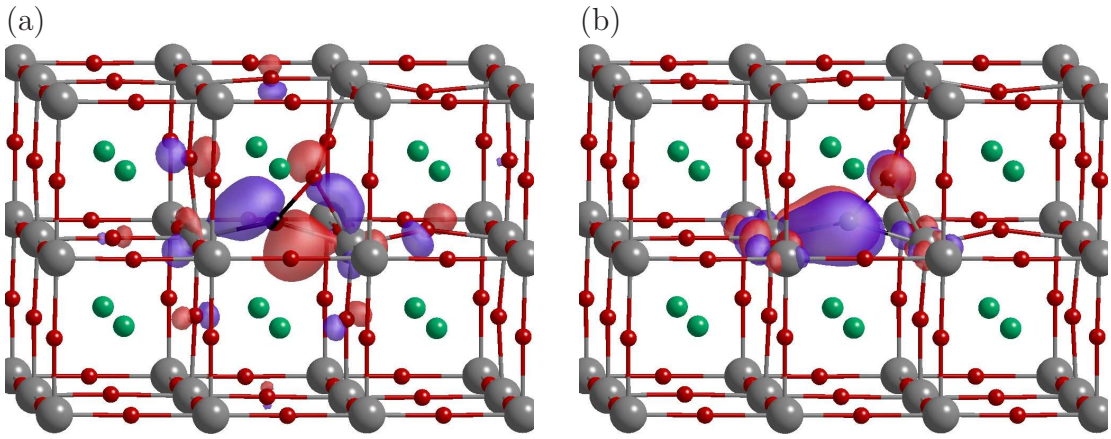

Figure 4.12: Plots (a) and (b) showing the wave function (red and blue 0.1 iso-surfaces) for the two occupied levels related to the combination of π^* CO and σ_{pd} with the neighboring Ti atoms for $(CO)_{(2O)}$ defect in $SrTiO_3$. Colours and orientation are as indicated in Fig. 4.5.

modes increase to 1104 cm^{-1}, and 1345 cm^{-1} for the +2 charge state, corresponding to increased bond-order. For the $(CO_2)_{(3O)}$ form, the increase in the number of C–O bonds means that the +3 and +4 charge states yield two stretch modes each, estimated at 1125 and 1294 cm^{-1} for the +3, and 1121 and 1348 cm^{-1} for the +4 state. The difference in geometry leads to the difference in vibrational modes, which can be easily distinguished experimentally.

4.3.3 C substituting for Sr

The optimised structure of Sr substituted by carbon, C_{Sr}, shown schematically in Fig. 4.13(a), shows the spontaneous displacement of C to form three C–O bonds. Their length is calculated at 1.29 Å, close to that in a carbonate anion. The formation of the carbonate leaves the $SrTiO_3$ lattice deficient by one Sr cation and three oxygen anions. This results in a net excess of four electrons to be accounted for. Two of these are associated with the carbonate group, but this means that the reaction of carbon on the Sr site with three oxygen atoms is expected to result in a double donor.

Indeed, this is also what would be expected on the basis of the valences of Sr and C.

(a)

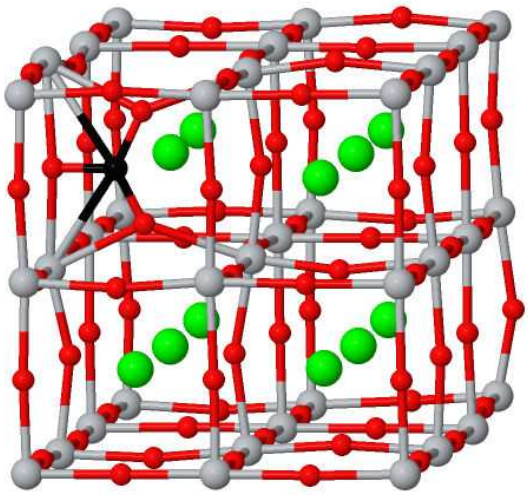

(b)

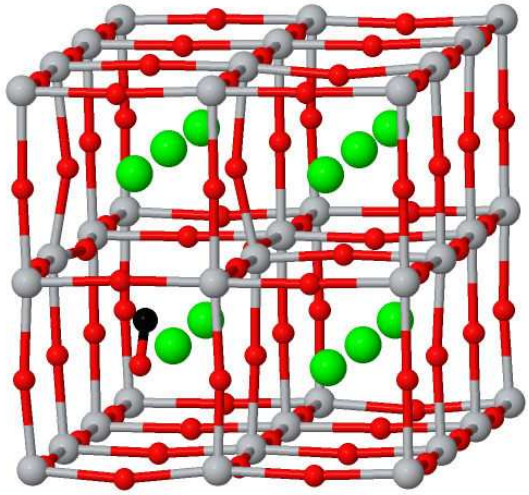

Figure 4.13: Schematic of C_{Sr} in $SrTiO_3$ in the (a) CO_3 and (b) $(CO)_{Sr}$–V_O forms. Colours and orientation are as indicated in Fig. 4.5.

However, there is an alternative chemical rearrangement that results in an isoelectronic centre. If C reacts with a single oxygen atom, so that a CO anion resides at the Sr site and an oxygen vacancy is formed, then no excess of deficit of charge results. Numerous relative orientations of the CO ion and oxygen vacancy have been analysed,

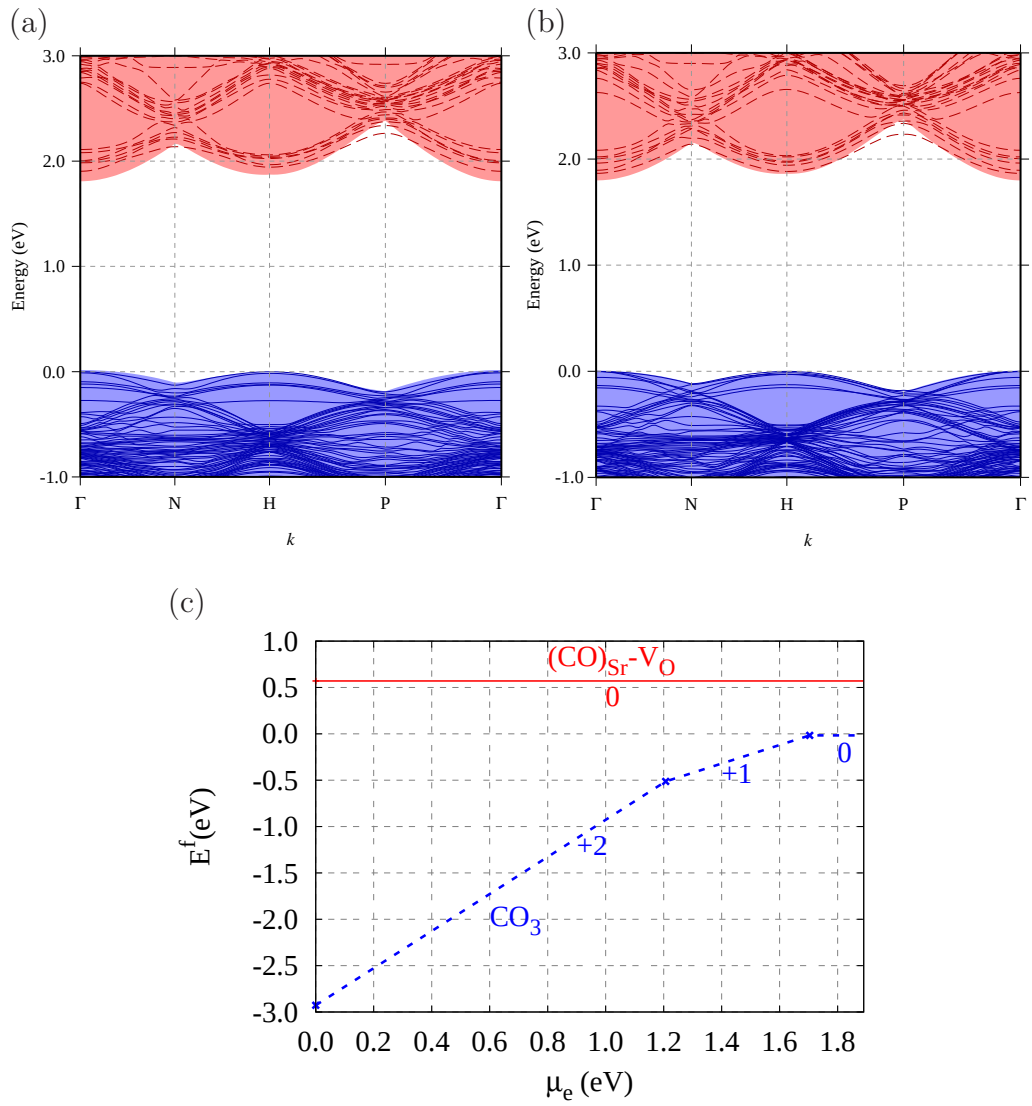

Figure 4.14: Band structures in the vicinity of the band-gap for C_{Sr} in: (a) +2 charge state of CO_3 and (b) the $(CO)_{Sr}$–V_O configurations, plotted along high-symmetry branches in the first Brillouin zone; and (c) showing $E^f(\mu_e)$ for various charge states of each structure. Lines, shading and scales in (a) and (b) are as defined in Fig. 4.7. In (c) the (red) solid line and (blue) dashed line representing the $(CO)_{Sr}$–V_O and $(CO_2)_{(3O)}$ configurations respectively. The gradient indicates the charge state, and the energy scale is defined by $E^f((CO_3)^0) = 0\,\text{eV}$.

and the one shown is the lowest in energy. The C–O bond length has been calculated to be 1.13 Å, which is close to the bond length of a carbon monoxide molecule. The structure shown schematically in Fig. 4.13(b) is metastable, but unstable compared with the carbonate form (see Fig. 4.14(c)), which can be accounted for on the basis of the relative favourability of the formation of three covalent bonds.

The expectations based upon oxidation states for the two structures illustrated are confirmed by their band structures (Fig. 4.14). In the +2 charge state of the carbonate form, and the neutral charge state of the CO form, the band-gap is devoid of states.

The vibration modes for C_{Sr} have also been calculated for the two structures. The CO_3 form in the overall neutral charge state has modes at 1079, 1369, and 1517 cm^{-1} associated with C–O stretches. The ionised forms have modes within 8 cm^{-1} of the neutral charge state, which is consistent with the shallow donor behaviour predicted for this centre. However, in the neutral charge state, the vibrational mode of C_{Sr} in the CO form is observed to be at 2086 cm^{-1}, which is in reasonable agreement with the experimental value of carbon monoxide molecule frequency.

4.3.4 C substituting for Ti

The final form for C impurity in $SrTiO_3$ is substitution of titanium, C_{Ti}, which may be anticipated on the grounds of both C and Ti being group-IV elements. A configuration has been optimised where the initial structure has been perturbed from the ideal octahedral symmetry, avoiding any artificial symmetry constraint. The relaxed structure has three C–O bonds (1.29 Å), which is significantly shorter than the Ti–O inter-nuclear distances in $SrTiO_3$ (1.93 Å). The calculated C–O bond-lengths in C_{Ti} are close to those of the carbonate group and those of strontianite [82], $SrCO_3$, so that the relaxation of the structure into the highly distorted geometry can be interpreted in terms of the formation of a carbonate ion, CO_3^{-2} associated with a single Sr^{+2} cation. The structure is shown schematically in Fig. 4.15, and after structural optimization it has been found to be very close to C_{3v} symmetry. Here, carbon forms

covalent bonds with three of its O neighbours, leaving three oxygen ions effectively under co-ordinated, but overall the anions and cations are balanced. For the simulation supercell, $(SrTiO_3)_{32}$, the substitution of Ti by C might be expressed as resulting in $(SrTiO_3)_{31}(SrCO_3)_1$, or approximately $(SrTiO_3)_{0.97}(SrCO_3)_{0.03}$.

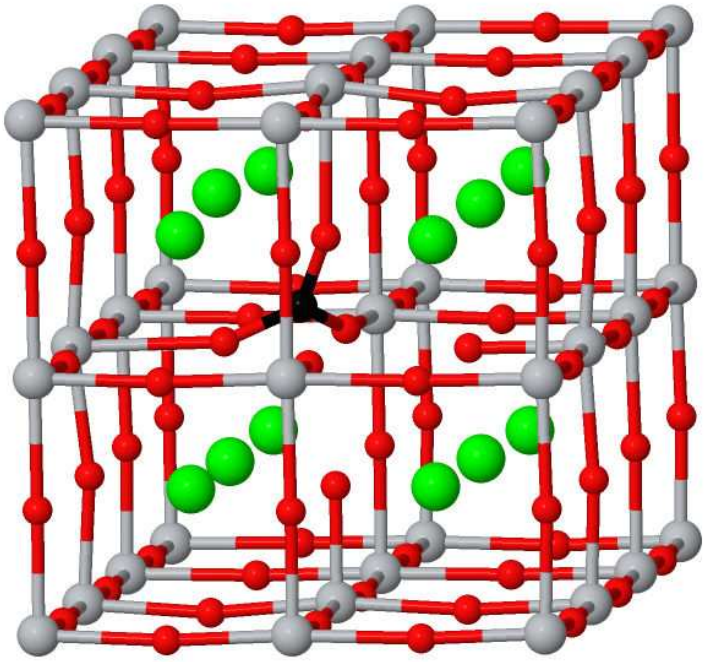

Figure 4.15: Schematic of C_{Ti} in $SrTiO_3$. Colours and orientation are as indicated in Fig. 4.5.

The band structure for C_{Ti} is shown in Fig. 4.16. It should first be noted that the inclusion of carbon has the apparent effect of increasing the band-gap, and the extent of this depends upon the effective concentration of C, with the increase being larger where C_{Ti} is modeled in a smaller simulation cell. This is to be expected since the band gap of pure $SrTiO_3$ at 3.25 eV is smaller than that of $Sr(CO_3)$ at around 4.3 eV [83], and so the 1% alloy might well be expected to have a band gap slightly larger than that of pure $SrTiO_3$.

To provide a mechanism for the experimental direct identification of C_{Ti}, a local vibrational mode above the one-phonon maximum could prove highly effective. It is

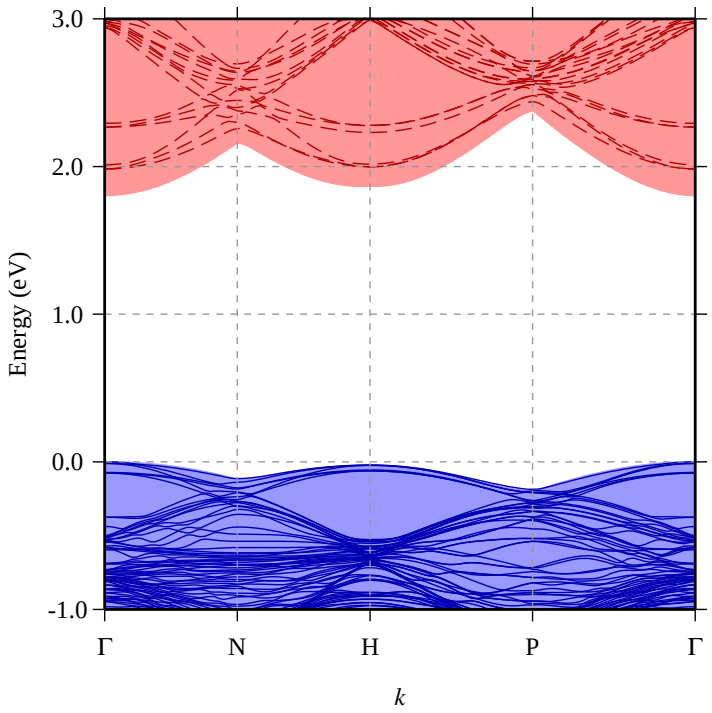

Figure 4.16: Band structures in the vicinity of the band-gap for C_{Ti} in $SrTiO_3$, plotted along high-symmetry branches in the first Brillouin zone. Lines, shading and scales are as defined in Fig. 4.7.

of particular note that for the C_{3v} C_{Ti} centre a degenerate (E) C–O stretch mode was found at 1414 cm^{-1}, and a breathing stretch-mode with A_1 symmetry at 1081 cm^{-1}. These are close to the experimental values for gas phase CO_3^{-2} (see table 4.2) and with the carbonate related $SrCO_3$ vibrational modes [84].

Lower frequency modes of the carbonate group are also present for C_{Ti}, but are resonant with the one-phonon density of states. Both of the local modes are infra-red and Raman active, and given sufficient concentrations one might seek to confirm the presence of this form of carbon centre directly via either IR or Raman spectroscopy.

Moreover, the energetics for the reorientation of the carbonate group have been examined. The initial and final structures, and the energy profile along the minimum

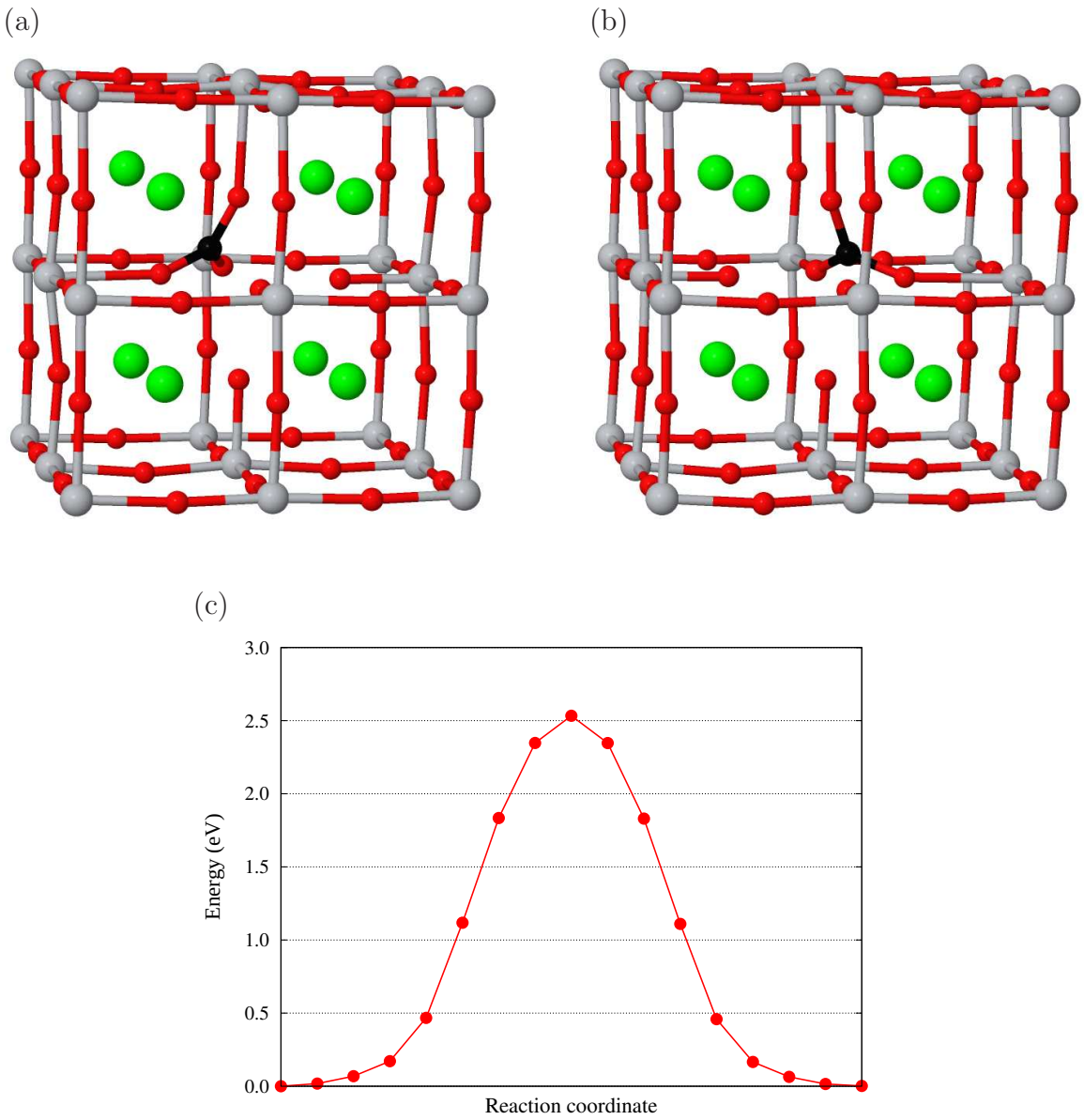

Figure 4.17: Schematic of (a) initial, and (b) final structure of C_{Ti} in $SrTiO_3$ in a simple reorientation process; with (c) showing the calculated reorientation barrier of C_{Ti} in $SrTiO_3$ between the initial and final structures. Colours and orientation are as indicated in Fig. 4.5.

energy path between them, are shown in Fig. 4.17. The activation energy for reorientation is predicted to be around 2.5 eV. This relatively high value is a consequence of the covalent bonding within the carbonate group, so that reorientation involves both

the breaking and formation of strong chemical bonds. The carbonate group may be oriented with the principal axis along any of the eight ⟨111⟩ directions if randomly orientated. However, under specific conditions, such as (111) biaxial strain induced by interface mismatch, the different orientations would have different energies, and given the high energy for reorientation, may be preferentially aligned. Since the C_{Ti} structure has a permanent electric dipole, a polarised population of defect centres that are unable to reorient under normal temperature and electric field conditions would be expected to have an impact upon the dielectric anisotropy. Furthermore, where ferroelectric distortions are induced under strain, C_{Ti} would be expected to alter both the details of the phase and the resulting dielectric constant.

4.3.5 Formation energy comparison

Finally, a thermodynamic assessment of the relative stability of the four sites discussed above is considered, where the atomic and electron chemical potentials must be taken into account.

The most stable forms of carbon defect centres as a function of μ_{Sr} and μ_{Ti} for three selected electron chemical potentials are plotted in Fig. 4.18. For example, for $\mu_e = E_v$ (Fig. 4.18(a)), with $\mu_{Sr} = -7\,\text{eV}$ and $\mu_{Ti} = -10\,\text{eV}$ which lies in the $SrTiO_3$ stable region towards the oxygen-rich limit, the lowest energy carbon defect is found to be C_{Ti}. The areas indicated by the dashed lines show which carbon source material specifies the carbon chemical potential, which in the example is $SrCO_3$ (see section 4.1, page 50).

For p-type $SrTiO_3$ (Fig. 4.18(a)), unsurprisingly, electron-donating systems are favoured. This is also consistent with the expectations that metal substitution is favoured in the oxygen-rich conditions, with both C_{Sr} and C_{Ti} stable for the left-hand half of the $SrTiO_3$-stable region. In oxygen-lean conditions, the +4 charge state of the CO_2 configuration of C_O is favoured. What is perhaps less obvious is that, in p-type conditions, *all* of the carbon centres analysed contain C–O covalent bonds, two of which are of a carbonate form, so that the observation of carbonate-related vibrations

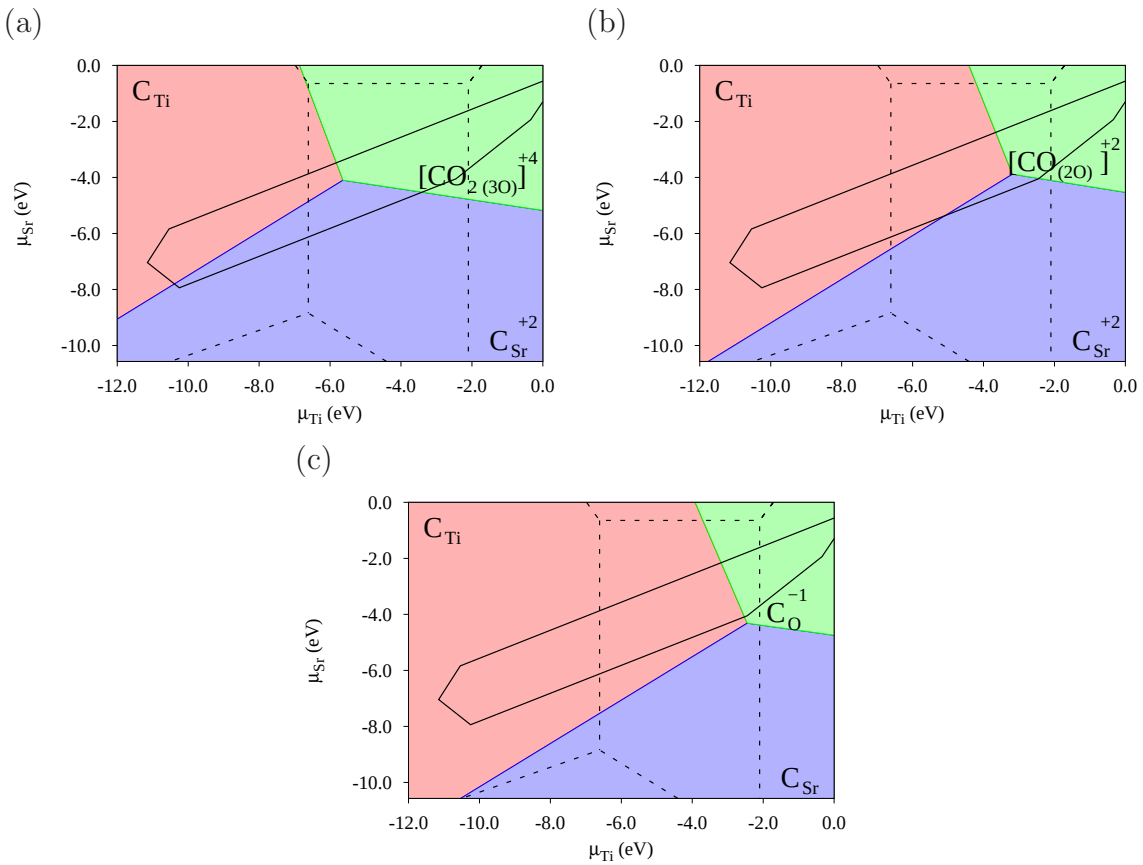

Figure 4.18: Graph showing the calculated equilibrium form of C-related defects, coloured according to defect, with respect to the atomic chemical potentials for different electron chemical potentals: (a) $\mu_e = E_v$ (p-type $SrTiO_3$); (b) $\mu_e = E_g/2$; and (c) $\mu_e = E_c$. The $SrTiO_3$-stable region is superimposed (solid black line), and the C source phase is indicated by the dashed lines (*c.f.* Fig. 4.4).

cannot be correlated only with the formation of C_{Ti}.

As the electron chemical potential moves from the valence to conduction bands, C_{Ti} dominates more and more of the $SrTiO_3$-stable region, until the acceptor levels of the C-containing defects fall below μ_e. Then, in n-type conditions ($\mu_e = E_c$), the possibility exists of the formation of C_O in the negative charge state with the anion lying on-site.

According to the current calculations, interstitial carbon is never thermodynamically favoured, but it remains possible that such a centre might exist transiently during the carbon migration processes.

4.4 Conclusion

Using first-principles density-functional calculations, the characteristics of carbon impurity in cubic $SrTiO_3$ have been examined, including structural configuration, electronic properties, vibrational modes, reorientation barriers and formation energies. It is found that carbon energetically favours the formation of carbonate groups for interstitial and both Ti and Sr substitutions. The vibrational characteristics of the defect centres therefore have some similarities, and for the CO_3 forms occupy similar locations in the frequency domain. However, due to site symmetry and the influence of local co-ordination, the vibrational frequencies offer a potential route to discrimination between different sites. Furthermore, from a combination of the band structure and electrical level calculations, depending upon which site the carbon occupies it may form donor, acceptor, or isoelectronic centres. The reorientation barrier for the carbonate group has been estimated, with C_{Ti} taken as an example. Here, because the process involves the breaking of CO covalent bonds, the barrier is at a relatively high value of around 2.5 eV.

Finally, the formation energies calculated to determine thermodynamic stability suggest that, although carbon favours substitution at the Ti site for a wide range of electron chemical potentials and growth conditions, in oxygen-lean growth and especially where μ_e is close to the valence band substitution for either Sr or O is also likely. Where carbon substitutes for Sr, it may be a source of free electrons as based upon the electronic structure, and C_{Sr} is a candidate for a shallow donor.

These results apply to cubic $SrTiO_3$. The next chapter presents a discussion of the effect of carbon impurities on the characteristics of tetragonal $PbTiO_3$, which is a ferroelectric material at room temperature, and the differences between carbon

impurities in $SrTiO_3$ and $PbTiO_3$ are also considered.

Chapter 5

Carbon impurities in lead titanate

$PbTiO_3$, a room-temperature ferroelectric, high-κ material, is of great interest for technological applications. However, organic species present during growth make carbon a key impurity. This chapter presents the results of a study using density functional calculations of the structural configuration that carbon is most likely to adopt in tetragonal $PbTiO_3$ under varying growth conditions. The calculations show that, for most conditions, the electrically passive substitution of Ti is most likely, but under specific conditions donor species are occasionally possible. Highly characteristic vibrational modes are predicted to provide a route to experimental identification.

5.1 Introduction

Ferroelectric materials are valued for applications such as optoelectronics and high capacity computer memory cells [23, 27, 85], with the nonlinear characteristics of ferroelectric materials and high-κ dielectrics used to make nano-scaled capacitors with a tunable capacitance. In particular, thin films of perovskite lead titanate, $PbTiO_3$ [86–89], in memory applications exhibit low operating voltages and high switching speeds [90].

$PbTiO_3$ is piezoelectric and ferroelectric at room temperature due to its non-cubosymmetric, tetragonal structure where the oxygen octahedra are displaced along

the [001] direction [91]. The Ti ions in O-Ti-O chains along the [001] direction move parallel to this direction, as shown in Fig. 5.1, alternately strengthening and weakening the Ti-O bonds. The strong bonds result from hybridisation between Ti-3d states and O-2p states and are essential for ferroelectricity [92]. The strength of the Pb-O bonds arises from the hybridisation of the Pb-6s and O-2p orbitals, which has been reported to theoretically be a key factor of the much larger ferroelectricity of $PbTiO_3$. The covalent nature of the Pb-O bonds stabilises the ferroelectricity of the tetragonal ground state, which has been experimentally confirmed [93].

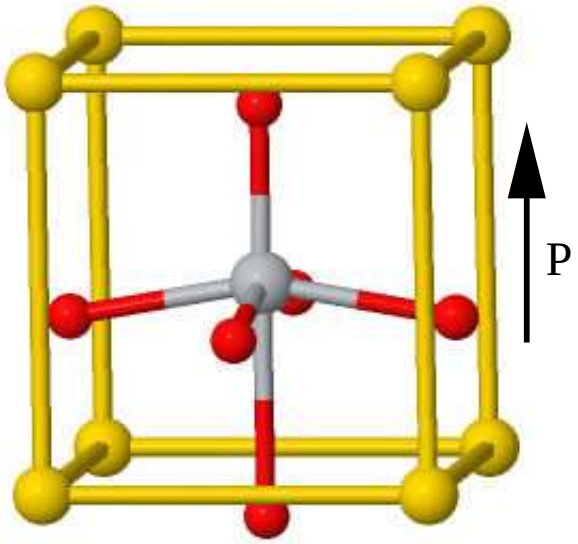

Figure 5.1: Perovskite structure of tetragonal $PbTiO_3$ at room temperature with a displacement of the oxygen octahedra relative to both the Ti and Pb cation which corresponds to a spontaneous polarisation (P). Gold, grey and red spheres represent Pb, Ti and O, respectively. Vertical and horizontal axes are approximately [001] and [010] respectively, with the tilted view adopted to aid clarity.

Above 490 °C, $PbTiO_3$ adopts a cubic, paraelectric form [94], but relatively small stresses [95] can affect the polarisation beyond this temperature. Polarisation in the host also impacts upon the polarisation of defects within the crystal: defect dipoles

favour alignment with the spontaneous polarisation direction of the host, such as is observed for the complex made up from Fe^{3+} at the Ti site adjacent to an oxygen vacancy [96].

Both theory and experimentation have been used to optimise the $PbTiO_3$ properties of $PbTiO_3$ [10, 97, 98]. Defects, many which remain to be identified, significantly impact remnant polarisation, the motion of domain walls, the dielectric constant and leakage current [99,100]. Amongst these defects, oxygen vacancies are well established dopants in the perovskites, reducing the titanium from Ti^{+4} to Ti^{+3} and doping the material n-type [101]. However, both theoretical and experimental studies have shown that the ferroelectric properties of $PbTiO_3$ are controllable by the dopants substituting at the A or B sites, as they mediate the concentration of the intrinsic defects [102–106].

$PbTiO_3$ growth methods include flux crystal growth [94], magnetron sputtering [107–109], pulsed laser deposition [110], photochemical deposition [111], sol-gel methods [112–115] and chemical vapour deposition (CVD) [116, 117]. Metalorganic CVD (MOCVD) [118–120], which uses organic precursors, has been extensively used to deposit oriented thin films. For practical applications, the $PbTiO_3$ films have to meet some quality demands such as high chemical homogeneity and low surface roughness [121, 122]. Compared to MOCVD, atomic layer deposition (ALD) operates at lower temperatures while using the same precursors.

However, the use of the organic precursors leads to carbon contamination [100, 123, 124]. For example, in lead zirconate titanate, the infrared spectrum has peaks attributed to carbon-oxygen group vibrations [100]. Additionally, hysteresis effects have been assigned to organic content in the material [100]. These considerations motivate the present work, in which density functional theory calculations are employed to study the structural, electrical, electronic, vibrational and energetic properties of carbon defects for different sites in tetragonal $PbTiO_3$. The results for each of the most plausible configurations are presented in this chapter, and the same type of thermodynamic model as used in $SrTiO_3$ will be applied in this case to determine which are most likely to appear in practice.

5.2 Computational Method

The method used in this study is as described in section 4.2. In addition, the Pb atoms are represented by basis sets made up from independent sets of s, p and d functions with four widths (constituting 40-functions per atom). Norm-conserving, separable pseudopotentials have been used [16] with valance sets for Pb being $6s^2 6p^2$. The valance sets for Ti, O and C are listed in section 4.2. Integration over the Brillouin-zone is achieved via k-points sampling [14], and matrix elements of the Hamiltonian are determined using a plane-wave expansion of the density and Kohn-Sham potential [67] with a cut-off of 150 Ha, resulting in the absolute convergence of the total energy with respect to the expansion of the charge density to better than 0.03 meV.

For bulk, tetragonal $PbTiO_3$, this computational approach yields equilibrium lattice parameters of a=3.85 Å and c=4.09 Å. As is typical of LDA calculations, the calculated lattice parameters are slightly underestimated. Hence, the calculated lattice constants are smaller than experimental values by around 1% [97, 125–127]. The tetragonal structure of $PbTiO_3$ is defined by the a and c lattice constants, and by three internal coordinates u_i (i=Pb, Ti and O). Table 5.1 summarises the structural information of tetragonal $PbTiO_3$ in the five atom unit cell. As shown in this table, the optimised internal displacements agree well with experimental values and with previous calculations. The calculated band-gap of 1.5 eV, reflecting the well-documented underestimate arising from the underpinning methodology, is consistent with previous comparable calculations of 1.47 eV [128].

Defects are modelled using supercells with lattice vectors $2\sqrt{3}[a\bar{a}\bar{c}]$, $2\sqrt{3}[\bar{a}a\bar{c}]$ and $2\sqrt{3}[\bar{a}\bar{a}c]$, where a and c are the lattice constants in the tetragonal unit cell. The supercells that are used are exactly the same as those used to analyse the C impurities in $SrTiO_3$, except that the $PbTiO_3$ structure is in tetragonal symmetry. In the current work, the bulk tetragonal $PbTiO_3$ supercell is built from an $SrTiO_3$ cubic structure by considering the diagonals in the a and c direction, meaning that the supercell in the absence of any defect is $Pb_{32}Ti_{32}O_{96}$. For all defect calculations, the Brillouin zone integration was reformed using a $2 \times 2 \times 2$ Monkhorst-Pack mesh [14].

Table 5.1: Calculated, theoretical and experimental bulk properties of tetragonal $PbTiO_3$ including lattice constant (a_0, Å), axial ratio (c/a) and internal coordinates along the z direction (u) are given in terms of the c lattice constant. The experimental and theoretical data is taken from published studies [125, 129].

	Current calculations	Experiment	Previous calculations
a_0	3.85	3.90	3.90
c/a	1.063	1.063	1.063
u_{pb}	0.000	0.000	0.000
u_{Ti}	0.539	0.540	0.549
$u_{(\mathrm{O}_1,\mathrm{O}_2)}$	0.621	0.612	0.630
u_{O_3}	0.107	0.112	0.125

As for $SrTiO_3$ vibrational modes have been calculated by obtaining the second derivatives of the energy with respect to atomic positions, which are then assembled into the dynamical matrix, as mentioned in section 3.2. The second derivatives are obtained from a finite difference approximation involving the forces calculated on atom i when displacing atom j in each of the three Cartesian directions.

Finally, the reaction pathways and activation energies are determined using the climbing nudged-elastic-band (NEB) method [21, 22], and the convergence of the saddle point energy with respect to the number of images and the image-forces has been established to within a few meV (see section 3.6).

5.3 Results and discussion

5.3.1 Interstitial C

As for $SrTiO_3$ (see chapter 4), the first site examined is the interstitial (C_i). Since there are many plausible locations for an interstitial ion in the lattice, a wide range of initial geometries have been optimised. Based on the calculations, two distinct configurations have been identified for different charge states, with C bonded to either one (CO) or three (CO_3) oxygen atoms (Fig. 5.2).

In the CO structure, C_i prefers to form a covalent bond with one oxygen neighbour, resulting in a C_{2v} symmetry group (see Fig. 5.2(b)). The calculations show that carbon is likely to link with O along the [001] direction. The C–O bond length is 1.25 Å, which is consistent with a CO^{-2} ion substituting for the host oxygen ion. This structure is stabilised by a partial *p*-*d* covalent bonding between the carbon atom and the two nearest Ti ions, as shown in Fig. 5.3.

The CO_3 structure (Fig. 5.2(c)) exhibits a more dramatic impact upon the host, with the formation of three C–O bonds close to C_{3v} symmetry, located in the $[00\bar{1}]$ (anti-polar) direction, which is completely different from that found for $SrTiO_3$ (see section 4.3). The C–O distances have been calculated to be 1.29 Å in the polar direction and 1.27 Å in the a-b plane. The calculations show that the configuration with the CO_3 in the $[00\bar{1}]$ direction is more stable than that with the CO_3 in the [001] direction by around 0.2 eV. The reorientation energy of the carbonate group between these directions has been examined. The initial and final structures are shown in Fig. 5.4. The forward activation energy for reorientation is predicted to be around 2.6 eV as a result of the breaking and formation of strong covalent chemical bonds. The stable defect is polarised in the $[00\bar{1}]$ direction which is opposite the the bulk polarisation [001] and, upon switching, the bulk polarisation can be reversed easily. However, it is difficult to reverse the the defect fixed dipole, which has an effect on the ferroelectric response.

Since the normal charge state of the carbonate ion is -2, the formation of this

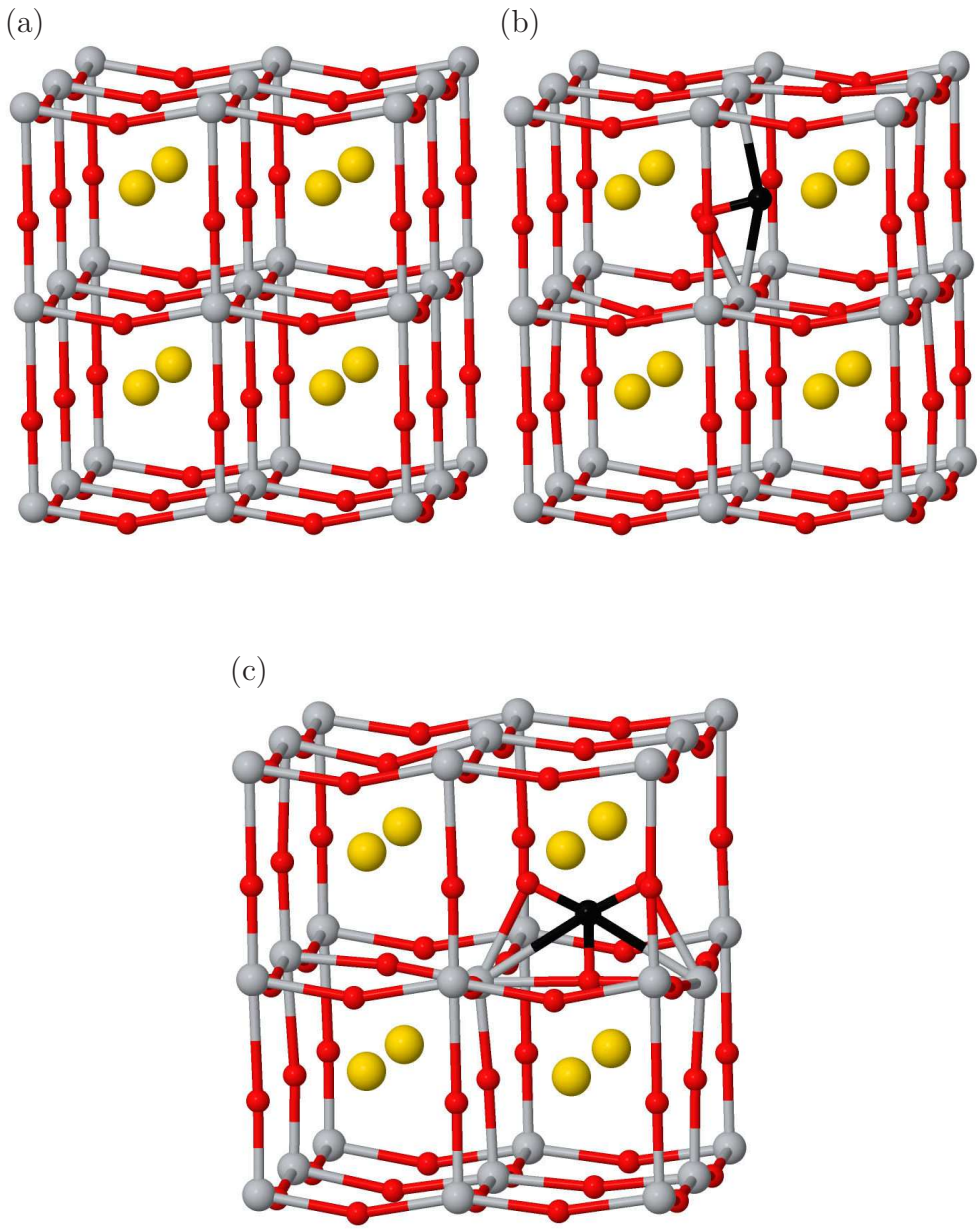

Figure 5.2: Schematics of (b) CO and (c) CO_3 forms of C_i in $PbTiO_3$. An equivalent section of defect-free $PbTiO_3$ is shown in (a) for comparison. Gold, grey, red and black spheres represent Pb, Ti, O and C, respectively. Vertical and horizontal axes are approximately [001] and [010] respectively, with the tilted view adopted to aid clarity.

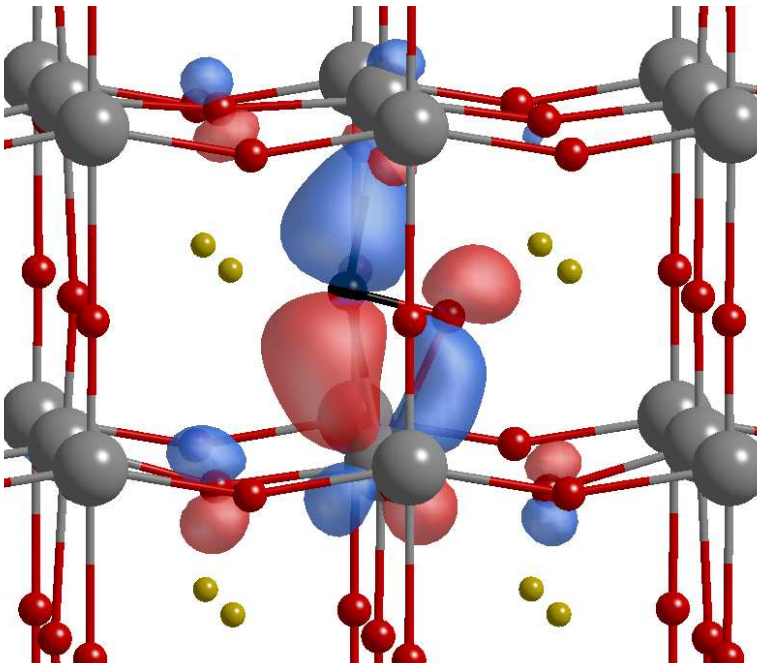

Figure 5.3: Wave function of the orbital state for the CO C_i configuration in $PbTiO_3$. Red and blue volumes showing wave function iso-surfaces of equal magnitude (0.1) and opposite sign. Colours and orientation are as indicated in Fig. 5.2.

geometry may be viewed as unlikely: the CO_3^{-2} ion is effectively replacing three host O^{-2} ions, leading to a surplus of four electrons.

Indeed, it is shown below that, although the carbonate form is unstable in the neutral charge state, it is expected to act as a donor and thus favour positive charge states.

The band structures in the vicinity of the band-gap for the neutral charge state of the CO form and the overall +4 charge state of the carbonate form are shown in Fig. 5.5. For the CO form (Fig. 5.5(a)), there are occupied states within the middle of the gap indicating that the defect is a deep donor and may act as recombination centre. This state can be attributed to π^* CO molecular orbitals. The carbonate group is not so simply accommodated. If all components adopted their normal formal oxidation states, this would result in an overall +4 charge, since the CO_3^{-2} ion accounts

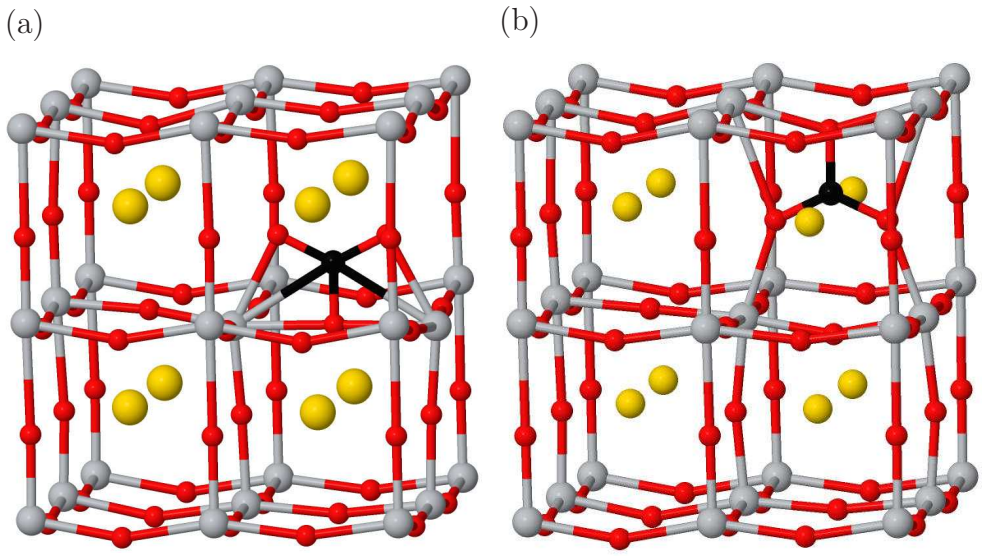

Figure 5.4: Schematics of (a) initial, and (b) final structures of C_i in tetragonal $PbTiO_3$ in a simple reorientation process. Colours and orientation are as indicated in Fig. 5.2

for only one of the three oxygen atoms affected. The band structure for the +4 charge state configuration (Fig. 5.5(b)) indicates that there are no states in the gap.

Based upon the band structures and expected oxidation states of CO and CO_3, the charge dependent formation energies as a function of Fermi level have been investigated (Fig. 5.5(c)). The results indicate that the neutral charge state of the CO form and the +2, +3 and +4 charge states of the CO_3 form are stable.

In addition to the electrical levels, local modes corresponding to C–O stretches would be expected. For the neutral, CO-bonded configuration, the stretch mode is estimated at $1437\,\mathrm{cm}^{-1}$, which is much lower than the vibrational mode of CO gas [78]. With respect to the C_{1h} CO_3 centre, the +4 charge state local vibrational modes have the E-mode with an average frequency of $1467\,\mathrm{cm}^{-1}$ split by $80\,\mathrm{cm}^{-1}$, and non-degenerate breathing mode at $1062\,\mathrm{cm}^{-1}$. These are close to those of gas phase CO_3^{-2} (Table 4.2). Similarly, the +3 charge state is predicted to have E and A_1 modes at 1467 and $1061\,\mathrm{cm}^{-1}$ respectively, whereas for +2 these are at 1466 and $1059\,\mathrm{cm}^{-1}$.

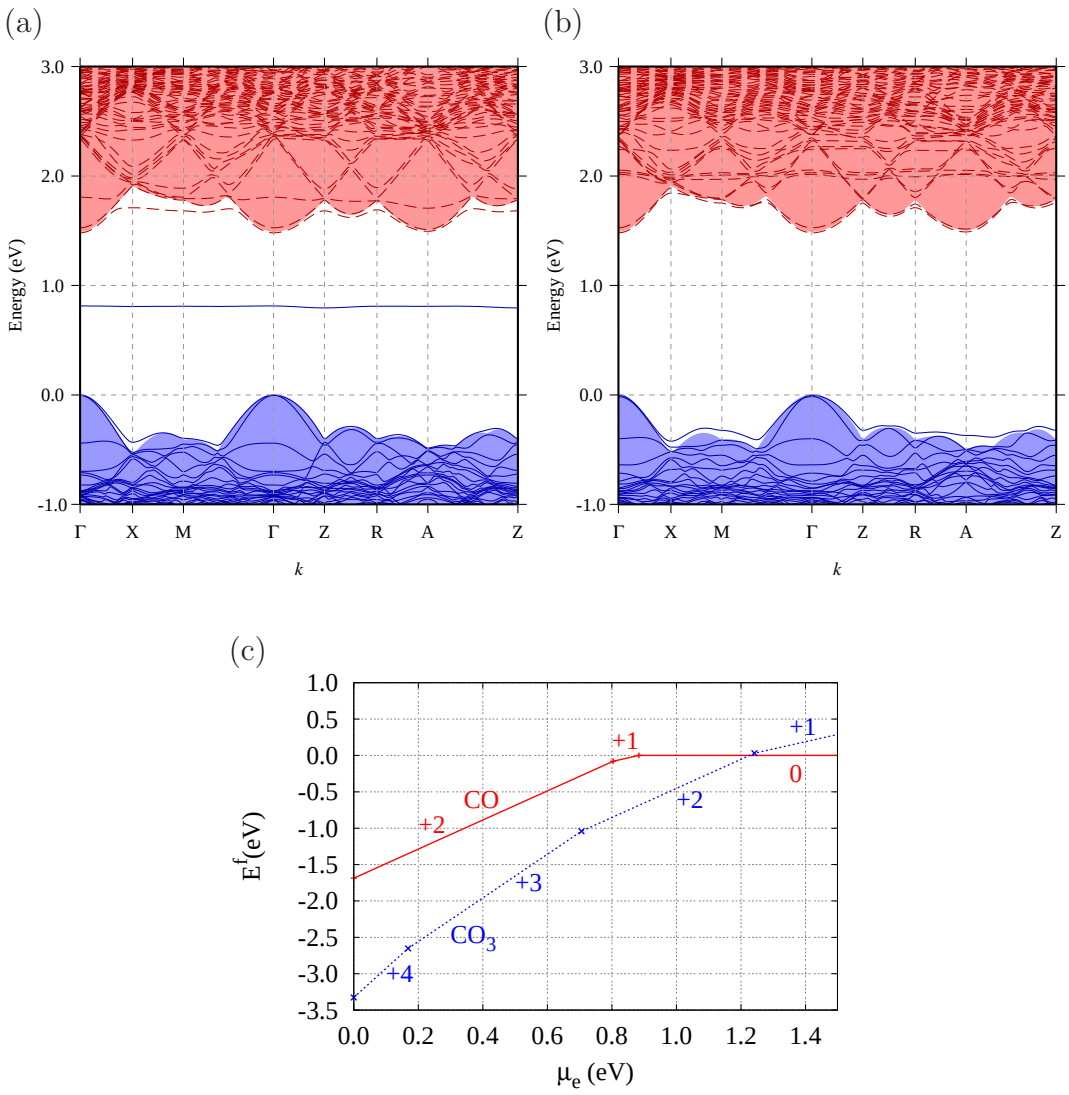

Figure 5.5: Band structures in the vicinity of the band-gap for C_i in: (a) the CO and (b) the $(CO_3)^{+4}$ configuration, plotted along high-symmetry branches in the first Brillouin zone; and (c) showing $E^f(\mu_e)$ for various charge states of each structure. Occupied and empty bands in (a) and (b) are shown in solid (blue) and dashed (red) lines, respectively. The underlying shaded areas show the regions of the bands for the corresponding bulk supercell. The energy scale is defined such that the valence band maxima are at zero. In (c) the red solid line and blue dotted line represent the CO and CO_3 configurations respectively. The gradient indicates the charge state, and the energy scale is defined by $E^f((CO)^0) = 0\,\text{eV}$.

5.3.2 C substituting for O

Next, carbon in the oxygen site, C_O, is discussed. Two types of oxygen atoms can be distinguished in the tetragonal $PbTiO_3$ structure; the first is in Ti–O–Ti chains along the c-axis ([001] direction) and the second in Ti–O–Ti chains along the a and b axes, (equatorial directions), perpendicular to the c axis. The two distinct oxygen sites can give rise, therefore, to two types of C_O defects: carbon substitution for O along the c-axis represented here by $(C_O)_c$ (Fig. 5.6(a)) or, carbon substitution for O in the ab-plane denoted by $(C_O)_{ab}$, Fig. 5.6(b). The calculations have shown that $(C_O)_c$ has nearly the same energy as $(C_O)_{ab}$ in the neutral charge state. The Ti–C bond lengths at 2.08 Å for $(C_O)_{ab}$ are only slightly longer than the Ti–O bond at 1.94 Å in the defect-free system. Ti–C bond lengths for $(C_O)_c$ are 2.28 and 1.98 Å along the polar and anti-polar directions respectively. However, with -1, -2 charge state the $(C_O)_{ab}$ structures are more stable than the forms in $(C_O)_c$, as shown in Fig. 5.7(c).

As was found for $SrTiO_3$ this structure is relatively unstable, and chemical reactions between carbon and nearby host oxygen ions are energetically favourable for the neutral charge state, $(CO)_{(2O)}$ (see Fig. 5.6(c)). In the neutral charge state, the bond length of carbon monoxide has been calculated to be 1.41 Å, which is significantly longer than the CO bond length in the free gas phase (Table 4.2) but close to that of the CO^{-2} ion. This long bond is due to a combination of the charge state of the group and bonding interactions with the neighbouring Ti atoms. The C–O bond length is shorter for +1 and +2 charge states, at 1.33 and 1.26 Å respectively, which is consistent with the depopulation of an anti-bonding orbital. Moreover, this structure is relatively unstable in the +3 and +4 charge states and spontaneous chemical reactions between carbon monoxide and another nearby oxygen atom are energetically favourable, causing the carbon dioxide form $(CO_2)_{(3O)}$, to occur, (Fig. 5.6(d)).

The electronic structures of carbon substitution for oxygen are instructive in terms of the origin of their relative stabilities. The on-site configuration $(C_O)_c$ has two levels in the band gap related to the carbon atom (Fig. 5.7(a)), which are largely comprised of an occupied p-state along the Ti–C–Ti axis and a partially filled, degenerate pair

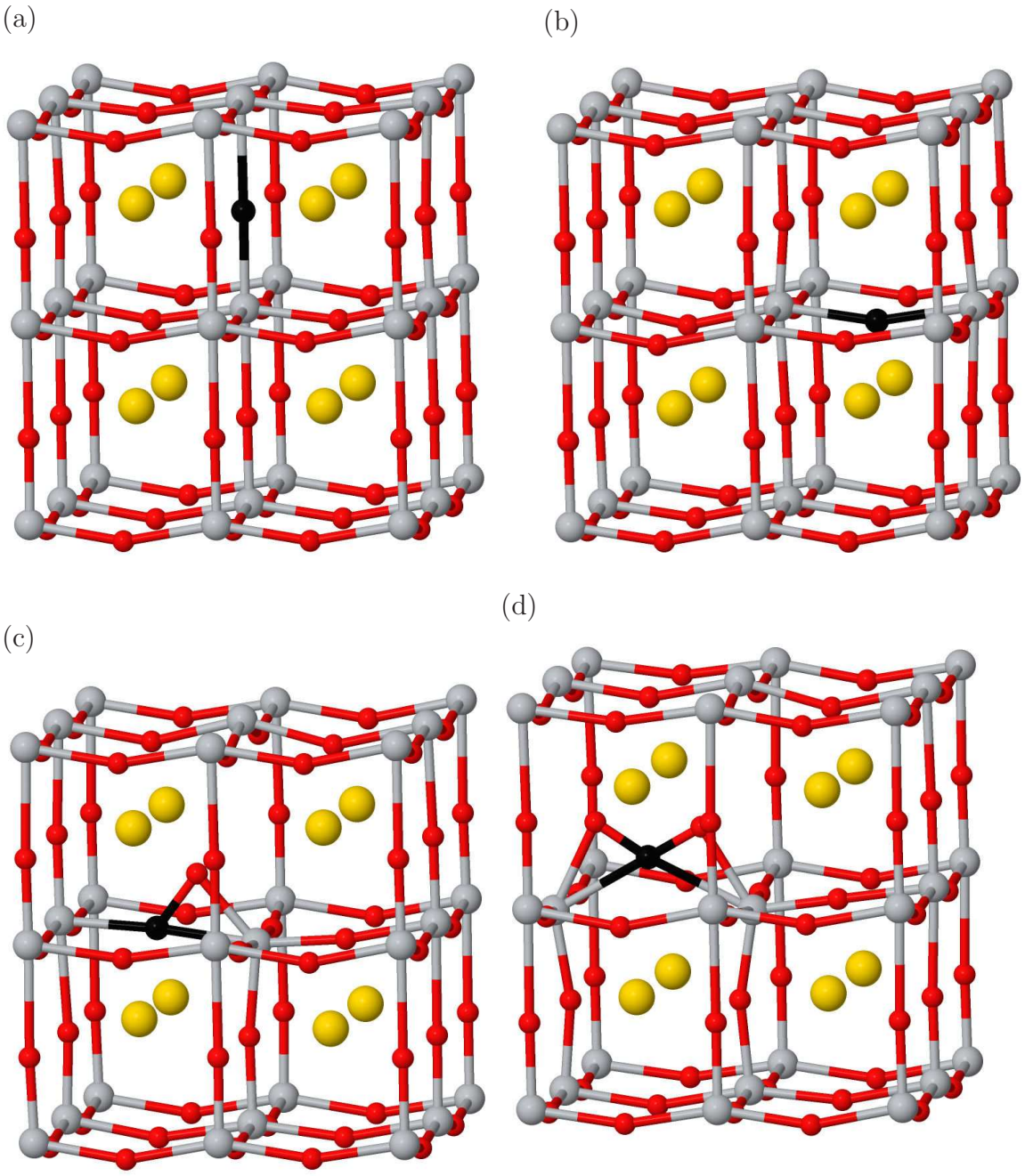

Figure 5.6: Schematics of (a) $(C_O)_c$, (b) $(C_O)_{ab}$, (c) $(CO)_{(2O)}$ and (d) $(CO_2)_{(3O)}$ configurations in $PbTiO_3$. Colours and orientation are as indicated in Fig. 5.2.

made up of the perpendicular p components. To confirm this result, wave functions iso-surface have been calculated and are shown in Fig. 5.8. The on-site centre would therefore be expected to act as a donor, and possibly as an acceptor.

Fig. 5.7(b) shows the electronic structure of the $(CO)_{(2O)}$ structure in the neutral charge state. The states in the upper part of the band-gap are related to the combination of π^* CO and σ_{pd} with the neighbouring Ti atoms, as illustrated in Fig. 5.9.

Electrical levels for C_O have been estimated with the formation energies as a function of the chemical potential of electron (Fig. 5.7(c)). For the on-site centre, the calculations show that both $(C_O)_{ab}$ and $(C_O)_c$ have nearly the same energy in the neutral charge state. However, at -1 and -2 charge states, the $(C_O)_{ab}$ structures are more stable than the same charge states in the $(C_O)_c$. Overall, for the n-type condition, the $(C_O)_{ab}$ -2 charge state is the stable structure. Hence, the structure can accept one or two electrons which would render it iso-electronic with oxygen. However, the existence of the occupied states in the gap are found to result single and double donor levels, with the depopulation of the π^* state corresponding to a decrease in the C–O bond-length. The removal of three or four electrons is also possible, but with a spontaneous reconstruction to form a centre where carbon is bonded to *two* oxygen neighbours, $(CO_2)_{(3O)}$, as in Fig. 5.6(d).

As with C_i, C_O is likely to give rise to characteristic vibrational modes. For the on-site form, stretching vibrational modes lie at 770 and 857 cm^{-1} in the -1 and -2 charge states respectively. The vibrational modes of the $(CO)_{(2O)}$ provide further insight into the nature of the defect. In the neutral charge state the calculated mode is 969 cm^{-1}, which is close to the calculated vibrational mode of CO^{-2}. In the $+1$ charge state, the vibrational mode increases to 1138 cm^{-1}, and then to 1380 cm^{-1} for the $+2$ charge state, corresponding to increased bond-order. For the $(CO_2)_{(3O)}$ form, the increase in the number of C–O bonds means that the $+3$ and $+4$ charge states yield two stretch modes each, estimated at 1235 and 1353 cm^{-1} for the $+3$, and 1006 and 1336 cm^{-1} for the $+4$ charge state, and these might be easy to identify experimentally.

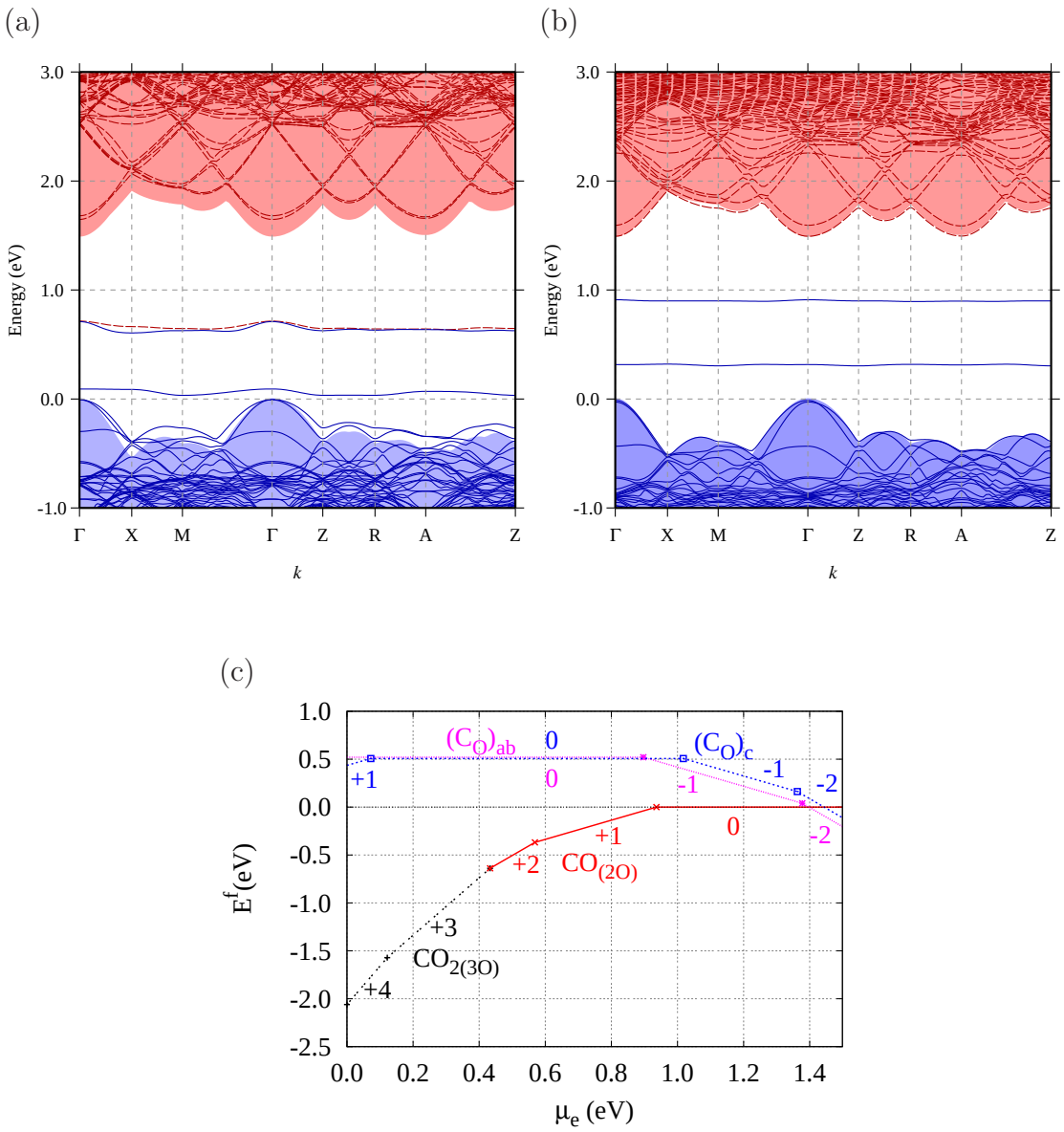

Figure 5.7: Band structures in the vicinity of the band-gap for C_O in: (a) the neutral charge state of the on-site,$(C_O)_c$, and (b) the $(CO)_{(2O)}$ configurations, plotted along high-symmetry branches in the first Brillouin zone; and (c) showing $E^f(\mu_e)$ for various charge states of each structure. Lines, shading and scales in (a) and (b) are as defined in Fig. 5.5. In (c) the red solid line, blue dotted line, and black dotted line represent the $(CO)_{(2O)}$, C_O, and $(CO_2)_{(3O)}$ configurations respectively. The gradient indicates the charge state, and the energy scale is defined by $E^f(((CO)_{(2O)})^0) = 0\,\text{eV}$.

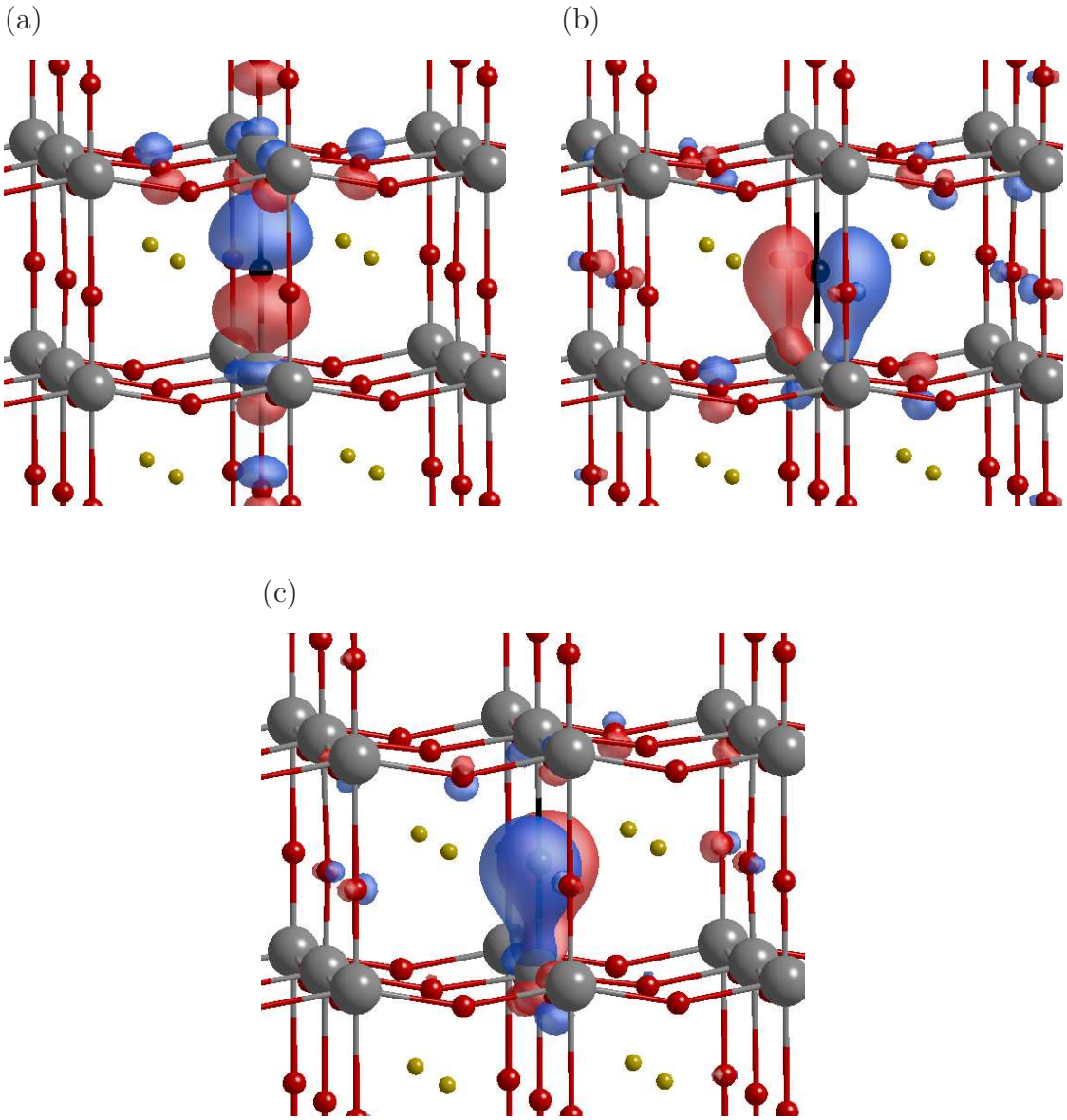

Figure 5.8: Schematics showing wave functions of $(C_O)_c$: (a) lowest occupied p-state along the Ti-C-Ti axis; (b) and (c) a partially filled, degenerate pair made up of the perpendicular p components. Red and blue volumes show wave function iso-surfaces of equal magnitude (0.1) and opposite sign. Colours and orientation are as indicated in Fig. 5.2.

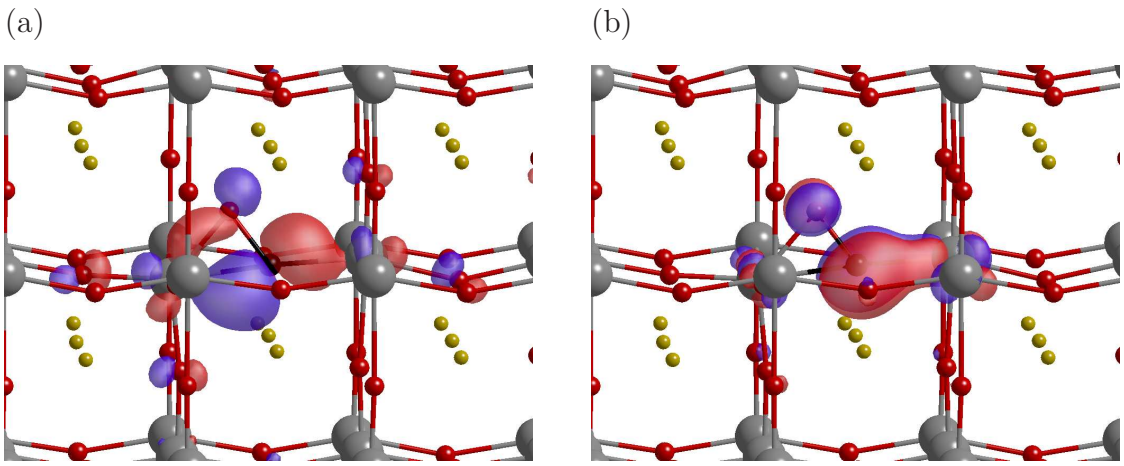

Figure 5.9: Schematics (a) and (b) showing the origin of two occupied states in the gap for $(CO)_{(2O)}$ defect in $PbTiO_3$. Red and blue volumes show wave function iso-surfaces of equal magnitude (0.1) and opposite sign. Colours and orientation are as indicated in Fig. 5.2.

5.3.3 C substituting for Pb

Now, the carbon substitution for the cation is discussed for the case of lead substituted by carbon, C_{Pb}. The stable structures are shown schematically in Fig. 5.10, indicating that replacing a Pb with a C atom in $PbTiO_3$ results in significant structural changes. The carbon atom is displaced toward the three nearest neighbour oxygen atoms and coordinates forming a carbonate group CO_3 ion leaving off centre behind, as in Fig. 5.10(a). The C–O bond lengths are calculated to be 1.37 Å in the polar direction [001] and 1.27 Å in the other directions, $[0\bar{1}\bar{1}]$ and $[0\bar{1}1]$, by assuming that the principal axis is in the centre of the carbonate group. The structure is energetically more stable in the polar direction than with the CO_3 in the anti-polar direction by around 0.23 eV. A reorientation barrier similar to the previous calculations, C_i, has been obtained using NEB calculations. There are several distinct orientations for the carbonate group in tetragonal $PbTiO_3$. Depending on the direction of the host dipole and the stability of the structures, the reorientation energy has been calculated between the polar [001] and anti-polar $[00\bar{1}]$ directions. The forward and reverse reac-

tions are calculated to be activated by energies of 1.97 and 1.74 eV respectively. The defect dipole is aligned with the domain polarisation, and upon switching at normal temperature, the reversal of this dipole might take place at a sufficiently slow rate to effect the ferroelectric response. The effect of the carbonate group orientation on the polarisation of the system has been explained in section 5.3.4.

The formation of the carbonate leaves the $PbTiO_3$ lattice deficient by one Pb cation and three oxygen anions. This results in a net excess of four electrons to be accounted for. Two of these are associated with the carbonate group, but this means that the reaction of carbon on the Pb site with three oxygen atoms is expected to result in a double donor. Indeed, this is also what would be expected on the basis of the valences of Pb and C, and that is what was found for C_{Sr} in $SrTiO_3$.

As for C_{Sr} in $SrTiO_3$ (section 4.3.3), there is also an alternative chemical rearrangement that results in an iso-electronic centre. Carbon in the lead site reacts with a single oxygen neighbour, yielding the formation of CO anion resides in the Pb site leaving the V_O behind, and then no excess of deficit in charge results. Numerous relative orientations of the CO ion and oxygen vacancy have been analysed and the one shown is the lowest in energy. The structure shown schematically in Fig. 5.10(b) is metastable, but not more stable than the carbonate form (Fig. 5.11(c)). The bond length of C–O has been calculated to be 1.13 Å, which is in good agreement with the bond length in the carbon monoxide molecule.

Depending on the expectations of oxidation states band structures for the two configurations have been calculated which confirm these results (see Fig. 5.11). In the +2 charge state of the carbonate form, and the neutral charge state of the CO form, the band-gap is devoid of states.

As with C_i and C_O, C_{Pb} is likely to give rise to characteristic vibrational modes. The CO_3 form in the overall +2 charge state has modes at 1073, 1356, and 1474 cm^{-1} and the +1 charge state has modes at 1073, 1359, and 1469 cm^{-1}, which is associated with CO stretches, However, in the neutral charge state, the vibrational mode of C_{Pb} in the CO form is observed to be at 2072 cm^{-1}, which is in reasonable agreement

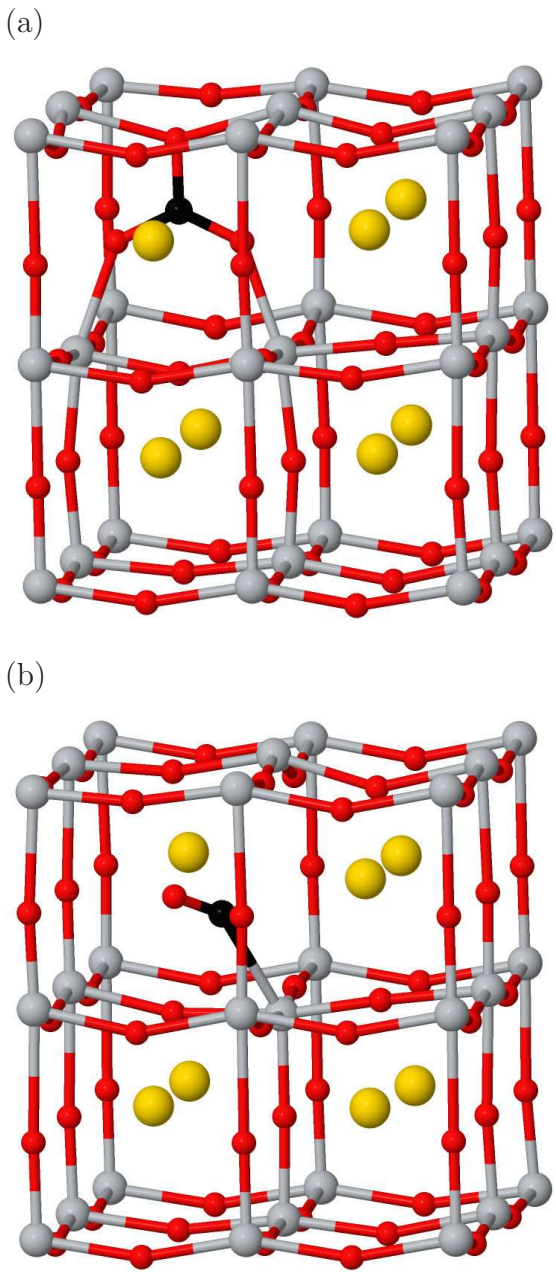

Figure 5.10: Schematic of C_{Pb} in $PbTiO_3$ in (a) CO_3 and (b) $(CO)_{Pb}$–V_O forms. Colours and orientation are as indicated in Fig. 5.2.

with the experimental value for the carbon monoxide molecule (Table 4.2). For both structures, within the range of computational uncertainty, it has been found that the vibrational modes have the same values as those obtained for C_{Sr} in $SrTiO_3$.

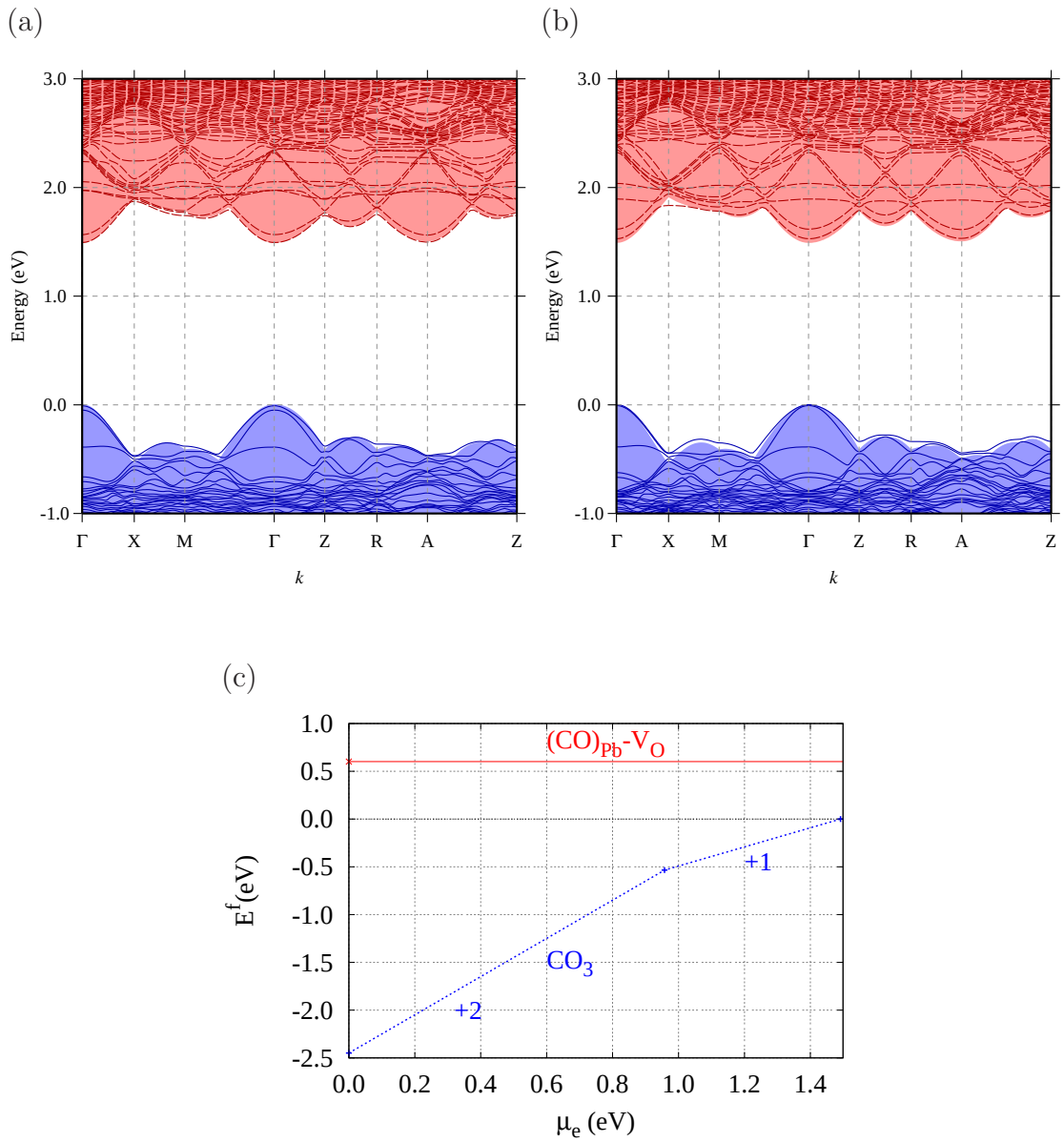

Figure 5.11: Band structures in the vicinity of the band-gap for C_{Pb} in (a) +2 charge state of CO_3 and (b) neutral charge state of the $(CO)_{Pb}$–V_O configurations, plotted along high-symmetry branches in the first Brillouin zone; and (c) showing $E^f(\mu_e)$ for various charge states of each structure. Lines, shading and scales in (a) and (b) are as defined in Fig. 5.5. In (c) the (red) solid line and (blue) dotted line representing the $(CO)_{Pb}$–V_O and $(CO_2)_{(3O)}$ configurations respectively. The gradient indicates the charge state, and the energy scale is defined by $E^f((CO_3)^0) = 0\,\text{eV}$.

5.3.4 C substituting for Ti

Another structure for carbon substituting for a cation in $PbTiO_3$ is the carbon substitution of titanium, denoted by C_{Ti}. The first structure analysed was created from the ideal tetragonal material, with a Ti ion simply replaced with carbon. In the absence of any symmetry constraint, the optimised structure of C_{Ti} exhibits significant structural change from the initial geometry. The carbon is displaced from the centre where it was initially co-ordinated with six oxygen ions, toward the centre of a triangular group composed of three oxygen ions, as shown in Fig. 5.12. This orientation is denoted as the parallel orientation, since the electric dipole estimated on a point charge basis for the defect has a component parallel to the bulk polarisation, that is, along the [001] direction. The optimised structure has three C–O bonds which are significantly around 35% shorter than the average Ti–O bond length. It therefore seems reasonable to conclude that the carbon and its nearby oxygen neighbours form a carbonate group. To further support this hypothesis, it is noted that the calculated C–O bond-lengths in C_{Ti} are close to those of the carbonate group and those of cerussite [130], $PbCO_3$. The initial supercell composition simulation was $(PbTiO_3)_{32}$; then, after the substitution of Ti by C, one could expect that the structure is transformed to $(PbTiO_3)_{31}(PbCO_3)_1$, or approximately $(PbTiO_3)_{0.97}(PbCO_3)_{0.03}$.

The band structure for C_{Ti} in tetragonal $PbTiO_3$ has been calculated and is shown in Fig. 5.13. As shown in this graph, the inclusion of a carbon atom at a Ti site does not have any significant effect on the width of the band-gap, which is in contrast to the situation with C_{Ti} in cubic $SrTiO_3$ (see section 4.3.4). In addition, carbon substitution for titanium is therefore expected to lead to electrically inactive defects, where these centres do not introduce any electrical states in the band-gap.

Turning to vibrational characteristics, it is found that the calculation frequencies are consistent with the picture of C_{Ti} resulting in the formation of carbonate ions. A set of characteristic local vibrational modes lies above the one-phonon maximum, which could prove highly effective in the experimental identification of this centre: with a nearly degenerate C–O stretch mode at $1395\,cm^{-1}$ and $1314\,cm^{-1}$, and

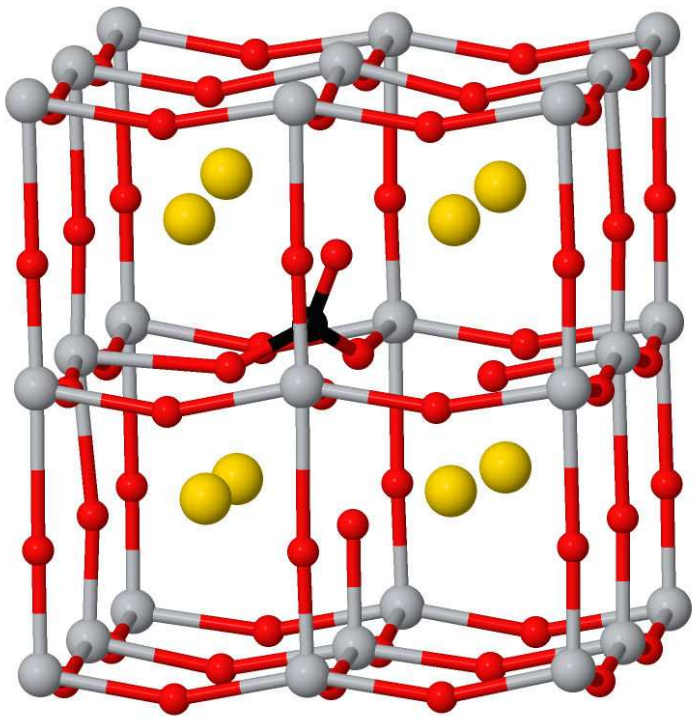

Figure 5.12: Schematic of C_{Ti} in $PbTiO_3$. Colours and orientation are as indicated in Fig. 5.2.

a breathing stretch-mode found at $1055\,cm^{-1}$. It is noted that, as with the case of $SrTiO_3$, these C_{Ti} modes are close to the experimental values for gas phase CO_3^{-2}. They also agree [131] with those modes assigned to the carbonate groups in $PbCO_3$. Lower frequency modes of the carbonate group are also present for C_{Ti}, but are resonant with the one-phonon density of states. All three local modes listed here are, by symmetry, infra-red and Raman active, and given sufficient concentrations one might seek to confirm the presence of this form of carbon centre directly via either IR or Raman spectroscopy.

Finally, the reorientation processes for C_{Ti} have been evaluated. In general there are several distinct orientations for the carbonate group in tetragonal $PbTiO_3$. For the "parallel" orientation described above, one might describe the orientation via the principle axis of the carbonate group, which in Fig. 5.12 is $[\bar{1}\bar{1}1]$. Other "parallel" orientations can be envisaged with C associated with the same Ti site, including one

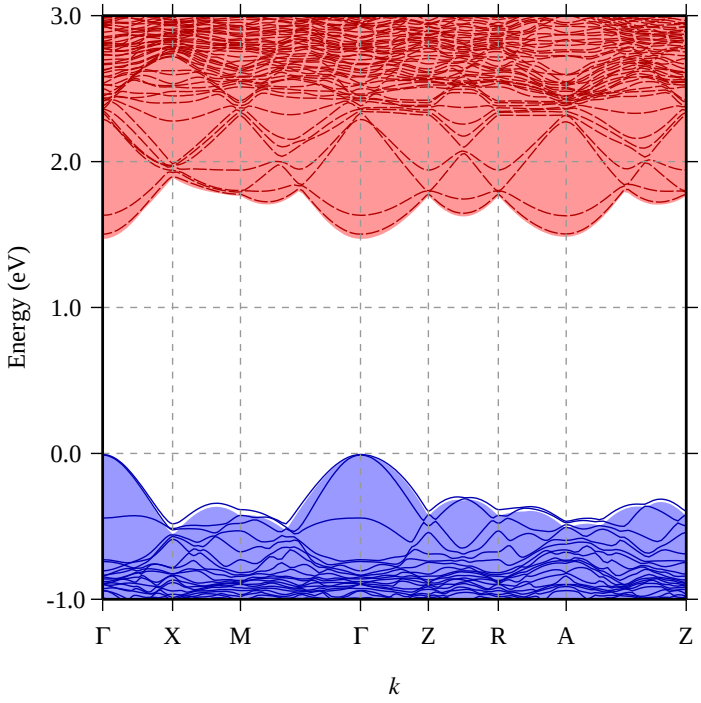

Figure 5.13: Band structure in the vicinity of the band-gap for C_{Ti} in $PbTiO_3$, plotted along high-symmetry branches in the first Brillouin zone. Lines, shading and scales are as defined in Fig. 5.5.

oriented along the $[\bar{1}11]$. These two orientations are shown in Fig. 5.14(a) and (b), and by symmetry these are equivalent (and therefore have the same energy). Alternatively, the second orientation might be $[\bar{1}\bar{1}\bar{1}]$, as shown in Fig. 5.15(b). By symmetry, this is not equivalent to the starting structure, and so in general will be different in energy. In the current simulations the structure in Fig. 5.14(b), which is termed anti-parallel to contrast it with the previous structure, is about 1.3 eV higher in energy.

The processes linking these structures have been evaluated using NEB simulations. An in-plane process between the two equivalent structures shown in Fig. 5.14 is first presented.

The activation energy for this symmetrical reorientation process is calculated to be 1.8 eV, with the barrier plotted in Fig. 5.14(c). The barrier is found to be comparatively high in energy compared to, for example, diffusion of the oxygen vacancy,

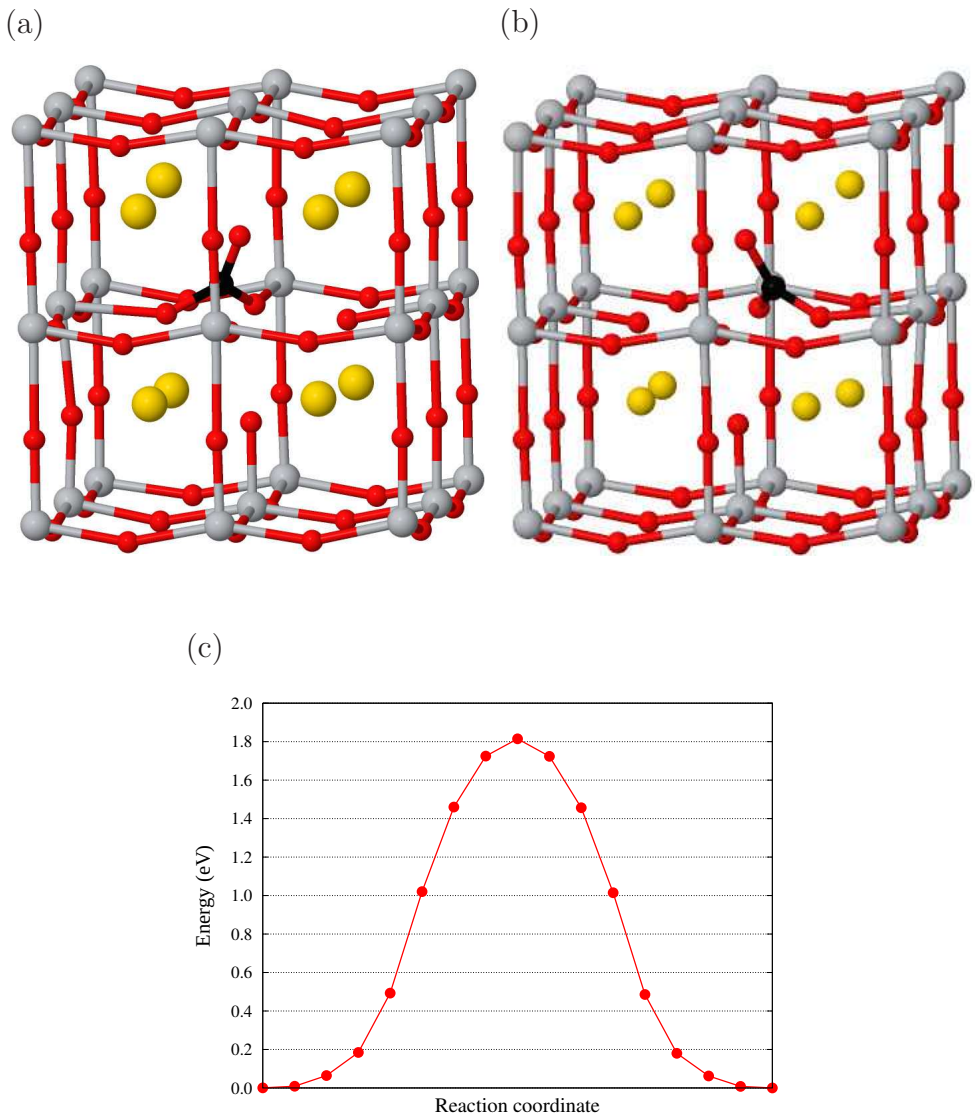

Figure 5.14: Schematics of (a) initial, and (b) final structure of C_{Ti} in $PbTiO_3$ in a simple reorientation process; with (c) showing the calculated reorientation barrier of C_{Ti} in $PbTiO_3$ between the initial and final structures in the *ab*-plane. Colours and orientation are as indicated in Fig. 5.2.

but this can be understood as it was for the comparable process in $SrTiO_3$, since the reorientation requires the breaking and formation of strong covalent C–O bonds. It is noted, however, that this activation energy is somewhat smaller than the activation energy for the equivalent path in cubic $SrTiO_3$, which was calculated to be around

2.5 eV, but it is still expected to lead to a relatively slow reorientation process at room temperature.

Turning to the second type of reorientation process, the NEB simulation produces an asymmetric barrier, as shown in Fig. 5.15. The forward and reverse reactions are calculated to be activated by energies of 2.8 and 1.5 eV respectively.

This is expected to have some impact upon the hysteresis seen in the electric polarisation under an applied electric field. This can be understood as follows:

Let it be assumed that initially the C_{Ti} centres are equilibrated in tetragonal $PbTiO_3$ so that, due to the large energy difference between the two non-equivalent orientations in Fig. 5.15, the vast majority of these centres are in the energetically equivalent, low energy orientations. If this material is then subjected to an external force that reverses the bulk polarisation, such as the application of an external bias, then a number of possible outcomes may ensue. First, assuming that the bias does not significantly impact on the reorientation process as depicted in Fig. 5.15(c), after the tetragonal $PbTiO_3$ has been switched, the vast majority of C_{Ti} centres will be in the high-energy, non-equilibrium orientation shown in Fig. 5.15(b). This defect has an intrinsic dipole which opposes the bulk polarisation, and therefore the polarisation of the sample as a whole will be reduced relative to both the initial polarisation, and relative to a defect-free form. The relatively high barrier to reorientation between Fig. 5.15(c) and Fig. 5.15(b) of 1.5 eV means that at room temperature these dipoles will not equilibrate over a typical experimental time-scale.

It must be noted, however, that the assumption that the application of an external field sufficient to reorient the bulk polarisation would not change the reorientation barrier may not be true. Since the carbonate groups have an intrinsic dipole, this will also be affected by the external field, and it is possible that the switching of the host will also switch these defects. However, given the high barrier for such a process, this seems unlikely, and it can be concluded that the most likely impact of C_{Ti} in $PbTiO_3$ in terms of the bulk polarisation is in line with that expected for fixed dipoles, such as is observed to arise from Fe-related complexes [132]. This is important

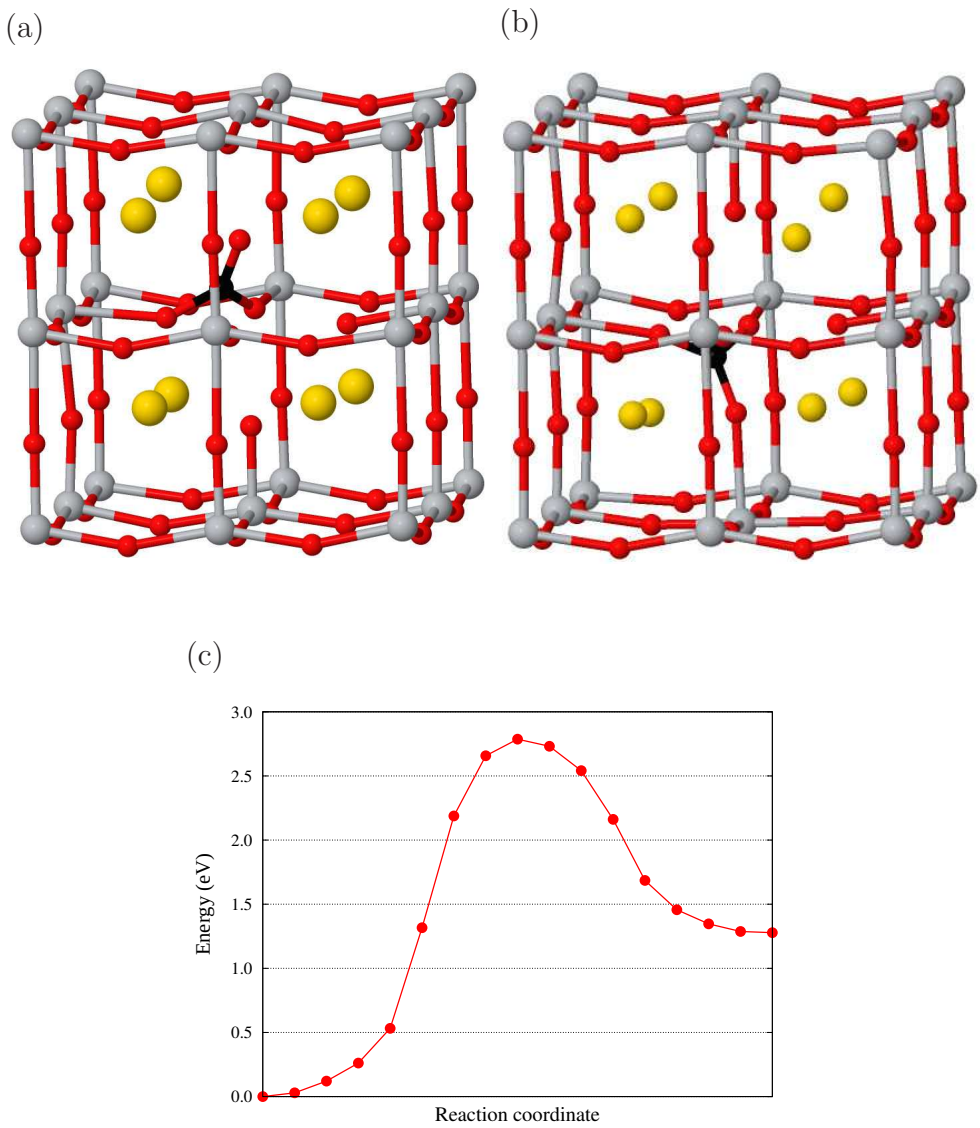

Figure 5.15: Schematics of (a) initial, and (b) final structure of C_{Ti} in $PbTiO_3$ in a simple reorientation process; with (c) showing the calculated reorientation barrier of C_{Ti} in $PbTiO_3$ between the initial (polar direction) and final structure (antipolar direction). Colours and orientation are as indicated in Fig. 5.2.

when considering the operation of ferroelectric device applications.

5.3.5 Formation energy comparison

Finally, as for $SrTiO_3$, a thermodynamic assessment of the relative stability of the four sites above is considered, where the atomic and electron chemical potentials must be taken into account. The formation energies of each defect in various charge states with respect to the chemical potential of atoms, along with the Fermi level, have been calculated using Eq. 3.9. In the $PbTiO_3$ system, μ_i denotes the chemical potential of the species (here i =Pb, Ti, O and C).

First, the limitations of the atomic chemical potentials have been assessed by considering the energies of bulk $PbTiO_3$ and related materials. The chemical potentials of components μ_{Pb}, μ_{Ti} and μ_{O} are related through

$$\mu_{\mathrm{Pb}} + \mu_{\mathrm{Ti}} + 3\mu_{\mathrm{O}} = \mu_{\mathrm{PTO(bulk)}} \tag{5.1}$$

Here μ_{PTO} is the total energy per formula unit of pure $PbTiO_3$ which is found to be $-13.06\,\mathrm{eV}$, and this is in reasonable agreement with the previously calculated value of $-13.41\,\mathrm{eV}$ [133]. μ_{Pb} is the energy per atom of pure Pb metal, and μ_{Ti} and μ_{O} have been defined and calculated in section 4.2. A parameter space describing the values of the chemical potentials for which $PbTiO_3$ is stable can be established in terms of μ_{Ti} and μ_{Pb} using Eq. 5.1, with boundaries formed where related materials become thermodynamically more stable than $PbTiO_3$. For example, for sufficiently high values of the chemical potentials of Ti and Pb, it would become more favourable to form bulk metals rather than the compound. An equilibrium lattice constant of 4.85 Å has been calculated for fcc Pb; which is in reasonable agreement with the experimental equivalent of 4.91 Å [134]. The Ti metal lattice constant has been presented in section 4.3.5. Other boundaries are formed by PbO, PbO_2, TiO_2, and oxygen gas

$$\Delta H_{\mathrm{PbO}} = \mu_{\mathrm{PbO(bulk)}} - \mu_{\mathrm{Pb}} - \mu_{\mathrm{O}} \tag{5.2}$$

$$\Delta H_{\mathrm{PbO_2}} = \mu_{\mathrm{PbO_2(bulk)}} - \mu_{\mathrm{Pb}} - 2\mu_{\mathrm{O}} \tag{5.3}$$

The heat of formation for TiO_2 has been defined in section 4.2. The current calculations suggest that the chemical potential of PbO has a further restriction on the

$PbTiO_3$ phase diagram, in contrast to the phase relations suggested by Boonchun *et al.* [133]. PbO has a tetragonal structure, and the enthalpy of formation has been calculated to be $-2.5\,\mathrm{eV/f.u.}$ which is in an excellent agreement with the experimental value of -2.37 [135]. For PbO_2 (tetragonal, space group $P4/mnm$), the enthalpy of formation has been calculated to be $-3.30\,\mathrm{eV/f.u.}$ which is in reasonable agreement with the theoretical value [136]. Other competing phases such as TiO and Ti_2O_3 have been considered, but were found to give no further restriction on the allowed chemical potentials. The shaded area in Fig. 5.16(a) shows the resulting phase diagram for the stable growth of $PbTiO_3$ as a function of μ_{Pb} and μ_{Ti}.

Following the procedure adopted for the Cr doping of $SrTiO_3$ [76] and the current calculations of carbon impurities in $SrTiO_3$ (section 4.3.5), the selection of the impurity chemical potential based upon the appropriate carbon containing phase is required. μ_{C} has been calculated based upon graphite (C) and $PbCO_3$. Other carbon containing systems such as CO, CO_2, CO_3, TiC and PbC_2 have been examined but were not found to be in the equilibrium phase under the simulation conditions. Fig. 5.16(b) illustrates the carbon chemical potential diagram as a function of μ_{Pb} and μ_{Ti}, with μ_{O} defined by Eq. 5.1. Using Eq. 3.9 and by considering the conditions for $PbTiO_3$ stability described in the previous section, the likely locations of carbon in $PbTiO_3$ have been examined.

Two different chemical potential settings have been selected: (μ_{Ti}, μ_{Pb}, μ_{O}), which correspond to the points X and Y in Fig. 5.16(a)and (c). The point X (-9.25, -2.30, -0.54) eV describes the Ti, O rich growth conditions, and this point has the highest possible value of μ_{O}, and lean growth conditions for Pb. Metal-rich and O-poor growth conditions occur at points $\mathrm{Z}(-5.45, 0, -2.54) \longrightarrow \mathrm{Y}(-4.64, 0, -2.83)\,\mathrm{eV}$ and there is no specific point within the boundary of the $PbTiO_3$ stable phase which is in equilibrium with the Ti metal. The carbon chemical potential is associated with $PbCO_3$ in O-rich conditions, while the graphite chemical potential is dominate in O-lean conditions as shown in Fig. 5.16 (c) and (d).

The formation energies for carbon species as a function of the values of μ_e of two

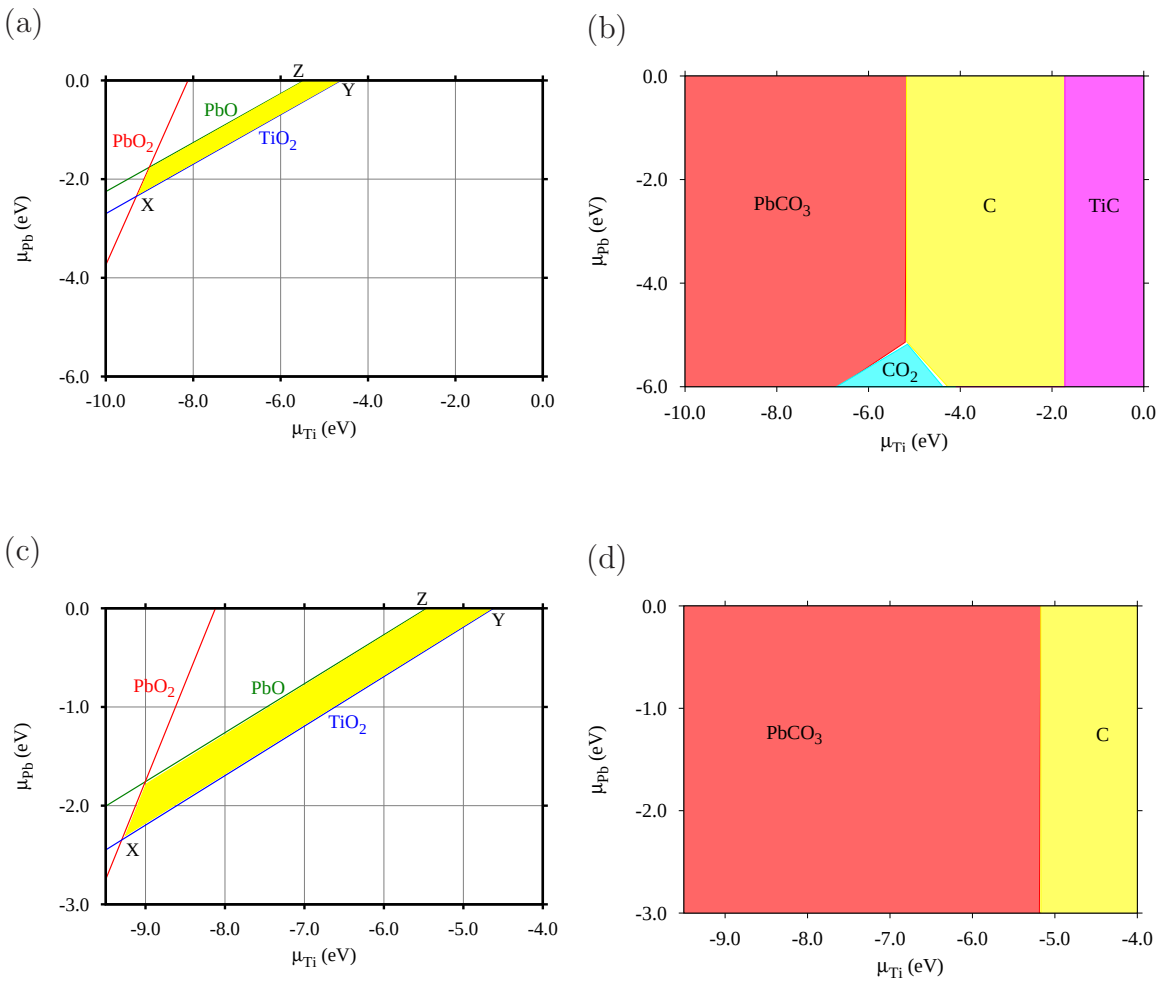

Figure 5.16: Plots showing the equilibrium phases for $PbTiO_3$ related materials as a function of μ_{Pb} and μ_{Ti}: (a) shows the $PbTiO_3$ stable region of the parameter space, indicated by the shaded area, and the X point describes the Ti and O-rich growth conditions whereas Y and Z points denote O-poor and metal rich growth conditions; (b) shows the phases containing carbon over the same ranges of chemical potentials; (c) and (d) represent the zoom demo in the regions where $PbTiO_3$ and carbon phases respectively are stable.

selected growth conditions have been plotted in Fig. 5.17. The gradient of each line reflects the most stable charge state under the Fermi level conditions. For example, $(C_O)_c$ is thermodynamically stable in the +1 charge state in p-type growth conditions;

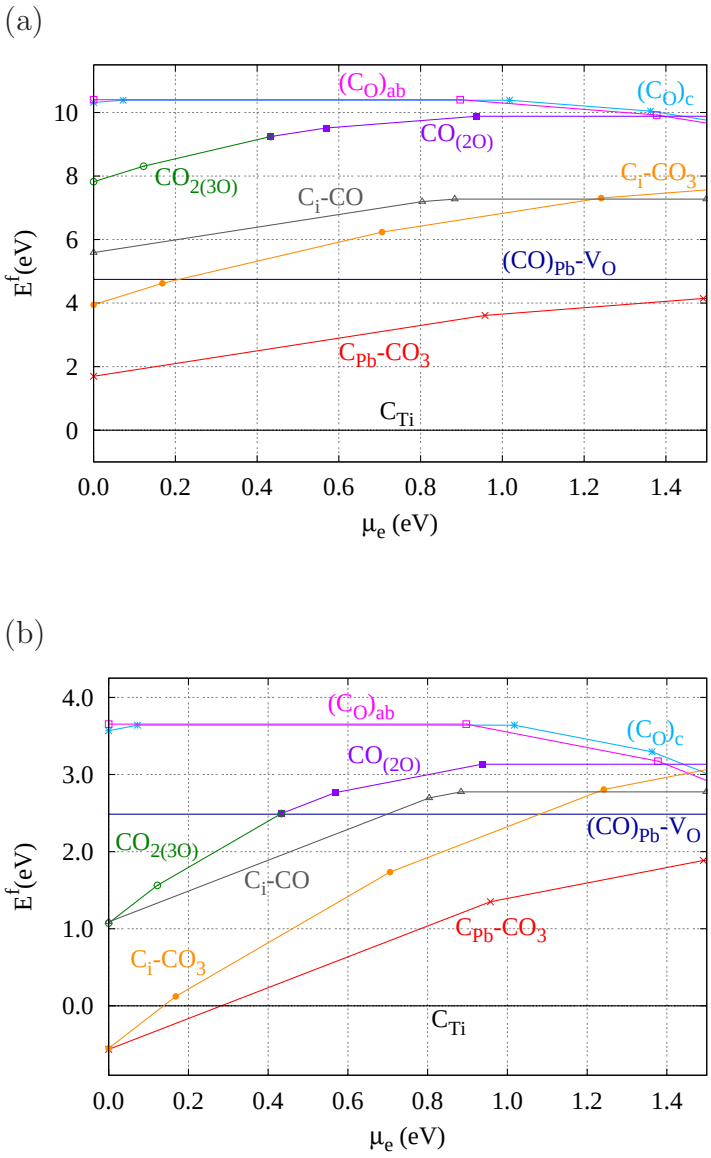

Figure 5.17: Graph showing the calculated equilibrium form of C-related defects with respect to electron chemical potentials for different atomic chemical potentials of Ti, Pb and O in different growth conditions. (a) corresponds to O-rich conditions at the X-point and (b) corresponds to O-poor conditions at the Y-point. The gradient indicates the charge state of the defects and the kinks in the plots reflect the energy positions at which transitions from one charge state to another take place.

however, as the Fermi level increases, the neutral, -1 and -2 charge states become more stable. This suggests that $(C_O)_c$ is an amphoteric defect and can behave as both a donor and acceptor. It must be noted that the formation energy of C_O is always higher than that of other defects under the growth conditions examined, even when C has the best opportunity to substitute O, under O-lean conditions (Fig 5.17(b)).

At point X (Fig. 5.17(a)), the calculations indicate that the formation energy of C_{Ti} is always significantly lower than that for the other forms (C_{Pb}, C_i and C_O). Even though there is the best chance for carbon to substitute Pb, the formation energy of C_{Pb} is still higher than that of C_{Ti} by more than 1.8 eV. In the *p*-type condition, the formation energy of C_i is also larger than that of the C_{Ti} defect by about 4 eV and it increaseds with increasing Fermi level. Under almost all conditions, the carbonate form C_i is the equilibrium phase. However, the next most likely defect will be C_{Pb} with the CO_3 form in the positive charge state. Although the C_{Ti} does not have a significant impact electrically, it has a ferroelectric impact because the polarisation density of the material changes, but the carbon contribution in the Pb site leads to the electrical effect.

At point Y (Fig. 5.17(b)), metal substitution is favoured with both C_{Pb} and C_{Ti}. However, C_{Ti} is stable for a wide range of Fermi level. In *p*-type $PbTiO_3$, the +2 charge state with a CO_3 configuration of the C_{Pb} is favoured. The formation energy of the +4 charge state with CO_3 forms of C_i is very slightly higher in energy than that of the +2 C_{Pb} defect. As the electron chemical potential moves from the valance to the conduction bands, C_{Ti} dominates more and more of the stable region.

Depending on the current results of carbon stability in the X and Y conditions, it is clear that C_{Ti} will be expected to be stable for the whole range of Fermi level in Z point conditions. Therefore the formation energies explanation in Z point is not included.

According to the calculations, the formation energy of C_O is larger than those of C_{Pb}, C_i and C_{Ti} and it is never thermodynamically favoured. Hence, we can safely conclude that carbon substituting for oxygen in different structures such as on site,

CO and CO_2 is unlikely to occur under equilibrium conditions in $PbTiO_3$ crystal.

For all thermal equilibrium growth conditions of $PbTiO_3$, the vast majority of carbon impurities will substitute for Ti and will have a neutral charge state. In addition, the current calculations indicate that, under O-rich conditions, C-doped $PbTiO_3$ cannot be grown as the *p*-type under thermal equilibrium, due to the spontaneous formation of positively charged C_{Pb}, which possibly pushes the sample into the donor region. On the other hand, the formation energy of C_O is larger than those of C_{Pb} and C_i and it is never thermodynamically favoured.

5.4 Conclusion

In summary, based on first-principles density-functional calculations, the characteristics of carbon impurities in tetragonal $PbTiO_3$ have been examined, such as structural configuration, electronic properties, electrical levels, vibrational modes, reorientation barriers of the carbonate group and formation energies. The calculations reveal that carbon energetically favours the formation of carbonate groups for interstitial and both Ti and Pb substitutions. The calculations suggest that the carbon substitution of host species in $PbTiO_3$ could be either electrically active, such as in the substitution of Pb or O, or electrically passive, which is the case with the iso-electronic substitution of Ti. Hence, depending upon which site the carbon occupies, it may form donor, acceptor, or iso-electronic centres. Where carbon substitutes for Pb, it may be a source of free electrons since, based upon the electronic structure, C_{Pb} is a candidate for a shallow donor.

The vibrational characteristics of the defect centres therefore have some similarities, and for the CO_3 forms occupy similar locations in the frequency domain. However, due to site symmetry and the influence of local co-ordination, the vibrational frequencies offer a potential route to discrimination between different sites.

The reorientation barrier for the carbonate group in an interstitial site and both C_{Pb} and C_{Ti} has been estimated. In general, because the process involves the break-

ing and forming of C–O covalent bonds, the barrier has a relatively high value. With respect to the C_{Ti}, two crystallographically distinct sites for carbonate group reorientation have been investigated. The first is a systematic reorientation along the $[\bar{1}11]$ direction and the second is in the $[\bar{1}\bar{1}\bar{1}]$ direction between two non-equivalent structures. Hence, two kinds of reorientation barrier have been classified. Under specific conditions such as applying an external electric field or strain, this is expected to have an impact on the polarisation switching and then the ferroelectric characteristics of $PbTiO_3$.

Finally, formation energy calculations indicate that, among lattice sites, C atoms will often prefer the Ti site in the neutral charge state in bulk $PbTiO_3$ systems. However, there is an opportunity for the C defect to be p-type under O-rich growth conditions.

From the present calculations it can be emphasized that carbon impurities have an important impact on the properties of both $SrTiO_3$ and $PbTiO_3$. Hence, these results have motivated a study of the effect of carbon impurities in another perovskite titanate material which is very important in the technological applications. The next chapter presents a discussion of the effect of carbon impurities on the different characteristics of rhombohedral $BaTiO_3$.

Chapter 6

Carbon impurities in barium titanate

The perovskite family includes many titanates which have been used in various applications. $BaTiO_3$ is one of the most interesting materials among the perovskite oxides due to its ferroelectric properties at room temperature and lack of toxicity. As is the case for the previously mentioned perovskites ($SrTiO_3$ and $PbTiO_3$), carbon defects play a potentially important role upon the properties of $BaTiO_3$. This chapter presents a state of the art a first principles study of the structural and electronic properties of carbon in $BaTiO_3$. Interstitial and substitutional point defects are considered, and the relative stability of different charge states for each type of point defect is assessed. The local vibrational modes of the defect centres are calculated and suggested as a possible route to experimental validation. Through a careful consideration of the chemical potential space of the constituent species, the relative stability of the different point defects in various thermodynamic conditions is investigated.

6.1 Introduction

$BaTiO_3$ is a common ferroelectric material with a high dielectric constant and low loss characteristics, and it is widely utilised in the manufacture of electronic components such as multilayer dielectric capacitors and high refractive index thin films [137]. Its piezoelectric and pyroelectric properties mean that it is also utilised in passive infrared

detectors [138], piezoelectric actuators and sonar devices (SNR) [139]. Furthermore, given its positive temperature coefficient of resistivity (PTCR) properties, semiconducting barium titanate is used in sensor applications [139]. Despite its relative low Curie temperature, and piezoelectric properties inferior to those of $Pb(Zr,Ti)O_3$, lead-free $BaTiO_3$ remains attractive for environmental reasons [140].

Barium titanate crystallises in at least two polymorphic structures: perovskite structure and a hexagonal (6H) phase (space group $P6_3/mmc$) [141, 142]. Hexagonal $BaTiO_3$ is stable at high-temperatures. It is difficult to generate, only being stable at temperatures above 1460 °C. An unusual feature of this structure is the sharing of the faces of TiO_6 octahedra to form Ti_2O_9 co-ordination groups [142]. Each polymorph undergoes its own series of phase transitions. Both are ferroelectric material but with different ferroelectric properties. In the present work, only the perovskite structure is considered. At high temperature the perovskite form is stable in a classic $BaTiO_3$ structure with a simple cubic lattice. However, as the temperature decreases, $BaTiO_3$ transforms from a paraelectric to a ferroelectric phase with a tetragonal structure at about 130 °C [143]. At 5 °C, it undergoes another phase transition to an orthorhombic structure. The stable structure of $BaTiO_3$ below -90 °C is rhombohedral. In the rhombohedral phase, the oxygen octahedron surrounding the Ti^{+4} ion is slightly elongated along the $\langle 111 \rangle$ axis. The point symmetry of the Ti^{+4} site is C_{3v} and the trigonal distortion of the $(TiO_6)^{-8}$ octahedron is due mainly to the off-centre displacement of Ti^{+4} along the $\langle 111 \rangle$ axis [144–148], as shown in Fig. 6.1.

In recent years, significant attention has been directed towards ferroelectric $BaTiO_3$. Numerous studies have investigated the origin of ferroelectricity in $BaTiO_3$ perovskite [149–155]. Both theoretical and experimental studies have shown that intrinsic and extrinsic defects affect various of the properties of $BaTiO_3$, such as its electronic structures, photonic properties, remnant polarisation, the motion of domain walls, dielectric constant and leakage current [156–159].

Pure barium titanate is an insulator, whereas upon doping it is transformed into a semiconductor. For example, pentavalent dopants (Sb, Nb and Ta) can produce the

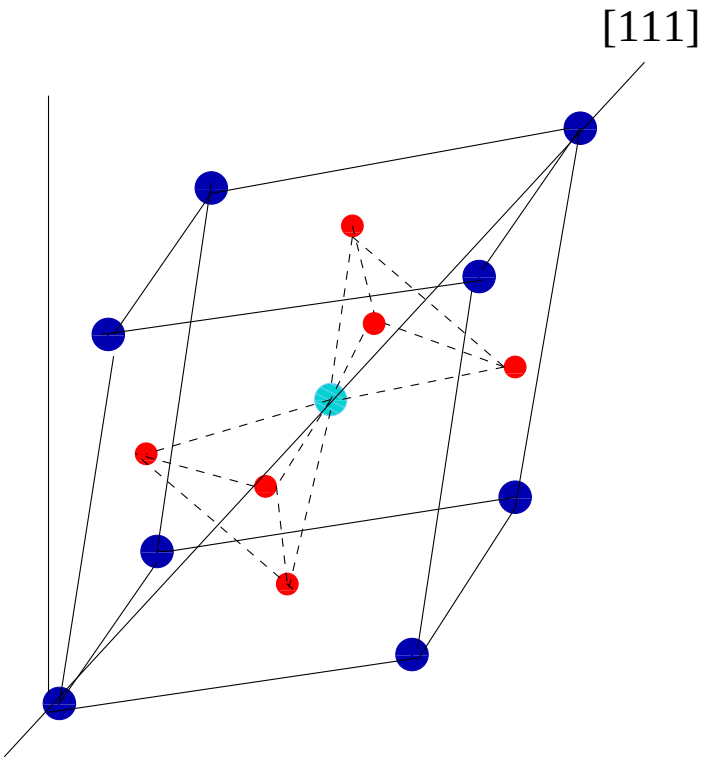

Figure 6.1: Structure diagram of rhombohedral $BaTiO_3$ unit cell. The oxygen octahedron surrounding Ti^{+4} ion is slightly elongated along $\langle 111 \rangle$ axis. Blue, cyan and red spheres represent Ba, Ti and O, respectively.

semiconductor by substitution at Ti^{+4} lattice sites [137]. Similarly, oxygen vacancies play an essential role in increasing the mobility meaning that the semiconductor is donor-type [160]. Typically, dopant additions to the host $BaTiO_3$ are needed to achieve the enhancement of its properties such as photoconductivity, piezoelectric and PTCR [139, 161, 162].

The successful synthesis of barium titanate with its unique dielectric properties largely depends on the purity and crystal structure, which greatly influence its final properties [90, 163]. Hence, various different techniques have been used to synthesis $BaTiO_3$ thin films, including solid-state reaction [164], the Sol-Gel method (solprecipitation) [157, 160, 165–167], the coprecipitation method [140, 168], mechanochemical synthesis [169, 170], solvothermal synthesis methods [171], sputter deposition [172],

pulsed-laser deposition [173], chemical vapour deposition [174] and atomic layer deposition [174, 175], in order to eliminate problems such as heterogeneity, impurities, inaccurate thickness control and the poor electrical properties of sintered ceramics. In these methods, the organic precursors have been introduced as sources of Ba. Therefore, carbon contamination has been reported in $BaTiO_3$ thin films [163,167,169,175]. For example, sharp absorption peaks at 1425, 1050, 860, and 695 cm^{-1} were observed and attributed to the carbonate ions (CO_3^{-2}) [176]. $BaTiO_3$ ceramics with excellent ferroelectric and piezoelectric properties have been successfully obtained using ordinary $BaCO_3$ and TiO_2 powders [139].

As for $SrTiO_3$, first principles calculations in the frame work of density functional theory have been used to accurately determine the formation energy of pure $BaTiO_3$, and this is then extended to explore the stable structures of carbon impurities in rhombohedral $BaTiO_3$. All possible carbon sites, such as substituting for Ba, Ti and O as well as interstitial positions have been considered in a range of possible charge states. Physical properties including geometry, electronic structure and electrical level have been calculated. Vibrational modes for the stable structures have been investigated and compared with the relevant experimental results. Activation energy calculations have been investigated to identify the probability of carbonate group reorientation in $BaTiO_3$ crystal.

6.2 Computational Method

In the present work, the same computational approach has been used as in the previous application chapters and described in sections 4.2 and 5.2. As for $SrTiO_3$ and $PbTiO_3$, atoms are modelled using norm-conserving, separable pseudo potentials [16] with valance sets of Ba of $5s^2 5p^6 6s^2$. The valance sets for Ti, O and C are listed in section 4.2. The Kohn-Sham eigen-functions are expanded using atom centred Gaussian basis sets [66], with four sets of independent s, p and d functions being used for each atom, representing a basis of 40 functions per atom for Ti, Ba, O and C, as

discussed in section 2.7.

Matrix elements of the Hamiltonian are determined using a plane-wave expansion of the density and Kohn-Sham potential [67] with a cut-off of 150 Ha. To obtain the ground state properties of rhombohedral $BaTiO_3$, the lattice parameters and fractional positions of atoms were fully optimised. Ionic and cell relaxations were performed with the convergence of the total energy with respect to the expansion of the charge density to be better than 0.03 meV.

For bulk rhombohedral $BaTiO_3$ symmetry, the calculated properties are given in Table 6.1, where they are compared with the available theoretical [177, 178] and experimental [146, 179] data. The values in Table 6.1 show that the deviations of optimised lattice constant a_0 and cell angle θ from the experimental values are less than 1% and 0.06% respectively. The fractional displacements X_{A} and Z_{A} of atom A have been calculated with respect to the ideal cubic location (Ba: 1a (0, 0, 0); Ti: 1a ($0.5 + X_{\mathrm{Ti}}$, $0.5 + X_{\mathrm{Ti}}$, $0.5 + X_{\mathrm{Ti}}$); O: 3b ($0.5 + X_{\mathrm{O}}$, $0.5 + X_{\mathrm{O}}$, Z_{O}). The technique for computing the total energy was presented in section 3.1. The Monkhorst-Pack [14] scheme for $10 \times 10 \times 10$ k-point mesh was applied for BZ sampling. Table 6.1 shows that good agreement between the calculated atomic displacements and both previous calculations and experimental values. It should be noted that the rhombohedral distortion does not have a significant ferroelectric impact on the energy of orientation, as shall be seen below in section 6.3.4. Therefore, the $BaTiO_3$ calculations do not focus on the reorientation process because the energy difference is small compared with the significance level of the calculations.

The calculated band gap is 2.3 eV, reflecting the well-documented-underestimate arising from the underpinning methodology. However, the current value is in excellent agreement with a previous calculation [178]. On average, LDA gives good agreement with experimental structural data for the rhombohedral $BaTiO_3$ phase.

In this work, the supercells used to model defects have been built from the $SrTiO_3$ cubic structure by changing lattice parameters and then optimising it with the $2\times2\times2$ mesh grid. This supercell is comprised of 32 formula units, meaning that the supercell

Table 6.1: Calculated, theoretical and experimental bulk properties of rhombohedral $BaTiO_3$ including lattice constant (a_0, Å), cell angle (θ, degrees), band gap (E_g, eV) and fractional displacements with respect to the ideal cubic location (X_{Ti}, X_{O} and Z_{O}). Experimental and theoretical data are taken from published studies [146, 177–179].

Properties	Current calculations	Previous calculations	Experiment
a_0	3.969	3.966	4.004
θ	89.85	89.87	89.80
E_g	2.30	2.30	3.40
X_{Ti}	−0.0114	−0.0110	−0.0128
X_{O}	0.0129	0.0133	0.0109
Z_{O}	0.0188	0.0192	0.0193

is $Ba_{32}Ti_{32}O_{96}$.

As for $SrTiO_3$ and $PbTiO_3$, the second derivatives of the total energy over atomic displacements have been used to calculate the vibrational frequencies of defects, which are then assembled into the dynamic matrix as discussed in section 3.2. Finally, the reaction pathways and activation energies are determined using the NEB method [21,22], and the convergence of the saddle point energy with respect to the number of images and the image-forces has been established to within a few meV (see section 3.6).

6.3 Results and discussion

A one hundred and sixty-atom supercell was exploited to discover the effects produced by a carbon atom impurity in the otherwise pure rhombohedral $BaTiO_3$ crystal. As mentioned before in section 4.3, there are four possible ways to include a carbon atom in the $BaTiO_3$ lattice (substitution at the Ba, Ti or O sites and an interstitial). Various possibilities for situating carbon impurities in rhombohedral $BaTiO_3$ have

been examined to obtain the structures that give the lowest total energies of the system in each site. Each of these configurations has been analysed and its observable properties assessed, as explained extensively below.

6.3.1 Interstitial C

Geometrically, there are different ways to incorporate carbon atom as an interstitial in rhombohedral $BaTiO_3$ crystal. The first position is between neighbouring Ba–Ba atoms; the second between Ba–Ti atoms; the third between O–O atoms, and so on. Numerous structures have been investigated to find out the stable structure either in the $\langle 111 \rangle$ direction (C_3) or in the other directions. Different minimum energies have been obtained. However, as is the case with $SrTiO_3$ and $PbTiO_3$, two configurations, which may be characterised as CO and CO_3 in terms of the co-ordination with oxygen (Fig. 6.2), are of particular importance, being the lowest in energy for different charge states.

In the CO structure (Fig. 6.2(b)), carbon prefers to form a covalent bond with one oxygen neighbour to form carbon monoxide. The C–O bond length of 1.23 Å is consistent with a CO^{-2} ion substituting for a host oxygen ion. This structure is stabilised by a partial *p*-*d* covalent bonding between the carbon atom and the two nearest Ti ions, as illustrated in Fig. 6.3. The C–Ti distances have been calculated to be 2.15 Å, which is 2% longer than the original Ti–O in bulk $BaTiO_3$. From these calculations, it can be remarked that the carbon in the $SrTiO_3$ has a greater effect on the structure of the defect than it does for $BaTiO_3$.

In the case of CO_3 (Fig. 6.2(c)), as with $SrTiO_3$ and $PbTiO_3$, carbon prefers to form three C–O bonds yielding a centre of C_{3v} symmetry. The normal charge state of the carbonate ion is -2 and the formation of this geometry may be viewed as unlikely: the CO_3^{-2} ion is effectively replacing three host O^{-2} ions, leading to a surplus of four electrons. The C–O distances have been found to be 1.3 Å, which are close to the bond length of CO_3^{-2} ions. The CO_3 in the neutral charge state is non-planar, However, by adding electrons, the bond angles become smaller as the bonding interaction between

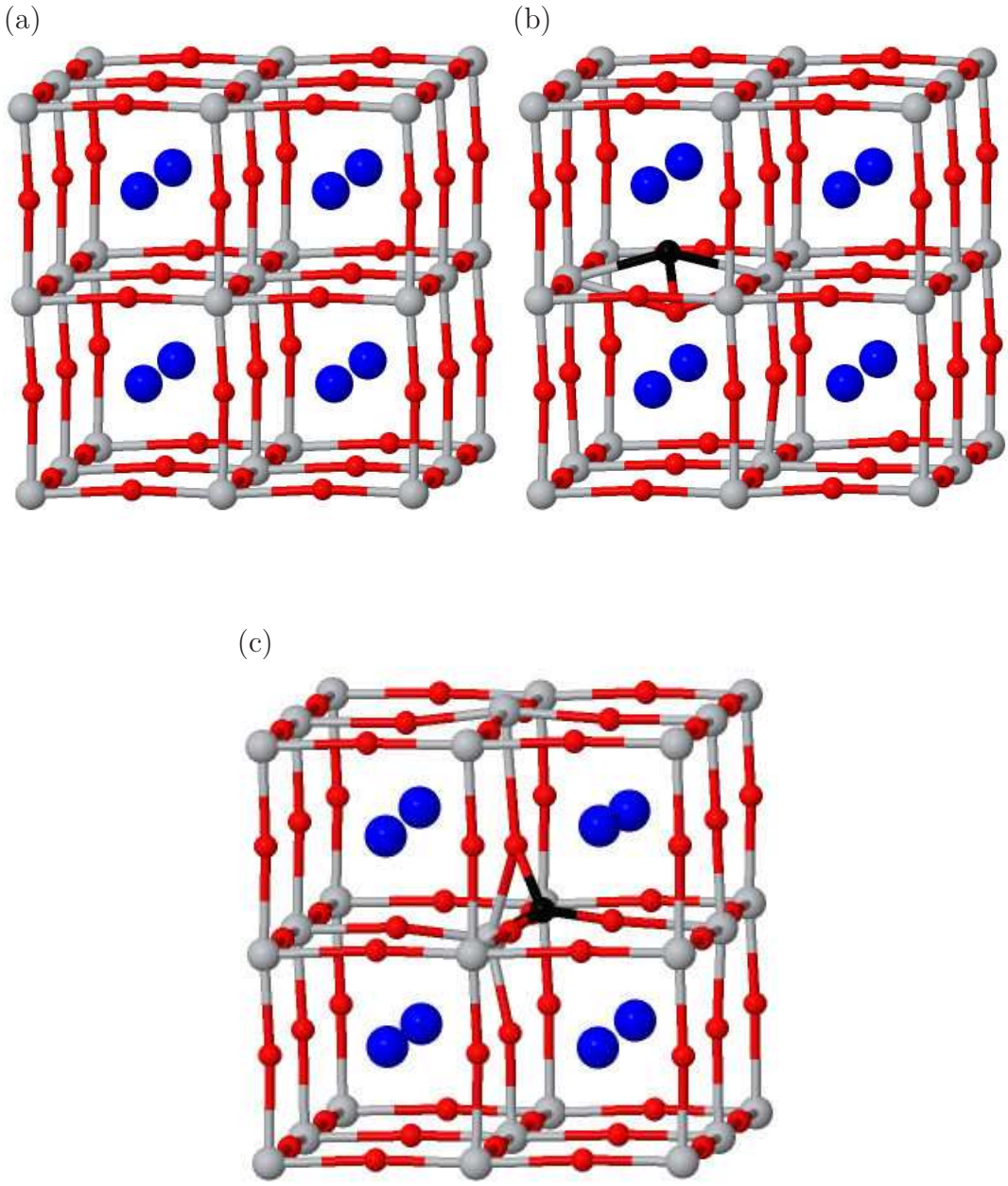

Figure 6.2: Schematics of the (b) CO and (c) CO_3 forms of C_i in $BaTiO_3$. An equivalent section of defect-free $BaTiO_3$ is shown in (a) for comparison. Blue, grey, red, and black spheres represent Ba, Ti, O, and C atoms respectively. Vertical and horizontal axes are approximately [001] and [010] respectively, with the tilted view adopted to aid clarity.

(a)

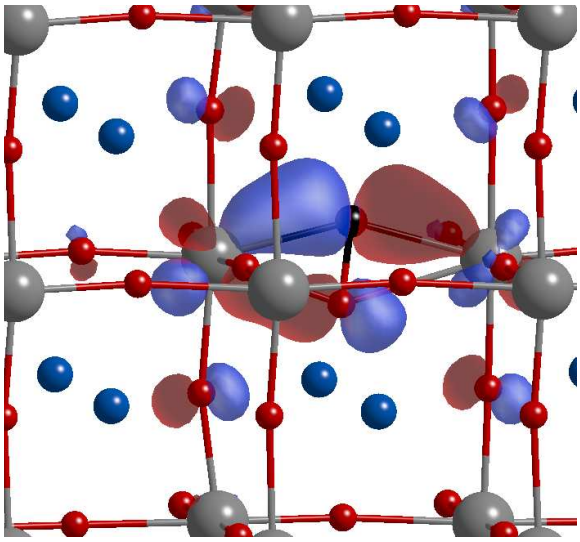

(b)

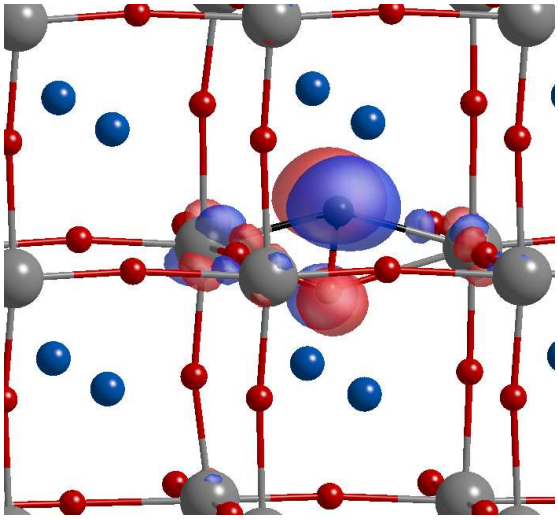

Figure 6.3: Plot of the wavefunction distribution of CO C_i configurations in $BaTiO_3$: (a) a partial *p*-*d* covalent bonding between the carbon atom and the two nearest Ti ions in the CO form; and (b) π^* CO molecular orbitals associated with the empty state in the gap. Red and blue volumes show wave function iso-surfaces of equal magnitude (0.1) and opposite sign. Colours and orientation are as indicated in Fig. 6.2.

the Ti and carbon atom increases the strength, and then CO_3 will be close to the planar. Indeed, it is shown below that, although the carbonate form is metastable in the neutral charge state, it is expected to act as a donor, thus favouring positive charge states.

The important effect of any impurity doping is its influence upon the band structure properties of a given crystal. Such interference might be responsible for a variety of features, such as changes in electric conductivity as well as dielectric and other behaviour. The band structures in the vicinity of the band-gap for the neutral charge state of the CO form and the overall +2 charge state of the carbonate form are shown in Fig. 6.4. The analysis of the influence of carbon upon the $BaTiO_3$ band structure provides the following data. In the case of CO form there are both occupied and empty bands within the gap, which may be related to the two π^* CO molecular orbitals, split by the crystal field. The wave function of the states are plotted in Fig. 6.3. The lowest energy occupied state wave function is depicted in Fig. 6.3(a), whereas Fig. 6.3(b) represent the wave function of the higher empty state in the gap, which is similar to that found in the case of $SrTiO_3$.

For the carbonate group, the neutral defect introduces two occupied levels, one of which is localised close to the bottom of the conduction band and the other at about the middle of the gap. In contrast, at +4 charge states, the band gap is devoid of states. The band structure for the +2 charge state configuration (Fig. 6.4(b)) consists of a single occupied band in the upper half of the band-gap. The state is a combination of a molecular orbital on the carbonate group and the neighbouring Ti cation. It is made up of the parallel p orbital on all four sites, but in anti-bonding combinations between C and the three oxygen, with the Ti d-orbital forming a σ bond with the p-orbital on the carbon, as shown in Fig. 6.5.

Based upon the band structures and expected oxidation states of CO and CO_3, it is natural to expect electrical levels to be present for interstitial carbon. The charge-dependent formation energies are shown in Fig. 6.4(c), indicating that the the neutral charge state of the CO configuration is not stable, in contrast to that for $SrTiO_3$ and

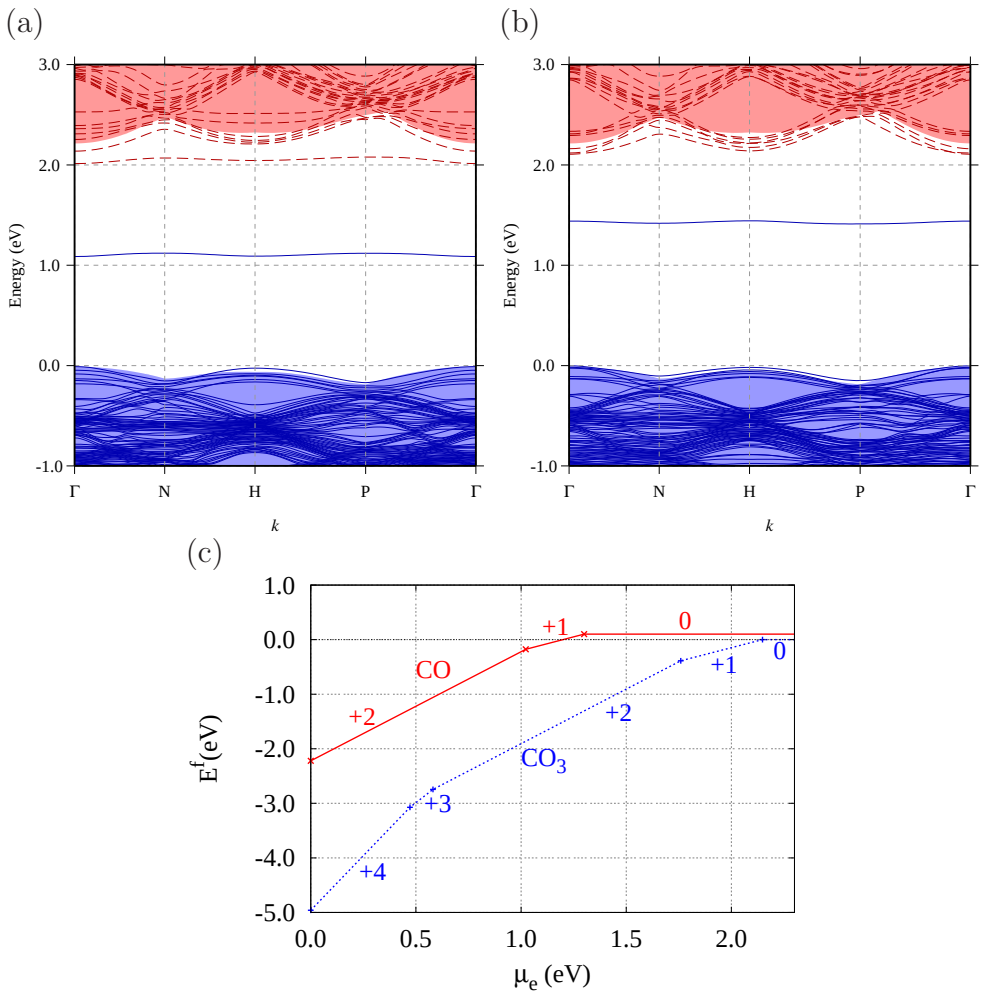

Figure 6.4: Band structures in the vicinity of the band-gap for C_i in: (a) the CO; and (b) the $(CO_3)^{+2}$ configurations, plotted along high-symmetry branches in the first Brillouin zone; and (c) showing $E^f(\mu_e)$ for various charge states of each structure. Occupied and empty bands in (a) and (b) are shown in solid (blue) and dashed (red) lines respectively. The underlying shaded areas show the regions of the bands for the corresponding bulk supercell. The energy scale is defined such that the valence band maxima are at zero. In (c) the (red) solid line and (blue) dashed line represent the CO and CO_3 configurations respectively. The gradient indicates the charge state, and the energy scale is defined by $E^f((CO_3)^0) = 0\,\text{eV}$.

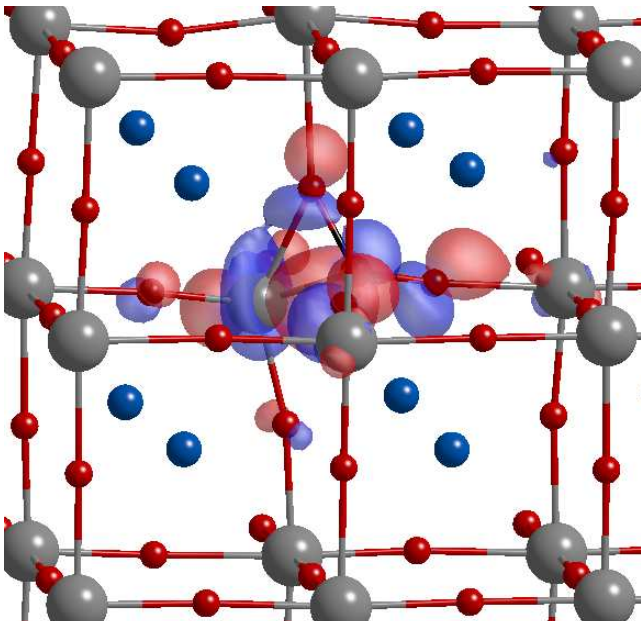

Figure 6.5: Wave function of the orbital state for the CO_3 C_i configuration in $BaTiO_3$. Red and blue volumes show wave function iso-surfaces of equal magnitude (0.1) and opposite sign. Colours and orientation are as indicated in Fig. 6.2.

$PbTiO_3$. Furthermore, the neutral and +1 charge states of CO_3 are stable compared with the equivalent structures in $SrTiO_3$ and $PbTiO_3$. In addition, the CO_3 +4 charge state is stable, which is in agreement with the same results for $PbTiO_3$ in contrast to the situation for $SrTiO_3$, which could be related to the difference in the location of the host band edge relative to the molecular orbitals of the CO_3 ion.

In addition to the electrical levels, one would expect local modes corresponding to C–O stretches. For the neutral, CO bonded configuration the stretch mode is estimated at 1571 cm^{-1}, which is much lower than the vibrational mode of CO gas. In the case of the +4 charge state, local vibrational modes are calculated for the CO_3 centre. There is an E-mode (anti-symmetric combination of C–O stretches) at around 1375 cm^{-1} and a non-degenerate breathing-mode (A_1) at 1042 cm^{-1}, which are close to those of gas phase CO_3^{-2} (see Table 4.2), and for the +3 charge state is 1233

and 908 cm^{-1}, whereas for +2 they are 1123 and 854 cm^{-1} and for +1 they are 1119 and 834 cm^{-1}. The increase in frequency with charge results from the differences in bonding, with the σ-bond between the Ti and C atoms resulting in a non-planar CO_3 group in the +2 charge state, and this is lost by the +4 state where the CO_3 group is close to planar.

6.3.2 C substituting for O

The possibility of carbon occupation in the oxygen sites has been examined. The geometry-optimised atomic structure of such a centre (C_O) is shown in Fig. 6.6(a). The bond-lengths of a simple substitution are very similar to those of the host, with the Ti–C bond-length at 2.08 Å, which is only slightly longer than the original Ti–O internuclear distances in bulk $BaTiO_3$ by 1%.

There is another structure of C_O in the $BaTiO_3$ as a result of chemical reactions between the carbon and nearby host oxygen ions, which is energetically favourable for the neutral charge state. Fig. 6.6(b) shows the resulting structure for the neutral charge state, which can be characterised as a CO species shared between two oxygen sites, $(CO)_{(2O)}$. In the neutral charge state, the bond length of carbon monoxide has been calculated to be 1.42 Å, which is significantly longer than that in a CO molecule, but close to a free CO^{-2} ion which has been calculated using this method to be 1.44 Å. This long bond is due to a combination of the charge state of the group and the bonding interactions with the neighbouring Ti atoms. The C–O bond length is shorter for the +1 and +2 charge states, are 1.35 and 1.26 Å respectively, which is consistent with the depopulation of an anti-bonding orbital. However, under p-type conditions, carbon prefers to form another bond with the nearest neighbour oxygen, forming carbon dioxide. Fig. 6.6(c) shows the resulting structure for the +4 charge state, which can be characterised as a CO_2 species shared between three oxygen sites, $(CO_2)_{(3O)}$.

Having described the defect geometry, the relative electronic structures for the two configurations are now explained. Fig. 6.7 shows the band structures corresponding to

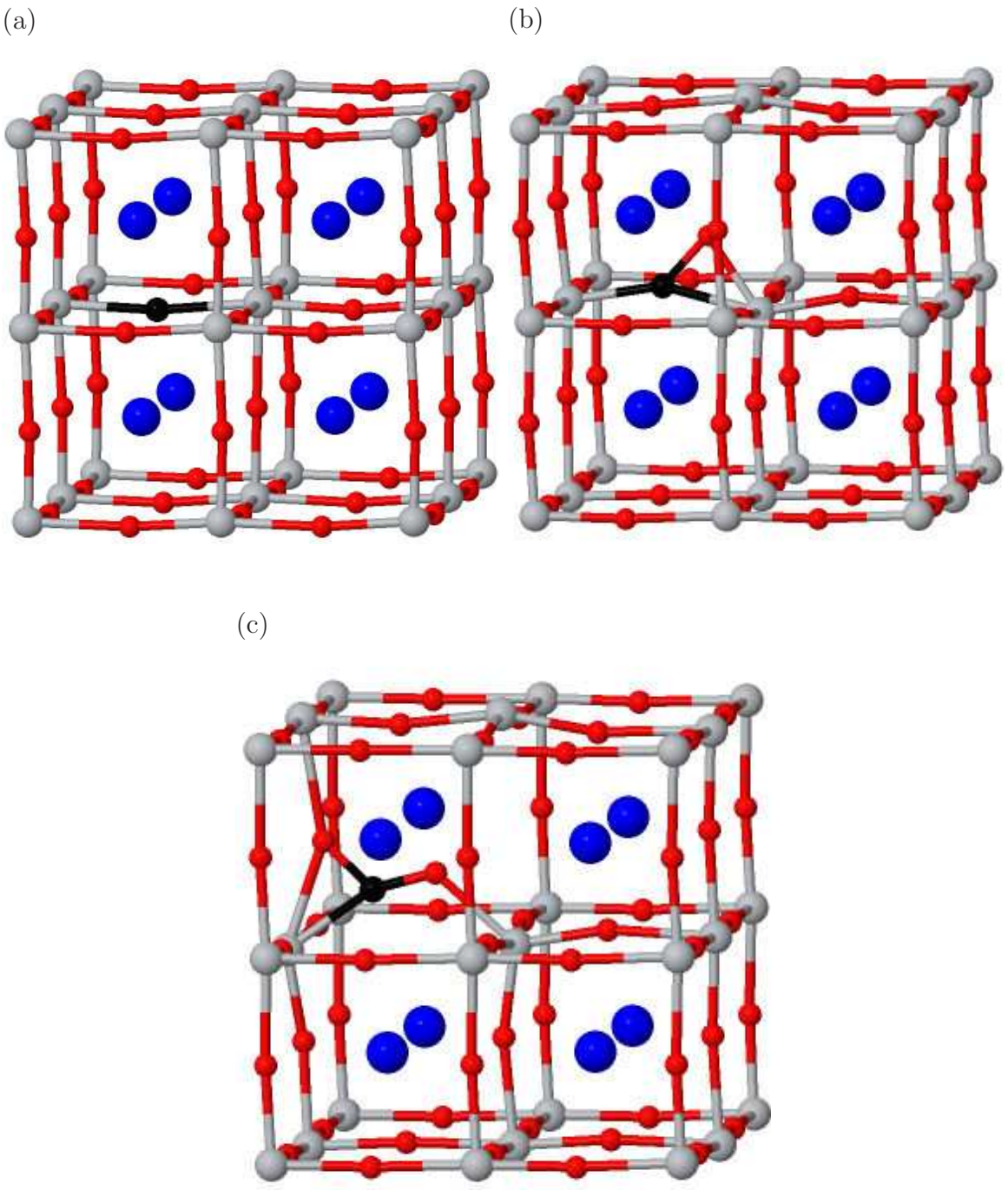

Figure 6.6: Schematics of (a) C_O, (b) $(CO)_{(2O)}$ and (c) $(CO_2)_{(3O)}$ in $BaTiO_3$. Colours and orientation are as indicated in Fig. 6.2.

different configurations of carbon in the oxygen sites. It can be noted that, as with the case of $SrTiO_3$, the on-site form (Fig. 6.7(a)) has two C-related levels in the band-gap. The lowest localised occupied states correspond to the p-state along the Ti-C-Ti axis, and the highest partially filled, degenerate pair are made up of the perpendicular p components split by the crystal field. One would therefore expect the on-site centre to act as a donor, and possibly as an acceptor. To clarify the combination of orbitals between the carbon dopant and adjacent host atoms, the wave functions of the iso-surface near the carbon dopant have been calculated, and the results are illustrated in Fig. 6.8.

Fig. 6.7(b) shows the electronic structure of the $(CO)_{(2O)}$ structure in the neutral charge state. The energy levels due to the C-impurity are localised in the upper part of the band-gap and are related to the combination of π^* CO and σ_{pd} with the neighbouring Ti atoms, as illustrated in Fig. 6.9.

Depending on the electronic structure, the electrical levels of carbon in the oxygen site have been investigated (see Fig. 6.7(c)), showing the formation energies of the two forms in different charge states as a function of the Fermi level. The C_O centre can accept an electron, but the addition of a second electron which would render it isoelectronic with oxygen is also energetically favoured. This agrees with the case of $PbTiO_3$ and contrasts with that of $SrTiO_3$. The picture for the CO form is slightly more complex as a result of the different structures. The existence of the occupied states in the band-gap is found to result in single and double donor levels, with the depopulation of the π^* state corresponding to a decrease in the C–O bond-length. However, the removal of three or four electrons is also possible, but with a spontaneous reconstruction to form a centre where C is bonded to *two* oxygen neighbours, $(CO_2)_{(3O)}$. Indeed, the formation energies of the charged defects vary with the Fermi level. For the $(CO_2)_{(3O)}$ form, the +4 charge state is energetically the most favourable when the Fermi level is low. With the increase in the Fermi level, its formation energy approaches that of the $(CO)_{(2O)}$ form with +2 and +1 charge states; then, finally, at the conduction band minimum the carbon defect is present in the C_O configuration

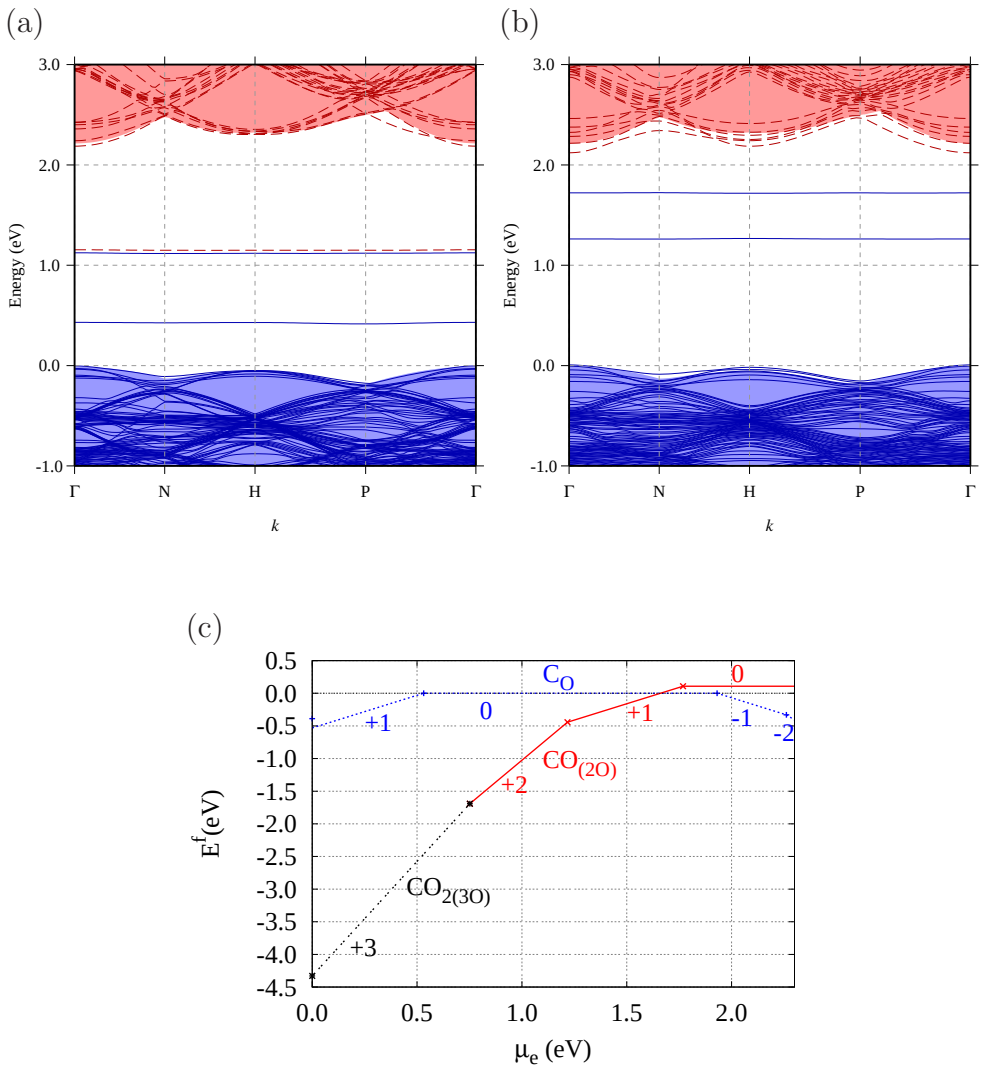

Figure 6.7: Band structures in the vicinity of the band-gap for C_O in: (a) the on-site, and (b) the $(CO)_{(2O)}$ configurations, plotted along high-symmetry branches in the first Brillouin zone; and (c) showing $E^f(\mu_e)$ for various charge states of each structure. Lines, shading and scales in (a) and (b) are as defined in Fig. 6.4. In (c) the (red) solid line, (blue) dashed line, and (black) dotted line represent the $(CO)_{(2O)}$, C_O, and $(CO_2)_{(3O)}$ configurations respectively. The gradient indicates the charge state, and the energy scale is defined by $E^f((C_O)^0) = 0\,\text{eV}$.

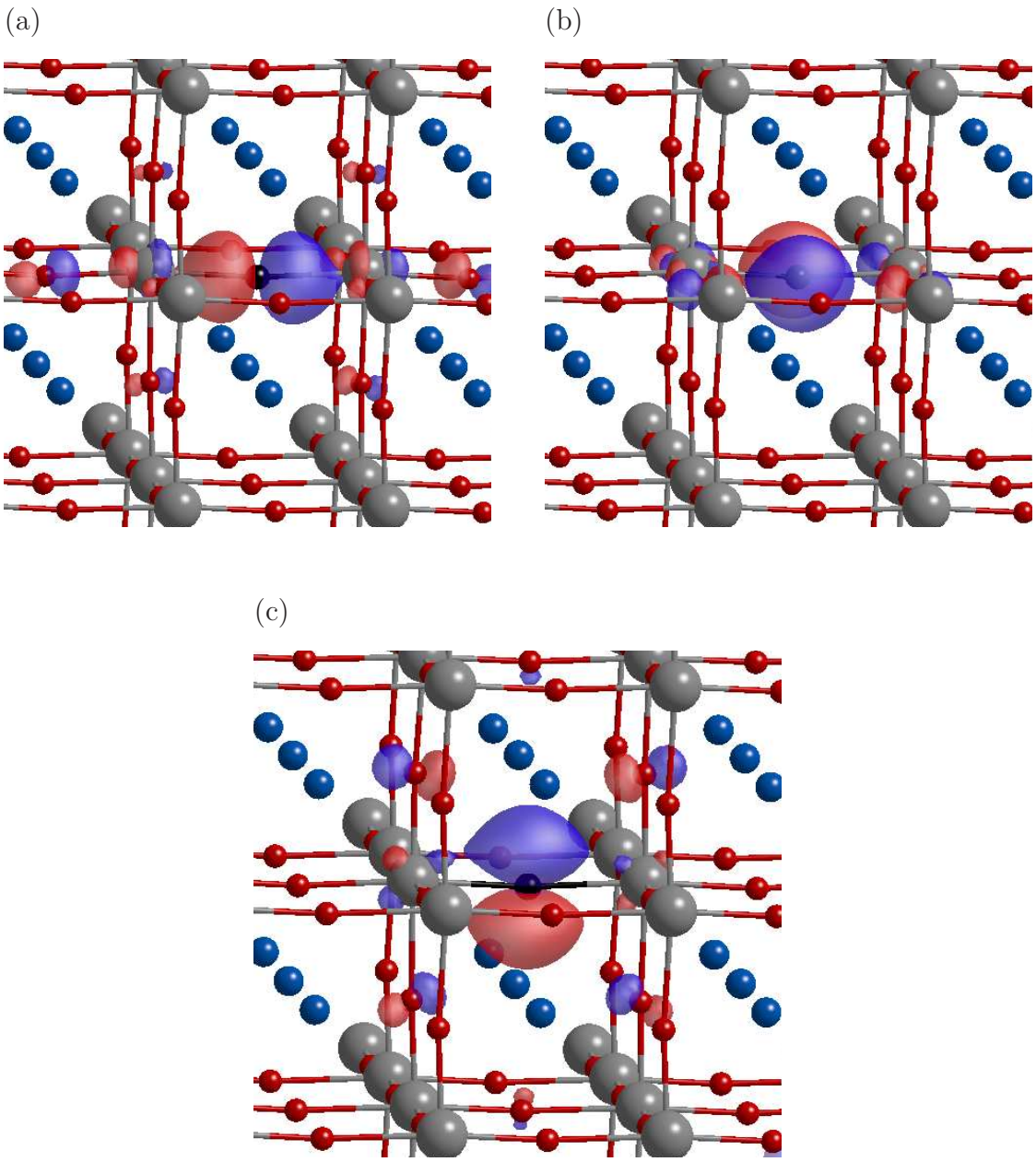

Figure 6.8: Schematics showing wave functions of C_O: (a) lowest occupied *p*-state along the Ti-C-Ti axis; (b) and (c) a partially filled, degenerate pair made up of the perpendicular *p* components. Red and blue volumes show wave function iso-surfaces of equal magnitude (0.1) and opposite sign. Colours and orientation are as indicated in Fig. 6.2.

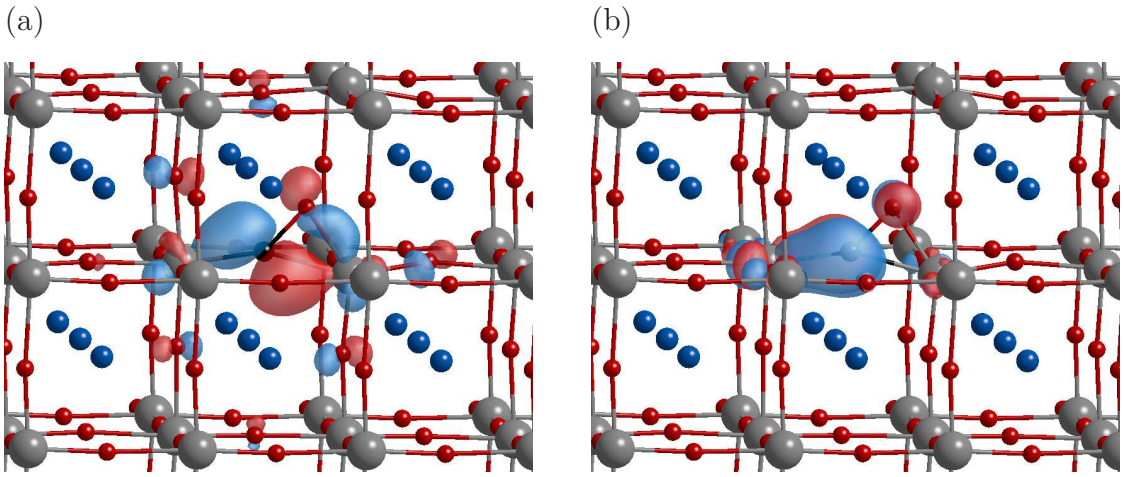

Figure 6.9: Plots (a) and (b) showing the wave function for the two occupied levels related to the combination of π^* CO and σ_{pd} with the neighbouring Ti atoms for the $(CO)_{(2O)}$ defect in $BaTiO_3$. Red and blue volumes show wave function iso-surfaces of equal magnitude (0.1) and opposite sign. Colours and orientation are as indicated in Fig. 6.2.

with neutral, -1 and -2 charge states (Fig. 6.7(c)).

As with C_i, C_O is likely to give rise to characteristic vibrational modes. For the on-site form, stretching vibrational modes lie at 646, 766 and 904 cm^{-1} in the neutral, for the -1 and -2 charge state respectively. Concerning the $(CO)_{(2O)}$ defect, the vibrational mode in the neutral charge state has been calculated at 959 cm^{-1}, which is close to the calculated vibrational mode of CO^{-2}. In the $+1$ charge state, the vibrational modes increase to 1100 cm^{-1}, and 1379 cm^{-1} for the $+2$ charge state, corresponding to increased bond-order. In the $(CO_2)_{(3O)}$ form, the increase in the number of C–O bonds means that the $+3$ charge state yields two stretch modes, estimated at 1129 and 1417 cm^{-1}. The difference in the geometry leads to the difference in the vibrational modes which can be easily distinguished experimentally.

6.3.3 C substituting for Ba

The following discussion considers the influence of carbon impurities as a cation, the Ba site, C_{Ba}. As in the C_i and C_O situations, there are different structures for Ba to take in the $BaTiO_3$ crystal. The results concerning the stable structure optimisation are presented in Fig. 6.10. The spontaneous displacement of C has been shown to form three C–O bonds (Fig. 6.10(a)). The C–O bond lengths are calculated to be in the range of 1.29 Å, which close to that in the carbonate group anion. However, the formation of the carbonate leaves the $BaTiO_3$ lattice deficient by one Ba cation and three oxygen anions. This results in a net excess of four electrons to be accounted for. Two of these are associated with the carbonate group, but this means that the reaction of carbon on the Ba site with three oxygen atoms is expect to result in a double donor.

In addition, during the simulations of C_{Ba}, another structure has been observed that results in an isoelectronic centre. Carbon reacts with a single neighbouring oxygen forming CO anion localised at the Ba site and an oxygen vacancy. Numerous relative orientations of the CO ion and oxygen vacancy have been analysed, and the one shown is the lowest in energy. The C–O bond length has been calculated to be 1.19 Å, which is in good agreement with the bond length in the carbon monoxide molecule. The structure shown schematically in Fig. 6.10(b) is metastable, but not more stable than the carbonate form (Fig. 6.11(c)), which can be accounted for on the basis of the relative favourability of the formation of three covalent bond. This is similar to the results obtained for C_{Sr} and C_{Pb} in the previous calculations in sections 4.3.3 and 5.3.3.

The expectations based upon oxidation states for the two illustrated structures are confirmed by their band structures shown in Fig. 6.11. In the +2 charge state of the carbonate form, and the neutral charge state of the CO form, the band-gap is devoid of states.

Next, the vibration signatures of these defects have been calculated. The CO_3 form in the overall neutral charge state has an (A_1) mode at 1056 and an E-mode

(a)

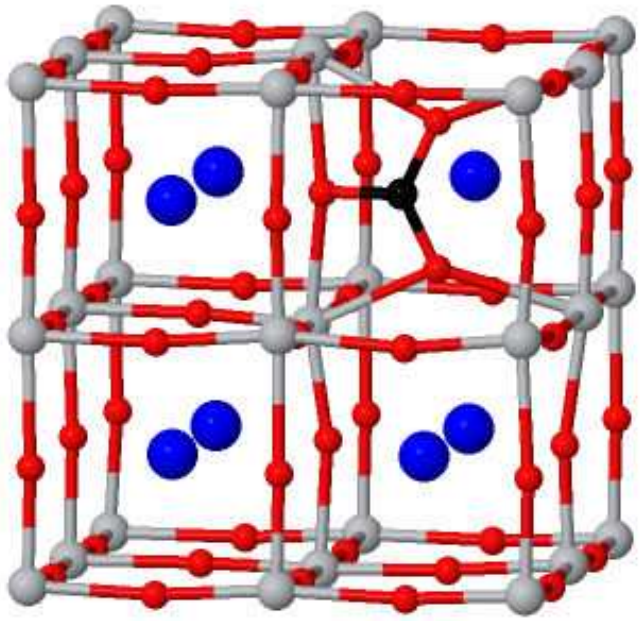

(b)

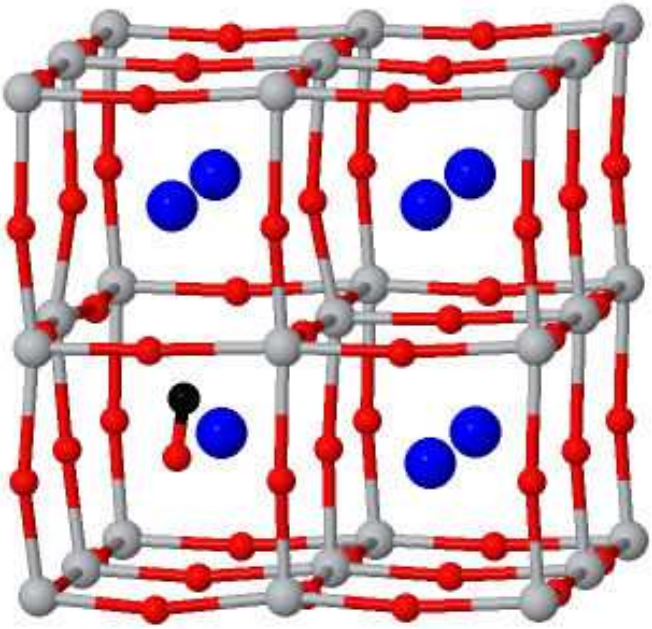

Figure 6.10: Schematic of C_{Ba} in $BaTiO_3$ in (a) CO_3 and (b) $(CO)_{Ba}$–V_O forms. Colours and orientation are as indicated in Fig. 6.2.

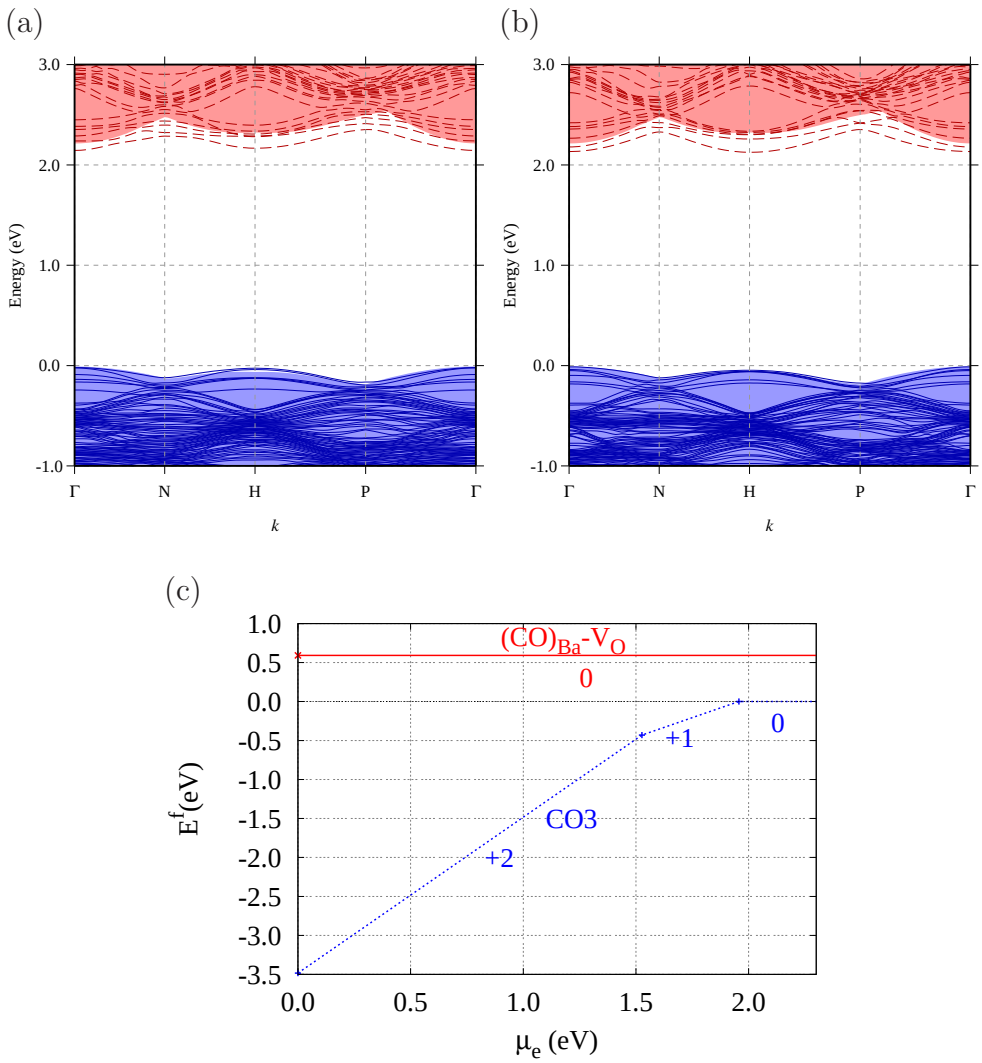

Figure 6.11: Band structures in the vicinity of the band-gap for C_{Ba} in: (a) +2 charge state of CO_3 and (b) the $(CO)_{Ba}$–V_O configurations, plotted along high-symmetry branches in the first Brillouin zone; and (c) showing $E^f(\mu_e)$ for various charge states of each structure. Lines, shading and scales in (c) and (b) are as defined in Fig. 6.4. In (c) the (red) solid line and (blue) dashed line represent the $(CO)_{Sr}$–V_O and $(CO_2)_{(3O)}$ configurations respectively. The gradient indicates the charge state, and the energy scale is defined by $E^f((CO_3)^0) = 0\,\text{eV}$.

at around 1480 cm^{-1}. The ionised forms have modes within 3 cm^{-1} of the neutral charge state, which is consistent with the shallow donor behaviour predicted for this centre. These vibrational modes are very similar to those obtained in the C_{Sr} of $SrTiO_3$ (see section 4.3.3). The vibrational mode of the C_{Ba} CO form is observed to be at 2094 cm^{-1}, which is in reasonable agreement with the experimental value for the carbon monoxide molecule frequency (Table 4.2) and significantly larger than that in C_i depending on electrons account.

6.3.4 C substituting for Ti

The last possibility considered is the substitution of titanium, C_{Ti}. Similar to the situations with C_{Ba} and C_i, the addition of one carbon atom exhibits a significant structural change from pure $BaTiO_3$. Fig. 6.12 shows that the doped carbon forms a carbonate group similar to that in the other materials. The relaxed structure has three C–O bonds 1.29 Å are significantly shorter than the Ti–O inter-nuclear distances in defect-free $BaTiO_3$ by about 35%. The calculated C–O bond lengths in C_{Ti} are close to those of the carbonate group (see Table 4.2), which are similar to the carbonate group bond lengths found in both $SrTiO_3$ and $PbTiO_3$. The structure optimisation calculations show that the carbonate ion is very close to the symmetry of C_{3v}. For the simulation supercell, the substitution of Ti by C might be expressed as resulting in the formation of one formula unit of ($BaCO_3$) and 31 formula units of $BaTiO_3$.

The band structure for C_{Ti} is shown in Fig. 6.13. It should be noted that the inclusion of carbon has no apparent effect on the the band-gap width.

To provide a mechanism for the direct experimental identification of C_{Ti}, a local vibrational mode above the one-phonon maximum could prove highly effective. Of particular note is that, for the C_{3v} C_{Ti} centre, the calculations indicate a degenerate (E) C–O stretch mode at 1383 cm^{-1}, and a breathing stretch-mode with A_1 symmetry at 1061 cm^{-1}. These are close to the experimental values of CO_3^{-2} gas phase [180] which have E' and A_1' stretch modes lying around 1415 cm^{-1} and 1064cm, respectively, and also agree both with the modes detected in $BaTiO_3$ [176], and with those modes

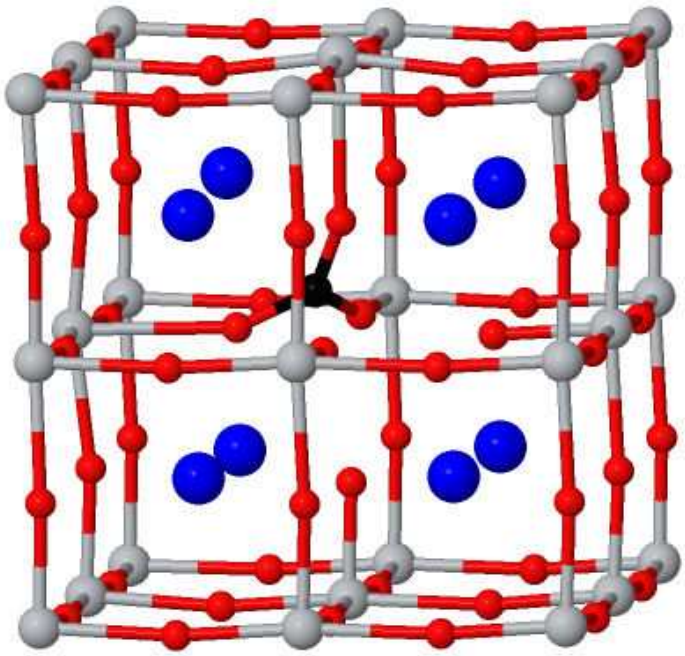

Figure 6.12: Schematic of C_{Ti} in $BaTiO_3$. Colours and orientation are as indicated in Fig. 6.2.

assigned to the carbonate groups in $BaCO_3$ [84]. Lower frequency modes of the carbonate group are also present for C_{Ti}, but are resonant with the one-phonon density of states. Both of the local modes are infra-red and Raman active, and given sufficient concentrations one might seek to confirm the presence of this form of carbon centre directly via either IR or Raman spectroscopy.

Furthermore, the energetics for the reorientation of the carbonate group have been examined. The initial and final structure are shown in Fig. 3.5, and the energy profile along the minimum energy path between them is shown in Fig. 6.13. The energy difference between the initial and final structure has been calculated to be about 50 meV, which is related to non-equivalence in the defect with respect to the rhombohedral distortion. The activation energy for reorientation is predicted to be around 2.5 eV, which is close to the activation energy for the CO_3 reorientation at C_{Ti} in $SrTiO_3$ (section 4.3.4). The impact of carbon in the Ti site in $BaTiO_3$ has a similar impact on the hysteresis as predicted for the other materials.

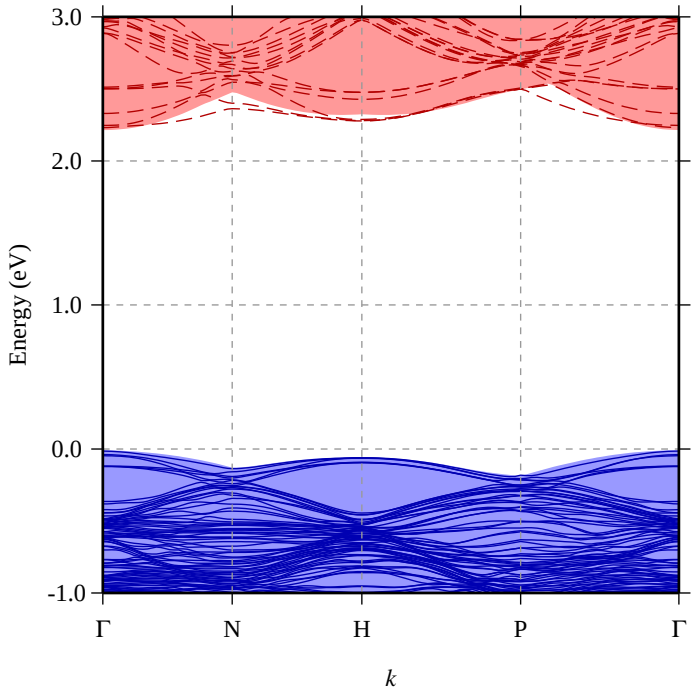

Figure 6.13: Band structures in the vicinity of the band-gap for C_{Ti} in $BaTiO_3$, plotted along high-symmetry branches in the first Brillouin zone. Lines, shading and scales are as defined in Fig. 6.4.

6.3.5 Formation energy comparison

Finally, as for $SrTiO_3$ and $PbTiO_3$, a thermodynamic assessment of the relative stability of the four sites has been conducted, where the atomic and electron chemical potentials must be taken into account. The formation energies of defects in various charge states has been calculated using Eq. 3.9. In the $BaTiO_3$ system μ_i denotes the chemical potential of the species (i =Ba, Ti, O and C). Firstly the atomic chemical potentials have been assessed by considering the energies of bulk $BaTiO_3$ and related materials. The chemical potentials of components μ_{Ba}, μ_{Ti} and μ_O are related through

$$\mu_{Ba} + \mu_{Ti} + 3\mu_O = \mu_{BTO} \tag{6.1}$$

Here μ_{Ba} is the energy per atom of pure Ba metal, μ_{Ti} and μ_O have been defined and calculated in section 4.2, and μ_{BTO} is the total energy per formula unit of pure $BaTiO_3$.

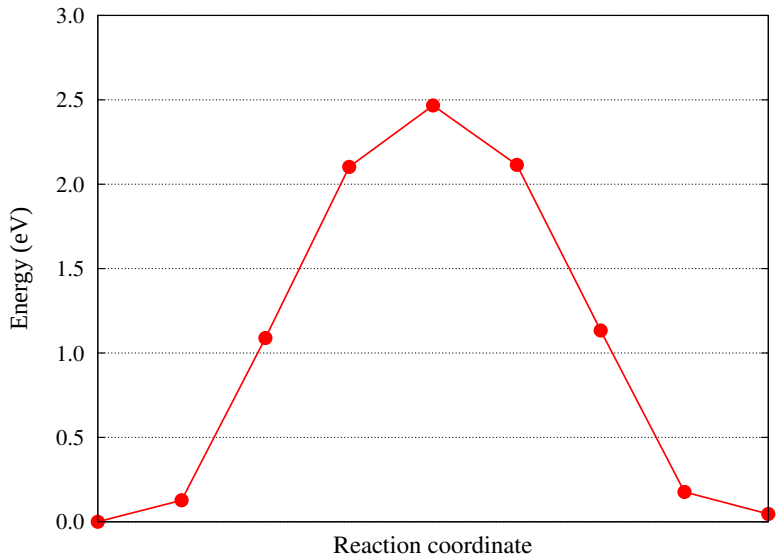

Figure 6.14: Calculated reorientation barrier of CO_3 C_{Ti} in $BaTiO_3$ between the initial and final structures.

The enthalpy of formation of $BaTiO_3$ is $\Delta H_{BaTiO_3} = \mu_{BaTiO_{3(bulk)}} - \mu_{Ba} - \mu_{Ti} - 3\mu_O$, and is found to be -17.54 eV which is in good agreement with experimental values [181] and previous calculations [182] (see Table 6.2). A parameter space describing the values of the chemical potentials for which $BaTiO_3$ is stable can be established in terms of μ_{Ti} and μ_{Ba} using Eq. 6.1, with boundaries formed where related materials become thermodynamically more stable than $BaTiO_3$. For example, for sufficiently high values of the chemical potentials of Ti and Ba, it would become more favourable to form bulk metals rather than the compound. Other thermodynamic boundaries are formed by BaO and BaO_2, TiO, TiO_2, Ti_2O_3 and oxygen gas. The thermodynamic boundaries of BaO and BaO_2 are

$$\Delta H_{BaO} = \mu_{BaO(bulk)} - \mu_{Ba} - \mu_O \tag{6.2}$$

$$\Delta H_{BaO_2} = \mu_{BaO_2(bulk)} - \mu_{Ba} - 2\mu_O \tag{6.3}$$

The other conditions for TiO, TiO_2, Ti_2O_3 and oxygen gas are as previously stated in section 4.2. To provide a benchmark for these calculations, the calculated properties for Ba and its compounds, in addition to the calculated heats of formation,

are presented in Table 6.2. This shows that the heats of formation are in excellent agreement with experiments, and the lattice constants are calculated to within about 5%, reflecting the tendency of LDA calculations to underestimate lattice constants, particularly in the case of Ba. There is also excellent agreement between the calculated and experimental enthalpy of formation energies. The calculated properties and heats of formation for Ti and it compounds have been listed in Table 4.1. In order to determine the properties of the phases in Table 6.2, the same computational settings as for $BaTiO_3$ have been employed but the number of k-points and basis set for each material are varied so as to ensure a convergence of the total energy. The shaded area in Fig. 6.15(a) shows the resulting phase diagram for the stable ternary $BaTiO_3$ growth as a function of μ_{Ba} and μ_{Ti}.

Following the procedure [76] adopted for the Cr doping of $SrTiO_3$ and the current calculations of carbon impurities in both $SrTiO_3$ (section 4.3.5) and $PbTiO_3$ (section 5.3.5), the impurity chemical potential based upon the appropriate carbon containing phase also needs to be selected. The value of μ_{C} has been calculated based upon graphite (C), TiC and $BaCO_3$. Other carbon-containing systems such as CO_2, CO_3 and BaC_2 were examined, but were not found to be equilibrium phases under the computational conditions. Fig. 6.15(b) illustrates the carbon chemical potential diagram as a function of μ_{Ba} and μ_{Ti}, with μ_{O} defined by Eq. 6.1. For example, in O- and Ba-rich conditions carbon is in equilibrium with $BaCO_3$, and the lowest energy carbon defect is C_{Ti}, similar to what was found for $SrTiO_3$.

Using Eq. 3.9 and by considering the $BaTiO_3$ stability conditions described above, the likely location of carbon in $BaTiO_3$ has been examined.

Fig. 6.16 illustrates the effect of an upward shift of Fermi level on the stabilisation of carbon defects in $BaTiO_3$ crystal at each chemical potential condition of μ_{Ba} and μ_{Ti}. These plots are for three choices of electron chemical potential, which are, $\mu_e = E_v$ (p-type $BaTiO_3$); (b) $\mu_e = E_g/2$ and (c) $\mu_e = E_c$. It should be noted that, given O- and Ba-rich equilibrium conditions in the stable region of $BaTiO_3$, carbon is in equilibrium with $BaCO_3$, and the lowest energy carbon defect is found to be C_{Ti}. Indeed, that is

Table 6.2: Calculated and experimental bulk properties and formation enthalpies for Ba and its compounds. Lattice constant (a_0, Å), axial ratio (c/a) and enthalpy of formation (ΔH^f, eV/f.u.). Experimental and theoretical data are taken from previous publications [181–189].

	Current calculations	Experiment	Previous calculations
	Ba, body-centred cubic ($Im\bar{3}m$)		
a_0	4.77	5.02	4.77
	BaO, sodium chloride ($Fm\bar{3}m$)		
a_0	5.46	5.49	5.46
ΔH^f	−5.71	−5.73	−5.18
	BaO_2, tetragonal ($I4/mmm$)		
a_0	3.75	3.78	3.76
c/a	1.78	1.79	1.78
ΔH^f	−6.70	−6.59	-
	$BaTiO_3$, simple Cubic ($Pm\bar{3}m$)		
a_0	3.94	3.99	3.93
ΔH^f	−17.54	−17.20	−17.5

the same situation for both $SrTiO_3$ and $PbTiO_3$. In general, depending on the location of the Fermi level, the present calculations reveal that the four sites of carbon defects is arise during thin film growth. This is in contrast with the case for $SrTiO_3$, where C_i is unstable, and for $PbTiO_3$ where C_i and C_O are unstable (see sections 4.3.5 and 5.3.5).

For p-type $BaTiO_3$ (Fig. 6.16(a)), unsurprisingly, an electron-donating system is favoured. Under O-rich conditions, carbon impurities that give the lowest formation energies are C_{Ti} and C_{Ba} which is consistent with the expectation that, in the metal-lean conditions metal substitution is favoured. As O-rich conditions decrease until the intermediate equilibrium conditions the stable region of in $BaTiO_3$, carbon prefers to

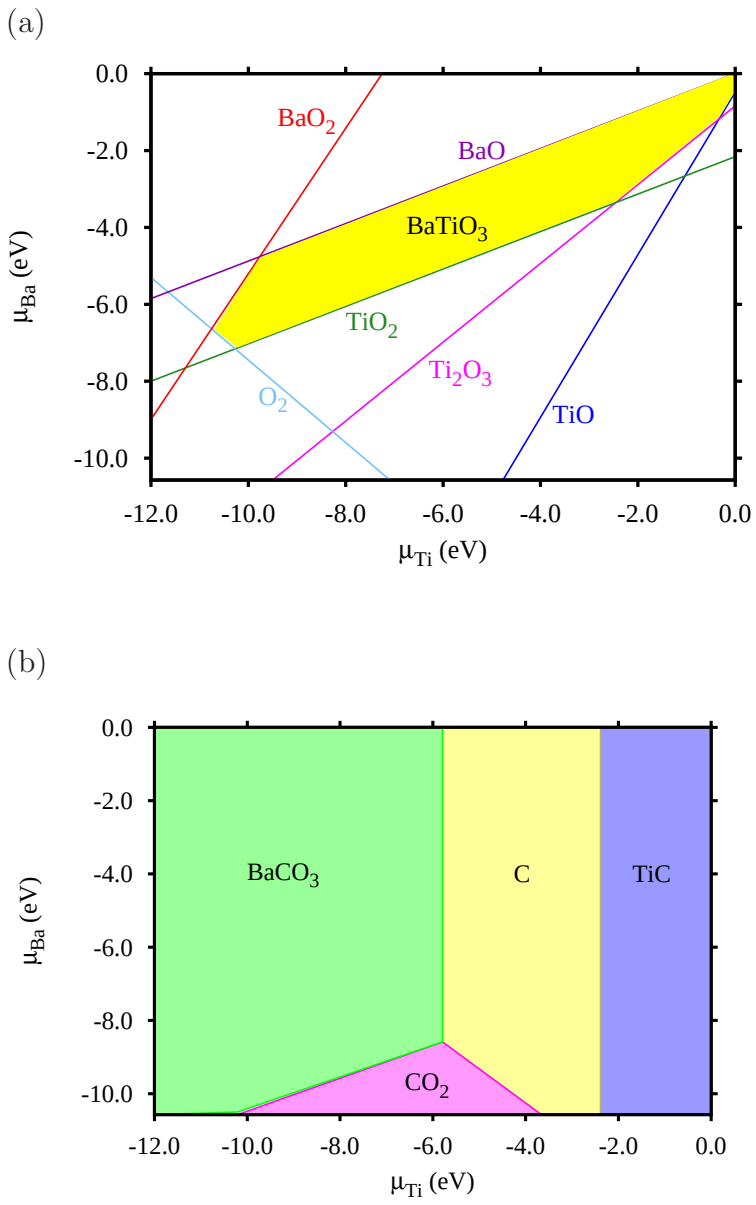

Figure 6.15: Plots showing the equilibrium phases for $BaTiO_3$ related materials as a function of μ_{ba} and μ_{Ti}: (a) shows the $BaTiO_3$ stable region of the parameter space, indicated by the shaded area; whereas (b) shows the stable phases containing carbon over the same ranges of chemical potentials.

form an interstitial site with a +4 charge state. It should be noted that *all* these configurations are related to the carbonate group. Finally, at the metal-rich limit,

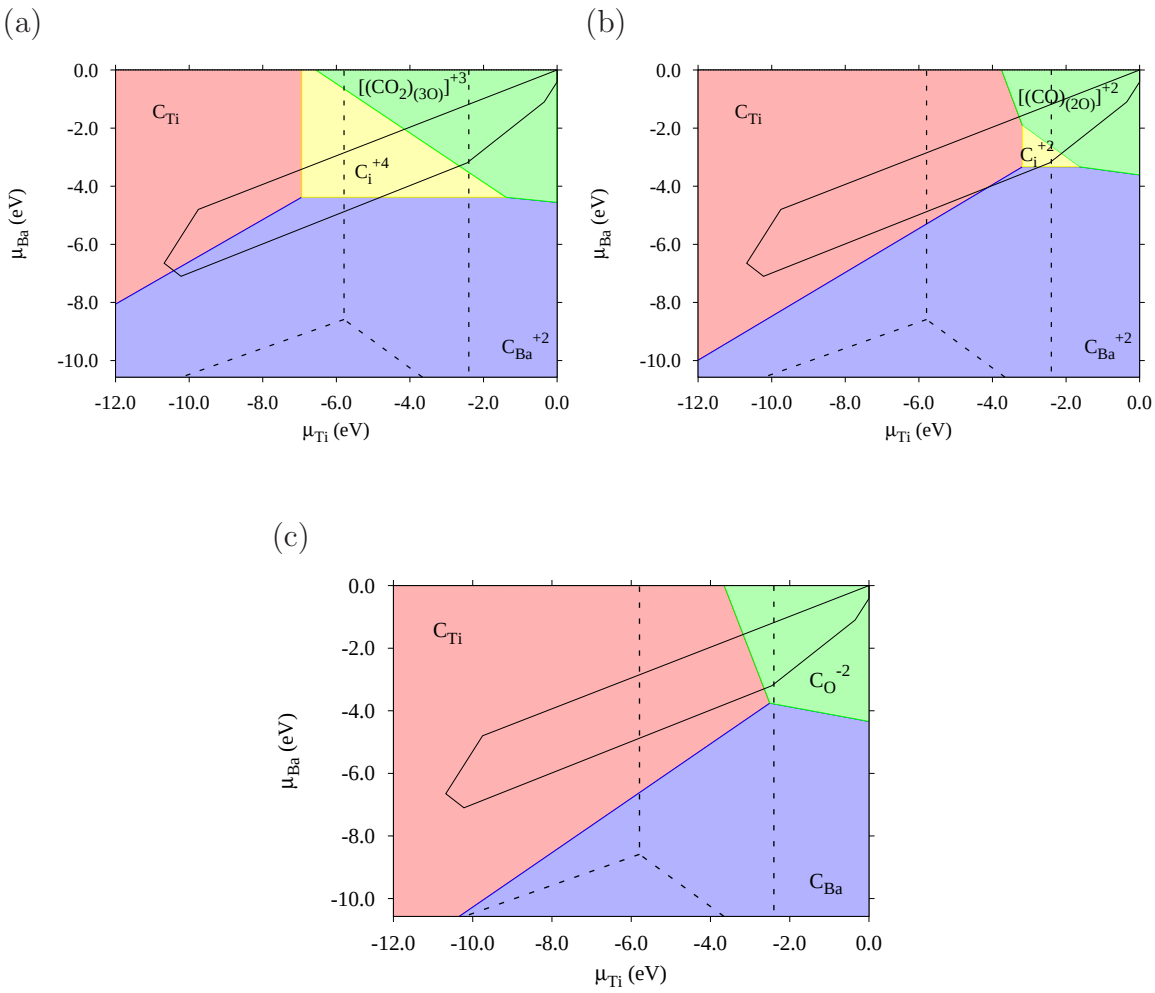

Figure 6.16: Graph showing the calculated equilibrium form of C-related defects with respect to the atomic chemical potentials for different electron chemical potentials: (a) $\mu_e = E_v$ (p-type BTO); (b) $\mu_e = E_g/2$; and (c) $\mu_e = E_c$. The $BaTiO_3$-stable region is superimposed (solid black line), and the C source phase is indicated by the dashed lines (see Fig. 6.15).

carbon in the oxygen site prevails, with a +3 charge state of the CO_2 configuration of C_O.

As the electron chemical potential moves from the valence to conduction bands, C_{Ti} dominates more and more of the $BaTiO_3$-stable region, whereas the C_i stable area decreases progressively until the acceptor levels of the C-containing defects fall below

μ_e. Then, in n-type conditions ($\mu_e = E_c$), there is the possibility of the formation of C_O in the negative charge state with the anion lying on-site.

The calculations show a sizeable preference for Ti substitutions over Ba substitutions. However, the sole expectation for impurities that favour the Ba site, is at O- and Ti-rich at p-type conditions.

6.4 Conclusion

In the present work, an extensive density functional theory study of the effects of carbon impurities in rhombohedral $BaTiO_3$ has been conducted, including the consideration of structural configurations, electronic properties, electrical levels and vibrational modes, and these are compared with available experimental data and previous theoretical calculations. All possible carbon sites and structural configurations have been considered in a range of possible charge states. Overall, carbon exhibits complex behaviour in $BaTiO_3$ and some of its configurations are related to carbonate groups, such as in interstitial and both Ti and Ba substitutions.

Defect formation energies have been investigated in the range of bulk the $BaTiO_3$ phase diagram. The formation energies suggest that *all* types of sites are stable. Under metal-lean conditions, for p-type $BaTiO_3$, both C_{Ti} and C_{Ba} are energetically more stable with the carbonate group configuration. However, C_{Ti} is dominant of a wide range of Fermi levels. Regardless of Fermi level location, carbon in the O site is always dominant in O-lean conditions with different structures and different charge states. Hence, under metal-rich conditions, carbon defects are energetically favoured in the CO_2 configuration in p-type conditions, and by shifting the Fermi level toward CB the structure transitions to CO whereas in n-type conditions on-site carbon is dominant. The C_i also has the opportunity to be positioned in the stable region of $BaTiO_3$ under intermediate growth conditions.

The vibrational frequency associated with each defect has been determined and compared with available theoretical and experiment values. In addition, for a com-

bination of the band structure and electrical level calculations and depending upon which site the carbon occupies it may form a donor, acceptor, or isoelectronic centre.

Having examined the different characteristics of carbon impurities in three different perovskite structures, and observed that the stability of structures depends on the growth conditions, the next chapter look at the significant distinguish characteristics among these three perovskite materials.

Chapter 7

Comparison of the properties of perovskite titanates

In the previous three chapters, the structural configurations, electronic structures, electrical levels, vibrational modes, activation energies and stability of carbon impurities in three promising perovskite titanates have been investigated separately. This chapter emphasises the main similarities and differences in the impact of carbon on the characteristics of these materials, providing useful insights which may shed light on the impact of carbon for a wider family of perovskite titanates.

7.1 Chemical configurations

Regarding geometry, various structural configurations of carbon impurities in the host materials ($SrTiO_3$, $PbTiO_3$ and $BaTiO_3$) have been investigated. Interstitial and substitutional point defects and their relative stability in different charge states are considered for each type of point defect. For the three perovskites, regardless of the structure of the host material, carbon prefers to form covalent bonds with host oxygen-neighbour(s). The current study reveals that, for carbon, the formation of carbonate groups is generally energetically favoured for interstitial and both A (Sr, Ba or Pb) and Ti site substitution. However, there is a possibility for carbon to form

other covalent structures, such as CO in both C_i and $(CO)_{(2O)}$ and CO_2 in the case of $(CO_2)_{(3O)}$.

Recent studies [60] predict that a carbon impurity prefers to locate at an oxygen site based on its location in the periodic table. However, the present calculations reveal that carbon in the O site is very unlikely, given the significant energy saved in covalent bond formation, and that the ionisation energy of carbon is very different from oxygen: the formation of a highly charged carbon to become isoelectronic with the relevant oxygen ions is energetically unfavourable.

According to the results presented in this thesis, it is natural to speculate that carbon impurities in other crystals such as $KNbO_3$, $CaTiO_3$, $KTaO_3$ and $PbZrO_3$ might have the similar structures and properties. However, the crystal structure of the host material could play an important role in influencing defect bond length(s) and hence the vibrational modes of the defect, as explored in this chapter.

7.2 Vibrational modes

The highly characteristic local vibrational modes predicted in the different configurations provide a possible route to experimental validation and identification of the structures in real materials. The estimated frequencies show that there are some similarities and variations between defects within a class (such as C substituting for Ti) in the three different materials. The calculated modes are listed in Table 7.1. The data show that the vibrational modes depend upon both structure and charge state. Both the frequencies and splittings are characteristic of the charge state, and since by symmetry they are all IR-active, this variation with conditions presents a route to the identification of experimental IR centres.

As the structures in $BaTiO_3$ and $PbTiO_3$ are similar to those found for $SrTiO_3$, it is unsurprising that the calculated vibrational modes are also similar. In approximately trigonal carbonate group cases, C–O stretch modes are correlated with the E and A modes, with the E-mode being split due to the lower symmetry of the site in

both $PbTiO_3$ and $BaTiO_3$. It has been shown that the difference between the E and A-modes in an interstitial defect is significantly higher in both $SrTiO_3$ and $BaTiO_3$ compared with in $PbTiO_3$.

It is noted that the calculated frequencies for C_O in $SrTiO_3$, $BaTiO_3$ and $PbTiO_3$ differ slightly (they are within around 7%), but are essentially the same in character. Moreover, the local vibrational modes for the $(CO)_{(2O)}$ defect increase with the charge state corresponding to increases in the bond-order.

The calculated vibrational frequencies for carbon in the A-site are also listed in Table 7.1. In addition to showing a substantial difference between the carbonate and CO forms, the data show that there is a very small charge state dependence, and that the modes are significantly higher than those of the similar form of bonding in interstitial carbon. These data are therefore of importance in the discrimination of the site adopted by carbon in both $SrTiO_3$ and $BaTiO_3$. In contrast, for $PbTiO_3$ they are close to those determined for interstitial carbon meaning the local vibrational modes for carbon in the Ti site are close to those modes assigned to the carbonate group in ACO_3 crystal structures.

The C–O bond length for carbon interstitial $PbTiO_3$ is 2% longer than in the other two materials, therefore the local vibrational mode for the CO form has been found to be lower in frequency than it is in both $SrTiO_3$ and $BaTiO_3$ by about $120\,cm^{-1}$. This result may reasonably be attributed to the difference in lattice constant, and hence, one may logically conclude that the corresponding local vibrational modes in other perovskites such as $BaZrO_3$, specified [190] as 4.19 Å, which is $\sim$ 7% greater than $PbTiO_3$, would be concomitantly lower still.

Given the substantial differences in the frequencies of vibration and charge state dependencies between the various sites, these vibrational characteristics may represent a route for experimental identification of the site and charge state of carbon in these materials. For example, suitable illumination that leads to an ionisation of a centre which exhibits a substantial spectral shift is more likely to be interstitial carbon in a carbonate group than carbon on the barium site.

Table 7.1: Calculated modes (ν, cm^{-1}) of the C-containing defects at the four sites in $SrTiO_3$, $BaTiO_3$ and $PbTiO_3$. "Form" indicates the structural form in each case and "Fragment" indicates the local bonding between carbon and oxygen. C_A refers to carbon substitution for Sr, Ba or Pb in $SrTiO_3$, $BaTiO_3$ and $PbTiO_3$ respectively.

Site	Form	Fragment	Q	ν_{SrTiO_3}	ν_{BaTiO_3}	ν_{PbTiO_3}
C_i	CO	CO	0	1554	1571	1437
C_i	CO_3	CO_3	+2	854, 1018	823, 1080, 1124	1069, 1421, 1512
C_i	CO_3	CO_3	+3	942, 1154	909, 1233, 1323	1061, 1424, 1511
C_O		C–Ti	−1	875	867	771
C_O		C–Ti	−2	–	904	857
C_O	$(CO)_{(2O)}$	CO	0	943	959	970
C_O	$(CO)_{(2O)}$	CO	+1	1104	1101	1138
C_O	$(CO)_{(2O)}$	CO	+2	1345	1380	1380
C_O	$(CO_2)_{(3O)}$	CO_2	+4	1121, 1348	1187, 1456	1006, 1337
C_A	CO	CO	0	2086	2094	2072
C_A	CO_3	CO_3	0	1396, 1517	1057, 1362, 1480	1052, 1336, 1532
C_A	CO_3	CO_3	+1	1396, 1517	1058, 1364, 1481	1067, 1356, 1475
C_A	CO_3	CO_3	+2	1395, 1518	1056, 1363, 1477	1073, 1356, 1475
C_{Ti}	CO_3	CO_3	0	1081, 1414	1048, 1379, 1384	1054, 1362, 1475

7.3 Electronic structure and electrical levels

The current work shows that carbon incorporated into one of the titanates examined could be either electrically active, such as in the substitution of either the A site metal or of oxygen, or electrically passive, such as with the iso-electric substitution of Ti. Accordingly, it may be predicted that in other perovskite, such as $PbZrO_3$ or $CdSnO_3$, carbon substitution at A-sites and oxygen-sites are likely to be electrically

active, whereas substitution for the B site is likely to be electrically passive.

Based upon the band structures and expected oxidation states, the electrical levels of the defect centres in $SrTiO_3$, $BaTiO_3$ and $PbTiO_3$ have been interpreted. Some differences in behaviour might be usefully noted.

Fig. 7.1 shows the gap-state at the Γ-point for selected defect-containing supercells. There are some clear similarities between different materials. For example, in all three materials, carbon substitution at the A-site results in a band close to the respective conduction band minima. Additionally, C_i(CO) has an occupied state around 1 eV above the valence band top in the neutral charge state. However, there are also some key differences. For example, the +4 charge state of C_i is unstable in both $SrTiO_3$ and $PbTiO_3$, but stable in $BaTiO_3$. Similarly, the −2 and −1 charge states of substitution at the oxygen site are unstable in $SrTiO_3$, but stable in both $BaTiO_3$ and $PbTiO_3$. This means that although behaviour in on titanate may be a guide to what might be expected to be found for another, the influence of differences in band-gap, for example, means that each materials should be analysed separately.

With respect to the electrical levels, the calculations show that the CO configuration for interstitial carbon is unfavourable compared with CO_3 in $BaTiO_3$. This is in contrast with $SrTiO_3$ and $PbTiO_3$ in which the neutral charge state of the CO is the equilibrium form for much of the band gap. The relative stability of the CO configuration in $BaTiO_3$ compared to $SrTiO_3$ and $PbTiO_3$ is likely to be due to the larger lattice constant in the former case, resulting in a greater strain in the formation of the two CO bonds.

For $SrTiO_3$, two C-related levels in the band gap have been found for C_O which lie slightly higher than in the corresponding defect in $BaTiO_3$. In $PbTiO_3$, the lower occupied state lies within the valence band and the energy difference between the occupied and empty state in the band gap is about 0.1 eV lower than for the corresponding defect in $SrTiO_3$ and $BaTiO_3$, probably as a result of the difference in symmetry. Finally, the band structures for the C_{Ti} in all three perovskites show no evidence of the introduction of defect states, which is consistent with the carbonate

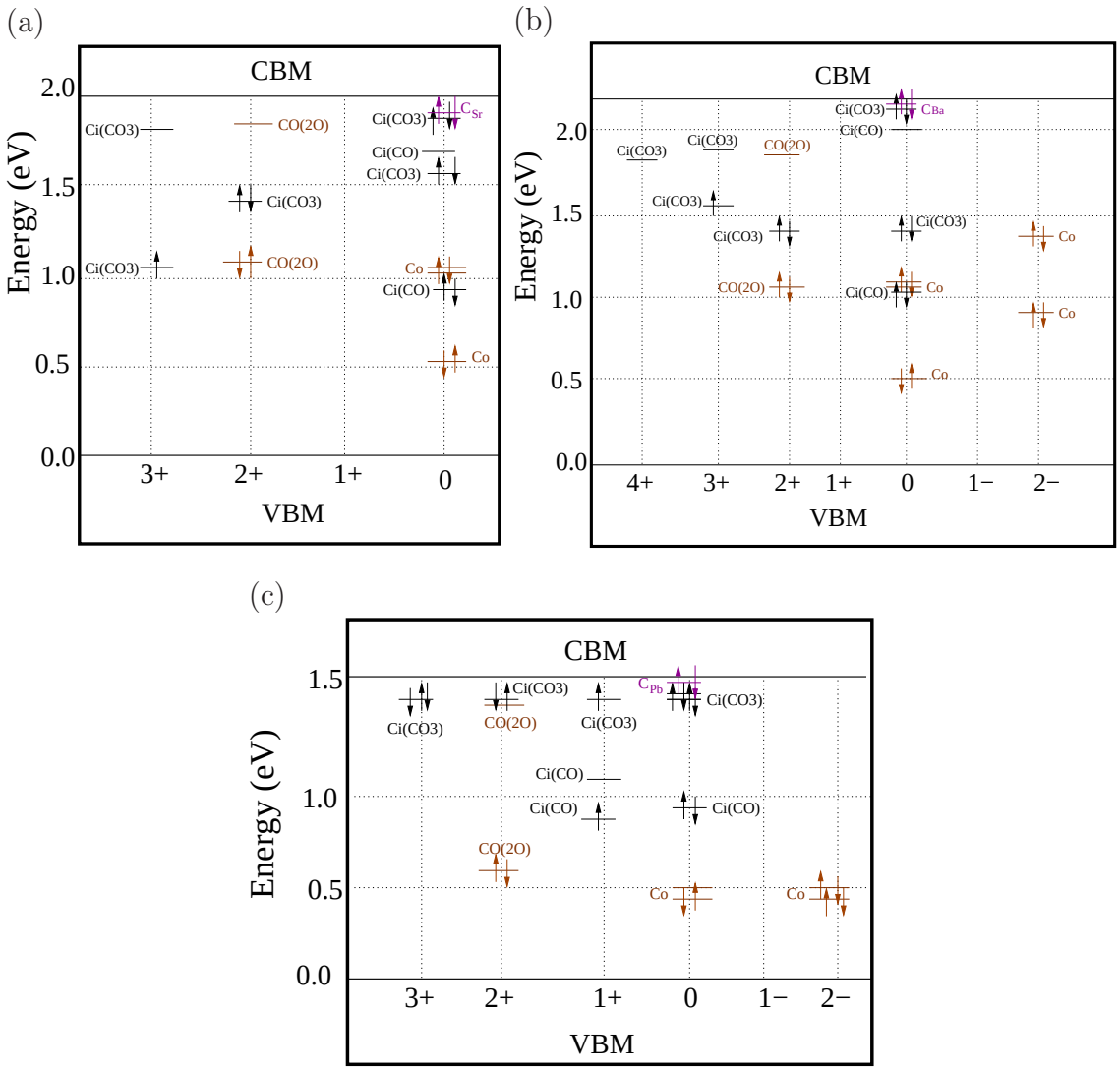

Figure 7.1: Diagram illustrating the location of gap-states at the Γ-point for C-containing defects in (a) $SrTiO_3$, (b) $BaTiO_3$ and (c) $PbTiO_3$. The valence band top is set at 0 eV.

ion replacing the isoelectronic TiO_3 group.

Finally, considering the range of available charge states determined for the three titanates, one must take care in making assumptions about those that may be present in other materials that have significantly different band-gaps. For example, the locations of the donor levels where substitution at the oxygen site results in the formation

of covalent bonds are roughly the same relative to the valence band for all of $SrTiO_3$, $BaTiO_3$ and $PbTiO_3$, although the $(+3/+4)$ transition in $PbTiO_3$ is closest to the valence band top. In similar structured materials with much larger band gaps, such as $BaZrO_3$, which is quoted as 5.3 eV [191], these higher charge states might logically be more important.

7.4 Carbonate group reorientation

Activation energy calculations have been performed to estimate the probability of carbonate group reorientation. The activation energy for carbonate group reorientation is predicted to be relatively high as a consequence of the covalent bonding within the carbonate group, so that reorientation involves the breaking and forming of strong chemical bonds. Such barriers, when combined with the fact that the defect has a permanent electric dipole, is anticipated to have an impact upon the dielectric properties and electrical-polarisation hysteresis of perovskite materials in an alternating electric field.

Several factors have been considered in attempting to identify the probability of carbonate group reorientation, such as the direction of the host dipole and the stability of the structures. For example, for carbon in the Ti site in $PbTiO_3$, several distinct orientations for the carbonate group have been considered. Hence, the reorientation energy has been calculated between the polar and anti-polar directions whereas for $SrTiO_3$ only one direction is needed because of the relatively higher crystal symmetry. The impact of orientational differences may be significant for perovskites which have large physical distortion, such as orthorhombic $CaTiO_3$.

In comparison, the reorientation barrier for the carbonate group in each perovskite ($SrTiO_3$, $BaTiO_3$ and $PbTiO_3$) is found to be comparatively high and similar on average, which can be understood as resulting from the breaking and formation of strong covalent C–O bonds [192] compared to, for example, diffusion of the oxygen vacancy [193]. Hence, it can be concluded that the activation energy for carbonate

group reorientation in a whole family of perovskite titanate or alloying perovskites such as $BaSrTiO_3$, $BaZrO_3$ and $PbZrTiO_3$ would be close in value to the activation energies in the ternary compounds.

Given the relatively high reorientation barrier, domain switching will be affected by these centres, and there is evidence that carbon is present in material currently employed in devices. For example, in lead zirconate titanate the infrared spectrum has peaks attributed to carbon-oxygen group vibrations, and hysteresis effects have been assigned to the carbon in the material [100].

7.5 Formation energy

Through a careful consideration of the chemical potential space of the constituent species, the relative stability of different carbon defects under various thermodynamic conditions has been assessed.

The corresponding formation energies suggest that in oxygen-rich conditions carbon substitution of Ti is generally more favourable for all three kinds of perovskites, as the carbon is in equilibrium with ACO_3. These defects are electrically inactive consisting of the carbonate ion replacing the isoelectric TiO_3 group.

For the *p*-type condition, unsurprisingly, electron-donating systems are favoured, such as C_A, which is consistent with the expectation that in oxygen-rich conditions metal substitution is favoured. For both $BaTiO_3$ and $PbTiO_3$, in *n*-type conditions there is a possibility of forming C_O in the negative charge state with the anion lying on-site.

In $BaTiO_3$, the calculations reveal that four carbon defects are expected to arise in equilibrium, which are C_{Ti}, C_i, C_{Ba} and C_O. It is noted that the presence of C_i in $BaTiO_3$ is in contrast with the case for $SrTiO_3$, where it is thermodynamically unstable, but it remains possible that such a centre might exist transiently during a carbon migration processes. Significantly, all stable C_{Ba}, C_{Ti} and C_i configurations are a form of a carbonate group.

In $PbTiO_3$, the story is quite different. The range of host chemical potentials where $PbTiO_3$ is thermodynamically stable is relatively small, and only carbon substitution of Ti is favourable, with the exception of extreme p-type, oxygen-lean conditions where carbon on the A-site in a positive charge state is possible.

7.6 Conclusion

Ferroelectric materials are valued in applications such as optoelectronics and high capacity computer memory cells. Several methods are used to grow perovskite crystals, and use of organic precursors leads to carbon contamination, as indicated by infrared bands attributed to carbon-oxygen bond vibrations and hysteresis effects.

A series of calculations of the carbon defect has been carried out to investigate the structural, electrical and electronic properties, vibrational modes and reorientation barriers of carbon defects in perovskite titanates. The calculations show that carbon defects have a qualitative impact upon perovskite properties. This effect is likely to be common for highly dielectric materials by affecting the ferroelectric and dielectric properties as well as the electrical conductivity.

Having reviewed the similarities and the differences of carbon impurity properties in the three perovskite titanates, the next chapter looks at another technologically important material that is used in various applications and particularly in photovoltaic devices.

Chapter 8

SO_2 impurity in cadmium telluride

Cadmium telluride,CdTe, is used in applications including photo-voltaic cells and particle detectors, and is known to be significantly impacted electrically by the presence of impurities, particularly of oxygen. Vibrational modes at 1096.78 and 1108.35 cm^{-1} have been variously assigned to oxygen-containing point defects, but most recently also to SO_2 molecules dissolved in the lattice. However, the precise structure and location of these centres, as well as the electrical properties of the defects, are yet to be determined. In this chapter, the results of density functional simulations of SO_2 in various locations in CdTe and comparison of the properties derived with experimental results are presented. It is proposed that the most plausible candidate for the vibrational centre is an interstitial species.

8.1 Introduction

CdTe is a technologically important II-VI compound semiconductor with a number of attractive properties. The room-temperature direct-bandgap of 1.5 eV, the high visible-spectrum optical absorption coefficient of $> 10^5\,cm^{-1}$, and the relatively low cost of fabrication lends CdTe to use in optoelectronic devices such as light emitting diodes [194], laser diodes [195], solar cells [196–198], and X- and gamma-ray detectors [199–201]. Impurities and structural defects have a significant impact upon the

characteristics of the material, and the determination of the properties of defects is critical to the manufacture of devices with the highest efficiency.

Perhaps the main issue in the fabrication of devices using CdTe is the difficulty in p-type doping. Although P, Au, As, and Li have been used with some success [202], it has proved difficult to obtain material with concentrations higher than around $6 \times 10^{16}\,\mathrm{cm}^{-3}$. For doping above this level, the electrical activity drops off sharply and hole mobility is reduced. The complexity in doping p-CdTe is due to strong compensation effects [203] as well as the low solubility of the usual dopant types [204].

Oxygen is a common impurity in CdTe, occurring in concentrations of around $10^{16}\,\mathrm{cm}^{-3}$ across a range of growth methods [205, 206]. Perhaps surprisingly, since it is isoelectronic with Te [207], oxygen can give rise to p-type conductivity [208], and its complexes with vacancies and hydrogen are of some significance in terms of electrical levels [209, 210].

In addition, for compound semiconductors, the incorporation of native defects such as vacancies (such as vacant Cd sites in CdTe, V_{Cd}) may occur, particularly when grown under conditions richer in one of the compound elements. V_{Cd} in CdTe is electrically active, having acceptor levels [211], and probably both acceptor and donor levels when complexed with other defects [202, 212–217]. These defects play a very important role in the electrical and optical properties of CdTe, and so the correct understanding of the nature and formation mechanisms of these defects is a critical step in the development of relevant technologies [218].

Experimentally, electrical, luminescent and vibrational-mode characteristics are important clues that provide detailed information about impurities. For vibration, isotope effects, polarisation, and the uniaxial stress response are helpful additions to vibrational frequency. Infrared spectroscopy, which yields information regarding vibrational modes involving a change in electric dipole, has delivered important information about defects in CdTe. In particular, vibrational modes related to oxygen impurities are prominent in both experimental [219,220] and theoretical studies [221,222]. Since O is lighter than Te, the substitution of Te by O ($\mathrm{O_{Te}}$) might be expected to

yield a high frequency local vibration mode (LVM). However, in practice, a peak at 349.8 cm^{-1} has been assigned to this centre, and this has been confirmed theoretically by first-principles calculations [221,222]. The relatively low frequency is an indication of the strength of the Cd-O bond, and the frequency is consistent with the phonon frequencies of bulk CdO [223].

More recently, low-temperature (5 K) sharp infrared (IR) peaks labelled ν_1 and ν_2 at 1096.78 and 1108.35 cm^{-1} respectively were initially attributed to LVMs associated with O_{Te}–V_{Cd} complexes [219]. The two modes are observed to merge into a single peak at around 1104 cm^{-1} [219] as the temperature increases towards 300K. Another pair of lines at 2198.7 and 2210.5 cm^{-1} have been assigned to the first overtones of these modes [219, 220]. However, first principles simulations [221, 222] show that O_{Te}–V_{Cd} has local modes much more in line with O_{Te} than with ν_1 and ν_2, and given agreement between experiments and theory in the case of the simpler O_{Te} centre, so that the assignment of the pair of peaks to the O_{Te}–V_{Cd} complex must be doubted.

Since the frequencies are high relative to the host phonons, an alternative source for ν_1 and ν_2 might involve species with a low mass. One suggestion was a hydrogen–oxygen complex, and it is well known that hydrogen can passivate acceptors in p-type CdTe [224, 225]. Hydrogen forms strong bonds with oxygen, and it is reasonable to expect H to be incorporated into CdTe together with oxygen [211]. In addition, vacancies in semiconductors are often good traps for hydrogen. However, there is no convincing assignment for ν_1 and ν_2 involving hydrogen [226]. An alternative explanation [227] is that the vibrational frequency of an O_2 molecule may be high enough to explain ν_1 and ν_2.

However, the clearest evidence for the chemical composition of the centre giving rise to ν_1 and ν_2 comes from isotopic splitting. Fourier-transform infrared (FTIR) absorption studies [1] of single crystal CdTe annealed in $CdSO_4$ vapour at 850 °C show spectra dominated by ν_1 and ν_2. In addition, weaker lines located at 1082.8, 1089.5, 1094.3, and 1101.1 cm^{-1} are observed. From the relative intensities and spectral shifts, it is argued that the weak modes are due to the natural abundances of sulphur iso-

topes: ^{32}S (95%), ^{33}S (0.75%), and ^{34}S (4.2%). Once the involvement of S has been established, the question remains as to how such high frequencies may be generated, and the model proposes that they are the asymmetric stretch modes of a sulphur-dioxide molecule or ion dissolved in the lattice. The temperature dependence of the modes, *viz.* the merging of the two peaks at room temperature, might be explained by the rapid reorientation of the SO_2 at this temperature so that the observed spectrum is due to the motional averaging of the defect. The presence of *two* oxygen atoms is less conclusive from the experiment, and the location of the sulphur-containing defect within the CdTe lattice is not known.

The main aims of the present study are to resolve the questions regarding the likely site of the SO_2 or related centre within the lattice, and reflect upon the possible mechanisms for motional averaging. To achieve these aims, first-principles calculations are used to determine the vibrational frequencies and reorientation energies for a range of candidates.

8.2 Computational Method

Density functional calculations [63] using the AIMPRO code [64, 65], have again been performed. All of the calculations were carried out using the LDA as described in chapter 2. Atoms are modelled using norm-conserving, separable pseudo-potentials [16] where the valance sets of Cd, Te, O, and S are $4d^{10}5s^2$, $5s^25p^4$, $2s^22p^4$ and $3s^23p^4$ respectively, and the Kohn-Sham eigen-functions are expanded using atom-centred Gaussian basis-functions [66]. The basis consists of independent sets of s- and p-type functions of four widths, with 2 sets of d-type polarisation functions per S atom and 4 sets for all others. Matrix elements of the Hamiltonian are determined using a plane-wave expansion of the density and Kohn-Sham potential [67] with a cutoff of 150 Ha, resulting in convergence of the total energy with respect to the expansion of the charge density to within around 10 meV.

As with previous calculations, structures are optimised using a conjugate gradients

scheme (see section 3.1), with the optimised structures having forces on atoms of $< 10^{-3}$ atomic units, and the final structural optimisation step is required to result in a reduction in the total energy of less than 10^{-5} Ha.

For bulk CdTe, the computational approach yields an equilibrium lattice parameter of 6.44 Å, within 1% of experimental results [228]. The calculated band-gap of CdTe is 0.6 eV, reflecting the underestimate arising from the underpinning methodology, which is consistent with previous calculations [229].

Defects are modelled using the supercell approximation explained in section 2.5, using simple cubic cells with a side length of either $2a_0$ or $3a_0$, containing 64 and 216 host atoms respectively. Generally the Brillouin zone is sampled using a uniform $2 \times 2 \times 2$ Monkhorst-Pack mesh [14].

Vibrational modes were calculated by obtaining the second derivatives of the energy with respect to atomic positions, assembling the dynamical matrix (see section 3.2), and diagonalising to obtain the vibrational frequencies and normal coordinates. The second derivatives are obtained by a finite difference approximation in the forces, where atoms are displaced from their equilibrium positions by 0.2 atomic units. From the present calculations it is found that frequencies depend only weakly ($< 3\,\mathrm{cm}^{-1}$) upon the cell size, sampling, and on which atoms are included in the dynamical matrix.

Isotopic effects in the vibrational spectra have also been established. In each case the vibrational modes have been determined, including all radio-stable isotopes of S and O (31.972071, 32.971458, 33.967867, and 35.967081 amu, with natural abundances of 94.93%, 0.76%, 4.29% and 0.02% respectively [230] for S, and 15.99492, 16.99913, and 17.99916 amu with abundances of 99.757%, 0.038%, and 0.205% respectively [230] for O). From the calculated frequencies, the model spectra have been constructed by combining Gaussian-broadened peaks of areas proportional to the natural abundance of each isotopic combination to allow for qualitative comparison with the experimental data. These spectra do not explicitly take the oscillator strength into account, but the low symmetry of the defects involved means that all modes are *in principle*

infrared and Raman active. Given that the oscillator strength is likely to be only very weakly dependent upon isotopes, the relative areas of peaks presented as described here are a reasonable approximation for corresponding infrared absorption peak areas. Comparisons between different defect centres and/or different vibrational modes cannot be considered in a quantitative fashion.

Formation energies are calculated using Eq. 3.9, where values of μ_i are the atomic chemical potentials for Cd and Te. μ_{Cd} and μ_{Te} are related through $E(\mathrm{CdTe}) = \mu_{\mathrm{Cd}} + \mu_{\mathrm{Te}}$, where $E(\mathrm{CdTe})$ is the total energy per formula unit of pure CdTe. At one limit, μ_{Cd} is the energy per atom of Cd metal, and at the other μ_{Te} is defined as the energy per atom in hexagonal Te. The enthalpy of formation of CdTe is $\Delta H_{\mathrm{CdTe}} = E(\mathrm{CdTe}) - \mu_{\mathrm{Cd}} - \mu_{\mathrm{Te}}$. The heat of formation for CdTe is calculated in this way to be -0.94 eV, which is in reasonable agreement with the theoretical value [202] of -7.9 eV and the experimental [231] value of -9.6 eV.

Finally, for activation energies, the climbing nudged elastic band (NEB) method has been used (see section 3.6). In each case the convergence of the saddle point energy with respect to image forces and the number of images has been established. For graphical presentation, the reaction co-ordinate is the sum of the displacements between images, with the zero located at the saddle point. As such, the reaction co-ordinate yields a semi-quantitative measure of the barrier widths in addition to heights.

8.3 Results and discussion

A number of configurations of SO_2 in CdTe have been simulated, substituting on both sub-lattices, and inserted as an interstice. In the following sections the geometry, energetics, vibrational properties and, where relevant, reorientational barriers are presented.

Firstly, to put the defect calculations into context, the properties of the free SO_2 molecule and its related ions are presented.

8.3.1 SO_2 molecule

SO_2^0 is a non-linear molecule with bond-angle and length as indicated in Table 8.1. In the gas-phase, the IR spectrum exhibits peaks at 1151, 1362, and 518 cm^{-1}, corresponding to the symmetric stretch, anti-symmetric stretch and scissor modes respectively.

Table 8.1: Bond lengths (d, Å) and ∠OSO angles (θ, degrees) for various charge states of SO_2, symmetric and anti-symmetric stretch modes (cm^{-1}), ν_s and ν_a, and scissor mode, ν_b. Experimental values are taken from published studies [232–234].

Properties	SO_2^{-2}	SO_2^{-}	SO_2^{0}	SO_2^{+}	SO_2^{+2}
			Calculated		
d	1.60	1.50	1.43	1.42	1.40
θ	111	115	121	135	180
ν_a	895	1147	1389	1369	1565
ν_s	854	1018	1159	1099	1092
ν_b	406	452	510	423	303
			Experiment		
d	-	1.52	1.43	1.42	-
θ	-	116	120	132	-
ν_a	-	1042	1362	-	-
ν_s	-	985	1151	-	-
ν_b	-	496	518	-	-

To simulate a single SO_2 molecule, a simple-cubic supercell has been used where the side-length is chosen to converge the derived quantities. The calculated structure and vibrational frequencies are listed in Table 8.1. The values of bond-length, angle and stretch mode frequency for SO_2^0 and SO_2^- are in excellent agreement with exper-

imental data, as is the structure of SO_2^+. From the calculations it is concluded that the structure and vibrational properties of SO_2 are captured using the methodology adopted for this study.

The potential for SO_2 to become ionised is clearly of importance for solution in an ionic solid. Since SO_2^{-2} is isoelectronic with Te ions in the lattice, substitution for Te is plausible, and this form is considered next.

8.3.2 SO_2 substituting for Te

The relaxed structure, shown schematically in Fig. 8.1(b), indicates that the placement of SO_2 on a Te site $(SO_2)_{Te}$ displaces the neighbouring material slightly outwards. The configuration has the oxygen atoms co-ordinated with two of the four Cd neighbours, with the remaining two Cd neighbours co-ordinating with the sulphur. One might then describe this centre as substitutional S on a Te site having trapped two interstitial oxygen impurities in puckered bond-centred structures. The S–O bond lengths are calculated at 1.53 Å, Table 8.2, close to that in the free anion and considerably larger than the neutral or positively charged species. The O–S–O bond-angle at 105° is considerably smaller than that in a free molecule or ions [232], and therefore $(SO_2)_{Te}$ should probably not be categorised as SO_2^{-2} at a Te site.

By calculating the charge-dependent formation-energy as a function of μ_e, the current calculations show that $(SO_2)_{Te}$ is thermodynamically stable only as a neutral charge state. The structure in Fig. 8.1(b) shows one of twelve possible orientations of neutral $(SO_2)_{Te}$. This defect may be able to reorient between these orientations, and thereby provide a mechanism for the observed temperature dependence of the IR. One process alters the orientation without changing the oxygen co-ordination or crystallographic mirror plane, resulting in a geometry resembling that in Fig. 8.1(b) after a reflection in the (110) plane containing the S-atom. From the current calculations it is found that this process is activated by a little more than 0.3 eV, which is the barrier indicated by circles in Fig. 8.2.

A second process involves a change in the Cd-O bonding, so that the system begins

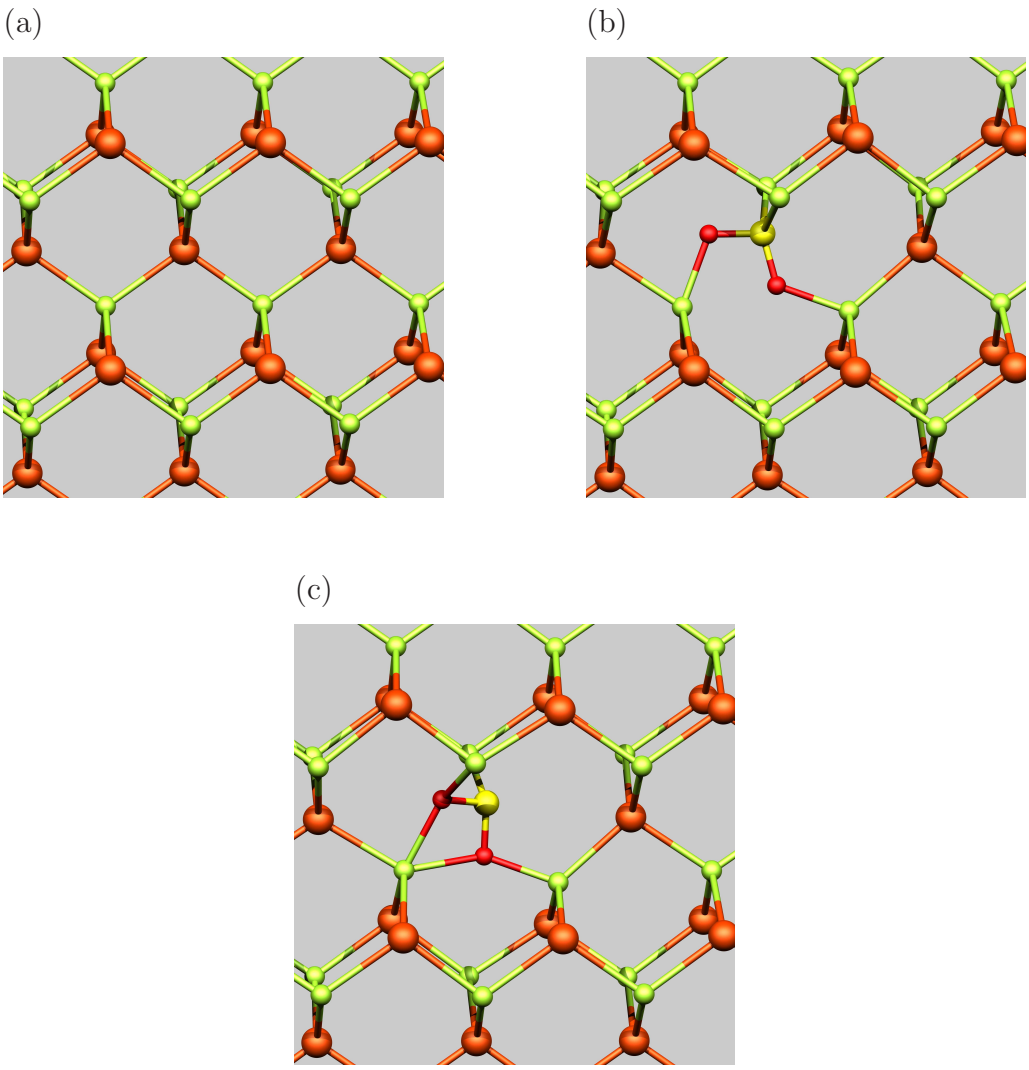

Figure 8.1: Schematic of (a) bulk CdTe, and (b) and (c) two configurations of $(SO_2)_{Te}$ in the neutral charge state. Orange and green spheres represent Te and Cd respectively, with small red and yellow spheres indicating O and S. Vertical and horizontal axes are approximately [001] and [110] respectively, with the tilted view adopted to aid clarity.

with the $(1\bar{1}0)$ mirror plane shown in the figure and ends with the structure with a $(10\bar{1})$ or $(0\bar{1}1)$ mirror plane. This reorientation involves an intermediate, metastable structure shown in Fig. 8.1(c). This structure is just 150 meV higher in energy than the lowest energy geometry and is characterised by three-fold co-ordinated oxygen atoms.

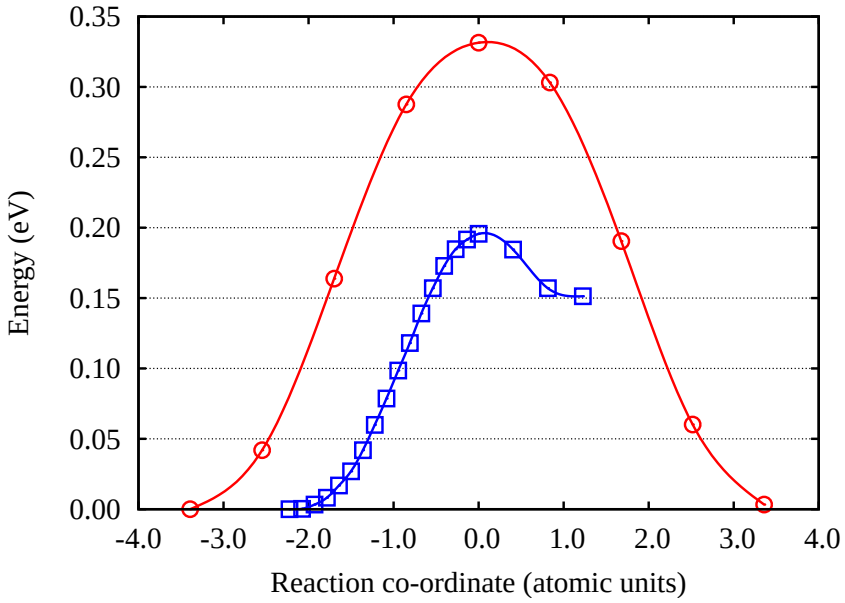

Figure 8.2: Reorientation barrier for $(SO_2)_{Te}$ in CdTe. The circles show reorientation without a change in O–Cd co-ordination within the (110) plane of the structure in Fig 8.1(b). The squares show the activation for the formation of the structure shown in Fig. 8.1(c), representing the mid-point in a reorientation step resulting in a change of mirror plane.

The barrier to reorientation is found to be close to 0.2 eV (shown by the squares in Fig. 8.2). This process is necessary but insufficient to access all twelve orientations, and a combination of both this and the first process is required.

Based upon the structures of the $(SO_2)_{Te}$ complex, one might expect at least two local modes, loosely corresponding to symmetric and antisymmetric stretch modes of SO_2, which for a free molecule are 1362 and 1151 cm^{-1} respectively (Table 8.1). The calculated vibrational modes for $(SO_2)_{Te}$ are listed in Table 8.3, but the values of 889 and 944 cm^{-1} are far from the measured values [1, 220].

Given the significance of the isotopes in the identification of the chemical make-up of the vibrational centre, the shifts with isotopic mass have been determined. Model spectra are shown in figure 8.3, noting that these are effectively vibrational

Table 8.2: S–O bond-lengths (d, Å) and O–S–O bond-angles (θ, degrees) for the four configurations of SO_2 in CdTe in the various stable charge states, Q.

	Q	d	θ
$(SO_2)_{Te}$	0	1.53	105
$(SO_2)_{Cd}$	0	1.48	110
$(SO_2)_{Cd}$	-1	1.47	114
$(SO_2)_{Cd}$	-2	1.47	115
$(SO_2)_{CdTe}$	0	1.46	116
$(SO_2)_{CdTe}$	-1	1.50	109
$(SO_2)_{CdTe}$	-2	1.52	105
$(SO_2)_i$	0	1.48	113

densities of states rather than absorption spectra, since the oscillator strengths are not included. However, since the vibrational modes are IR-active, at least in principle, and since the oscillator strengths are only very weakly dependent upon the oscillator mass, the relative areas in each plot, as well as the spectral splittings, may be viewed as being of a quantitative value. Comparison between the areas under the peaks of different vibrational modes should not be made, as they may have significantly different oscillator strengths.

Additionally, the splittings between the experimental modes are included in figure 8.3, with the highest frequency experimental mode shifted down in frequency to align with the highest frequency calculated mode. It should be noted that, qualitatively, the patterns of modes with isotopic mixtures follow those from experiment, but the calculated splittings are quantitatively in poor agreement with those measured.

Additionally, note that the modes calculated for the metastable structure shown in Fig. 8.1(c) are similarly low at 853 and 834 cm^{-1} in comparison to the experimental values.

Based upon the current simulations for the vibrational properties, it seems unlikely

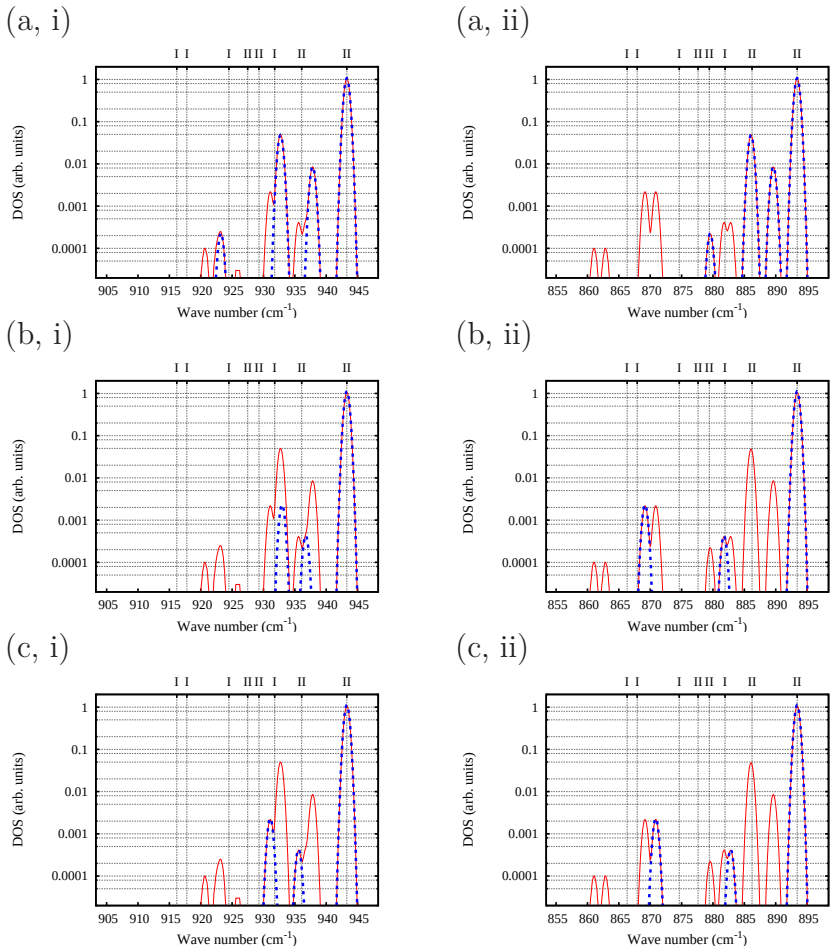

Figure 8.3: Model vibrational spectrum for $(SO_2)_{Te}$ with a Gaussian-broadening of $0.5\,cm^{-1}$. The solid line shows the spectrum including the four S and three O isotopes, and the dashed line that where only the following masses are varied: (a) S, (b) the oxygen approximately along $[00\bar{1}]$ from S in Fig. 8.1(b), and (c) the oxygen approximately along $[\bar{1}\bar{1}0]$ from S. In each case, the labels i and ii indicate the higher and lower frequency combinations of S–O stretch-modes. The vertical lines labelled I and II indicate the relative positions of the experimental vibrational frequencies from the I and II sets [1], aligned to the highest calculated frequencies of $(SO_2)_{Te}$, as described in the text.

that $(SO_2)_{Te}$ is responsible for the experimental observations, but would be expected to give rise to vibrational modes at a significantly lower frequency.

8.3.3 SO_2 substituting for Cd

An alternative location for SO_2, especially in Cd-lean or Te-rich material, would be SO_2 substituting for Cd, $(SO_2)_{Cd}$, where SO_2 might possibly be expected to adopt a positive charge state.

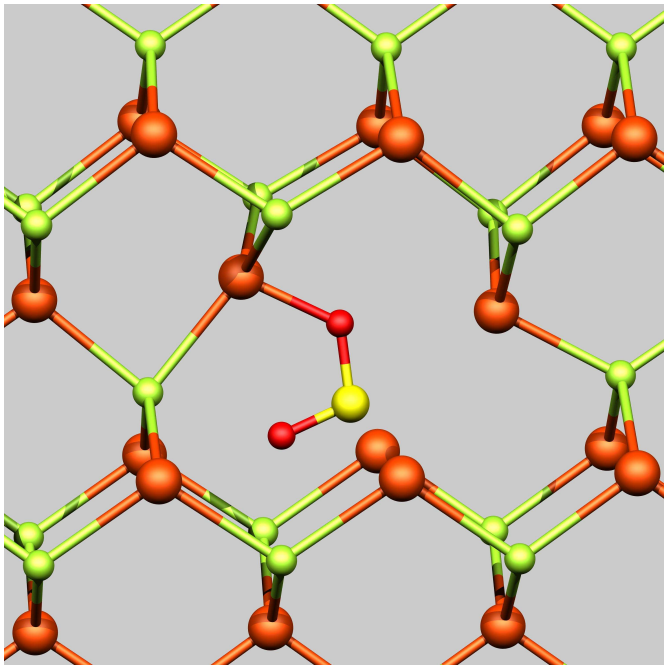

Figure 8.4: Schematic of $(SO_2)_{Cd}$ in CdTe. Colours and orientation are as indicated in Fig. 8.1.

Previous calculations have suggested that V_{Cd} is an important intrinsic acceptor, retaining the T_d site symmetry [211, 216, 235]. Since V_{Cd} is a double acceptor, a simplistic assumption for $(SO_2)_{Cd}$ might be the formation of a V_{Cd}^{-2}–SO_2^{+2} complex. A schematic of the structure obtained is shown in Fig. 8.4. SO_2 is associated with one of the nearest Te neighbours, and there is a distortion involving the outward movement of the other Te neighbours. Noting that SO_2^{+2} is expected to be linear, it is clear

$(SO_2)_{Cd}$ is not V_{Cd}^{-2}–SO_2^{+2}. Instead, in the neutral charge state, there are empty states toward the top of the band-gap, suggesting that the SO_2 is effectively a neutral or negatively charged molecule. Indeed, the bond-length and angle of SO_2 are closer to those of SO_2^- or SO_2^{-2} than the neutral or positively charged varieties (Tables 8.1 and 8.2).

The charge dependent formation energies have been calculated for $(SO_2)_{Cd}$, which suggests that the 0 and -2 charge states are thermodynamically stable, as shown in Fig. 8.5. This is consistent with the complex being a perturbed V_{Cd}. The gap levels would mean that such complexes would compensate shallow donors, but would be unlikely to contribute to p-type conductivity.

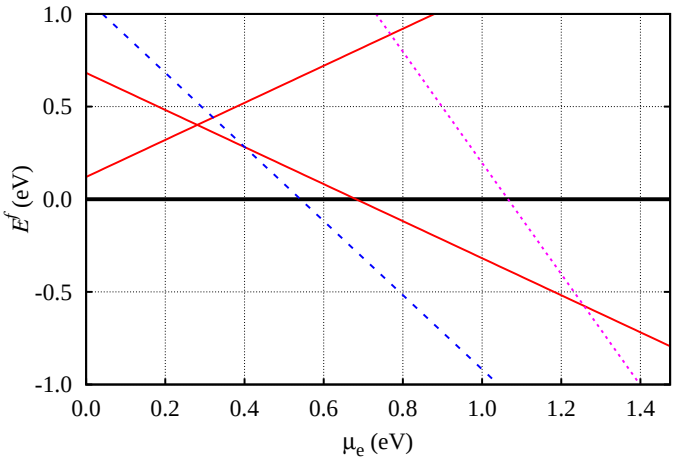

Figure 8.5: Plot of E^f as a function of μ_e for $(SO_2)_{Cd}$. E^f is defined as zero for the neutral charge state. Solid, dashed, and dotted lines are for the single, double and triple charge states respectively, with the sign of the slope indicating the sign of the charge state.

Just as with $(SO_2)_{Te}$, $(SO_2)_{Cd}$ can reorient. In the neutral charge state, reorientation occurs around the O–Te bond with a barrier of 0.55 eV. Motion of this sort might lead to an average C_{3v} symmetry. Amongst numerous reorientation paths that result in the SO_2 molecule bonded to a different Te-site, the lowest barrier found was 0.77 eV.

Table 8.3: Vibrational modes (cm^{-1}) of SO_2 with different charge states (Q) and sites. Values here are taken from the Γ-point approximation calculations and the 216 atom supercell. Experimental values [219, 220] were observed to be 1096.8 and 1108.4 cm^{-1}, for comparison.

	Q	ν_1	ν_2
$(SO_2)_{Te}$	0	889	944
$(SO_2)_{Cd}$	0	709	1069
$(SO_2)_{Cd}$	−2	867	972
$(SO_2)_{CdTe}$	−1	962	1051
$(SO_2)_{CdTe}$	−2	823	902
$(SO_2)_{i}$	0	991	1123

The vibration modes for $(SO_2)_{Cd}$ have been calculated for the two thermodynamically stable charge states. The key results are listed in Table 8.3 and there is some agreement with the experimental modes. The upper mode primarily involves the O atom bonded to the Te site, whereas the lower frequency mode is more associated with the "free" oxygen site. Examination of the isotopic splittings is inconclusive. What seems clear, however, is that for $(SO_2)^0_{Cd}$ to be responsible for the experimental modes, one could not associate the various lines with the symmetric and antisymmetric modes of SO_2.

Based upon the available energetic barrier, there is no clear support for a $(SO_2)_{Cd}$ model for the experimentally observed centre.

8.3.4 SO_2 substituting for a Cd–Te pair

The third model to considers is comprised of the substitution of a Cd–Te pair by the SO_2 molecule, $(SO_2)_{CdTe}$. The most stable form of this system that has been found is depicted in Fig. 8.6, with the O-atoms co-ordinated with neighbouring Cd atoms.

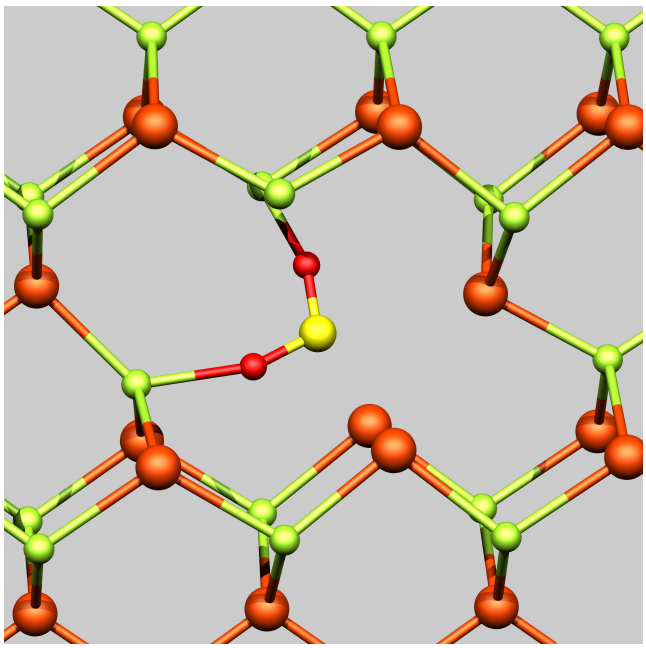

Figure 8.6: Schematic of $(SO_2)_{CdTe}$ in CdTe in the neutral charge state. Colours and orientation are as indicated in Fig. 8.1.

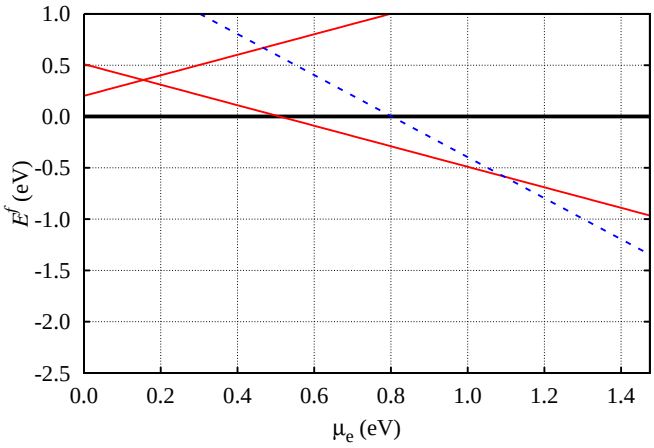

Figure 8.7: Plot of E^f as a function of μ_e for $(SO_2)_{CdTe}$. E^f is defined as zero for the neutral charge state. Solid and dashed lines are for the single and double charge states respectively, with the sign of the slope indicating the sign of the charge state.

Since a pair of vacancies is in principle an iso-electronic defect, $(SO_2)_{CdTe}$ might be expected to be iso-electronic, with the SO_2 system being a neutral molecule.

However, the similarity in structure in the vicinity of the Te-site to $(SO_2)_{Te}$ suggests that in practice $(SO_2)_{CdTe}$ is a $(SO_2)_{Te}$–V_{Cd} complex. By comparing the SO_2 bond-lengths and bond angle with gas-phase SO_2, for the overall neutral charge state the structure fits most closely with a negatively charged ion. This is consistent with the formation of a SO_2^{-2} ion at a Te site, but the band structure does not suggest any deep acceptor states associated with this structure.

The neutral charge state of $(SO_2)_{CdTe}$ has been found to be stable, with potentially -1 and -2 charge states also possible (Fig. 8.7). However, the underestimate of the band-gap must cast the location of these acceptor levels in some doubt, and although an empty defect state exists, it lies above the theoretical conduction band minimum.

Vibrational modes for $(SO_2)_{CdTe}$ have been calculated, with the values determined indicated in Table 8.3. From the calculations it is found that the single and double negative charge states have pairs of modes around 962 and 1051 cm^{-1}, 823 and 902 cm^{-1} respectively, whereas the vibrational modes for the neutral charge state are 921 and 1177 cm^{-1}. The values for the single negative charge state lie closer to the experimental bands than do those for the double charge state, but it is not possible to be conclusive purely on the basis of these calculations.

8.3.5 Interstitial SO_2

Finally, the possibility for SO_2 to lie in an interstitial site,$(SO_2)_i$, has also been examined. SO_2 has been relaxed starting from a wide range of initial structures, including non-bonded structures in cage sites with both sub-lattice species as well as bond-centred configurations. The results suggest that a bond-centred arrangement would be energetically preferred, with the structure as depicted schematically in Fig. 8.8. To accommodate the interstitial molecule, the nearest neighbour host sites are displaced significantly, so that the distance between the S and Cd(Te) nucleii is 2.57 Å(2.55 Å). The Cd–S distance agrees with the bond length of bulk CdS (2.53 Å) [236] .

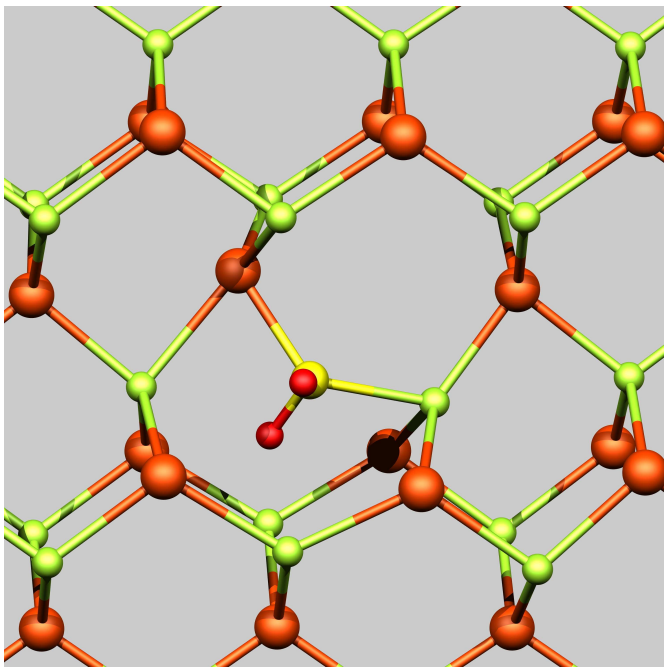

Figure 8.8: Schematic of $(SO_2)_i$ in CdTe. Colours and orientation are as indicated in Fig. 8.1.

The charge state dependent formation energies for $(SO_2)_i$ in CdTe are presented in Fig. 8.9. They suggest that $(SO_2)_i$ is an isoelectronic defect with only the neutral charge state being stable.

For this centre, the reorientation barrier has been determined, consisting of a precession about the [111] axis of the Cd–Te bond into which the SO_2 molecule has been inserted. A full step involves a swing of 120°, which has two parts. Defining the direction in which SO_2 is aligned at any time by the direction bisecting the O–S–O bond angle, the two parts can be understood as follows. Viewed along the [111] axis, the arrangement of the three Te and three Cd atoms back-bonded to the Cd–Te bond in which the SO_2 sits, the 360° can be divided into six 60° sectors. The two barriers are shown in Fig. 8.10, with the rate limiting step being around 0.35 eV.

Partial reorientation by alternating between neighbouring structures, but only overcoming the smaller energy barrier, would lead to a motionally averaged symmetry of C_s, whereas a complete precession raises the effective symmetry to C_{3v}. The barriers

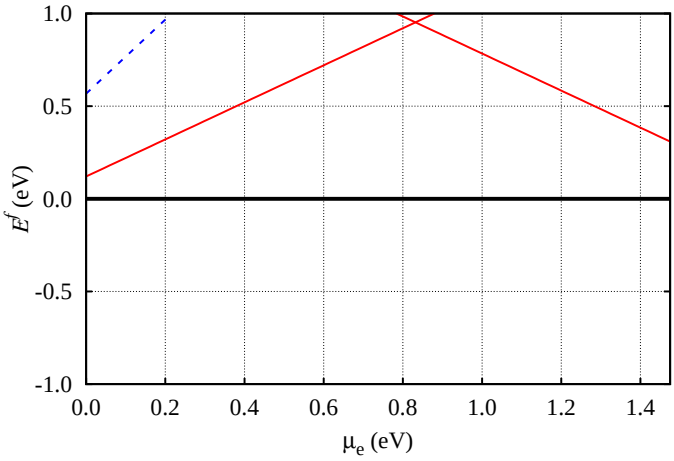

Figure 8.9: Plot of E^f as a function of μ_e for $(SO_2)_i$. E^f is defined as zero for the neutral charge state. Solid and dashed lines are for the single and double charge states respectively, with the sign of the slope indicating the sign of the charge state.

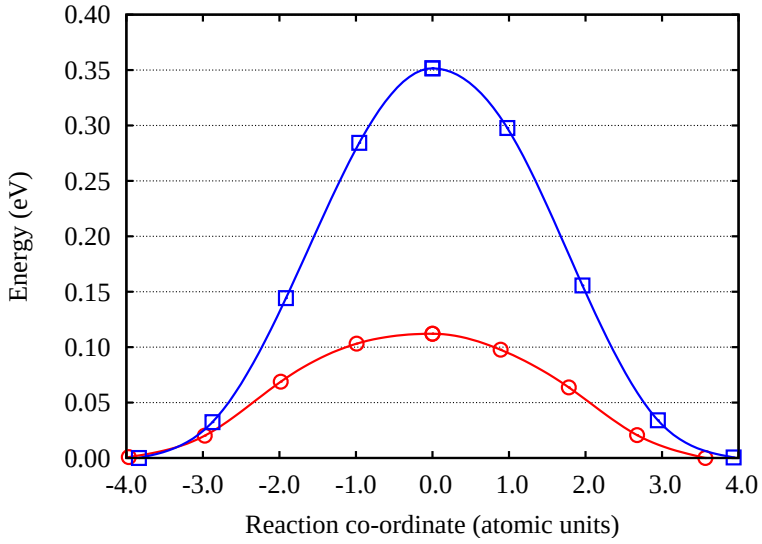

Figure 8.10: NEB calculated reorientation barrier for $(SO_2)_i$ in CdTe. Circles and squares show the two directions of rotation.

of around 0.10 and 0.35 eV would be easily overcome at room temperature, but not at cryogenic temperatures, consistent with the observed temperature dependence of the IR peaks.

From results it is found that there are two LVMs, calculated to lie at 991 and 1123 cm^{-1}, which is in broad agreement with the experimental observations. The isotopic shifts of sulphur and oxygen with S and O are also in broad agreement with experiment, and the calculated shifts are negligible ($\ll 1\,\mathrm{cm}^{-1}$) where the isotope of either the Te or Cd neighbour is varied.

A combination of these vibrational properties with the potential for motional effects and the electrical inactivity of the defect suggest that interstitial SO_2 may be responsible for the experimentally observed vibrational modes.

However, it remains to be determined whether such a form is energetically viable in comparison to other sites.

8.3.6 Formation energy comparison

Having reviewed the structure, energetics, and vibrational frequencies of the individual candidates examined in this study, it is now possible to compare them, and to critically analyse which, if any, is the best model for the vibrational system observed in experiments. Perhaps the most important question concerns which one of these defects is most energetically stable. The formation energies as a function of the chemical potential of Cd (μ_{Cd}) for the four systems in the neutral charge state have been calculated, as shown in Fig. 8.12(a), where the systems are also taken to be in equilibrium with SO_2 gas. The calculations indicate that $(SO_2)_{\mathrm{Te}}$ is the more stable defect at both limits in both p-type and intrinsic conditions. However, the second most likely defect to occur is $(SO_2)_i$ with an energy difference of about 0.2 eV in Te-rich conditions (see Fig. 8.12(a) and (b)). The formation energy of $(SO_2)_{\mathrm{Cd}}$ is higher than that for other sites, even in Cd-lean conditions where its formation energy is lowest. There are no conditions where either $(SO_2)_i$ or $(SO_2)_{\mathrm{CdTe}}$ are favoured energetically.

In n-type conditions, $(SO_2)_{\mathrm{Te}}$ is more stable than the other defects in Cd-rich

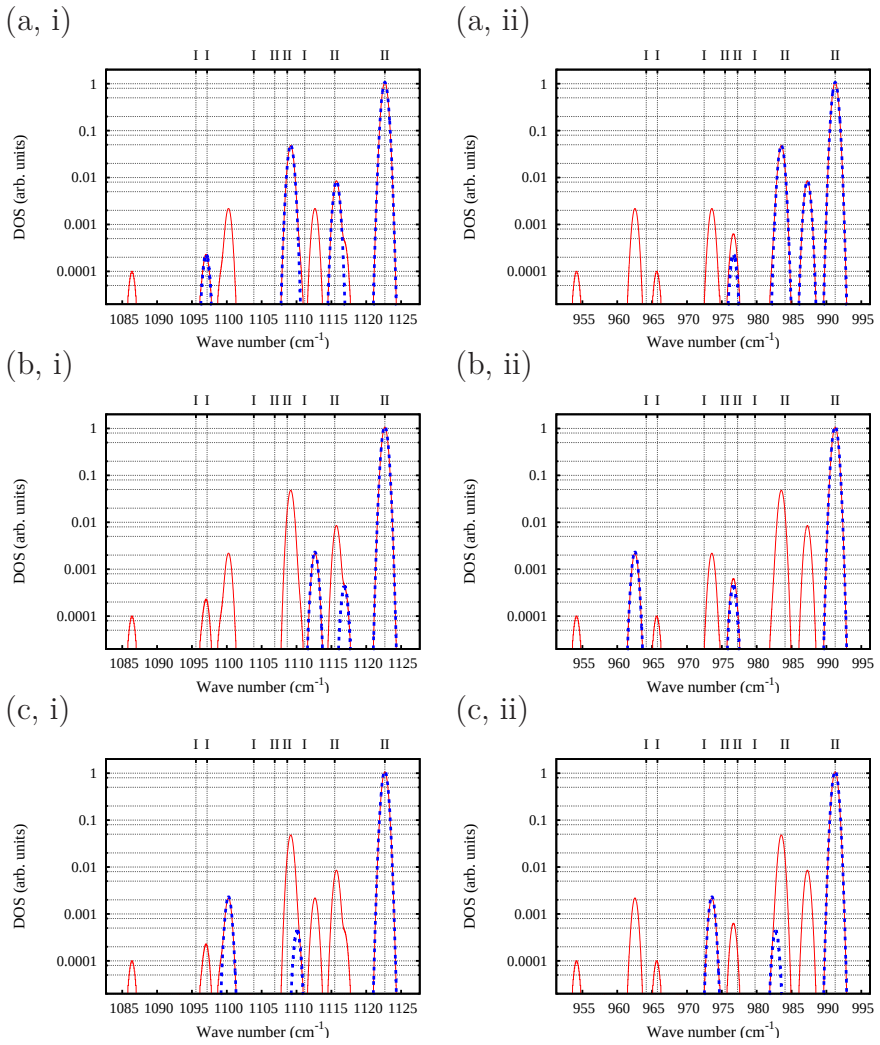

Figure 8.11: Model vibrational spectrum for $(SO_2)_i$ with a Gaussian-broadening of $0.5\,cm^{-1}$. The solid line shows the spectrum, including the four S and three O isotopes, and the dashed line that where only the following masses are varied: (a) S, (b) the oxygen below S in Fig. 8.8, and (c) the oxygen approximately out of the page from S. In each case, the labels i and ii indicate the higher and lower frequency combinations of S–O stretch-modes. The vertical lines labelled I and II indicate the relative positions of the experimental vibrational frequencies from the I and II sets [1], aligned to the highest calculated frequencies of $(SO_2)_i$, as described in the text.

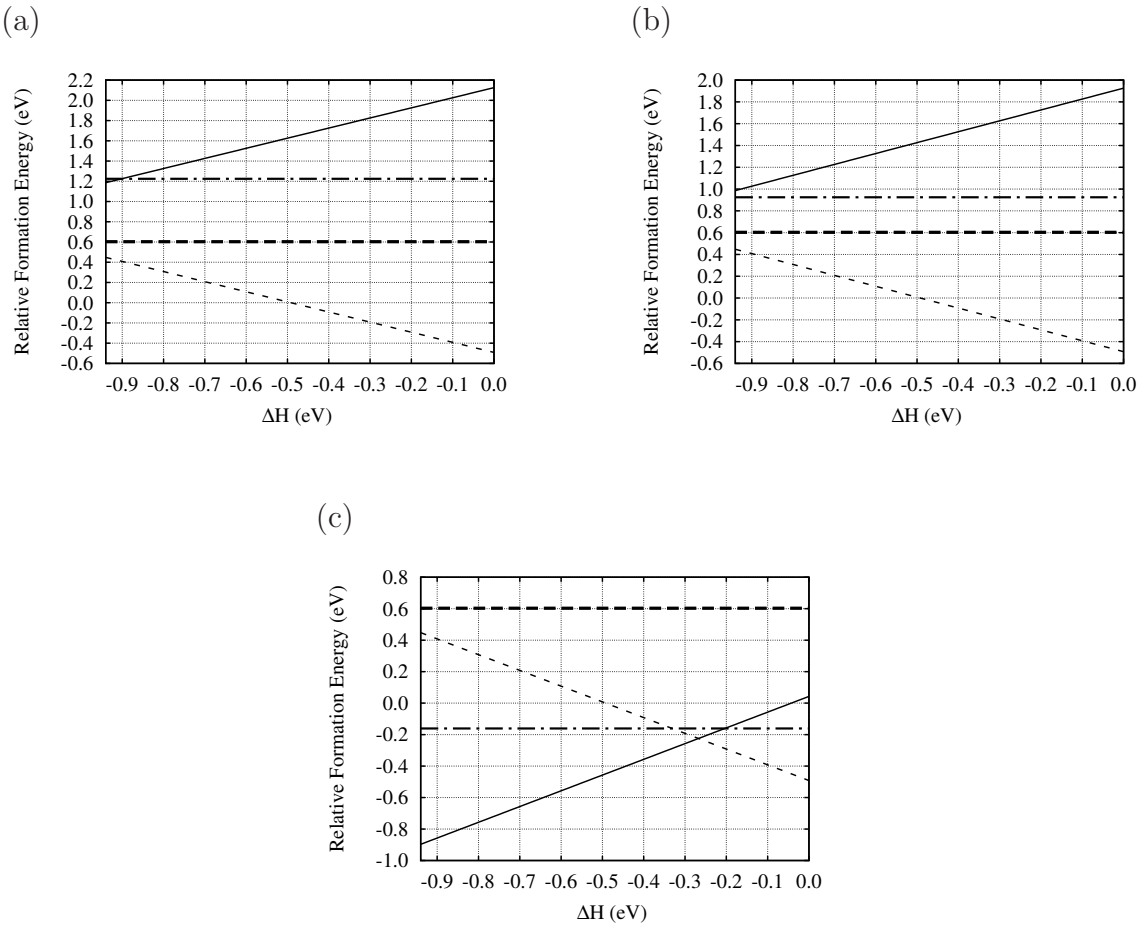

Figure 8.12: Plots of E_f as a function of μ_{Cd} for the various SO_2 defects in CdTe. In each case the solid, dotted, dashed, and dot-dashed line refer to $(SO_2)_{\mathrm{Cd}}$, $(SO_2)_{\mathrm{Te}}$, $(SO_2)_i$ and $(SO_2)_{\mathrm{CdTe}}$ respectively. (a) shows the plot for the neutral charge state of in each case and also the equilibrium charge states with $\mu_e = E_v$. (b) and (c) show the plots for the equilibrium charge states with $\mu_e = (E_c + E_v)/2$, and $\mu_e = E_c$ respectively.

conditions, whereas $(SO_2)_{\mathrm{Cd}}$ is the favourite structure with a -2 charge state in Te-rich conditions.

In practice, as-grown CdTe is often p-type as a result of O-contamination. In such material, it is Fig. 8.12(a) that the most relevant, and the expectation is that SO_2 at the Te and interstitial sites are most relevant. Both forms are predicted to be electri-

cally inactive, and therefore will only be expected to impact device material through changes to the mobility. Similarly, in CdTe where V_{Cd} is the dominant electrically active defect (V_{Cd} is a deep acceptor), the CdTe is semi-insulating and most closely resembles the intrinsic material formation energies, shown in Fig. 8.12(b). Again, the dominant defects are the electrically inactive forms at the Te and interstitial sites. However, in strong contrast, deliberately n-type material is expected to drive the formation of SO_2 at the Cd site in Cd-lean conditions, with this deep acceptor compensating the donors.

Based on the current calculations, CdTe might be unstable due to the resulting negative formation energies, particularly in n-type conditions, which suggests that the SO_2 could be incorporated in CdTe if the available concentration is high.

It should be noted, however, that the energy differences are very modest.

8.4 Conclusion

Using first principles density functional theory, the structural configurations, transition energy levels and vibrational modes of SO_2 defects in CdTe have been studied. The present calculations show that the incorporation of SO_2 in the CdTe material displaces the neighbouring atoms outward.

Formation energies as a function of electron chemical potential have been determined. It is found that both $(SO_2)_{\mathrm{Te}}$ and $(SO_2)_i$ are iso-electric defects, whereas $(SO_2)_{\mathrm{Cd}}$ and $(SO_2)_{\mathrm{CdTe}}$ could be electrically active by adding acceptor levels to the band gap.

The formation energies as a function of μ_{Cd} have been estimated in order to identify which structure is more stable under equilibrium conditions. The current work has revealed that $(SO_2)_{\mathrm{Te}}$ is the most thermodynamically stable defect under p-type conditions. The second most stable candidate defect in these growth conditions is $(SO_2)_i$. As the electron chemical potential moves from the valance to the conduction bands, there is an opportunity for SO_2 to be electrically active by forming an $(SO_2)_{\mathrm{Cd}}$

defect.

The vibrational characteristic of the four defect centres have been investigated and used to interpret the two recently identified sharp IR absorption lines at 1097 and 1108 cm^{-1}. A summaries of the structural and expected local vibrational modes for each structure in the relevant charge states are presented in Tables 8.2 and 8.3. Isotopic effects in the vibrational spectra, including all isotopes of S and O with natural abundances, have also been established.

Based on the current calculations, there are two defect centres which could be the reason for these two vibrational modes. $(SO_2)_{Te}$ has the lowest formation energy compared with the other sites. The absolute vibrational modes are significantly lower than the experimental data and the spectrum shift with isotopic mass does not correlate well with experimental data. Although the reorientation barrier is relatively small, the motional average is not obvious. The LVMs of the $(SO_2)_i$ centre is in broad agreement with experimental values, and the sulphur and oxygen isotopic shifts with S and O also agree with experimental measurements. An energetic barrier separates the metastable states, which gives rise to these two modes. Thus, when temperature increases, the rotational barrier can be overcome and only one line occurs in the IR absorption spectrum. However, the formation energy of this centre seems to be higher than that of the $(SO_2)_{Te}$ defect.

Part III

Conclusions

Chapter 9

Summary, Conclusions and Suggestions for Further Work

This chapter brings the thesis to a close and reflects on the various subjects considered. At the end of each application chapter, a separate conclusions section has been included. This presents a general summary of the main results.

9.1 Summary and conclusions

A body of work has been covered which focuses on the investigation and identification of the various properties of selected impurities which are present due to specific growth conditions in a range of technologically important materials, starting from those used in nano-applications and ending with photovoltaic application materials. In the context of this project, first principles density functional theory and the supercell approach, as implemented in the `AIMPRO` computer code have been employed.

The initial work focused on the study of the impact of carbon impurities on the high-κ perovskite titanate, including structural configurations, electronic properties, electrical levels, vibrational modes, ferroelectric properties and formation energies. Three promising perovskite titanates have been chosen for this study corresponding to their applications, starting with $SrTiO_3$ which is a perovskite oxide with a para-

electric cubic structure and is usually employed in nano-size devices such as transistor applications. Then, ferroelectric $PbTiO_3$ with a tetragonal ground state structure is considered, which is used to make nano-scale capacitors with tunable capacitance related to low operating voltage and high switching speed, and finally rhombohedral ground state $BaTiO_3$ is investigated according to its ferroelectric properties at room temperature and its lack of toxicity.

Nowadays, various types of perovskite can be grown using different techniques. However, carbon contamination is highly likely to occur as a result of organic species present during thin-film growth. Since the carbon defects potentially play a significant role in affecting the properties of perovskite oxides, several important results have been obtained.

Various structural configurations of carbon impurities in $SrTiO_3$, $PbTiO_3$ and $BaTiO_3$ have been investigated. Interstitial and substitutional point defects are considered and their relative stability in different charge states for each type of point defect. For the three perovskites, regardless of the structure of the host material, carbon prefers to form covalent bonds with the host oxygen-neighbour(s). The current study reveals that for carbon the formation of carbonate groups is energetically favoured for interstitial and both B and A site substitution. However, there is an opportunity for carbon to form CO in both C_i and $(CO)_{(2O)}$ and also to form CO_2 as a spontaneous reconstruction in the case of the $(CO_2)_{(3O)}$ defect.

The current work shows that carbon involved in the host material ($SrTiO_3$, $BaTiO_3$ and $PbTiO_3$) could be either electrically active, such as in the substitution of either A (Sr, Ba or Pb) or O, and as an interstice, or electrically passive which is the case with the iso-electric substitution of Ti.

Based upon the band structures and expected oxidation states, the electrical levels of the defect centres have been presented. In comparison, the results show that for C_i the CO_3 configuration in the +4 charge state in $SrTiO_3$ is an unstable centre with a slightly higher energy than the +3 charge state. With respect to the C_O on-site, in *n*-type conditions, it has been found that the −2 charge state is stable in both

$BaTiO_3$ and $PbTiO_3$. Finally, for carbon substitutions of the A site, the calculations show that the neutral charge state for CO_3 is energetically stable in both $SrTiO_3$ and $BaTiO_3$ but not in $PbTiO_3$. This disparity in the results might be related to the differences in the location of the valance band top in the defect system relative to that for bulk, and to the width of the band gap.

The highly characteristic local vibrational modes predicted for the different configurations provide a possible route to experimental validation. The estimated values show that the frequencies depend upon structure in a systematic way, depending in a straightforward way upon both bonding and charge state. It should be noted that the CO for the interstitial has a mode comparable in frequency to that of the CO_3 group for both $SrTiO_3$ and $PbTiO_3$. However, since the CO has only one local mode, such systems might still be distinguished experimentally by the absence of any correlated modes corresponding to the A and E related modes of CO_3. From the calculations it is conclude that the local vibrational frequencies offer a potential route to the discrimination between different sites.

The activation energy calculations have been estimated to identify the probability of carbonate group reorientation in perovskite titanate crystals. The activation energy for carbonate group reorientation is predicted to be relatively high as a consequence of the covalent bonding within the carbonate group, so that reorientation involves the breaking and forming of strong chemical bonds. Such a barrier, when combined with the fact that the defect has a permanent electric dipole, is anticipated to have an impact upon the dielectric properties and hysteresis of perovskite materials in an alternating electric field. Several factors have been considered in attempting to identify the carbonate group reorientation, such as crystal symmetry, the direction of the host dipole and the stability of the structures. For example, C_{Ti} in $SrTiO_3$ has an equivalent structure whereas in $PbTiO_3$ two non-equivalent structures have been distinguished. Since the distortion is small in $BaTiO_3$ and the energy per formula unit much smaller than the energy scales differentiating between the systems explored in this study, the various reorientations for the C_{Ti} defect related to symmetry have been

ignored. In comparison, the activation energy for each perovskite is relatively high and nearly similar on average; therefore, it can be concluded that the activation energy for a whole family of perovskite titanate such as $BaSrTiO_3$, $BaZrO_3$ and $PbZrTiO_3$ would be around these values.

Through a careful consideration of the chemical potential space of the constituent species, the relative stability of different point defects under various thermodynamic conditions has been assessed. The corresponding formation energies suggest that the carbon substitution of Ti is generally more favourable for all three kinds of perovskites; however, for *p*-type material the substitution of the A-site is also possible. Under O-lean conditions oxygen substitution becomes significant for both $SrTiO_3$ and $BaTiO_3$. In addition, the carbon interstitial has an opportunity to be energetically stable in $BaTiO_3$.

The second phase of the project dealt with SO_2 defects in CdTe crystal. The incorporation of SO_2 in CdTe material has been chosen as a subject for this study because of the recent experimentally observation of two low temperature (5K) sharp IR peaks at 1096.78 and 1108.35 cm^{-1}. As temperature increases towards 300K, these two modes merge together into a single peak. Another pair of lines at 2198.7 and 2210.5 cm^{-1} has been assigned to the first overtones of these modes. These modes have been attributed experimentally to LVMs of the SO_2 molecule or ion dissolved in the lattice. However, the precise structure and the location of these centres, as well as their electrical properties, of are yet to be determined. Thus, the key reason for this study is to resolve the question regarding the likely site of the SO_2 in the lattice and to reflect upon the possible mechanisms for motional averaging.

Numerous structures have been built to obtain the lowest energy structures for SO_2 defects in CdTe for each site. The charge-dependent formation energy as a function of electron chemical potential has been calculated. The present results reveal that SO_2 in both Cd and CdTe complex sites are electrically active defects which might have an impact in the photovoltaic applications where the control of *n*-type and *p*-type conductivity is needed.

Vibrational modes for each site have been estimated to identify which defect is responsible for the experimental frequencies. From current calculations it is found that the LVMs of $(SO_2)_i$ are in a good agreement with the experimental observation. However, based on the formation energy calculations, the most likely candidate will be SO_2 in the Te site, but the vibrational modes for this defect do not match well with experimental frequencies and it is difficult for these modes to match isotopic shifts. Both the interstitial and the Te sites have advantages. Under equilibrium conditions, the difference in formation energy between $(SO_2)_{Te}$ and $(SO_2)_i$ is relatively small in the p-type and intrinsic material in Te-lean conditions, and the mechanism of reorientation for $(SO_2)_i$ is more obvious than that for $(SO_2)_{Te}$. Therefore, it seems logical to expect that with temperature dependence the most plausible candidate for the vibrational centre is an interstitial species.

9.2 Further Work

A weakness of the current work is the dependence on LDA, which was regarded as state-of-the-art prior to 2005, new for these materials screened exchange (SX) [237–239] is regarded as best practice. One of the well established short comings of the underpinning theory used in many atomistic simulation packages is that density functional methods typically underestimate the electronic band-gap for both semiconductors and insulators. For example, the band-gap of silicon is underestimated by around 50% compared to experiments. The extension of the method to the SX approach is expected to largely eliminate this error and the evaluation of the resulting properties of defects in materials problems currently examined. Hence, there is need to re-examine current work with screen exchange, both looking for differences, but also to test the new implementation of SX in `AIMPRO`. It is crucial that the models proposed above are assessed using a quantitatively accurate approach, and these are important examples amongst the many defect centres that will receive the screened exchange treatment in the future.

In the case of perovskite titanate, the O vacancy is a common defect, there is growing evidence that oxygen vacancies have a significant impact upon the properties of perovskite materials designed for various applications. Such calculations would include the effect of oxygen vacancies associated with carbon impurity defects upon the structural, electrical, electronic and ferroelectric properties of these materials. Moreover, computational results for the oxygen vacancy diffusion associated with carbon impurity defects can help to provide a clearer picture of many phenomena, such as the leakage current in transistors, for example.

Hydrogen impurities, which are present in many grown perovskite crystals, have been observed experimentally. It has been considered that these impurities are a potential source of *n*-type conductivity. In addition, experimental measurements have found that, in $SrTiO_3$, strontium vacancy could be passivated by two hydrogen atoms. These results provide the motivation to extend this project by including hydrogen impurities in the defect structures in order to determined the effect of hydrogen complex defects on the physical and thermodynamic properties of perovskite titanate.

In the case of CdTe, the current calculations provide plausible evidence about the source of the two low temperature vibrational frequencies which have been observed experimentally. However, the evidence for the second oxygen atom is very weak experimentally. Therefore, the assumption of the incorporation of sulphur monoxide as a defect in CdTe crystal might be suitable, or the inclusion of the intrinsic defects associated with SO_2 could be used to identify the appropriate structure for these two peaks.

Bibliography

[1] E. V. Lavrov, D. Bastin, and J. Weber, "Reassignment of the O_{Te}-V_{Cd} complex in CdTe," *Phys. Rev. B* **84**, p. 233201, 2011.

[2] F. Mittendorfer and J. Hafner, "Initial steps in the desulfurization of thiophene/Ni(100)–A DFT study," *J. Catal.* **214**(2), p. 234, 2003.

[3] J. F. Dobson, M. P. Das, and G. Vignale, eds., *Electronic Density Functional Theory: Recent Progress & New Directions*, Kluwer Academic Publishers, New York, April 1998.

[4] R. M. Dreizler and E. K. U. Gross, *Density Functional Theory*, Springer, Berlin, 1990.

[5] W. Kohn and L. J. Sham, "Quantum density oscillation in an inhomogeneous electron gas," *Phys. Rev.* **137**(6), pp. A1697–A1705, 1965.

[6] P. Hohenberg and W. Kohn, "Inhomogeneous electron gas," *Phys. Rev.* **136**(3B), pp. 864–871, 1964.

[7] W. Kohn and L. J. Sham, "Self-consistent equations including exchange and correlation effects," *Phys. Rev.* **140**(4A), pp. A1133–A1138, 1965.

[8] W. Kohn, "Nobel lecture: electronic structure of matter-wave functions and density functionals," *Rev. Mod. Phys.* **71**, pp. 1253–1266, Oct. 1999.

[9] A. Becke, "Density-functional thermochemistry. iii. the role of exact exchange," *J. Chem. Phys.* **98**, p. 5648, 1993.

[10] S. Piskunov, E. Heifets, R. I. Eglitis, and G. Borstel, "Bulk properties and electronic structure of $SrTiO_3$, $BaTiO_3$, $PbTiO_3$ perovskites: an *Ab initio* HF/DFT study," *Comp. Mater. Sci.* **29**(2), p. 165, 2004.

[11] G. Shirane, R. Pepinsky, and B. C. Frazer, "X-ray and neutron diffraction study of ferroelectric $PbTiO_3$," *Acta Crystrallogr.* **9**(2), pp. 131–140, 1956.

[12] K. V. Benthem, C. Elsösser, and R. H. French, "Bulk electronic structure of $SrTiO_3$: Experiment and theory," *J. Appl. Phys.* **90**, p. 6156, 2001.

[13] S. H. Wemple, "Polarization fluctuations and the optical-absorption edge in $BaTiO_3$," *Phys. Rev. B* **2**, pp. 2679–2689, 1970.

[14] H. J. Monkhorst and J. D. Pack, "Special points for Brillouin-zone integrations," *Phys. Rev. B* **13**(12), pp. 5188–5192, 1976.

[15] M. L. Cohen and T. Bergstresser, "Band structure and pseudopotential form factors for fourteen semiconductors of the diamond and zinc-blende structures," *Phys. Rev.* **141**, pp. 789–796, 1966.

[16] C. Hartwigsen, S. Goedecker, and J. Hutter, "Relativistic separable dual-space gaussian pseudopotentials from H to Rn," *Phys. Rev. B* **58**(7), pp. 3641–3662, 1998.

[17] R. Jones, J. Goss, C. Ewels, and S. Öberg, "*Ab initio* calculations of anharmonicity of the C–H stretch mode in HCN and GaAs," *Phys. Rev. B* **50**(12), pp. 8378–8388, 1994.

[18] R. Ahuja, O. Eriksson, and B. Johansson, "Electronic and optical properties of $BaTiO_3$ and $SrTiO_3$," *J. Appl. Phys.* **90**(4), p. 1854, 2001.

[19] G. Makov and M. C. Payne, "Periodic boundary conditions in *ab initio* calculations," *Phys. Rev. B* **51**(7), pp. 4014–4122, 1995.

[20] A. Saedi, "A study on mutual interaction between atomistic and macroscopic phenomena during electrochemical processes using coupled finite difference kinetic monte carlo model: Application to potential step test in simple copper sulfate bath," *J. Electroanalytical Chem.* **588**(2), p. 267, 2006.

[21] G. Henkelman, B. P. Uberuaga, and H. Jónsson, "A climbing image nudged elastic band method for finding saddle points and minimum energy paths," *J. Chem. Phys.* **113**(22), pp. 9901–9904, 2000.

[22] G. Henkelman and H. Jónsson, "Improved tangent estimate in the nudged elastic band method for finding minimum energy paths and saddle points," *J. Chem. Phys.* **113**(22), pp. 9978–9985, 2000.

[23] F. M. Pontes, E. R. Leite, J. H. Lee, E. Longo, and J. A. Varela, "Preparation, microstructural and electrical characterization of $SrTiO_3$ thin films prepared by chemical route," *J. Euro. Ceramic Soc.* **21**, pp. 419–426, 2001.

[24] C. H. Ahn, K. M. Rabe, and J.-M. Triscone, "Ferroelectricity at the nanoscale: Local polarization in oxide thin films and heterostructures," *Science* **303**(5657), pp. 488–491, 2004.

[25] D. Kan, R. Kanda, Y. Kanemitsu, Y. Shimakawa, M. Takano, T. T., and A. Ishizumi, "Blue luminescence from electron-doped $SrTiO_3$," *Appl. Phys. Lett.* **88**(19), p. 191916, 2006.

[26] H. W. Jang, A. Kumar, S. Denev, M. D. Biegalski, P. Maksymovych, C. W. Bark, C. T. Nelson, C. M. Folkman, S. H. Baek, N. Balke, C. M. Brooks, D. A. Tenne, D. G. Schlom, L. Q. Chen, X. Q. Pan, S. V. Kalinin, V. Gopalan, and C. B. Eom, "Ferroelectricity in strain-free $SrTiO_3$ thin films," *Phys. Rev. Lett.* **104**, p. 197601, 2010.

[27] E. Bellingeri, L. Pellegrino, D. Marré, I. Pallecchi, and A. S. Siri, "All-$SrTiO_3$ field effect devices made by anodic oxidation of epitaxial semiconducting thin films," *J. Appl. Phys.* **94**(9), p. 5976, 2003.

[28] S. H. Jeon, B. H. Park, J. Lee, B. Lee, and S. Han, "First-principles modeling of resistance switching in perovskite oxide material," *Appl. Phys. Lett.* **89**(4), p. 042904, 2006.

[29] F. W. Lytle, "X-ray diffractometry of low-temperature phase transformations in strontium titanate," *J. Appl. Phys.* **35**, p. 2212, 1964.

[30] H. A. Jahn and E. Teller, "Stability of polyatomic molecules in degenerate electronic states. i. orbital degeneracy," *Proceedings of the Royal Society of London. Series A - Mathematical and Physical Sciences* **161**(905), p. 220, 1937.

[31] R. Evarestov, E. Blokhin, D. Gryaznov, E. A. Kotomin, R. Merkle, and J. Maier, "Jahn-teller effect in the phonon properties of defective $SrTiO_3$ from first principles," *Phys. Rev. B* **85**, p. 174303, 2012.

[32] H. Köppel, D. R. Yarkony, and H. Barentzen, eds., *The Jahn-Teller Effect*, Springer, New York, 2009.

[33] M. Dawber and J. F. Scott, "A model for fatigue in ferroelectric perovskite thin films," *Appl. Phys. Lett.* **76**(8), p. 1060, 2000.

[34] J. A. Brehm, J. W. Bennett, M. R. Schoenberg, I. Grinberg, and A. M. Rappe, "The structural diversity of ABS_3 compounds with d^0 electronic configuration for the b-cation," *J. Chem. Phys.* **140**(22), p. 224703, 2014.

[35] H. Kronmüller and S. Parkin, eds., *Handbook of Magnetism and Advanced Magnetic Materials*, vol. 4, Wiley, Weinheim, 2007.

[36] B. K. Choudhury, K. V. Rao, and R. N. P. Choudhury, "Dielectric properties of $SrTiO_3$ single crystals subjected to high electric fields and later irradiated with X-rays or γ-rays," *J. Mater. Sci.* **24**(10), p. 3469, 1989.

[37] S. Seiji, Y. Tetsuya, S. Hiroshi, K. Kenichi, T. Kazuhiko, and Y. Yorinobu, "Fabrication and characterization of $Ba_{1-x}K_xBiO_3$/Nb-doped $SrTiO_3$ all-oxide-type schottky junctions," *J. Appl. Phys.* **81**(10), pp. 6830–6836, 1997.

[38] J. H. Haeni, P. Irvin, W. Chang, R. Uecker, P. Reiche, Y. L. Li, S. Choudhury, W. Tian, M. E. Hawley, B. Craigo, A. K. Tagantsev, X. Q. Pan, S. K. Streiffer, L. Q. Chen, S. W. Kirchoefer, J. Levy, and D. G. Schlom, "Room-temperature ferroelectricity in strained $SrTiO_3$," *Nature* **430**, p. 758, 2004.

[39] M. P. Warusawithana, C. Cen, C. R. Sleasman, J. C. Woicik, Y. Li, L. F. Kourkoutis, J. A. Klug, H. Li, P. Ryan, L. Wang, M. Bedzyk, D. A. Muller, L. Chen, J. Levy, and D. G. Schlom, "A ferroelectric oxide made directly on silicon," *Science* **430**, p. 758, 2004.

[40] S. H. Baek, J. Park, D. M. Kim, V. A. Aksyuk, R. R. Das, S. D. Bu, D. A. Felker, J. Lettieri, V. Vaithyanathan, S. S. N. Bharadwaja, N. Bassiri-Gharb, Y. B. Chen, H. P. Sun, C. M. Folkman, H. W. Jang, D. J. Kreft, S. K. Streiffer, R. Ramesh, X. Q. Pan, S. Trolier-McKinstry, D. G. Schlom, M. S. Rzchowski, R. H. Blick, and C. B. Eom, "Giant piezoelectricity on Si for hyperactive MEMS," *Science* **334**(6058), p. 958, 2011.

[41] A. Kinaci, C. Sevik, and T. Cagin, "Electronic transport properties of $SrTiO_3$ and its alloys:$Sr_{1-x}La_xTiO_3$ and $SrTi_{1-x}M_xO_3$ (M=Nb,Ta)," *Phys. Rev. B* **82**, p. 155114, 2010.

[42] J. F. Schooley and W. R. Hosier, "Superconductivity in semiconducting $SrTiO_3$," *Phys. Rev. Lett.* **12**, pp. 474–475, 1964.

[43] L. Ryen, X. Wang, U. Helmersson, and E. Olsson, "Determination of the complex dielectric function of epitaxial $SrTiO_3$ films using transmission electron energy-loss spectroscopy," *J. Appl. Phys.* **85**(5), p. 2828, 1999.

[44] A. Kalabukhov, R. Gunnarsson, J. Börjesson, E. Olsson, T. Claeson, and D. Winkler, "Effect of oxygen vacancies in the $SrTiO_3$ substrate on the electrical properties of the $LaAlO_3/SrTiO_3$ interface," *Phys. Rev. B* **75**, p. 121404, 2007.

[45] C. Chang and Y. Shen, "Synthesis and characterization of chromium doped $SrTiO_3$ photocatalyst," *Mater. Lett.* **60**(1), p. 129, 2006.

[46] H. Kato and A. Kudo, "Visible-light-response and photocatalytic activities of TiO_2 and $SrTiO_3$ photocatalysts codoped with antimony and chromium," *J. Phys. Chem. B* **106**(19), p. 5029, 2002.

[47] K. Sayama, K. Mukasa, R. Abe, Y. Abe, and H. Arakawa, "A new photocatalytic water splitting system under visible light irradiation mimicking a Z-scheme mechanism in photosynthesis," *J. Photochem. Pthoboil. A, Chem.* **148**(13), p. 71, 2002.

[48] R. Asahi, T. Morikawa, T. Ohwaki, K. Aoki, and Y. Taga, "Visible-light photocatalysis in nitrogen-doped titanium oxides," *Science* **293**(5528), pp. 269–271, 2001.

[49] M. Djermouni, A. Zaoui, S. Kacimi, and B. Bouhafs, "Vacancy defects in strontium titanate: *Ab initio* calculation," *Comp. Mater. Sci.* **49**(4), 2010.

[50] W. Wei, D. Ying, G. Meng, Y. Lin, and H. Baibiao, "Density functional characterization of the electronic structure and optical properties of N-Doped, La-Doped, and N/La-Codoped $SrTiO_3$," *J. Phys. Chem. C* **113**(33), p. 15046, 2009.

[51] Z. Song, B. R. Rogers, and N. D. Theodore, "Spectroscopic ellipsometry characterization of ZrO_2 films on Si(100) deposited by high-vacuum-metalorganic chemical vapor deposition," *J. Vac. Sci. and Technol. A* **22**(3), pp. 711–718, 2004.

[52] R. A. McKee, F. J. Walker, and M. F. Chisholm, "Crystalline oxides on silicon: The first five monolayers," *Phys. Rev. Lett.* **81**(14), pp. 3014–3017, 1998.

[53] L. Yan, M. R. Suchomel, C. Grygiel, H. J. Niu, S. R. C. McMitchell, J. Bacsa, J. H. Clark, M. Werner, P. R. Chalker, and M. J. Rosseinsky, "High permittivity $SrHf_{0.5}Ti_{0.5}O_3$ films grown by pulsed laser deposition," *Appl. Phys. Lett.* **94**(23), p. 232903, 2009.

[54] R. L. Puurunen, "Surface chemistry of atomic layer deposition: A case study for the trimethylaluminum/water process," *J. Appl. Phys.* **97**(12), p. 121301, 2005.

[55] C. B. Zhang, L. Wielunski, and B. G. Willis, "Formation of strontium template on Si(100) by atomic layer deposition," *Appl. Surf. Sci.* **257**(11), pp. 4826–4830, 2011.

[56] A. Kosola, M. Putkonen, L. Johansson, and L. Niinistö, "Effect of annealing in processing of strontium titanate thin films by ALD," *Appl. Surf. Sci.* **211**(14), p. 102, 2003.

[57] B. G. Willis and A. Mathew, "Growth of ordered SrO layers on Si(100) using metal-organic surface reactions," *J. Vac. Sci. and Technol. A* **26**(1), p. 83, 2008.

[58] S. W. Lee, J. H. Han, S. Han, W. Lee, J. H. Jang, M. Seo, S. K. Kim, C. Dussarrat, J. Gatineau, Y. Min, and C. S. Hwang, "Atomic layer deposition of $SrTiO_3$ thin films with highly enhanced growth rate for ultrahigh density capacitors," *Chem. of Materials* **23**(8), p. 2227, 2011.

[59] M. Vehkamäki, T. Hänninen, M. Ritala, M. Leskelä, T. Sajavaara, E. Rauhala, and J. Keinonen, "Atomic layer deposition of $SrTiO_3$ thin films from a novel strontium precursorstrontium-bis(tri-isopropyl cyclopentadienyl)," *Chem. Vapor Dep.* **7**(2), p. 75, 2001.

[60] H. F. Liu, "Effect of nitrogen and carbon doping on electronic properties of $SrTiO_3$," *Solid State Commun.* **152**(22), p. 2063, 2012.

[61] N. Li and K. L. Yao, "The electronic and optical properties of carbon-doped $SrTiO_3$: Density functional characterization," *AIP Advances* **2**(3), p. 032135, 2012.

[62] J. Liu, L. Wang, J. Liu, T. Wang, W. Qu, and Z. Li, "DFT study on electronic structures and optical absorption properties of C, S cation-doped $SrTiO_3$," *Central European Journal of Physics* **7**(4), p. 762, 2009.

[63] J. P. Perdew and Y. Wang, "Accurate and simple analytic representation of the electron-gas correlation-energy," *Phys. Rev. B* **45**(23), pp. 13244–13249, 1992.

[64] P. R. Briddon and R. Jones, "LDA calculations using a basis of Gaussian orbitals," *Phys. Status Solidi B* **217**(1), pp. 131–171, 2000.

[65] M. J. Rayson and P. R. Briddon, "Rapid iterative method for electronic-structure eigenproblems using localised basis functions," *Computer Phys. Comm.* **178**, pp. 128–134, JAN 15 2008.

[66] J. P. Goss, M. J. Shaw, and P. R. Briddon, "Marker-method calculations for electrical levels using gaussian-orbital basis sets," in *Theory of Defects in Semiconductors*, D. A. Drabold and S. K. Estreicher, eds., *Topics in Applied Physics* **104**, pp. 69–94, Springer, Berlin/Heidelberg, 2007.

[67] M. J. Rayson and P. R. Briddon, "Highly efficient method for kohn-sham density functional calculations of 500-10000 atom systems," *Phys. Rev. B* **80**(20), p. 205104, 2009.

[68] R. A. Evarestov, S. Piskunov, E. A. Kotomin, and G. Borstel, "Single impurities in insulators: *ab initio* study of Fe-doped $SrTiO_3$," *Phys. Rev. B* **67**, p. 64101, 2003.

[69] C. B. Samantaray, H. Sim, and H. Hwang, "The electronic structures and optical properties of $BaTiO_3$ and $SrTiO_3$ using first-principles calculations," *Microelec. Journal* **36**, p. 725, 2005.

[70] M. Marques, L. K. Teles, V. Anjos, L. M. R. Scolfaro, J. R. Leite, V. N. Freire, G. A. Farias, and E. F. da Silva, "Full-relativistic calculations of the $SrTiO_3$ carrier effective masses and complex dielectric function," *Appl. Phys. Lett.* **82**, p. 3074, 2003.

[71] K. Jacob and G. Rajitha, "Thermodynamic properties of strontium titanates: Sr_2TiO_4, $Sr_3Ti_2O_7$, $Sr_4Ti_3O_{10}$, and $SrTiO_3$," *The Journal of Chemical Thermodynamics* **43**(1), p. 51, 2011.

[72] P. Haas, F. Tran, and P. Blaha, "Calculation of the lattice constant of solids with semilocal functionals," *Phys. Rev. B* **79**, p. 085104, 2009.

[73] J. Bashir, R. T. A. Khan, N. M. Butt, and G. Heger, "Thermal atomic displacement parameters of SrO," *Powder Diffraction* **17**, p. 222, 2002.

[74] K. Kholiya and B. R. K. Gupta, "Theoretical investigation of phase transition properties in strontium chalcogenides using potential model," *Phase Transitions* **81**(5), p. 403, 2008.

[75] T. Tanaka, K. Matsunaga, Y. Ikuhara, and T. Yamamoto, "First-principle study on structures and energetics of intrinsic vacancies in $SrTiO_3$," *Phys. Rev. B* **68**, p. 205213, 2003.

[76] P. Reunchan, N. Umezawa, S. Ouyang, and J. Ye, "Mechanism of photocatalytic activities in Cr-doped $SrTiO_3$ under visible-light irradiation: an insight from hybrid density-functional calculations," *Phys. Chem. Chem. Phys.* **14**, p. 1876, 2012.

[77] P. Reunchan, S. Ouyang, N. Umezawa, H. Xu, Y. Zhang, and J. Ye, "Theoretical design of highly active $SrTiO_3$-based photocatalysts by a codoping scheme towards solar energy utilization for hydrogen production," *J. Mater. Chem. A* **1**, pp. 4221–4227, 2013.

[78] D. R. Lide, ed., *Handbook of Chemistry and Physics*. Boca Raton, Florida: CRC Press., 91st ed., 2010.

[79] R. I. Kaiser and A. M. Mebel, "On the formation of higher carbon oxides in extreme environments," *Chem. Phys. Lett.* **465**(13), pp. 1–9, 2008.

[80] E. B. Scheetz and B. W. White, "Vibrational spectra of the alkaline earth double carbonates," *Am. Miner.* **62**, pp. 36–50, 1977.

[81] M. Patzschke and D. Sundholm, "Density-functional-theory studies of the infrared spectra of titanium carbide nanocrystals," *J. Phys. Chem. B* **109**(25), pp. 12503–12508, 2005.

[82] J. P. R. De Villiers, "Crystal structures of aragonite, strontianite, and witherite," *Am. Miner.* **56**, pp. 758–766, 1971.

[83] Z. Ci and Y. Wang, "Preparation, electronic structure, and photoluminescence properties of Eu^{2+}-activated carbonate $Sr_{1-x}Ba_xCO_3$ for white light-emitting diodes," *J. Electrochemical Soc.* **156**(9), pp. J267–J272, 2009.

[84] D. Krishnamurti, "The raman spectra of aragonite, strontianite and witherite," *Proceedings of the Indian Academy of Sciences - Section A* **51**(6), pp. 285–295, 1960.

[85] Y. Yuan, Z. Xiao, B. Yang, and J. Huang, "Arising applications of ferroelectric materials in photovoltaic devices," *J. Mater. Chem. A* **2**, pp. 6027–6041, 2014.

[86] G. H. Haertling and C. E. Land, "Hot-pressed (Pb,La)(Zr,Ti)O_3 ferroelectric ceramics for electrooptic applications," *J. Am. Ceramic Soc.* **54**(1), pp. 1–11, 1971.

[87] H. Miki and Y. Ohji, "Uniform ultra-thin Pb(Zr,Ti)O_3 films formed by metal-organic chemical vapor deposition and their electrical characteristics," *Japan J. Appl. Phys.* **33**, pp. 5143–5146, 1994.

[88] H. Nakasima, S. Hazumi, T. Kamiya, K. Tominaga, and M. Okada, "Electrical properties for capacitors of dynamic random access memory on (Pb,La)(Zr,Ti)O_3 thin films by metalorganic chemical vapor deposition," *Japan J. Appl. Phys.* **33**, pp. 5139–5142, 1994.

[89] W. Ren, Y. Liu, J. Qiu, L. Zhang, and X. Yao, "Properties of PLT thin films by thermal decomposition of metallo-organic compounds," *Ferroelectrics* **152**(1), p. 201, 1994.

[90] G. H. Haertling, "Ferroelectric ceramics: History and technology," *J. Am. Ceramic Soc.* **82**(4), pp. 797–818, 1999.

[91] P. Duran, J. F. Fdez Lozano, F. Capel, and C. Moure, "Large electromechanical anisotropic modified lead titanate ceramics," *J. Mater. Sci.* **23**(12), pp. 4463–4469, 1988.

[92] R. E. Cohen, "Origin of ferroelectricity in perovskite oxides," *Nature* **358**, pp. 136–138, 1992.

[93] Y. Kuroiwa, S. Aoyagi, A. Sawada, J. Harada, E. Nishibori, M. Takata, and M. Sakata, "Evidence for Pb–O covalency in tetragonal $PbTiO_3$," *Phys. Rev. Lett.* **87**, p. 217601, 2001.

[94] B. N. Sun, Y. Huang, and D. A. Payne, "Growth of large $PbTiO_3$ crystals by a self-flux technique," *J. Cryst. Growth* **128**(14), pp. 867–870, 1993.

[95] E. B. Tadmor, U. V. Waghmare, G. S. Smith, and E. Kaxiras, "Polarization switching in $PbTiO_3$: an *ab initio* finite element simulation," *Acta Mater.* **50**(11), p. 2989, 2002.

[96] H. Meštric, R.-A. Eichel, T. Kloss, K.-P. Dinse, S. Laubach, S. Laubach, and P. C. Schmidt, "Iron-oxygen vacancy defect centers in $PbTiO_3$: Newman superposition model analysis and density functional calculations," *Phys. Rev. B* **71**, p. 134109, 2005.

[97] A. G. Kalinichev, J. D. Bass, B. N. Sun, and D. A. Payne, "Elastic properties of tetragonal $PbTiO_3$ single crystals by brillouin scattering," *J. Mater. Res.* **12**, p. 2623, 1997.

[98] K. Oka, H. Unoki, H. Yamaguchi, and H. Takahashi, "Crystal growth of $PbTiO_3$ by the top-seeded solution-growth method," *J. Cryst. Growth* **166**(14), pp. 380–383, 1996.

[99] D. Vanderbilt, "First-principles based modelling of ferroelectrics," *Current Opinion in Solid State and Mater. Sci.* **2**(6), pp. 701–705, 1997.

[100] M. Mai, C. Lin, Z. Xiong, H. Xue, and L. Chen, "Preparation and characterization of lead zirconate titanate ceramic fibers with alkoxide-based sol-gel route," *J. Phys. Conf. Ser.* **152**(1), p. 012077, 2009.

[101] X. Liang, Z. Meng, and W. Wu, "Effect of acceptor and donor dopants on the dielectric and tunable properties of barium strontium titanate," *J. Am. Ceramic Soc.* **87**(12), pp. 2218–2222, 2004.

[102] M. V. Raymond, J. Chen, and D. M. Smyth, "Degradation of ferroelectric thin films: A defect chemistry approach," *Integrated Ferroelectrics* **5**(1), pp. 73–78, 1994.

[103] Q. Y. Jiang, E. C. Subbarao, and L. E. Cross, "Effect of composition and temperature on electric fatigue of La-doped lead zirconate titanate ceramics," *J. Appl. Phys.* **75**(11), p. 7433, 1994.

[104] K. Miura and M. Tanaka, "Effect of La-doping on fatigue in ferroelectric perovskite oxides," *Japan J. Appl. Phys.* **35**(3), p. 3488, 1996.

[105] S. B. Majumder, Y. N. Mohapatra, and D. C. Agrawal, "Fatigue resistance in lead zirconate titanate thin ferroelectric films: Effect of cerium doping and frequency dependence," *Appl. Phys. Lett.* **70**(1), pp. 138–140, 1997.

[106] M. Dawber, J. F. Scott, and A. J. Hartmann, "Effect of donor and acceptor dopants on schottky barrier heights and vacancy concentrations in barium strontium titanate," *J. Euro. Ceramic Soc.* **21**(1011), pp. 1633–1636, 2001.

[107] S. Kim, Y. Kang, and S. Baik, "Sputter deposition of ferroelectric $PbTiO_3$ thin films," *Ferroelectrics* **152**(1), pp. 1–6, 1994.

[108] C. C. Chang and W. J. Lin, "Study and fabrication of the $PbTiO_3$ thin film acoustic sensors," *Ultramicrosc.* **37**(8), pp. 585–588, 2000.

[109] K. Tsuchiya, T. Kitagawa, and E. Nakamachi, "Development of RF magnetron sputtering method to fabricate PZT thin film actuator," *Precision Eng.* **27**(3), pp. 258–264, 2003.

[110] Z. J. Wang, H. Kokawa, and R. Maeda, "Electrical properties and microstructure of lead zirconate titanate (PZT) thin films deposited by pulsed-laser deposition," *Cer. Int.* **30**(7), pp. 1529–1533, 2004.

[111] H. Park, S. Yoon, H. Park, and R. H. Hill, "Electrical properties of PZT thin films by photochemical deposition," *Thin Solid Films* **447448**, pp. 669–673, 2004.

[112] A. Li, D. Wu, C. Ge, H. Wang, M. Wang, Z. Liu, and N. Ming, "Structural and electrical properties of $PbTiO_3$ thin films on conductive oxide $LaNiO_3$ coated Si substrates prepared by sol-gel method," *Thin Solid Films* **375**(12), pp. 220–223, 2000.

[113] D. Bao, X. Yao, N. Wakiya, K. Shinozaki, and N. Mizutani, "Structural, dielectric, and ferroelectric properties of $PbTiO_3$ thin films by a simple sol-gel technique," *Mater. Sci. Eng. B* **94**(23), pp. 269–274, 2002.

[114] M. R. Mohammadi, S. A. Tabei, A. Nemati, D. Eder, and T. Pradeep, "Synthesis and crystallization of lead zirconiumtitanate (PZT) nanotubes at the low

temperature using carbon nanotubes (CNTs) as sacrificial templates," *Advanced Powder Technology* **23**(5), p. 647, 2012.

[115] J. Schäfer, W. Sigmund, S. Roy, and F. Aldinger, "Low temperature synthesis of ultrafine Pb(Zr, Ti)O_3 powder by sol-gel combustion," *J. Mater. Res.* **12**, pp. 2518–2521, 1997.

[116] K. Nishida, K. Shirakata, M. Osada, and T. Katoda, "Preparation and characterization of ultra-thin ferroelectric PZT films grown by plasma-assisted CVD," *J. Cryst. Growth* **272**, pp. 789–794, 2004.

[117] L. D. Madsen, E. M. Griswold, and L. Weaver, "Domain structures in Pb(Zr, Ti)O_3 and $PbTiO_3$ thin films," *J. Mater. Res.* **12**, pp. 2612–2616, 1997.

[118] D. Leinen, A. Caballero, A. Fernández, J. P. Espinós, A. Justo, A. R. González-Elipe, J. M. Martin, and B. Maurin-Perrier, "Structural characterization of $PbTiO_3$ thin films prepared by ion beam induced CVD and evaporation of lead," *Thin Solid Films* **272**(1), p. 99, 1996.

[119] T. Hirai, T. Goto, H. Matsuhashi, S. Tanimoto, and Y. Tarui, "Preparation of tetragonal perovskite single phase $PbTiO_3$ film using an improved metal-organic chemical vapor deposition method alternately introducing Pb and Ti precursors," *Japan J. Appl. Phys.* **32**, p. 4078, 1993.

[120] H. Meštric, R.-A. Eichel, K.-P. Dinse, A. Ozarowski, J. Tol, and L. C. Brunel, "High-frequency electron paramagnetic resonance investigation of the Fe^{3+} impurity center in polycrystalline $PbTiO_3$ in its ferroelectric phase," *J. Appl. Phys.* **96**(12), pp. 7440–7444, 2004.

[121] Y. S. Yoon, J. H. Kim, W. K. Choi, and S. J. Lee, "Characteristics of $PbTiO_3$ thin films on Pt/Ti/SiO_2/Si by continuous cooling process," *J. Mater. Sci.* **31**(22), p. 5877, 1996.

[122] J. Harjuoja, A. Kosola, M. Putkonen, and L. Niinistö, "Atomic layer deposition and post-deposition annealing of $PbTiO_3$ thin films," *Thin Solid Films* **496**(2), pp. 346–352, 2006.

[123] W. G. Hwang, J. H. Lee, K. Lee, and S. C. Hwang, "Atomic layer deposition and electrical properties of $PbTiO_3$ thin films using metallorganic precursors and H_2O," *J. Electrochemical Soc.* **154**, pp. G69–G76, 2007.

[124] O. S. Kwon, S. K. Kim, M. Cho, C. S. Hwang, and J. Jeong, "Chemically conformal ALD of $SrTiO_3$ thin films using conventional metallorganic precursors," *J. Electrochemical Soc.* **152**, pp. C229–C236, 2005.

[125] F. Jona and G. Sherane, *Ferroelectric Crystals*, Dover, New York, 1993.

[126] A. M. Glazer and S. A. Mabud, "Powder profile refinement of lead zirconate titanate at several temperatures. II. pure $PbTiO_3$," *Acta Crystrallogr. B* **34**(4), p. 1065, 1978.

[127] A. García and D. Vanderbilt, "First-principles study of stability and vibrational properties of tetragonal $PbTiO_3$," *Phys. Rev. B* **54**, pp. 3817–3824, 1996.

[128] P. Erhart, R. Eichel, P. Träskelin, and K. Albe, "Association of oxygen vacancies with impurity metal ions in lead titanate," *Phys. Rev. B* **76**, p. 174116, 2007.

[129] A. García and D. Vanderbilt, "First-principles study of stability and vibrational properties of tetragonal $PbTiO_3$," *Phys. Rev. B* **54**, p. 3817, 1996.

[130] G. Chevrie, G. Giester, G. Heger, D. Jarosch, M. Wildner, and J. Zemann, "Neutron single-crystal refinement of cerussite, $PbCO_3$, and comparison with other aragonite-type carbonates," *Z. Kristallogr.* **199**, pp. 67–74, 1992.

[131] F. A. Miller and C. H. Wilkins, "Infrared spectra and characteristic frequencies of inorganic ions," *Acta Crystrallogr.* **24**(8), pp. 1253–1294, 1952.

[132] P. Erhart, R. Eichel, P. Träskelin, and K. Albe, "Formation and switching of defect dipoles in acceptor-doped lead titanate: A kinetic model based on first-principles calculations," *Phys. Rev. B* **88**, p. 024107, 2013.

[133] A. Boonchun, M. F. Smith, B. Cherdhirunkorn, and S. Limpijumnong, "First principles study of Mn impurities in $PbTiO_3$ and $PbZrO_3$," *J. Appl. Phys.* **101**(4), p. 43521, 2007.

[134] H. P. Klug, "A. redetermination of the lattice constant of lead," *J. Am. Chem. Soc.* **68**(8), p. 1493, 1946.

[135] C. B. Kubaschewski and P. J. Spencer, *Materials Thermochemistry*, Pergamon, New York, 1993.

[136] D. O. Scanlon, A. B. Kehoe, G. W. Watson, M. O. Jones, I. F. D. William, D. J. Payne, R. G. Egdell, P. P. Edwards, and A. Walsh, "Nature of the band gap and origin of the conductivity of PbO_2 revealed by theory and experiment," *Phys. Rev. Lett.* **107**(24), p. 246402, 2011.

[137] S. Chatterjee, B. D. Stojanovic, and H. S. Maiti, "Effect of additives and powder preparation techniques on PTCR properties of barium titanate," *Mater. Chem. Phys.* **78**(3), pp. 702–710, 2003.

[138] G. Akcay, S. Zhong, S. P. Alpay, and J. V. Mantese, "Dynamic pyroelectric enhancement of homogeneous ferroelectric materials," *Solid State Commun.* **137**(11), pp. 589–594, 2006.

[139] B. Ertug, "The overview of the electrical properties of barium titanate," *Am. J. Eng. Res.* **2**(8), pp. 1–7, 2013.

[140] L. Simon-Seveyrat, A. Hajjaji, Y. Emziane, B. Guiffard, and D. Guyomar, "Re-investigation of synthesis of $BaTiO_3$ by conventional solid-state reaction and oxalate coprecipitation route for piezoelectric applications," *Cer. Int.* **33**(1), pp. 35–40, 2007.

[141] H. D. Megaw, "Temperature changes in the crystal structure of barium titanium oxide," *Proceedings of the Royal Society of London. Series A. Mathematical and Physical Sciences* **189**(1017), p. 261, 1947.

[142] P. Vousden, "An explanation of the structures of hexagonal barium titanate and titanium dioxide," *Acta Crystrallogr.* **9**(2), p. 141, 1956.

[143] T. Ishidate, S. Abe, H. Takahashi, and N. Môri, "Phase diagram of $BaTiO_3$," *Phys. Rev. Lett.* **78**, pp. 2397–2400, 1997.

[144] L. carlsson, "Crystal structure changes in $BaTiO_3$," *Acta Crystrallogr.* **20**(3), p. 459, 1966.

[145] T. A. Colson, M. J. S. Spencer, and I. Yarovsky, "A DFT study of the perovskite and hexagonal phases of $BaTiO_3$," *Comp. Mater. Sci.* **34**(2), p. 157, 2005.

[146] G. H. Kwei, A. C. Lawson, S. J. L. Billinge, and S. W. Cheong, "Structures of the ferroelectric phases of barium titanate," *J. Phys. Chem.* **97**(10), p. 2368, 1993.

[147] L. Mager, G. Pauliat, M. H. Garrett, D. Rytz, and G. Roosen, "Photorefractive $BaTiO_3$: an efficient material for laser wavefront correction," *Optical Materials* **4**(23), p. 381, 1995.

[148] H. Kröse, E. Possenriede, R. Scharfschwerdt, T. Varnhorst, O. F. Schirmer, H. Hesse, and C. Kuper, "Optically induced charge transfer paths between defects in $BaTiO_3$ containing rhodium," *Optical Materials* **4**(23), p. 153, 1995.

[149] K. Kinoshita and A. Yamaji, "GrainâĂŘsize effects on dielectric properties in barium titanate ceramics," *J. Appl. Phys.* **47**(1), pp. 371–373, 1976.

[150] M. H. Frey and D. A. Payne, "Grain-size effect on structure and phase transformations for barium titanate," *Phys. Rev. B* **54**, pp. 3158–3168, 1996.

[151] R. D. King-Smith and D. Vanderbilt, "First-principles investigation of ferroelectricity in perovskite compounds," *Phys. Rev. B* **49**, pp. 5828–5844, 1994.

[152] S. Saha, T. P. Sinha, and A. Mookerjee, "Electronic structure, chemical bonding, and optical properties of paraelectric $BaTiO_3$," *Phys. Rev. B* **62**, pp. 8828–8834, 2000.

[153] R. Roussev and A. J. Millis, "Theory of the quantum paraelectric-ferroelectric transition," *Phys. Rev. B* **67**, p. 014105, 2003.

[154] W. Zhong, D. Vanderbilt, and K. M. Rabe, "Phase transitions in $BaTiO_3$ from first principles," *Phys. Rev. Lett.* **73**, pp. 1861–1864, 1994.

[155] K. Miura, M. Azuma, and H. Funakubo, "Electronic and structural properties of ABO_3: Role of the B-O coulomb repulsions for ferroelectricity," *Materials* **4**(1), pp. 260–273, 2011.

[156] S. Pöykkö and D. J. Chadi, "Dipolar defect model for fatigue in ferroelectric perovskites," *Phys. Rev. Lett.* **83**, pp. 1231–1234, 1999.

[157] V. J. Ghosh, B. Nielsen, and T. Friessnegg, "Identifying open-volume defects in doped and undoped perovskite-type $LaCoO_3$, $PbTiO_3$, and $BaTiO_3$," *Phys. Rev. B* **61**, pp. 207–212, 2000.

[158] R. N. Schwartz and B. A. Wechsler, "Spectroscopic properties of photorefractive $BaTiO_3$ double doped with cerium and rhodium," *Phys. Rev. B* **61**, pp. 8141–8149, 2000.

[159] A. Stashans and J. Chimborazo, "Effect of interstitial hydrogen on structural and electronic properties of $BaTiO_3$," *Phil. Mag. B* **82**(10), p. 1145, 2002.

[160] H. I. Yoo, M. W. Chang, T. S. Oh, C. E. Lee, and K. D. Becker, "Electrocoloration and oxygen vacancy mobility of $BaTiO_3$," *J. Appl. Phys.* **102**(9), p. 093701, 2007.

[161] X. Chen, W. Lu, and S. C. Shen, "First-principles study of photoconductivity in $BaTiO_3$ with oxygen vacancies," *Solid State Commun.* **130**(10), pp. 641–645, 2004.

[162] M. Rao, K. a. R. M. Ramesh, and B. Rao, "Effect of copper doping on structural, dielectric and dc electrical resistivity properties of $BaTiO_3$," *Adv. in Mat. Phys. Chem.* **87**(7), pp. 77–82, 2013.

[163] V. Vinothini, P. Singh, and M. Balasubramanian, "Synthesis of barium titanate nanopowder using polymeric precursor method," *Cer. Int.* **32**(2), p. 99, 2006.

[164] H. S. Potdar, S. B. Deshpande, and S. K. Date, "Chemical coprecipitation of mixed (ba0ti) oxalates precursor leading to $BaTiO_3$ powders," *Mater. Chem. Phys.* **58**(2), pp. 121–127, 1999.

[165] W. Cho, "Structural evolution and characterization of $BaTiO_3$ nanoparticles synthesized from polymeric precursor," *J. Phys. Chem. Solids* **59**(5), pp. 659–666, 1998.

[166] W. Cho and E. Hamada, "Synthesis of ultrafine $BaTiO_3$ particles from polymeric precursor: their structure and surface property," *J. Alloys and Compounds* **266**(12), pp. 118–122, 1998.

[167] B. Li, X. Wang, and L. Li, "Synthesis and sintering behavior of $BaTiO_3$ prepared by different chemical methods," *Mater. Chem. Phys.* **78**(1), pp. 292–298, 2003.

[168] A. Prasadarao, M. Suresh, and S. Komarneni, "pH dependent coprecipitated oxalate precursors a thermal study of barium titanate," *Mater. Lett.* **39**(6), p. 359, 1999.

[169] B. D. Stojanovic, A. Z. Simoes, C. O. Paiva-Santos, C. Jovalekic, V. V. Mitic, and J. A. Varela, "Mechanochemical synthesis of barium titanate," *J. Euro. Ceramic Soc.* **25**(12), pp. 1985–1989, 2005.

[170] B. D. Stojanovic, C. Jovalekic, V. Vukotic, A. Z. Simoes, and J. A. Varela, "Ferroelectric properties of mechanically synthesized nanosized barium titanate," *Ferroelectrics* **319**(1), pp. 65–73, 2005.

[171] H. Lee, S. Moon, C. Choi, and D. K. Kim, "Synthesis and size control of tetragonal barium titanate nanopowders by facile solvothermal method," *J. Am. Ceramic Soc.* **95**(8), p. 2429, 2012.

[172] G. J. Reynolds, M. Kratzer, M. Dubs, H. Felzer, and R. Mamazza, "Sputtered modified barium titanate for thin-film capacitor applications," *Materials* **5**(4), pp. 575–589, 2012.

[173] M. G. Norton, C. Scarfone, J. Li, C. B. Carter, and J. W. Mayer, "Epitaxy of barium titanate thin films grown on mgo by pulsed-laser ablation," *J. Mater. Res.* **6**, pp. 2022–2025, 1991.

[174] T. P. Holme and F. B. Prinz, "Atomic layer deposition and chemical vapor deposition precursor selection method application to strontium and barium precursors," *J. Phys. Chem. A* **111**(33), pp. 8147–8151, 2007.

[175] M. Vehkamäki, T. Hatanpää, M. Ritala, M. Leskelä, S. Väyrynen, and E. Rauhala, "Atomic layer deposition of $BaTiO_3$ thin filmseffect of barium hydroxide formation," *Chem. Vapor Dep.* **13**(5), pp. 239–246, 2007.

[176] J. Tsay, T. Fang, T. A. Gubiotti, and J. Y. Ying, "Evolution of the formation of barium titanate in the citrate process: the effect of the pH and the molar ratio of barium ion and citric acid," *J. Mater. Sci.* **33**(14), pp. 3721–3727, 1998.

[177] A. V. Bandura and R. A. Evarestov, "First-principles calculations on thermodynamic properties of $BaTiO_3$ rhombohedral phase," *J. Comp. Chem.* **33**(18), p. 1554, 2012.

[178] P. Ghosez, X. Gonze, and J. P. Michenaud, "First-principles characterization of the four phases of barium titanate," *Ferroelectrics* **220**(1), pp. 1–15, 1999.

[179] A. W. Hewat, "Structure of rhombohedral ferroelectric barium titanate," *Ferroelectrics* **6**(1), pp. 215–218, 1973.

[180] S. M. Tavender, S. A. Johnson, D. Balsom, w. A. Parker, and R. H. Bisby, "The carbonate, CO_3^- in solution studied by ressonance spectroscopy," *Laser Chem.* **19**, pp. 311–316, 1999.

[181] H. Moriwake, "First-principles calculation of formation energy of neutral point defects in perovskite-type $BaTiO_3$," *Int. J. Quant. Chem.* **99**(5), pp. 824–827, 2004.

[182] H.-S. Lee, T. Mizoguchi, T. Yamamoto, S.-J. L. Kang, and Y. Ikuhara, "First-principles calculation of defect energetics in cubic-$BaTiO_3$ and a comparison with srtio3," *Acta Mater.* **55**(19), pp. 6535–6540, 2007.

[183] P. D. Vernooy, "Redetermination of the structure of barium peroxide by single-crystal X-ray diffraction," *Acta Crystallogr. C* **49**(3), p. 433, 1993.

[184] P. Erhart and K. Albe, "Thermodynamics of mono- and di-vacancies in barium titanate," *J. Appl. Phys.* **102**(8), p. 084111, 2007.

[185] R. G. Amorim, M. Veríssimo-Alves, and J. P. Rino, "Energetics of phase transitions in bao through dft calculations with norm-conserving pseudopotentials: Lda vs. gga results," *Comp. Mater. Sci.* **37**(3), pp. 349–354, 2006.

[186] J. A. Dawson, J. H. Harding, H. Chen, and D. C. Sinclair, "First-principles study of intrinsic point defects in hexagonal barium titanate," *J. Appl. Phys.* **111**(9), p. 094108, 2012.

[187] I. Massalimov, M. Kireeva, and Y. Sangalov, "Structure and properties of mechanically activated barium peroxide," *Inorg. Mater.* **38**(4), pp. 363–366, 2002.

[188] L. Till, "Thermochemical data of barium peroxide from thermogravimetric measurements," *J. Therm. Anal.* **3**(2), pp. 177–180, 1971.

[189] R. J. Zollweg, "X-ray lattice constant of barium oxide," *Phys. Rev.* **100**, pp. 671–673, 1955.

[190] P. G. Sundell, M. E. Björketun, and G. Wahnström, "Thermodynamics of doping and vacancy formation in $BaZrO_3$ perovskite oxide from density functional calculations," *Phys. Rev. B* **73**, p. 104112, 2006.

[191] J. Robertson, "Band offsets of wide-band-gap oxides and implications for future electronic devices," *Journal of Vacuum Science and Technology B* **18**(3), pp. 1785–1791, 2000.

[192] J. C. Kotz, P. M. Treichel, and G. C. Weaver, eds., *Chemistry and Chemical Reactivity*, Thomason, USA, 2006.

[193] B. P. Uberuaga and G. Pilania, "Effect of cation ordering on oxygen vacancy diffusion pathways in double perovskites," *Chem. Mater.* **27**(14), pp. 5020–5026, 2015.

[194] k. Sato, m. Hanafusa, A. Noda, A. Arakawa, M. Uchida, T. Asahi, and O. Oda, "ZnTe pure green light-emitting diodes fabricated by thermal diffusion," *J. Cryst. Growth* **214-215**, pp. 1080–1084, 2000.

[195] V. A. Gnatyuk, S. N. Levytskyi, O. I. Vlasenko, and T. Aoki, "Laser-induced doping of CdTe crystals in different environments," *Appl. Magn. Reson.* **222**, p. 32, 2011.

[196] H. Hernández-Contreras, C. Mejía-García, and G. Contreras-Puente, "Optical study of the influence of $CdCl_2$ in large area CdS thin films grown by RF-sputtering," *Thin Solid Films* **451-452**, pp. 203–206, 2004.

[197] A. Romeo, D. L. Bätzner, H. Zogg, and A. N. Tiwari, "Recrystallization in CdTe/CdS," *Thin Solid Films* **361-362**, pp. 420–425, 2000.

[198] M. Becerril, O. Zelaya-Angel, J. R. Vargas-García, R. Ramírez-Bon, and J. González-Hernández, "Effects of Cd vacancies on the electrical properties

of polycrystalline CdTe sputtered films," *J. Phys. Chem. Solids* **62**, p. 1081, 2001.

[199] E. Guni, J. Durst, T. Michel, and G. Anton, "Material reconstruction with the Medipix2 detector with CdTe sensor," *Journal of Instrumentation* **6**, pp. 1–5, 2011.

[200] C. Szeles, "CdZnTe and CdTe materials for X-ray and gamma ray radiation detector applications," *Phys. Status Solidi* **241**, pp. 783–790, 2004.

[201] I. A. Sokolov, M. A. Bryushinin, V. V. Kulikov, A. S. Abyzov, L. N. Davydov, V. E. Kutny, A. V. Rybka, and V. V. Slezov, "Characterization of CdTe, $Cd_xZn_{(x-1)}Te$ and GaAs detectors," *Nucl. Instrum. Methods A* **610**, p. 298, 2009.

[202] S. Wei and S. B. Zhang, "Chemical trends of defect formation and doping limit in II-VI semiconductors: The case of CdTe," *Phys. Rev. B* **66**, p. 155211, 2002.

[203] Y. Marfaing, "Impurity doping and compensation mechanisms in CdTe," *Thin Solid Films* **387**, p. 123, 2001.

[204] A. L. Fahrenbruch, "II-VI compounds in solar energy conversion," *J. Cryst. Growth* **39**, pp. 73–91, 1977.

[205] N. Krsmanovic, K. G. Lynn, M. H. Weber, R. Tjossem, T. Gessmann, C. Szeles, E. E. Eissler, J. P. Flint, and H. L. Glass, "Electrical compensation in CdTe and $Cd_{0.9}Zn_{0.1}Te$ by intrinsic defects," *Phys. Rev. B* **62**(24), pp. R16 279–R16 282, 2000.

[206] S. A. Awadalla, A. W. Hunt, K. G. Lynn, H. Glass, C. Szeles, and S. Wei, "Isoelectronic oxygen-related defect in CdTe crystals investigated using thermoelectric effect spectroscopy," *Phys. Rev. B* **69**, p. 075210, 2004.

[207] G. Contreras-Puente, O. Vigil-Galán, J. Vidal-Larramendi, F. Gruz-Gandarilla, M. Hesiquio-Garduño, J. Aquilar-Hernández, and A. Cruz-Orea, "Influence of

the growth conditions in the properties of the CdTe thin films deposited by CSVT," *Thin Solid Films* **387**, pp. 50–53, 2001.

[208] K. Akimoto, H. Okuyama, M. Ikeda, and Y. Mori, "Isoelectronic oxygen in II-VI semiconductors," *Appl. Phys. Lett.* **60**, pp. 91–93, 1992.

[209] T. M. Hsu, R. J. Jih, P. C. Lin, H. Y. Ueng, Y. J. Hsu, and H. L. Hwang, "Oxygen doping in close-spaced-sublimed CdTe thin films for photovoltaic cells," *J. Appl. Phys.* **59**(10), pp. 3607–3609, 1986.

[210] M.-H. Du, H. Takenaka, and D. J. Singh, "Carrier compensation in semi-insulating CdTe: First-principles calculations," *Phys. Rev. B* **77**, p. 094122, 2008.

[211] M.-H. Du, H. Takenaka, and D. J. Singh, "Native defects and oxygen and hydrogen-related defect complexes in CdTe: Density functional calculations," *J. Appl. Phys.* **104**, p. 093521, 2008.

[212] Z. C. Huang, E. Eissler, and C. R. Wie, "Role of cadmium vacancy-related defects in cdte nuclear detectors," *Nucl. Instrum. Methods B* **100**(4), pp. 507–510, 1995.

[213] M. Fiederle, D. Ebling, C. Eiche, P. Hug, W. Joerger, M. Laasch, R. Schwarz, M. Salk, and K. W. Benz, "Studies of the compensation mechanism in CdTe grown from the vapour phase," *J. Cryst. Growth* **146**, pp. 142–147, 1995.

[214] M. Fiederle, C. Eiche, M. Salk, R. Schwarz, K. W. Benz, W. Stadler, D. M. Hofmann, and B. K. Meyer, "Modified compensation model of CdTe," *J. Appl. Phys.* **84**, pp. 6689–6692, 1998.

[215] T. E. Schlesinger, J. E. Toney, H. Yoon, E. Y. Lee, B. A. Brunett, L. Franks, and R. B. James, "Cadmium zinc telluride and its use as a nuclear radiation detector material," *Mater. Sci. Eng. R* **32**, pp. 103–189, 2001.

[216] M. Fiederle, V. Babentsov, J. Franc, A. Fauler, and J.-P. Konrath, "Growth of high resistivity CdTe and (Cd,Zn)Te crystals," *Cryst. Res. Technol.* **38**(7), 2003.

[217] M. A. Berding, "Native defects in CdTe," *Phys. Rev. B* **60**(12), pp. 8943–8950, 1999.

[218] G. Ghislotti, S. M. Pietralunga, and L. Ripamonti, "Effect of deep traps on photo-generated carrier dynamics in high-resistivity CdTe," *J. Cryst. Growth* **214-215**, pp. 212–215, 2000.

[219] G. Chen, I. Miotkowski, S. Rodriguez, and A. K. Ramdas, "Stoichiometry driven impurity configurations in compound semiconductors," *Phys. Rev. Lett.* **96**, p. 035508, 2006.

[220] G. Chen, I. Miotkowski, S. Rodriguez, and A. K. Ramdas, "Control of defect structure in compound semiconductors with stoichiometry: Oxygen in CdTe," *Phys. Rev. B* **75**, p. 125204, 2007.

[221] L. Zhang, J. T-Thienprasert, M.-H. Du, D. J. Singh, and S. Limpijumnong, "Comment on spectroscopic signatures of novel oxygen-defect complexes in stoichiometrically controlled CdSe," *Phys. Rev. Lett.* **102**, p. 209601, 2009.

[222] J. T-Thienprasert, S. Limpijumnong, A. Janotti, C. G. Van de Walle, L. Zhang, M.-H. Du, and D. J. Singh, "Vibrational signatures of O_{Te} and O_{Te}-V_{Cd} in CdTe: A first-principles study," *Comp. Mater. Sci.* **49**, pp. S242–S245, 2010.

[223] R. Cuscó, J. Ibáñez, N. Domenech-Amador, L. Artús, J. Zúñiga Pérez, and V. Muñoz Sanjosé, "Raman scattering of cadmium oxide epilayers grown by metal-organic vapor phase epitaxy," *J. Appl. Phys.* **107**(6), p. 063519, 2010.

[224] L. Svob and Y. Marfaing, "Hydrogen-acceptor interaction in CdTe and ZnTe studied by photoluminescence," *Solid State Commun.* **58**(6), pp. 343–346, 1986.

[225] A. P. Jacob, Q. X. Zhao, M. Willander, T. Baron, and N. Magnea, "Hydrogen passivation of nitrogen acceptors confined in CdZnTe quantum well structures," *J. Appl. Phys.* **90**(5), p. 2329, 2001.

[226] J. Polit, A. Kisiel, A. Mycielski, A. Marcelli, E. Sheregii, J. Cebulski, M. Piccinini, M. C. Guidi, B. V. Robouch, and A. Nucara, "Vibrational spectra of hydrogenated CdTe," *Phys. Status Solidi C* **2**(3), pp. 1147–1154, 2005.

[227] W. Cheng, L. Liu, P. Y. Yu, Z. X. Ma, and S. S. Mao, "A tale of two vacancies," *Ann. Phys.* **523**, pp. 129–136, 2011.

[228] O. Madelung, M. Schulz, and H. Weiss, *Numerical Data and Functional Relationships in Science and Technology*, vol. 17 of *Landolt-Börnstein, New Series*, Springer, Berlin, 1982.

[229] O. Zakharov, A. Rubio, X. Blase, L. M. Cohen, and S. G. Louie, "Quasiparticle band structures of six II-VI compounds: ZnS, ZnSe, ZnTe, CdS, CdSe, and CdTe," *Phys. Rev. B* **50**, p. 10780, 1994.

[230] D. R. Lide, ed., *CRC handbook of chemistry and physics*, CRC Press, Boca Raton, Florida, USA, 77 ed., 1996.

[231] D. R. Lide, *CRC Handbook of chemistry and physics*, Chemical Rubber Company, Boca Raton, 2008.

[232] L. Pauling, *General Chemistry*, Courier Dover, New York, 1988.

[233] M. R. Nimlos and G. B. Ellison, "Photoelectron spectroscopy of sulfur-containing anions SO_2^-, S_3^-, and S_2O^-," *J. Phys. Chem.* **90**(12), pp. 2574–2580, 1986.

[234] S. P. Belov, M. Y. Tretyakov, I. N. Kozin, E. Klisch, G. Winnewisser, W. J. Lafferty, and J.-M. Flaud, "High frequency transitions in the rotational spectrum of so_2," *J. Mol. Spectrosc.* **191**(1), pp. 17–27, 1998.

[235] T. E. Schlesinger, J. E. Toney, H. Yoon, E. Y. Lee, B. A. Brunett, L. Franks, and R. B. James, "Cadmium zinc telluride and its use as a nuclear radiation detector material," *Mater. Sci. Eng. R* **32**, p. 103, 2001.

[236] C. He-Ying, L. Zhao-Xia, Q. Guo-Li, K. De-Guo, W. Si-Xin, L. Yun-Cai, and D. Zu-Liang, "First-principles study of structures and electronic properties of cadmium sulfide clusters," *Chinese Physics B* **17**(7), p. 2478, 2008.

[237] J. Robertson, K. Xiong, and S. J. Clark, "Band structure of functional oxides by screened exchange and the weighted density approximation," *Phys. Status Solidi B* **73**(9), p. 2054, 2006.

[238] B. Lee and L.-W. Wang, "Nonlocal exchange correlation in screened-exchange density functional methods," *Phys. Rev. B* **76**(24), p. 245114, 2007.

[239] R. Gillen and J. Robertson, "The screened-exchange approximation as alternative method for DFT calculations on graphene structures," *Phys. Status Solidi B* **81**(11), p. 2945, 2010.